

学 位 論 文

Search for Supersymmetry and Universal Extra Dimensions

with Degenerate Mass Spectrum

in Proton-Proton Collisions at $\sqrt{s} = 7$ TeV

縮退したスペクトラムを持つ超対称性粒子や余剰次元の

LHC 7 TeV データを用いた探索

平成 24 年 12 月博士 (理学) 申請

東京大学大学院理学系研究科

物理学専攻

山口 博史

Doctoral Thesis

Search for Supersymmetry and Universal Extra Dimensions
with Degenerate Mass Spectrum
in Proton-Proton Collisions at $\sqrt{s} = 7$ TeV

December 18, 2012

Department of Physics, The University of Tokyo

Hiroshi Yamaguchi

Abstract

Searching for a supersymmetry (SUSY) and extra dimensions with degenerate mass spectrum in collision at a center-of-mass energy of 7 TeV is presented. This search is based on 4.7 fb^{-1} of data collected by ATLAS experiment and Large Hadron Collider (LHC).

This analysis focuses on “degenerate model” with the mass difference of $\Delta m/m \sim 5\text{-}30\%$ where m is mass for the heaviest particle and Δm is mass difference between the mass of the initially produced colored particles and the lightest particle in the model. So far, the SUSY searches are targeting models with large mass difference as $\Delta m/m \sim 80\%$ and the analyses do not have sensitivity to such degenerate model. In this analysis, the degenerate SUSY model and universal extra dimensions (UED) model are searched for by optimizing the event selection. The UED model has a similar mass spectrum to those of SUSY models and is characterized by three parameters; compactification scale $1/R$, cut-off scale Λ and Higgs boson mass, so that the analysis for the degenerate model are optimized to both signal models.

The final state of such degenerate model is characterized by leptons and jets with low transverse momentum (soft leptons and soft jets) due to small mass difference, a large missing transverse energy from the lightest neutral particles and an additional high transverse momentum jet derived from initial state radiation. Analyses in a high transverse momentum lepton channels optimized to general SUSY models are combined with this analysis to improve the sensitivity to the degenerate models.

The results show that the observed data are consistent with the background expectations in each signal region. In absence of an excess, 95% confidence level exclusion limits are set for the simplified SUSY model and UED model. The gluino pair production of simplified SUSY model is excluded in degenerate mass region where the mass of gluino $m_{\tilde{g}}$ and the lightest SUSY particle m_{LSP} are approximately below 540 GeV and 450 GeV, respectively. The UED model is also excluded below 840 GeV in $1/R$ space with $\Lambda R = 5$.

Contents

1	Introduction	4
1.1	The Standard Model	4
1.2	Grand Unification and Hierarchy Problem	6
1.3	The Beyond Standard Model	7
1.3.1	Minimal Supersymmetric Standard Model (MSSM)	7
1.3.2	Universal Extra Dimension (UED)	13
2	Event Topology	15
2.1	2011 Summer Results at $\int Ldt = 1.0\text{-}1.4 \text{ fb}^{-1}$ with Supersymmetry Model	15
2.2	Analysis Overview	15
3	LHC and ATLAS Detector	19
3.1	Large Hadron Collider (LHC)	19
3.1.1	Injector Chain	20
3.1.2	LHC Main Ring	20
3.2	ATLAS Detector	21
3.2.1	ATLAS Coordinate System	21
3.2.2	Magnet System	22
3.2.3	Inner Detector (ID)	23
3.2.4	Calorimeter	24
3.2.5	Muon Spectrometer (MS)	28
3.2.6	Trigger System	30
3.2.7	Luminosity Detector	30
4	Data and Monte Carlo samples	33
4.1	2011 Data	33
4.2	Monte Carlo (MC) Samples	34
4.2.1	Generations of Monte Carlo Samples	34
4.2.2	Monte Carlo Samples	37
5	Object Definition	40
5.1	Electron	40
5.2	Muon	40
5.3	Jet	40
5.4	Missing Transverse Energy E_T^{miss}	41
5.5	Definitions of variables	43
6	Event Selection	45
6.1	Event Cleaning	45
6.2	Trigger	46
6.3	Signal Region	47
6.3.1	Degenerate Model	48
6.3.2	MSUGRA High $m_{1/2}$ Region	51
6.3.3	MSUGRA High m_0 Region	51
6.4	Expected Significance	52

7	Background Estimation	54
7.1	Multijets Background	55
7.1.1	Identification Efficiency for Real Leptons	56
7.1.2	Misidentification Efficiency for Electrons in High p_T Region ($p_T^e > 25$ GeV)	56
7.1.3	Misidentification Efficiency for Muon in High p_T Region ($p_T^\mu > 20$ GeV)	59
7.1.4	Misidentification Efficiencies for Low p_T Leptons ($7 < p_T^e < 25$ GeV or $6 < p_T^\mu < 20$ GeV)	60
7.2	W +jets and $t\bar{t}$ Background	62
7.2.1	Fit Configurations	62
7.2.2	Shape Correction	63
7.2.3	Normalizations	64
7.3	Validation Regions	68
8	Uncertainties	73
8.1	Systematic Uncertainties	73
8.2	Theoretical Uncertainties	75
8.3	Signal Cross Section Uncertainties	77
8.3.1	Factorization and Renormalization Scale Uncertainty	77
8.3.2	PDF Uncertainty	77
8.3.3	ISR Uncertainty	77
8.3.4	Combined Uncertainty	78
8.4	Total Uncertainties Estimations	78
9	Results	82
9.1	Testing the background-only hypothesis	82
9.2	Exclusion Limit	86
9.3	Summary and Prospects	91
10	Conclusion	92
A	MSUGRA and UED Mass Spectrum	94
A.1	MSUGRA	94
A.1.1	Gauginos Mass	94
A.1.2	Neutralinos Mass	94
A.1.3	Charginos Mass	95
A.1.4	Squark and Slepton Mass	95
A.2	minimal UED	97
B	Performance	100
B.1	Electron	100
B.1.1	Electron Reconstruction	100
B.1.2	Electron Identification	100
B.1.3	Electron Energy Scale	101
B.1.4	Electron Energy Resolution	102
B.1.5	Electron Scale Factors	103
B.2	Muon	104
B.2.1	Muon Reconstruction	104
B.2.2	Muon Momentum Resolution	107
B.2.3	Muon Reconstruction Efficiency and Scale Factor	108
B.3	Jet	108
B.3.1	Jet Reconstruction	108
B.3.2	Jet Energy Scale Uncertainty	110
B.3.3	b -tag algorithm	111
B.3.4	b -tagging Efficiency and Scale Factor	112
B.4	Missing Transverse Energy E_T^{miss}	114
B.4.1	Systematic Uncertainties	116
B.5	Luminosity Measurements	118

C	Simultaneous Fit	122
C.1	Profiling Likelihood Method	122
C.2	Asymptotic approach	123
C.3	Experimental Sensitivity	124
C.4	Fit Configuration	125
C.4.1	Fit Parameters	125
C.4.2	Fit Configurations	126
C.4.3	Fit Options	126
C.5	Closure Test	127
C.6	Signal-Strength-Only Fit Results	131
C.7	Exclusion Region for SUSY models	133
D	Electromagnetic Scale Calibration in Tile Calorimeter	137
D.1	Introduction	137
D.2	Experimental Setup	137
D.2.1	CTB setup	137
D.2.2	The Tile calorimeter	138
D.3	Reconstruction and Event Selection	138
D.3.1	Reconstruction	138
D.3.2	Event Selection	140
D.3.3	The Monte Carlo simulation	140
D.4	Results	142
D.4.1	$dE/d\ell$ distributions	142
D.4.2	Data/MC ratios	142
D.4.3	Non uniformity of cell responses	144
D.4.4	Systematic uncertainties	146
D.5	Conclusion	147
	Bibliography	151

Chapter 1

Introduction

The Standard Model describes three interactions as electromagnetic, weak and strong interactions by gauge theory, and the electromagnetic and weak interactions are unified in the model [1,2]. Predictions in the Standard Model are consistent with results of high energy experiments around electroweak scale (~ 100 GeV). On basis of the Standard Model, grand unification theory (GUT) which unifies the electromagnetic, weak and strong interactions is expected.

If GUT scale ($\sim 10^{16}$ GeV) and Planck scale ($\sim 10^{19}$ GeV) exists, it is difficult for Higgs bosons to be stable due to contribution from Planck scale. To solve the problem, candidate models; supersymmetry (SUSY) model [3–11] and extra dimensions model [12–15] are proposed.

From 2010, Large Hadron Collider (LHC) and ATLAS experiment started the operation of proton-proton collision with center-of-mass energy of 7 TeV, and have searched for such models. Most of analyses for SUSY search are optimized to mass difference about 80% between the heaviest and the lightest particle in the model. This analysis focuses on a degenerate SUSY model and Universal Extra Dimensions (UED) [16–19] whose mass difference are 5-20% in final states with jets, missing transverse energy and an isolated low transverse momentum lepton.

In this chapter, the Standard Model, the hierarchy problem and beyond the Standard Model as the SUSY and the UED model are introduced.

1.1 The Standard Model

The Standard Model (SM) of the electroweak interactions is based on the gauge group $SU(2) \times U(1)$, with gauge bosons W_μ^i , $i = 1, 2, 3$, and B_μ for the $SU(2)$ and $U(1)$ factors, respectively, and the corresponding gauge coupling constants g_1 and g_2 . A complex scalar Higgs doublet, ϕ , is added to the model for mass generation through spontaneous symmetry breaking with potential given by,

$$V(\phi) = \mu^2 \phi^\dagger \phi + \frac{\lambda^2}{2} (\phi^\dagger \phi)^2. \quad (1.1.1)$$

For μ^2 negative, ϕ develops a vacuum expectation value, $v/\sqrt{2}$, where $v \approx 246$ GeV, breaking part of the electroweak gauge symmetry, after which only one neutral Higgs scalar, H , remains in the physical particle spectrum.

For these bosons, the covariant deviation D_μ and the Lagrangian density \mathcal{L} are described as following

$$D_\mu = \left(\partial_\mu - ig_1 \frac{\tau^a}{2} W_\mu^a - ig_2 \frac{Y}{2} B_\mu \right), \quad (\text{left-handed and scalar particles}) \quad (1.1.2)$$

$$D_\mu = \left(\partial_\mu - ig_1 \frac{Y}{2} B_\mu \right), \quad (\text{right-handed particles}) \quad (1.1.3)$$

$$\mathcal{L} = i\bar{\psi}\gamma^\mu D_\mu\psi + |D_\mu\phi|^2 - \frac{1}{4}\mathbf{W}_{\mu\nu} \cdot \mathbf{W}^{\mu\nu} - \frac{1}{4}B_{\mu\nu}B^{\mu\nu}, \quad (1.1.4)$$

where Y is hyper-charge, τ is isospin triplet, g_1 and g_2 are coupling strength for the electromagnetic and weak interactions, respectively. When the charged weak boson $W^\pm = (W^1 \mp W^2)/\sqrt{2}$ term, the vacuum expectation value v and the scalar potential $\phi = \begin{pmatrix} 0 \\ v \end{pmatrix}/\sqrt{2}$ are substituted, the gauge bosons and scalar potential interaction

term in the Lagrangian transfers

$$\begin{aligned} & \left| \left(-ig_1 \frac{\tau^a}{2} W_\mu^a - ig_W \frac{Y}{2} B_\mu \right) \phi \right|^2 \\ & = \left(\frac{1}{2} v^2 W_\mu^+ W_\mu^- \right) + \frac{1}{8} v^2 (W_\mu^3, B_\mu) \begin{pmatrix} g_1^2 & -g_1 g_2 \\ -g_1 g_2 & g_2^2 \end{pmatrix} \begin{pmatrix} W_\mu^3 \\ B_\mu \end{pmatrix}. \end{aligned} \quad (1.1.5)$$

Diagonalization can be applied to the second term in the right side of the above equation and the new state Z_μ and A_μ are introduced,

$$A_\mu = \frac{g_2 W_\mu^3 + g_1 B_\mu}{\sqrt{g_1^2 + g_2^2}} \quad \text{with} \quad m_A = 0, \quad (1.1.6)$$

$$Z_\mu = \frac{g_1 W_\mu^3 - g_2 B_\mu}{\sqrt{g_1^2 + g_2^2}} \quad \text{with} \quad m_Z = \frac{1}{2} v \sqrt{g_1^2 + g_2^2}, \quad (1.1.7)$$

$$m_W = \frac{1}{2} v g_1. \quad (1.1.8)$$

The m_W and m_Z indicate the W and Z boson mass. Thus when we introduce the interaction between the vector boson and the scalar field, we can unify the electromagnetic and weak interaction by using the g_1 and g_2 as $U(1)_Y$ and $SU(2)_L$ coupling constant, respectively. In addition the vector bosons have the mass spontaneously.

The Standard Model predictions for the electroweak precision observable measured by LEP, SLC, and Tevatron experiments are fully implemented [21]. Left figure of Figure 1.1 gives the pull values obtained from the difference between the theory and the measurement in units of the total experimental error [20]. The parameters in the figures are described in detail in [22]. The Standard Model parameters relevant for the prediction of the electroweak observables are the coupling constant of the electromagnetic (α), weak (G_F),

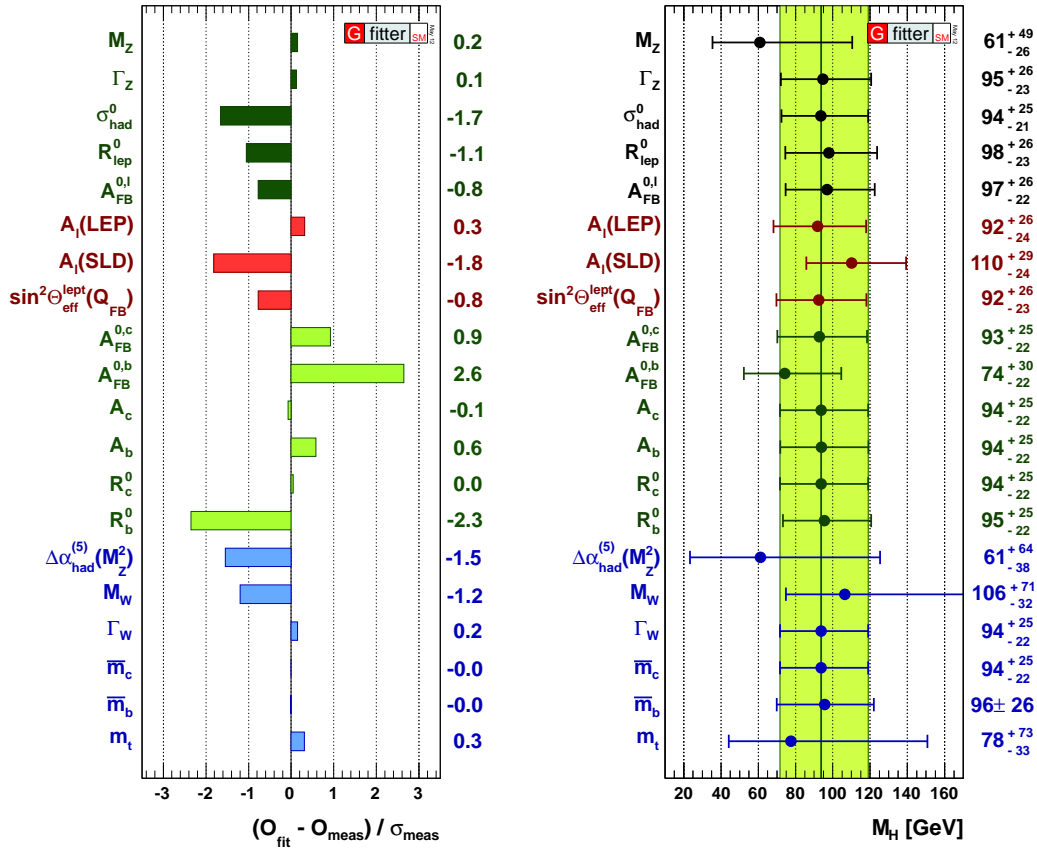


Figure 1.1: Comparing theory with results of experiments: pull values for the complete fit (left), and results for Higgs boson mass m_H from the standard fit excluding the respective measurements from the fit (right) [20].

and strong interactions (α_s), and the masses of the elementary bosons (m_Z, m_W, m_H) and fermions (m_f), where neutrino masses are set to zero. State-of-the-art calculations are used, in particular the full two-loop and leading beyond-two-loop corrections for the prediction of the W mass and the effective weak mixing angle, which exhibit the strongest constraints on the Higgs boson mass. The experimental results used in the pull include the electroweak precision data measured at the Z pole (Z resonance parameters, partial Z cross sections, neutral current couplings), their experimental correlations, and the W mass world average $m_W = 80.399 \pm 0.023$ GeV [23] and width $\Gamma_W = 2.098 \pm 0.048$ GeV [24]. Furthermore the average of the direct Tevatron top mass measurements $m_t = 173.3 \pm 0.9 \pm 0.6$ GeV is used [25].

The figure indicates that the Standard Model predictions are in agreement with the observables in experiments. In addition, the results imply a Higgs boson whose mass lies $67 < M_H < 120$ GeV as right of Figure 1.1.

1.2 Grand Unification and Hierarchy Problem

It is natural that this success with unification between electromagnetic and weak interaction is extended to the strong interaction $SU(3)_C$ whose coupling constant is g_3 . In addition it is preferable to describe the unification model by a single coupling constant since the Standard Model needs two coupling constants g_1 and g_2 in the electroweak scale ~ 100 GeV. The grand unification theory (GUT) is advocated to unify the electromagnetic, weak and strong interactions by a single coupling constant g_G . The normalized running coupling constants $\alpha_1 (= g_1^2/4\pi)$, $\alpha_2 (= g_2^2/4\pi)$, $\alpha_3 (= g_3^2/4\pi)$ are estimated by using the renormalization group equation

$$\frac{d\alpha_i}{dt} = -\frac{b_i}{2\pi}\alpha_i^2, \quad \left(\frac{d}{dt} (\alpha_i^{-1}) = \frac{b_i}{2\pi}\alpha_i^2 \right) \quad (1.2.1)$$

where $t = \log Q$ and Q is running energy scale. The coefficients b_i are determined by the gauge group and the matter multiplets to which the gauge bosons couple. The Equation 1.2.1 can be integrated immediately

$$\alpha_i^{-1}(Q) = \alpha_i^{-1}(Q_0) + \frac{b_i}{2\pi} \log \frac{Q}{Q_0}, \quad (1.2.2)$$

where the Q_0 is energy scale at which running commences. For the $SU(N)$ gauge theory, the coefficients b_i can be calculated

$$b_N = \frac{11}{3}N - \frac{1}{3}n_f - \frac{1}{6}n_s, \quad (1.2.3)$$

where n_f is a number of fermion multiplets (counting two chirality states separately) and n_s is a number of (complex) scalar multiplets which couple to the gauge bosons. The coefficient of each gauge coupling in the

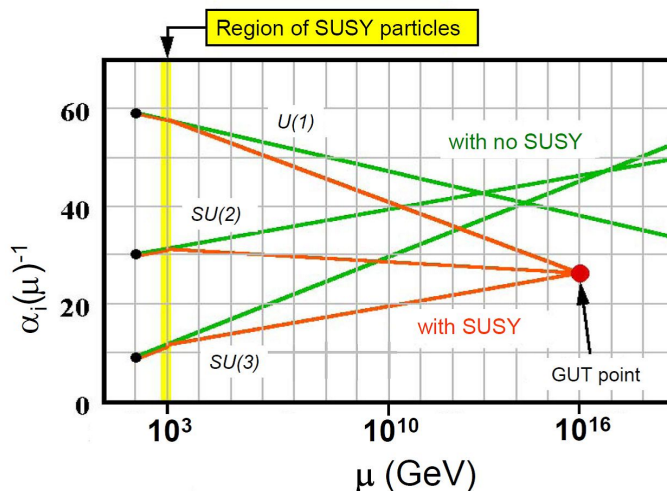


Figure 1.2: Coupling constant of the Standard Model and SUSY (MSSM) model as a function of energy scale.

Standard Model is

$$(b_1, b_2, b_3) = \left(-\frac{41}{10}, \frac{19}{6}, 7 \right). \quad (1.2.4)$$

The grand unification is calculated by using the Equation 1.2.1 as following

$$\log \left(\frac{m_G}{m_Z} \right) = \frac{10\pi}{28} [\alpha_1^{-1}(m_Z) - \alpha_2^{-1}(m_Z)] \sim 33.1. \quad (1.2.5)$$

This result implies

$$m_G \sim 10^{16} \text{ GeV}. \quad (1.2.6)$$

This huge discrepancy between the grand unification scale ($\sim 10^{16}$ GeV) and electroweak scale ($\sim 10^2$ GeV) is known as ‘‘hierarchy problem’’. The hierarchy problem often indicates a discrepancy between the Planck scale ($\sim 10^{19}$ GeV) where the all interactions are unified and electroweak scale as well.

Assuming the GUT scale and the Planck scale, very fine tuning is necessary to generate the Higgs potential around ~ 100 GeV. If a heavy complex scalar particle S with mass m_S exists, the particle couples to the Higgs with a Lagrangian term $-\lambda_S |H||S|$ where H and S are the field of the Higgs and the complex scalar particle, respectively. Radiative correction of Higgs mass due to the complex scalar particle is

$$\Delta m_H^2 = \frac{\lambda_S}{16\pi} \left[\Lambda_{\text{UV}}^2 - 2m_S^2 \log \left(\frac{\Lambda_{\text{UV}}}{m_S} \right) \dots \right]. \quad (1.2.7)$$

As well as a correction due to a heavy fermion particle mass m_F is

$$\Delta m_H^2 = C_H T_F \left(\frac{g^2}{16\pi^2} \right)^2 \left[a \Lambda_{\text{UV}}^2 + 24m_F^2 \log \left(\frac{\Lambda_{\text{UV}}}{m_F} \right) + \dots \right], \quad (1.2.8)$$

where Λ_{UV} is an ultraviolet momentum cut-off, C_H and T_F are group theory factors of order 1 and g is an appropriate gauge coupling. Both formulas are sensitive to the heavy particle mass. If the Higgs is stable around $m_H \sim 100$ GeV, we can not assume any heavy particles exist and couple with the Higgs field. To solve this hierarchy problem and unification, two theories; supersymmetry and extra dimensions are advocated. The SUSY cancels out the interaction from gauge bosons and fermions to the Higgs boson by the supersymmetric particles. On the other hand, the extra dimensions predicts the grand unification scale and Planck scale are around TeV scale actually, however they look like huge energy scale since the extra dimensions weaken the gravity interaction.

1.3 The Beyond Standard Model

1.3.1 Minimal Supersymmetric Standard Model (MSSM)

The Minimal Supersymmetric Standard Model (MSSM) consists of superpartners which are replaced from a bosonic state to a fermionic state and vice versa with the Standard Model particles. The superpartners are classified in Table 1.1. The radiative correction of Higgs mass including the SUSY particles is

$$\Delta m_H^2 = \frac{1}{8\pi^2} (\lambda_S - |\lambda_f^2|) \Lambda_{\text{UV}}^2 + \dots, \quad (1.3.1)$$

where the λ_f is the Higgs coupling strength with fermions. The Equation 1.3.1 implies that the effects of fermions are cancelled out by those of the scalar particles. In addition, coefficients of the running coupling constants for the MSSM model are calculated as following

$$(b_1, b_2, b_3) = \left(-\frac{33}{5}, -1, 3 \right). \quad (1.3.2)$$

These coefficients can be extrapolated as the coupling constant from the electroweak scale to the grand unification scale and these results are shown as the black lines in Figure 1.2. The lines of each coupling constant are crossing at 10^{16} GeV due to the effects of superpartners around TeV scale.

Names	Notations	SM partner	spin	SU(3) _C , SU(2) _L , U(1) _Y
squarks (right-handed)	$\tilde{u}_R, \tilde{c}_R, \tilde{t}_R$	u_R, c_R, t_R	0	$(3, 1, \frac{2}{3})$
	$\tilde{d}_R, \tilde{s}_R, \tilde{b}_R$	d_R, s_R, b_R	0	$(3, 1, -\frac{1}{3})$
squarks (left-handed)	$\tilde{u}_L, \tilde{c}_L, \tilde{t}_L$	u_L, c_L, t_L	0	$(3, 2, \frac{1}{6})$
	$\tilde{d}_L, \tilde{s}_L, \tilde{b}_L$	d_L, s_L, b_L	0	$(3, 2, \frac{1}{6})$
sleptons	$\tilde{e}_R, \tilde{\mu}_R, \tilde{\tau}_R$	e_R, μ_R, τ_R	0	$(1, 1, \frac{1}{2})$
	$\tilde{e}_L, \tilde{\mu}_L, \tilde{\tau}_L$	e_L, μ_L, τ_L	0	$(1, 2, -\frac{1}{2})$
	$\tilde{\nu}_L$	ν_L	0	$(1, 2, -\frac{1}{2})$
gluinos	\tilde{g}	g	1/2	$(8, 1, 0)$
winos	\tilde{W}	W	1/2	$(1, 3, 0)$
bino	\tilde{B}	B	1/2	$(1, 1, 0)$
higgsinos	$\tilde{H}_u^+, \tilde{H}_u^0$	H_u	1/2	$(1, 2, \frac{1}{2})$
	$\tilde{H}_d^-, \tilde{H}_d^0$	H_d	1/2	$(1, 2, -\frac{1}{2})$
goldstino gravitino	\tilde{G}	G	3/2	$(1, 1, 0)$

Table 1.1: Table of qualities of SUSY particles corresponding with the Standard Model particles.

The Lagrangian density for the MSSM is described

$$\mathcal{L} = \mathcal{L}_{\text{SUSY}} + \mathcal{L}_{\text{soft}}, \quad (1.3.3)$$

where the $\mathcal{L}_{\text{SUSY}}$ term contains all of the gauge and Yukawa interactions and preserves supersymmetry invariance, and $\mathcal{L}_{\text{soft}}$ term violates the supersymmetry but contains only mass terms and coupling parameters with positive mass dimension. The superpartners of MSSM corresponding with the Standard Model particles are described below

- Squark : \tilde{q}
Superpartners of quarks are named “squark”. The squarks are spin-0 scalar particles and the anti-particles have same properties as particles, thus the squarks are Majorana particles. The left-handed squarks can couple with the all gauge bosons meanwhile the right-handed squarks can not couple with the weak gauge bosons. Consequently, the right-handed squarks are lighter than the left-handed squarks $m_{\tilde{q}_R} \lesssim m_{\tilde{q}_L}$.
- Slepton : $\tilde{\ell}$
Superpartners of leptons are named “slepton”. The sleptons are spin-0 and Majorana particles as well as the squarks. The sleptons can couple with the weak bosons but can not couple with the strong bosons, thus the sleptons are lighter than squarks and gluino $m_{\tilde{\ell}} \lesssim m_{\tilde{q}}, m_{\tilde{g}}$ which couple with colored charge.
- Gaugino : $\tilde{g}, \tilde{W}, \tilde{B}$
Superpartners of gauge bosons are named “gaugino”. Each gaugino has a charge corresponding to the Standard Model partner, thus the gaugino can mediate the each interaction as well as the Standard Model gauge bosons.
- Higgsino : \tilde{H}
The SUSY model requires the SU(2)_L doublet H_u and H_d since the electroweak symmetry suffers from a gauge anomaly if the Higgs chiral supermultiplet is singlet. The superpartners of Higgs are called “higgsino” and consists of four fermionic particles $\tilde{H}_u^+, \tilde{H}_u^0, \tilde{H}_d^0, \tilde{H}_d^-$. The higgsinos have the same quantum state with the gauginos therefore the higgsinos, winos and bino are mixed and generate the four neutral fermions so-called “neutralino” $\tilde{\chi}_1^0, \tilde{\chi}_2^0, \tilde{\chi}_3^0, \tilde{\chi}_4^0$ and four charged fermions so-called “chargino” $\tilde{\chi}_1^\pm, \tilde{\chi}_2^\pm$. These particles are labeled by the order from lighter particle ($\tilde{\chi}_1^0, \tilde{\chi}_1^\pm$) to heavier particle ($\tilde{\chi}_4^0, \tilde{\chi}_2^\pm$).
- Gravitino : \tilde{G}
Superpartner of graviton is named “gravitino”. If supersymmetry is violated by gravity mediation, quantum state of gravitino is the same as the goldstino and the gravitino absorbs the goldstino which is analogous to the Higgs mechanism for the gauge theory. Therefore the gravitino obtains a mass $m_{3/2} \sim \langle F \rangle / M_P \sim 100 \text{ GeV}$ where $\langle F \rangle$ is the supersymmetry broken scale. However this supersymmetric particle does not play any role in the collider physics since the gravitino can interact with other

particles through the gravity. If supersymmetry is violated through the gauge particles, the expected gravitino mass $m_{3/2}$ is heavier than a keV.

These supersymmetric particles decay into the more lighter supersymmetric particle until there are no lighter supersymmetric particles due to R-parity conservation. The R-parity is positive for the Standard Model particles and negative for the supersymmetric particles, and it is supposed that this parity is conserved. The decay chains depend on the kinematics and the strengths of gauge coupling are the same as those of the Standard Model. These decay chains are described below in detail.

1. Gluino \tilde{g} and squark \tilde{q} decay

The colored supersymmetric particles decay into the chargino or neutralino. If kinematics allows, the gluino decays $\tilde{g} \rightarrow q\tilde{q}$ as two-body decay. If all squarks are heavier than gluino, the gluino decay $\tilde{g} \rightarrow qq'\tilde{\chi}^0$ or $\tilde{g} \rightarrow qq'\tilde{\chi}_1^\pm$ through an off-shell squark. If the $\tan\beta$ which is a ratio of vacuum expectation value of H_u to that of H_d is large, the virtual squarks prefer to the third generation squarks (\tilde{b} and \tilde{t}), thus the decay widths of \tilde{b} and \tilde{t} are made large. For the squarks production, the squark decay $\tilde{q} \rightarrow q\tilde{q}$ is dominant because of the strong coupling when the squarks are lighter than the gluino. If the gluino mass is heavier than the squark, the squark decay into the quark and either the neutralino or the chargino $\tilde{q} \rightarrow q\tilde{\chi}^0$ or $\tilde{\chi}_1^\pm$. The right-handed squarks prefer to decay into $\tilde{q}_L \rightarrow \tilde{\chi}_1^0$ because the $\tilde{\chi}_1^0$ is bino-like meanwhile the left-handed squarks is in favor to the decay into $\tilde{q}_R \rightarrow \tilde{\chi}_2^\pm$ because the $\tilde{\chi}_2^\pm$ is wino-like. Figure 1.3 is summarized above sentences. In the figures, the double lines show the SUSY particles.

2. Neutralino $\tilde{\chi}^0$ and chargino $\tilde{\chi}^\pm$ decay

The neutralino and chargino consist of the wino ($\tilde{W}^\pm, \tilde{W}^0$) and bino (\tilde{B}) admixture states. Therefore the $\tilde{\chi}_1^\pm \rightarrow \tilde{\ell}_L\nu$ decay chain is dominated. If a mass difference $\Delta m = m_{\tilde{\chi}_2^0} - m_{\tilde{\chi}_1^0}$ or $\Delta m = m_{\tilde{\chi}_1^\pm} - m_{\tilde{\chi}_1^0}$ are larger than Higgs, Z and W bosons masses, the decay chain from the neutralino and the chargino into the Higgs and the gauge bosons are opened kinematically. Figure 1.4 shows the chargino and neutralino decay. The decay chains of the center and the right of the figures are opened when the mass differences between $\tilde{\chi}_2^0, \tilde{\chi}_1^\pm$ and $\tilde{\chi}_1^0$ are larger than the Z mass and the W mass.

3. Slepton $\tilde{\ell}$ decay

The dominant decay of the slepton is $\tilde{\ell} \rightarrow \tilde{\chi}_1^0\ell$ but if the $\tilde{\chi}_2^0$ is lighter than slepton, then the decay chain

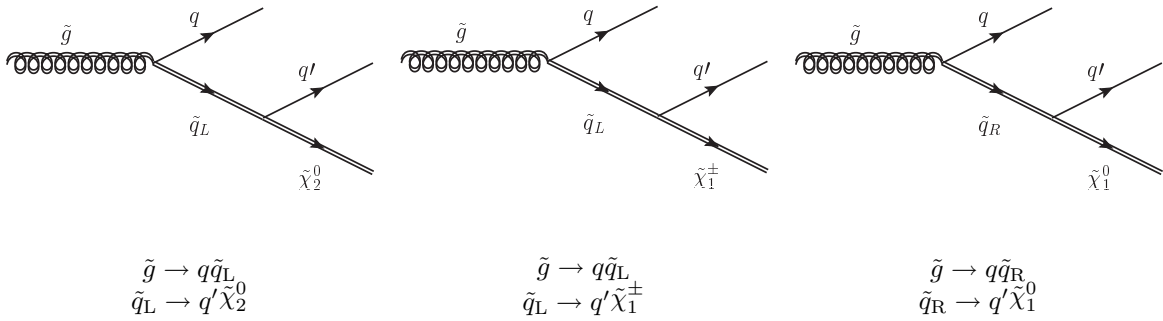


Figure 1.3: Diagrams of decay chains of the gluino \tilde{g} and squark \tilde{q} . If the $m_{\tilde{g}} > m_{\tilde{q}}$, the mediate squark is real particle. On the other hand the mediate squark is virtual if $m_{\tilde{g}} < m_{\tilde{q}}$.

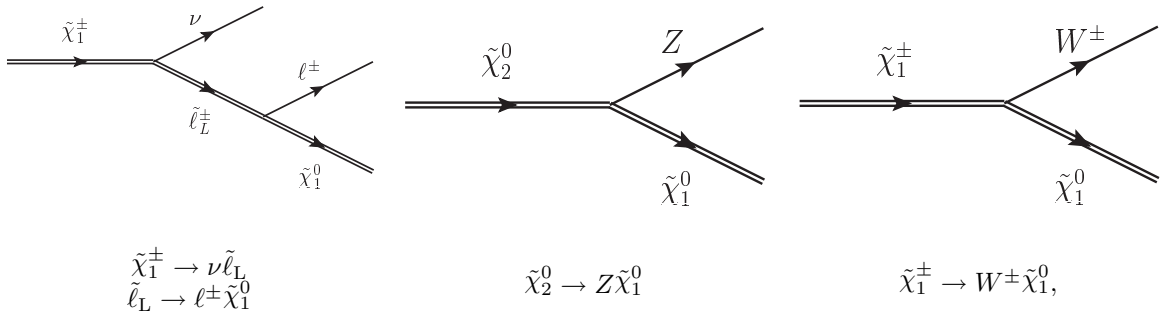


Figure 1.4: Diagrams of decay chains of the chargino $\tilde{\chi}_1^\pm$ and neutralino $\tilde{\chi}_2^0$.

of $\tilde{\ell} \rightarrow \tilde{\chi}_2^0 \ell$ is opened. In this case the left-handed slepton can couple with the $\tilde{\chi}_2^0$ meanwhile the right-handed slepton can not couple with $\tilde{\chi}_2^0$ because the $\tilde{\chi}_2^0$ is wino-like, thus the decay chain of $\tilde{\ell}_R$ prefer to the $\tilde{\ell}_R \rightarrow \tilde{\chi}_1^0 \ell$.

In general, the order of the heavy particle for supersymmetry tends the triplet particles with the strong interaction, doublet particles with the weak interaction and singlet particles with the hypercharge. However there are the huge kind of model for the supersymmetry. The mass spectrum depends on the such model. In this analysis, the minimal supergravity (MSUGRA) model and the model independent supersymmetry model (simplified SUSY model) are employed to search for physics beyond the Standard Model. Conditions of each model are mentioned in next two sections.

Minimal Supergravity SUSY Model (MSUGRA)

For the supersymmetry, it is considered that the spontaneous supersymmetry breaking occurs to mediate hidden sector particles. The hopeful candidates of the hidden sector are two scenarios, the gravity-mediated and gauge-mediated. In general the gravity-mediation is often used as a bench-mark for supersymmetry. The minimal supergravity (MSUGRA) and constrained minimal supersymmetry standard model (CMSSM) which are gravity-mediation models are simplified to constrain the parameters by theoretical assumptions [26,27]. The MSUGRA is described by five parameters m_0 , $m_{1/2}$, A_0 , $\tan \beta$, μ or sign of μ .

1. m_0 (universal scalar mass)

The squarks and sleptons have the same mass m_0 at the GUT scale.

2. $m_{1/2}$ (the universal gaugino mass)

The gauginos have the same mass $m_{1/2}$ at the GUT scale.

3. A_0 (trilinear coupling constant)

$A_{\tilde{f}}$ is coefficient that a squark or slepton \tilde{f} couples to the scalar particle with a strength $A_{\tilde{f}} y_{\tilde{f}L} \phi \tilde{f}_R$ and all $A_{\tilde{f}}$ runs to the A_0 at the GUT scale.

4. $\tan \beta = v_{H_u} / v_{H_d}$

$\tan \beta$ is a ratio of the vacuum expectation value of H_u to that of H_d .

5. μ (higgsino mass)

μ is coefficient as $\mu \tilde{H} \tilde{H}$.

These parameters determine the mass spectrum of SUSY particles. In the proton-proton collider, the gluino or squark pair productions are dominant since the strong coupling constant α_s and the colored parton density are larger than the electromagnetic coupling constant α and electroweak gauge bosons, respectively. Because the produced SUSY particles cause the cascade decay, the SUSY signal is leptons, quarks and gluons as jets and neutralino as missing transverse energy E_T^{miss} . Especially the E_T^{miss} tends to become larger than signals of the Standard Model since the mass difference between the produced SUSY particle and decayed particles are large. In the high m_0 region, the gluino mass $m_{\tilde{g}}$ is smaller than the squark mass $m_{\tilde{q}}$, therefore the gluino pair production is dominant. Meanwhile in the high $m_{1/2}$ region $m_{\tilde{q}}$ is smaller than the $m_{\tilde{g}}$, thus the squark pair production is dominant. Diagrams of representative cascade decay for MSUGRA are shown in Figure 1.5. Cross sections of MSUGRA depend on parton distribution function (PDF) and the mass of SUSY particles. Therefore the dominated SUSY particle in the production and its cross section are different between each signal grid point. The cross sections of the gluino pair production and squark pair production are shown in Figure 1.6. The typical mass spectrums of the MSUGRA in high m_0 (at $m_0 = 2820$ GeV and $m_{1/2} = 120$ GeV) and high $m_{1/2}$ signal point (at $m_0 = 580$ GeV and $m_{1/2} = 600$ GeV) are shown in Figure 1.7. Calculations to the masses of SUSY particles in the MSUGRA are described in Appendix A.1.

Simplified SUSY Model

For the MSUGRA and other SUSY models, the mass spectrum of the particles depends on theory and model parameters. Simplified SUSY model is aimed to optimize signal region and physics interpretation of the exclusion more straightforward [28, 29]. Definitions of this simplified model are described as follows.

- Only strong pair production (squarks pair production and gluino pair production).

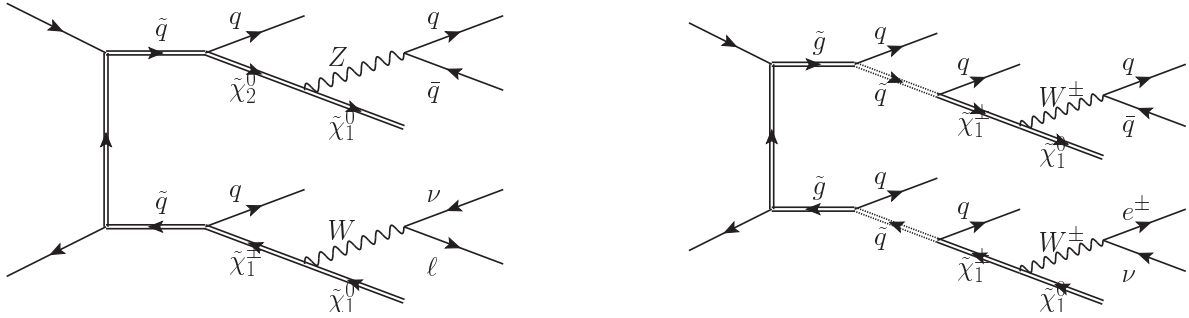


Figure 1.5: Example diagrams of decay chain for the squark pair production (left) and gluino pair production (right).

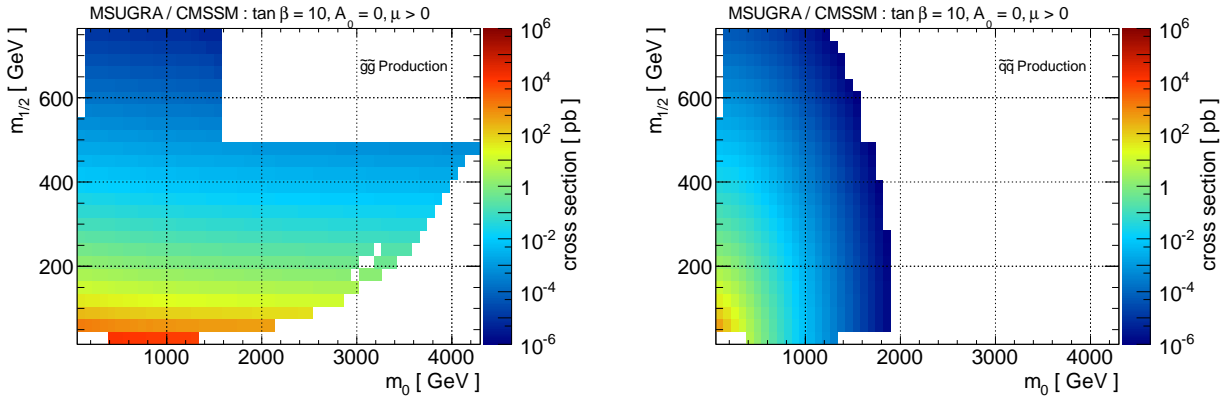


Figure 1.6: Cross section of MSUGRA for the gluino pair production (left) and squark pair production (right) as functions of m_0 and $m_{1/2}$. The region in which no signal MC samples is shown as white.

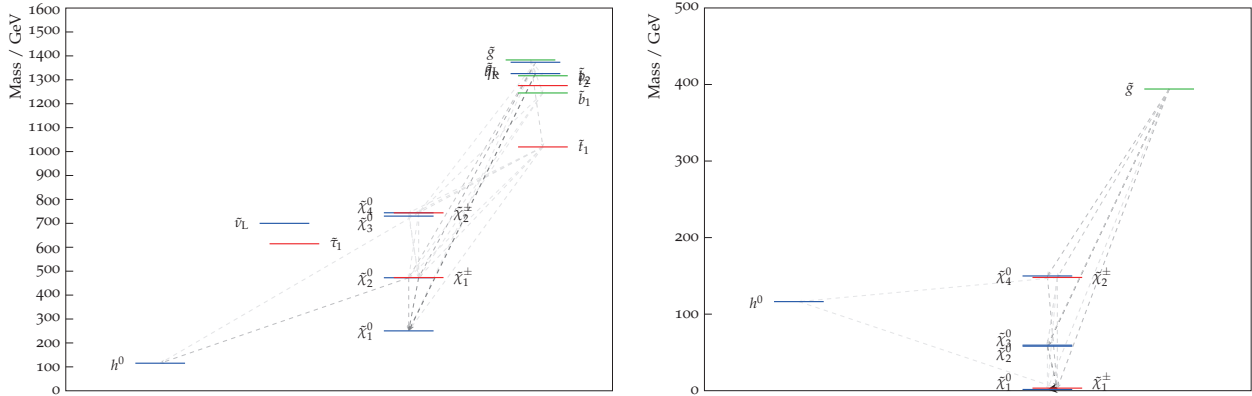
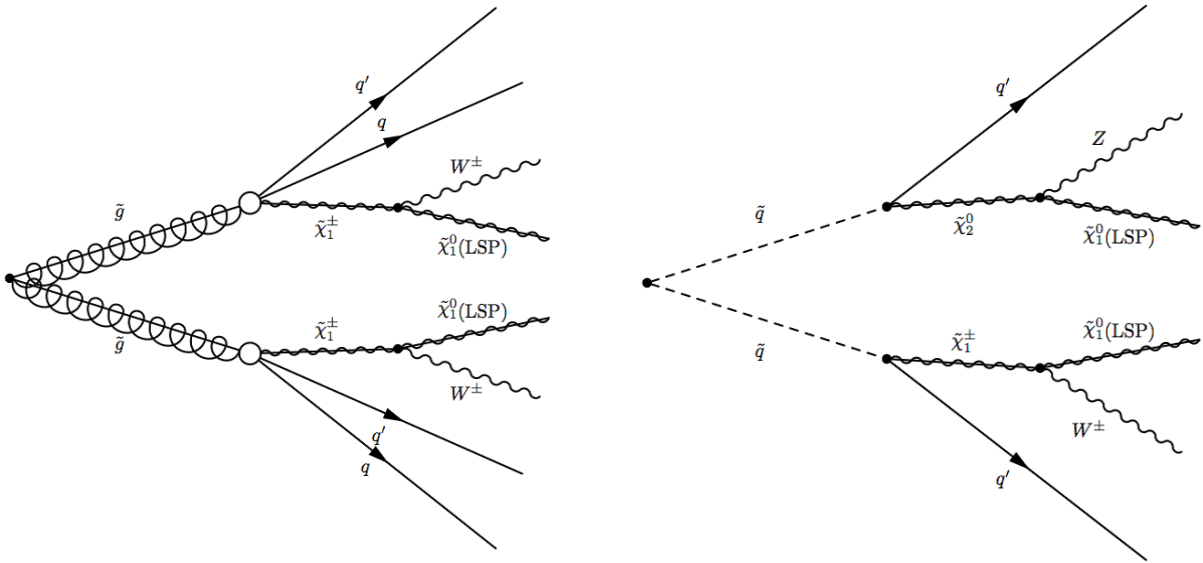


Figure 1.7: Typical mass spectrum of MSUGRA in the high $m_{1/2}$ region (at $m_0 = 580$ GeV and $m_{1/2} = 600$ GeV) (left) and the high m_0 region (at $m_0 = 2820$ GeV and $m_{1/2} = 120$ GeV) (right).

- Single production mode and single decay chain for SUSY particles.
- For the squark production, the gluino mass is set to high mass (4.5 TeV) meanwhile the squark mass is set to high mass (4.5 TeV) for the gluino production.
- The left-handed squark or gluino decays through the one or more mediate SUSY particles and finally into the stable particles as LSP.
- Emitted W bosons are allowed to decay into both leptonic and hadronic final states.
- The chargino ($\tilde{\chi}_1^\pm$) and neutralino ($\tilde{\chi}_1^0$) consist of pure wino and pure bino state, respectively.
- The first- and second- generation left-handed squarks ($\tilde{u}_L, \tilde{d}_L, \tilde{s}_L, \tilde{c}_L$) are mass-degenerated.
- The mass of the third-generation quarks (\tilde{b}, \tilde{t}) are set to large value at 4.5 TeV.



$$\begin{aligned} \tilde{g} &\rightarrow qq'\tilde{\chi}_1^\pm, \\ \tilde{\chi}_1^\pm &\rightarrow W^\pm\tilde{\chi}_1^0(\text{LSP}) \end{aligned}$$

$$\begin{aligned} \tilde{q} &\rightarrow q'\tilde{\chi}_1^\pm, \\ \tilde{\chi}_1^\pm &\rightarrow W^\pm\tilde{\chi}_1^0(\text{LSP}) \end{aligned}$$

Figure 1.8: Diagrams of the decay chain for the simplified SUSY model with the squark pair production (left) and gluino pair production (right).

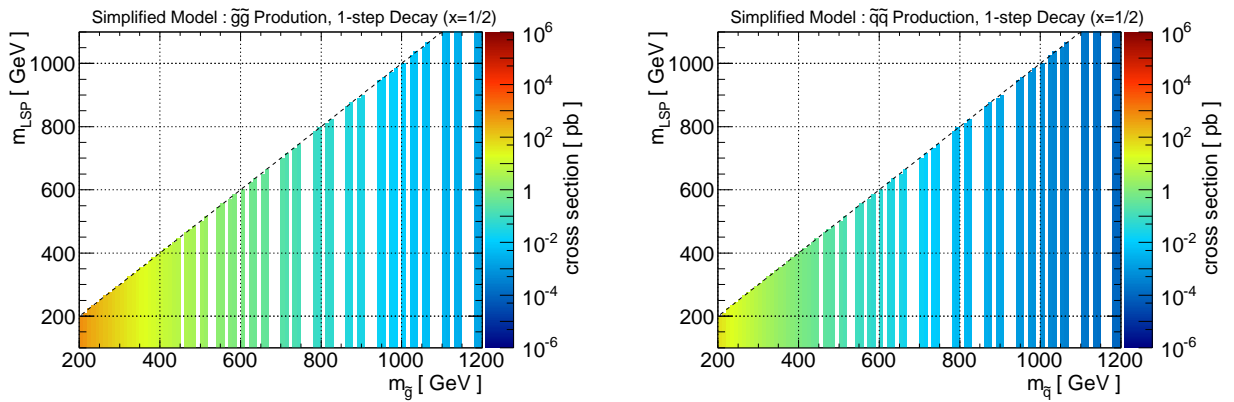


Figure 1.9: Cross section of simplified SUSY model with the gluino pair production (left) and squark pair production (right). No signal MC sample regions are shown as white.

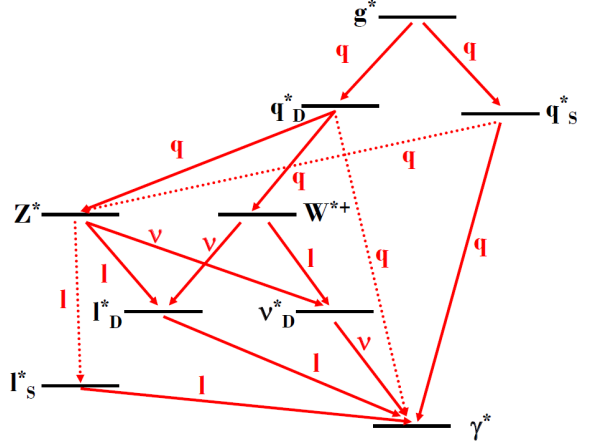
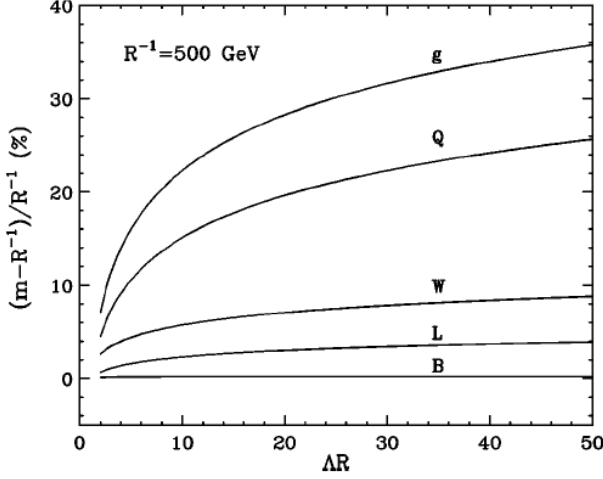


Figure 1.10: Radiative correction as a function of the cut-off scale ΔR (left) and typical mass spectrum for the UED model (right) [30].

- The mass of the right-handed quarks \tilde{q}_R are set to infinity because the wino-like chargino is not allowed to couple with \tilde{q}_R in this model.
- The other SUSY particles ($\tilde{\ell}$, $\tilde{\nu}$, $\tilde{\chi}_2^\pm$, $\tilde{\chi}_3^0$, $\tilde{\chi}_4^0$) have high masses, thus these particles do not contribute the decay chain.

The simplified model is performed by only three parameters, the gluino or squark mass ($m_{\tilde{g}}$ or $m_{\tilde{q}}$), the LSP mass ($m_{\tilde{\chi}_1^0}$) and mass of mediate particle for example chargino ($m_{\tilde{\chi}_1^\pm}$). Cross sections for the productions are determined by the gluino mass or squark mass and the parton distribution function (PDF) with the colliding protons. Figure 1.8 and Figure 1.9 show the decay chains and cross sections of the gluino pair production and the squark pair production.

1.3.2 Universal Extra Dimension (UED)

In 1920s, T.Kaluza and O.Klein advocated that the general relativity is extended to the five dimensions and the fifth dimension is compactified around a circle of very small radius [12, 13]. The original proposal from Kaluza and Klein could not solve some problems, but the concepts about the extra dimensions are expected to solve the hierarchy problem. The Arkani-Hamad Dimopoulos and Dvali (ADD) model [14] or Randall and Sundrum

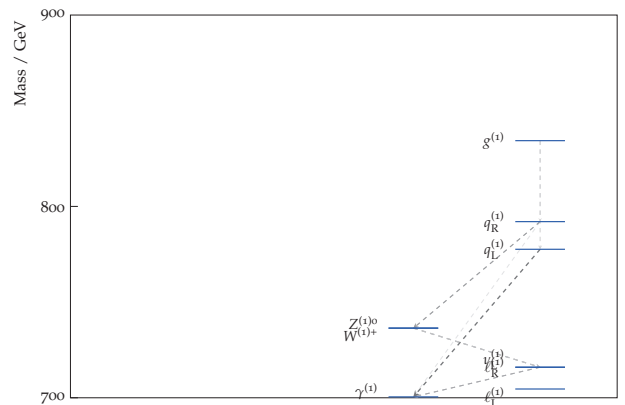
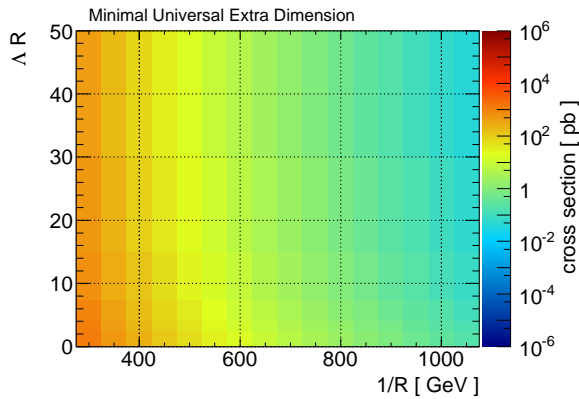


Figure 1.11: Cross section of minimal UED (left) and the mass spectrum of UED at $1/R = 700$ GeV and $\Delta R = 10$ (right).

(RS) model [15] propose the additional flat or curvature dimensions in which only gravity can propagate, thus the coupling strength of gravity weakens tremendously compared to the other interactions.

The UED is one of the extra dimensions models [16–19]. The features of this model are that each particle in UED model has a partner in the Standard Model and these particles propagate to the extra dimensions. The propagating particles in the extra dimensions are called “KK-particles”. In this analysis, one extra dimension model i.e. four spaces and one time dimensions so-called “minimal universal extra dimensions (mUED)” is considered.

Wave function of the UED particles ψ is described by using the radius of the extra dimension R so-called “compactification scale” as follows

$$\psi(x^\mu, y) = \frac{1}{\sqrt{\pi R}} \left[\psi^{\text{SM}}(x^\mu) + \sqrt{2} \sum_{n=0}^{\infty} \left\{ P_L \psi_{L,n}(x^\mu) \cos\left(\frac{ny}{R}\right) + P_R \psi_{R,n}(x^\mu) \sin\left(\frac{ny}{R}\right) \right\} \right], \quad (1.3.4)$$

where P_R and P_L are coefficients of the wave function for right-handed and left-handed particles, respectively. This equation implies that the $n = 0$ state means the Standard Model and $n \geq 1$ is UED model including the exciting states. Lagrangian in five dimensions is

$$L = \int d^5x \left[\frac{1}{2} (\partial_M \psi) (\partial^M \psi) - m_0^2 \psi^2 - \frac{1}{3!} g_5 \psi^3 + \dots \right] \quad (1.3.5)$$

$$= \int d^4x \left[\sum_{n=0}^{\infty} \left\{ \frac{1}{2} (\partial_\mu \psi_n) (\partial^\mu \psi_n) - \left(\frac{n^2}{R^2} + m_0 \right) (\psi_n)^2 \right\} - \frac{1}{3!} g'_5 (\psi^0)^2 - \frac{1}{2} g'_5 \sum_{n=1}^{\infty} \psi^0 \psi^n \psi^0 - \frac{1}{2} g'_5 \sum_{n,m=1}^{\infty} \psi^{n+m} \psi^n \psi^m + \dots \right], \quad (1.3.6)$$

where $M = 0, 1, 2, 3, 5$ indicate the dimensions, and g_5, g'_5 are the coupling constant in the fifth dimension and $g'_5 = g_5 / (2\pi R)^{1/2}$. From this equation, the mass of UED particles including the radiative correction are estimated as following

$$m_{X^n}^2 = \frac{n^2}{R^2} + m_{X^0}^2 + \delta m_{X^n}, \quad (1.3.7)$$

where the X^0 means the Standard Model particle and δm_{X^n} is radiative correction for the particle which is proportional to a cut-off scale Λ . The cut-off scale should be introduced because the couplings in the fifth dimension become strong and the theory is no longer perturbative. The equation shows the mass difference of UED particles are generated by taking the mass difference between the Standard Model particles and the radiative corrections, thus the mass difference becomes smaller than other new physics models comparatively. The large cut-off parameter indicates that the mass difference between the UED particles becomes large. Figure 1.10 (left) shows the value of radiative corrections for each KK-particle at $1/R = 500$ GeV.

According to above, the UED model can be described by only three parameters, the compactification scale $1/R$, the cut-off scale Λ and the Higgs mass m_H . These parameters determine the mass of UED particles. Figure 1.10 (right) shows a mass spectrum of the UED model. This figure shows that the spectrum is similar to the SUSY models. The masses of UED particles are calculated in Appendix A.2. The decay chain of UED model starts from the KK-gluons and ends at KK-photon due to K-parity conservation through the KK-quarks, KK-bosons and KK-leptons. Figure 1.11 (left) shows the cross section of mUED model as functions of $1/R$ and ΛR , and Figure 1.11 (right) shows the mass spectrum of mUED at $1/R = 700$ GeV and $\Lambda R = 10$.

Chapter 2

Event Topology

2.1 2011 Summer Results at $\int Ldt = 1.0\text{-}1.4 \text{ fb}^{-1}$ with Supersymmetry Model

Analysis results of the SUSY model in 2011 summer are established by using data with integral luminosity $1.0\text{-}1.4 \text{ fb}^{-1}$ and the exclusion limits on the MSUGRA and the simplified SUSY model are shown in Figure 2.1 [31–34]. MSUGRA is excluded $m_0 \sim 3000 \text{ GeV}$ and $m_{1/2} \sim 450 \text{ GeV}$ in no-lepton channel and $m_0 \sim 950 \text{ GeV}$ and $m_{1/2} \sim 340 \text{ GeV}$ in one-lepton channel. These analyses were optimized to MSUGRA where mass difference between the heaviest particle and the lightest particle in the model are about 80%, and do not have sensitivity to degenerate mass scenario. Therefore this analysis focuses on the degenerate scenario with the simplified SUSY model. For the simplified SUSY model, the region in degenerated mass difference corresponds to the diagonal region in Figure 2.2 which shows mass points of generated Monte Carlo (MC) signal samples in gluino pair production. In the region, the mass difference between the gluino (or squark) and LSP $\Delta m/m_{\tilde{g}}$ or $\Delta m/m_{\tilde{q}}$ is less than 30%.

On the other hand, the mass difference of UED model is also expected to be degenerated as $\Delta m/m_{\text{KK-gluon}} \sim 5\text{-}30\%$. The UED model have been analyzed in CDF experiment by taking multi-lepton search at integral luminosity of 87.5 fb^{-1} [35]. The analysis set an upper limit in $1/R$ parameter space below 280 GeV at $\Lambda R = 20$.

This analysis focuses on these diagonal region of the simplified SUSY model and UED model.

2.2 Analysis Overview

This section describes the features with kinematics of such degenerate model and key points for the search of the model. Typical kinematics of the degenerate model is illustrated in Figure 2.3. The features with the degenerate model are the soft leptons and the soft jets derived from the cascade decay. Thus these signals tend to hide behind the background, or can not overcome transverse momentum (p_T) threshold of each object in reconstructions. On the other hand, productions of SUSY or UED particles need large transfer momentum. Such transfer momentum is generated by initial state radiation (ISR). Thus the p_T of ISR jet becomes larger in the SUSY and UED particle production and the jet tends to be a leading jet. Consequently, E_T^{miss} is generated due to the heavier neutralino $\tilde{\chi}_1^0$ for SUSY or KK-photon for UED. The E_T^{miss} tends to be in opposite direction to ISR jet and become larger because of a hard ISR jet and soft decay products. Figure 2.4 (left) shows the lepton p_T distribution for the UED model and background when the exact one lepton is required. Figure 2.4 (right) shows the leading jet p_T distribution coming from both the ISR jets and the decayed particles by using the MC prediction in UED model at $1/R = 300 \text{ GeV}$ and $\Lambda R = 2$, here is more degenerate signal point for the UED model. These figures indicate the p_T of leptons are much smaller than the background and the ISR jet tend to become the leading jet for the degenerate model.

To summarize these features as following

- ISR jet with large p_T is emitted to generate large transfer momentum.
- Large E_T^{miss} due to neutralino or KK-photon in opposite direction to the ISR jet.
- The leptons and jets derived from the cascade particles have low p_T .

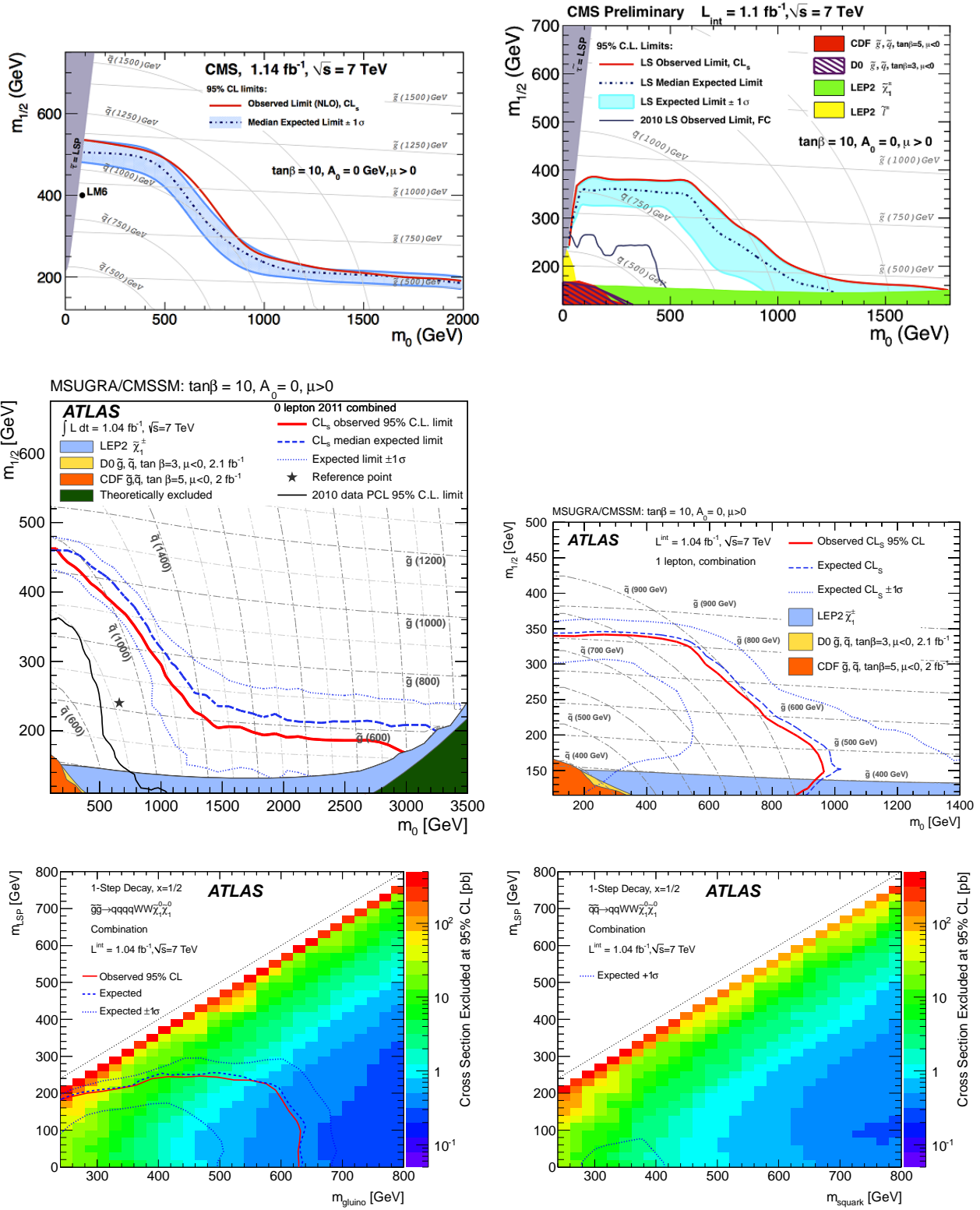


Figure 2.1: Exclusion limits at 95% CL by using 2011 summer data in integral luminosity 1.0-1.4 fb⁻¹. The results of CMS no-lepton channel (top-left) [31] and CMS one-lepton channel (top-right) [32], ATLAS no-lepton channel (middle-left) [33] and ATLAS one-lepton channel (middle-right) [34] for the MSUGRA as functions of m_0 and $m_{1/2}$ are shown. The bottom two figures show results of the simplified SUSY model of the \tilde{g} - \tilde{g} and the \tilde{q} - \tilde{q} pair production with ATLAS one-lepton μ channel.

- The multiplicity of leptons and jets are higher than that of the background, but it is possible that these objects can not get over the p_T threshold.

Therefore this analysis is optimized to the kinematics which are the soft one lepton and soft jets, and leading jet with large p_T and large E_T^{miss} .

For the kinematics, irreducible background candidates are W +jets and $t\bar{t}$ events. These background events have similar kinematics to the signal and larger cross section than the signal models. The background estimation for the W +jets and $t\bar{t}$ employs MC samples corrected by fitting to data in control regions where such background events are enhanced.

On the other hand, a reducible background is multijets events. The events consist of three components; 1) a photon conversion; 2) a neutral hadron associated with charged particles; and 3) a heavy flavor processing leptonic decay. A lepton from a heavy flavor decay and a photon conversion, or a cluster associated with tracks which are derived from hadrons is misreconstructed as a prompt electron or muon. These leptons are called “misidentified lepton” or “non-prompt lepton”, and its modeling is difficult. In this analysis, the misidentified lepton events are estimated by using observed data in control samples where the misidentified lepton events are dominant.

Other small backgrounds are estimated by using simulation only.

The signal yields are estimated in signal regions where the signal events are enriched and the background events are reduced. The cut-based signal regions are determined by using tight E_T^{miss} and leading jet p_T cut following the features of degenerate models. To discover the signal events or exclude the signal hypothesis, the observed data is compared with background-only hypothesis and signal-plus-background hypothesis in the signal regions. When the observed data is consistent with the background-only hypothesis, this analysis concludes the no signal evidence and estimates the exclusion limits for each signal models. If the observed data excesses over the background-only hypothesis, we conclude to discover a new physics phenomenon and the most probable signal mass point is estimated.

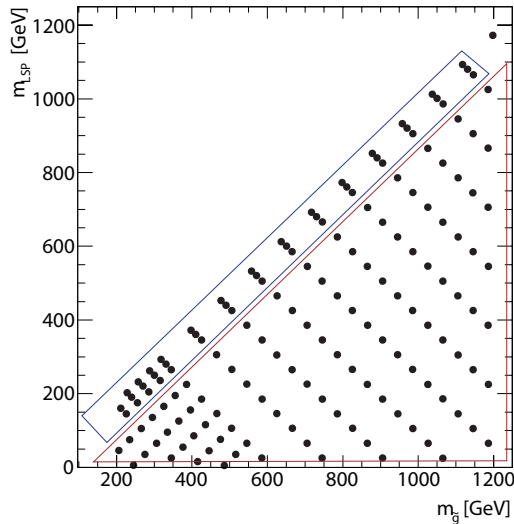


Figure 2.2: Prepared signal grid points with the $\tilde{g}\text{-}\tilde{g}$ pair production in simplified SUSY model. Blue square roughly shows the region with the degenerated mass spectrum. Considered mass degenerate $\Delta m/m_{\tilde{g}}$ is 5-30% approximately.

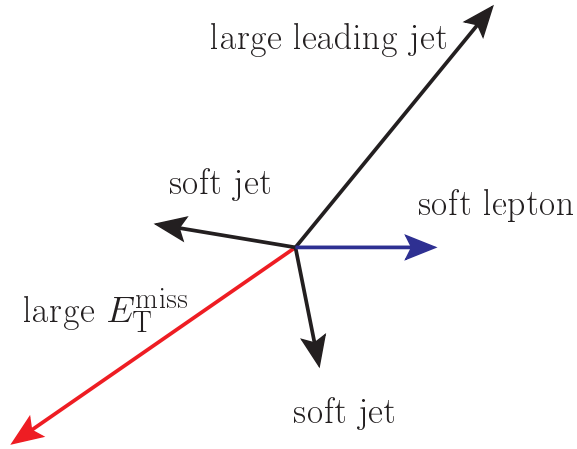


Figure 2.3: Illustration with the kinematics of the degenerate model.

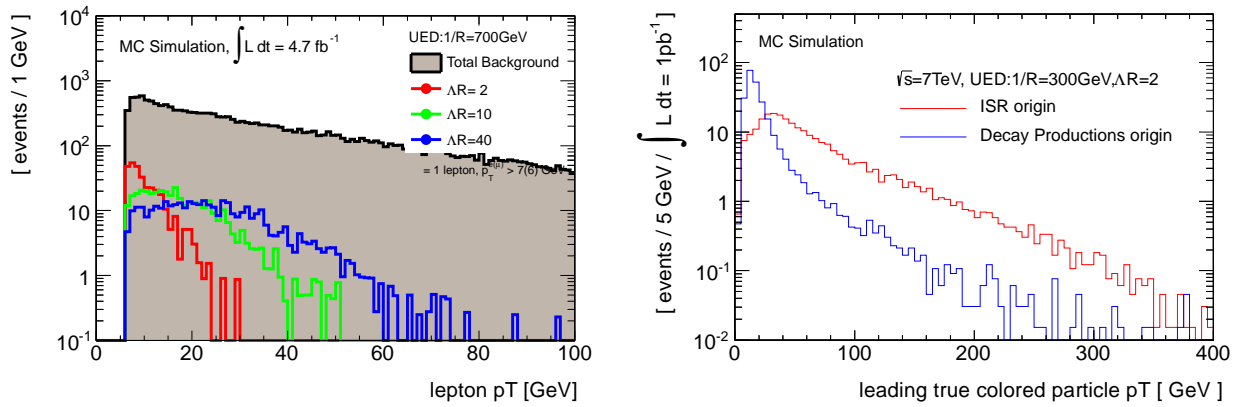


Figure 2.4: Distributions the p_T by using MC simulated events of backgrounds and UED at $1/R = 700$ GeV and $\Lambda R = 2, 10, 40$ applying one lepton cut (left), and p_T distribution of both ISR jet and jet derived from cascade decay (right) predicted by MC simulation.

Chapter 3

LHC and ATLAS Detector

This chapter describes the overview of LHC accelerator and ATLAS detector. LHC and ATLAS started the operation from 2010, and the 2011 operation was finished on October 30th without any crucial problems. In this section, firstly the proton injection and magnet with LHC. The next ATLAS detector is introduced.

3.1 Large Hadron Collider (LHC)

LHC is a hadron-hadron collider which is constructed in European Organization for Nuclear Research (CERN), Geneva, Switzerland [36]. This apparatus is aimed to search for the Higgs boson, SUSY such as between the electroweak and the TeV scale physics. The LHC main ring is built in tunnel with circumference of 26.7 km at depth between 45 m and 170 m. LHC are designed that center-of-mass energy is 14 TeV, peak luminosity is the $10^{34} \text{ cm}^{-2}\text{s}^{-1}$ and time spacing between proton bunch is 25 ns. A number of inelastic collision events is estimated to cause about 23 events at peak luminosity. However the operation of LHC and ATLAS in 2011 do not achieve this design. Currently, LHC is driven at center-of-mass energy of 7 TeV, the peak luminosity is $5 \times 10^{33} \text{ cm}^{-2}\text{s}^{-1}$, time space is 50 ns.

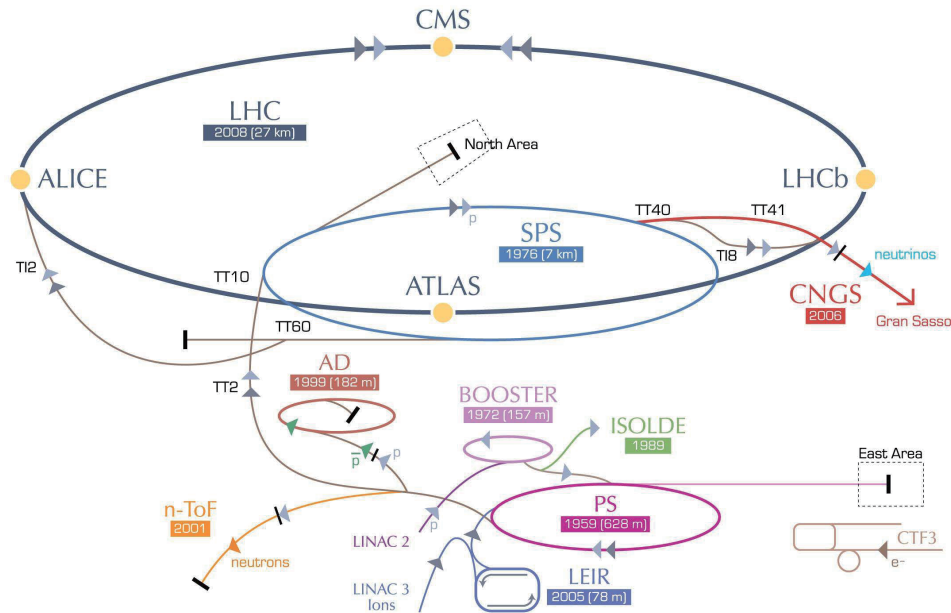


Figure 3.1: A schematic view of LHC and the injector complex

3.1.1 Injector Chain

LHC is supplied with protons by injector chain such as LINAC2, Proton Synchrotron Booster (PSB), Proton Synchrotron (PS) and Super Proton Synchrotron (SPS) as shown in Figure 3.1. At the beginning, hydrogen gas is injected into duoplasmatron, a metal cylinder which dissociates electron from hydrogen atom and generates protons with the kinetic energy of 90 keV. Then the protons are sent to a radio frequency quadrupole (QRF) which is an accelerating component that both speeds up and focuses the particles with RF field provided by four vanes. Spacing of the vanes bunches and accelerates the protons up to 750 keV. The particles are sent to LINAC2 from QRF, a linear accelerator whose tank is a multi-chamber resonant cavity tuned to a specific frequency which creates potential differences in the cavities that accelerate the particles up to 50 MeV. Protons cross LINAC2 and reaches PSB, a circular accelerator with circumference of 157 m which consists of four identical rings mounted one above another. The 20 quadrupole magnets focus the beam along the line and 2 bending and 8 steering magnets direct the beam, PSB accelerates them to 1.4 GeV. Then protons are injected to PS. PS is a circular accelerator with circumference of 628 m. Protons are accelerated to 25 GeV in it. PS forms 81 bunches packets of protons with 25 ns spacing for LHC. SPS is the final link in the injector chain to LHC with circumference of 7 km. Triplets of 81 bunches formed in PS are injected to SPS. Three or four triplets are accelerated in SPS to 450 GeV and finally transferred to LHC.

3.1.2 LHC Main Ring

The LHC main ring consists of eight arcs and eight straight sections called insertions as depicted in Figure 3.1. The length of each arc is 2.45 km and length of each insertion is 545 m.

Two proton beams are counter-rotate in beam pipes and collide at four out of eight Interaction Points (IP) in which experimental detectors are held. ATLAS detector is placed at point 1. CMS, ALICE and LHCb are located at point 5, point 2 and point 8, respectively. On upstream of each experiment, beams are focused by using three superconducting quadrupole magnets. Proton beams are designed to be focused into transverse radius of $16.7 \mu\text{m}$ at ATLAS and CMS, $70.9 \mu\text{m}$ at point ALICE and LHCb. The proton beams collide with the crossing angle of $142.5 \mu\text{rad}$ at ATLAS and CMS, $150 \mu\text{rad}$ at ALICE and LHCb. The other insertions at point 3 and point 7 have a collimation system to protect LHC against unavoidable beam losses by performing beam cleaning and at point 4 are housed cavities. The main role of the RF cavities is to keep 2808 proton bunches tightly bunched to ensure high luminosity at the IPs as well as delivering radio frequency power to the beams during acceleration. LHC uses eight cavity per beam, each cavity is operated at 4.5 K of temperature and delivering 2 MV accelerating voltage at 400 MHz of frequency.

The LHC ring consists of eight arcs and eight straight sections, and each sector is made of 23 arc cells. The arc cells are 106.9 m long and contains three 14.3 m long superconducting two-in-one dipole magnet. A schematic illustration of cross section of the dipole magnet is shown in Figure 3.2. Those dipoles produce the magnet field of 8.33 T which bends trajectory of protons to keep them along their orbit during acceleration.

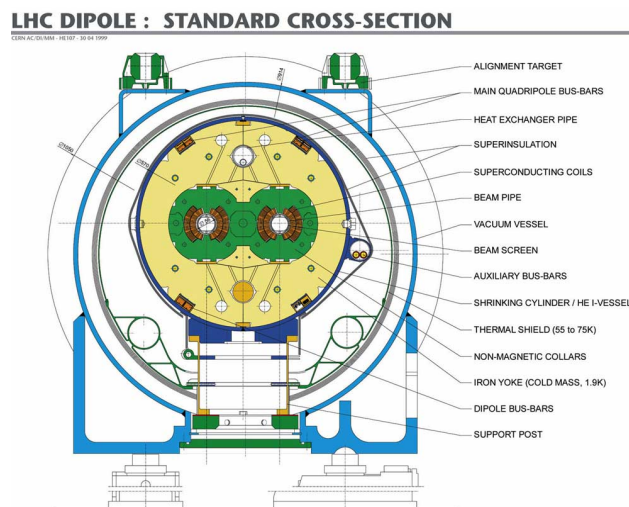


Figure 3.2: The cross section of the LHC two-in-one dipole magnet

Besides dipoles, LHC also deploys sextupole, octupole, and decapole magnets in order to correct for nonlinear movement due to magnetic field fluctuation.

3.2 ATLAS Detector

ATLAS detector is described in Figure 3.3. This detector is designed for general purpose, for example, discovery for the Higgs boson and the SUSY particles, precise measurement for the electroweak and top quark physics and stringent test of QCD. Size of ATLAS is $r \times z = 12.5 \text{ m} \times 44 \text{ m}$ as radius times length along beam pipe. This huge size is because of the precise measurement of tracks and complete energy deposition in calorimeters. In this section, coordinate where ATLAS employs are explained first. The next, structure and performance of each detector e.g. the magnet system, track detectors, and calorimeters are described.

3.2.1 ATLAS Coordinate System

Origin of the coordinate system for ATLAS is determined at the proton-proton collision point. The z -axis is oriented parallel to the beam line and positive direction of that is the counter-clockwise direction against the LHC ring. Direction of x -axis is pointing to the center of the LHC ring and the y -axis direction is upward. Azimuthal angle ϕ is an angle in x - y plane and originating from x -axis and increasing along clockwise. Polar angle θ is defined as an angle from the beam axis. Pseudo-rapidity η defined as

$$\eta \equiv -\ln \left(\tan \frac{\theta}{2} \right) \quad (3.2.1)$$

is used instead of the polar angle θ since state of particles in collider is highly Lorentz boosted. Distance between two points in the pseudorapidity-azimuthal angle plane are defined as $\Delta R = \sqrt{(\Delta\eta)^2 + (\Delta\phi)^2}$. Transverse momentum and energy are denoted as p_T and E_T which are in conservation in hadron collider. Missing transverse energy is denoted as E_T^{miss} .

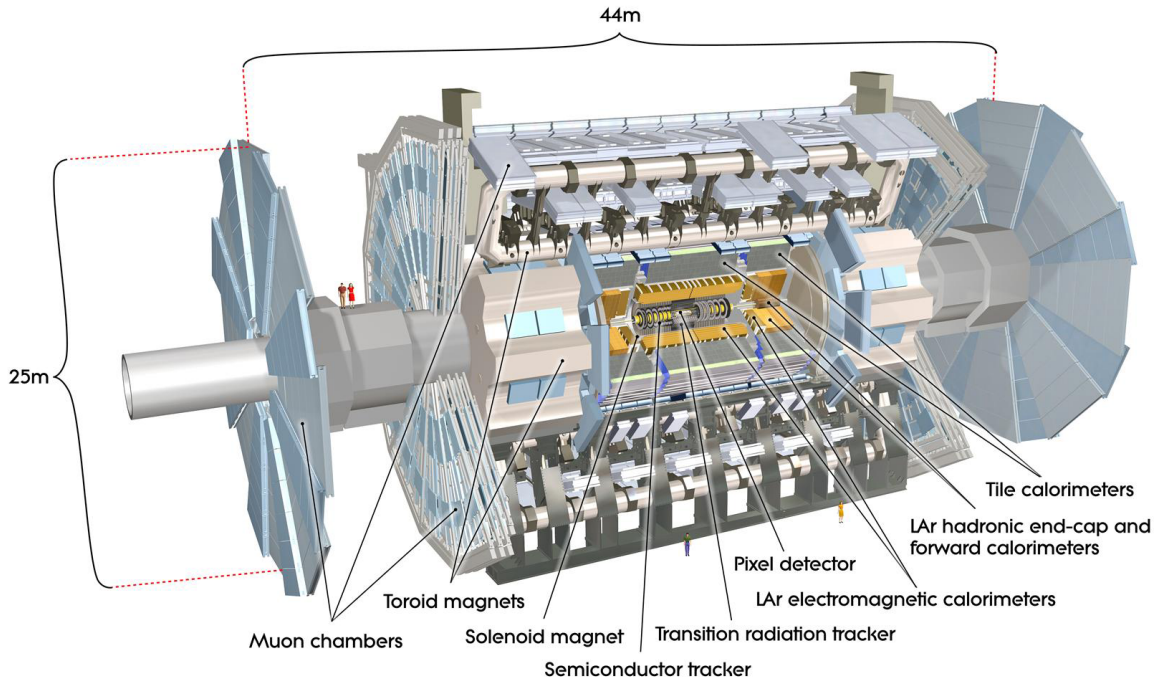


Figure 3.3: Cut-away view of ATLAS detector. Dimensions of the detector are 25 m in height and 44 m in length. Overall weight of the detector is approximately 7000 tones.

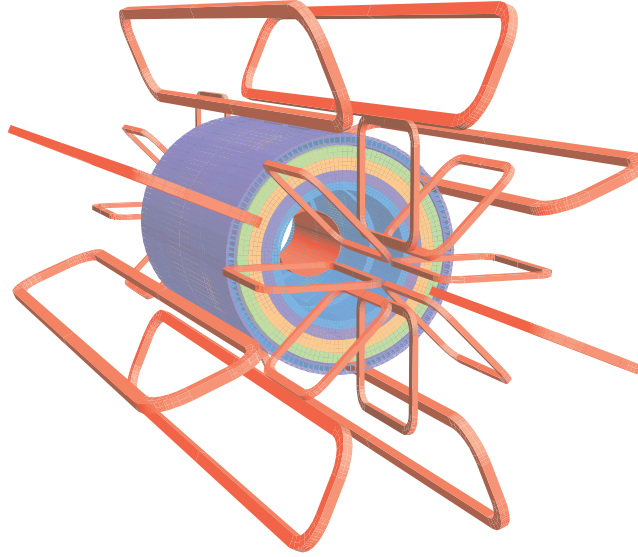


Figure 3.4: Structure of eight barrel and end-cap toroid coils and four solenoid layers.

3.2.2 Magnet System

ATLAS features a hybrid system of four large superconducting magnets. This magnetic system is 22 m in diameter and 26 m in length, with a stored energy of 1.6 kJ. The system consists of,

- a solenoid which is aligned on the beam axis and provides a 2 T axial magnetic field for the inner detector.
- a barrel toroid and two end-cap toroids which produce a toroidal magnetic field of approximately 0.5 T and 1 T for the muon detectors in the central and end-cap regions, respectively.

The structure of magnet system is shown in Figure 3.4. The solenoid and toroid magnets are described in following two sections. The strength of magnetic field at $r = 0.118$ m, 0.538 m and 1.058 m with the r and z components, and the magnetic field integral of muons passing from the innermost to the outermost are shown in Figure 3.5.

Solenoid Magnet

The solenoid magnet is located between the inner detector and the calorimeter with inner and outer diameter 2.46 m and 2.56 m and length 5.8 m. The solenoid provides a 2 T homogeneous axial magnetic field at nominal

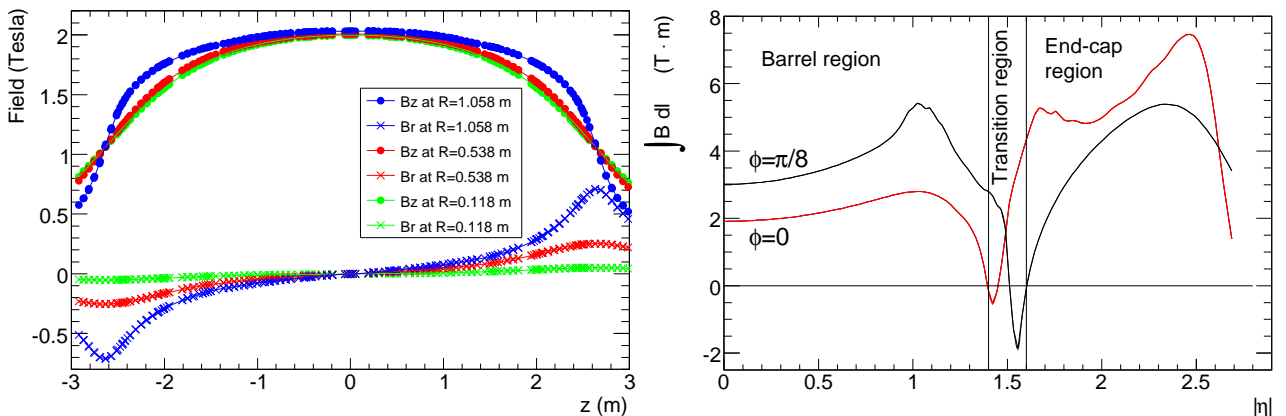


Figure 3.5: (Left) : Magnetic field components in the inner cavity along r - and z -dependence of the radial (B_r) and axial (B_z) at fixed azimuth. The lines are fitting results. (Right) : Predicted integral magnetic field as a function of $|\eta|$ from the innermost to the outermost MDT layer in one toroid octant for infinite momentum muons. The curves correspond to azimuthal angles $\phi = 0$ (red) and $\phi = \pi/8$ (black).

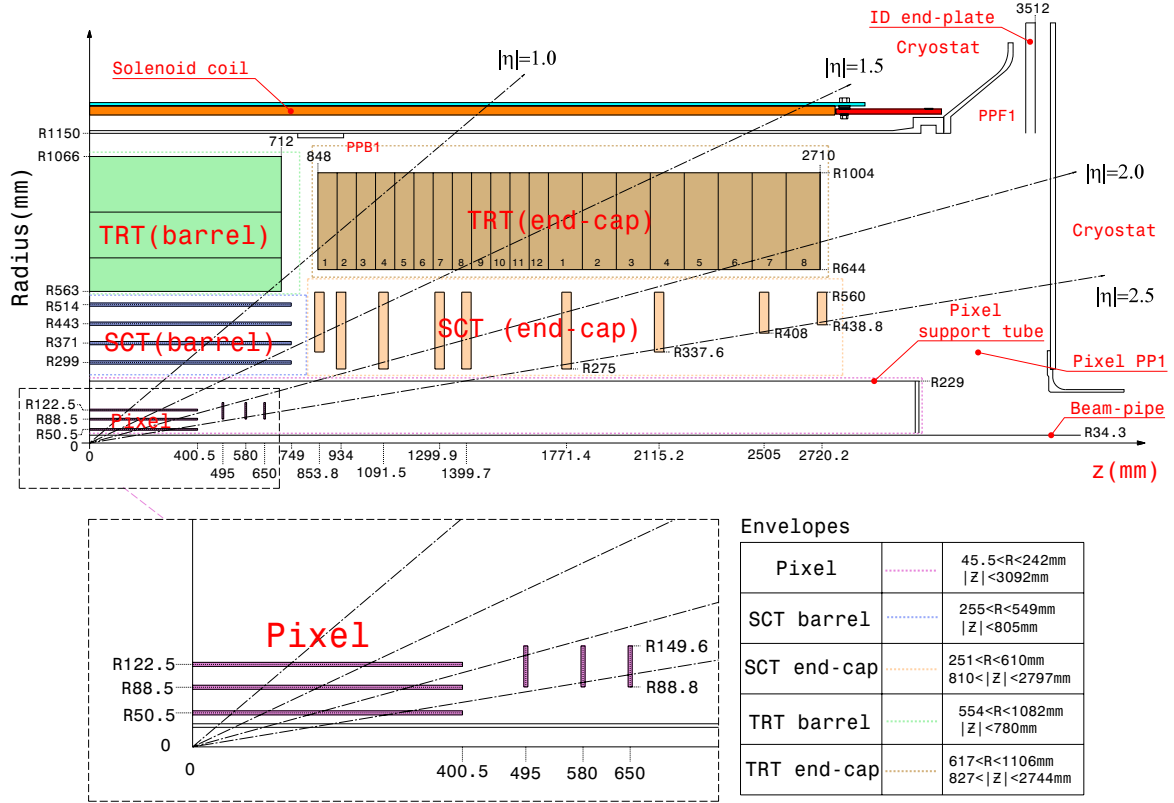


Figure 3.6: Plane view of a quarter-section of the ATLAS inner detector showing each of the major detector elements with its active dimensions and envelopes.

7.730 kA operational current. This magnet is designed to keep material thickness as possible so that total radiation length of solenoid is suppressed near to 0.66 at nominal incidence. The coil stores an energy of 40 MJ and the magnet flux is returned through the calorimeters as return yoke.

Toroid Magnet

The toroid magnets consist of eight barrel and eight end-cap toroid coils. Overall size of the barrel toroid system is 25.3 m in length, with inner and outer diameters of 9.4 m and 20.1 m, respectively. These magnets provide the magnetic field in the cylindrical volume surrounding the calorimeters and the strength of magnetic field is about 0.5 T at 10.5 kA operational current and 4.5 K temperature. The conductor and coil winding technology is based on winding a pure Al-stabilized Nb/Ti/Cu conductor into pancake-shaped coils, followed by vacuum impregnation. The two end-cap toroids form a magnetic field required in the end-cap regions of the muon spectrometer. These magnets cover $1.65 < r < 10.7$ m with axial length of 5.0 m. The field strength of the end-cap toroid is about 1.0 T in operation condition. The conductor and coil winding technology is basically the same as the one used for the barrel toroid.

3.2.3 Inner Detector (ID)

The ATLAS Inner Detector (ID) is designed to reconstruct tracks and primary and secondary vertex, and to measure particle momentum for the charged tracks above a given p_T threshold (normally 0.5 GeV). The inner detectors are composed of three sections; pixel detector (pixel), SemiConductor Tracker (SCT) and Transition Radiation Tracker (TRT). A cut-way view of the inner detectors is shown in Figure 3.6 and following sections describes the detectors.

Pixel Detector

The pixel detector consists of three high granularity (minimum pixel size is $50 \mu\text{m} \times 400 \mu\text{m}$) and very thin ($250 \mu\text{m}$) layers. In barrel region ($0 \text{ mm} < z < 400.5 \text{ mm}$) the three layers of pixel detector surrounds the beam pipe on ϕ - z plane, while in end-cap region ($495 \text{ mm} < z < 650 \text{ mm}$) three disks of pixel detector cover in r - ϕ plane within $88.8 \text{ mm} < r < 149.6 \text{ mm}$. Radii of position for each pixel layer are $r = 50.5 \text{ mm}$, 88.5 mm and 122.5 mm , and z positions of each pixel disk are $z = 495 \text{ mm}$, 580 mm and 650 mm , respectively. The most inner layer in the barrel is called “b-layer” and employed to reconstruct the secondary vertex for b -jets and distinguish between electron and photon by whether or not the particle hits the layer. Typical position resolution of the pixel detector is $10 \mu\text{m}$ in r - ϕ direction and $115 \mu\text{m}$ in z direction.

SemiConductor Tracker (SCT)

Silicon microstrip detector technology is applied to SCT. The detector consists of four layers in barrel region and nine disks in end-cap region as well as pixel detectors. Positions of layers are $r = 299 \text{ mm}$, 371 mm , 443 mm and 514 mm in $853.8 \text{ mm} < z < 2720.2 \text{ mm}$, and the positions of disks are $z = 853.8 \text{ mm}$, 934 mm , 1091.5 mm , 1299.9 mm , 1399.7 mm , 1771.4 mm , 2115.2 mm , 2505 mm , 2720.2 mm in $275 \text{ mm} < r < 560 \text{ mm}$, respectively. For the SCT layers, strip pitch is $80 \mu\text{m}$ along z -direction to provide accurate measurement on r - ϕ plane since the particle tracks curve ϕ direction due to the magnet. Meanwhile, in order to read the z direction position, the module of SCT consists of two layers and these two layers cross 40 mrad . Therefore the hit position with z direction can be read from the hit strip in both layer and the crossing point of these strips. The position resolution along r - ϕ is $17 \mu\text{m}$ and along z -direction is $580 \mu\text{m}$. On the other hand, the strip of SCT disks point to r -direction so that the resolution of r are replaced to that of ϕ - z and vice versa.

Transition Radiation Tracker (TRT)

TRT outputs the track information by using ionization and transition radiation, thus this detector prefers to electrons. The TRT is made of polyimide straw tubes with diameter of 4 mm and operated by mixing gas consisting of $\text{Xe} : \text{CO}_2 : \text{O}_2 = 70 : 27 : 3$ and the gas pressure is $5\text{-}10 \text{ mbar}$. The TRT with up to 73 tubes surround the SCT and cover between $r = 563\text{-}1066 \text{ mm}$ and $z < 712 \text{ mm}$ in the barrel region and the tubes lie along z -direction. On the other hand, in the end-cap region 160 straw planes are placed between $r = 644\text{-}1004 \text{ mm}$ and $z = 848\text{-}2710 \text{ mm}$ and the straws point toward the r -direction. A charged particle with $p_T > 5 \text{ GeV}$ is expected to excite at least 36 tubes. On average, $5\text{-}10$ high-threshold hits due to transition radiation are expected for a $p_T > 2 \text{ GeV}$ electron, meanwhile the low-threshold hits due to ionization are expected to have 32 hits on average for the same p_T electron. To use these hit information, the TRT can reconstruct the continuous tracks and identify the electron by using the number of high-threshold hits.

3.2.4 Calorimeter

The calorimeter in ATLAS is composed of Liquid Argon Calorimeter (LAr), Tile Calorimeter (Tile), End-cap calorimeter (EMEC and HEC) and Forward Calorimeter (FCal). The same technology except the absorber is employed for LAr, EMEC, HEC and FCal calorimeters. The electromagnetic calorimeters are the LAr calorimeter ($|\eta| < 1.475$) and EMEC ($1.375 < |\eta| < 3.2$) whose absorber medium is lead. The hadronic calorimeters are tile calorimeter ($|\eta| < 1.7$) and HEC ($1.5 < |\eta| < 3.2$) whose absorber media are the steel and copper, respectively. The FCal ($3.1 < |\eta| < 4.9$) plays on roles of both electromagnetic and hadronic calorimeters whose absorber media are copper and tungsten, respectively. Structure of these calorimeters are shown in Figure 3.7 and following two sections describe the calorimeters.

Electromagnetic Calorimeter (LAr)

The electromagnetic calorimeter so-called Liquid Argon Calorimeter (LAr) in ATLAS is designed with an accordion geometry for absorber and electrodes for a full coverage in ϕ without any cracks or dead materials and fast reading of signal by the electrodes. The particles interacts with the LAr absorber and generates cascade showers. The showers propagate through the liquid argon and are measured by the electrodes. A illustration of shower shape and LAr module is shown in Figure 3.8 [37] and left of Figure 3.9. For the accurate measurement of energy deposit, a lead absorber is used and active detector medium is liquid argon because of intrinsic linear behaviour and stability response over time. But the read out of this signal took about 400 ns due to drift velocity about $5 \mu\text{m}/\text{ns}$, then the signal shape is converted to the bipole signal and it is sampled at five point in each 25 ns . A right plot of Figure 3.9 shows the shape of detector signal and converted signal of LAr electrodes [38].

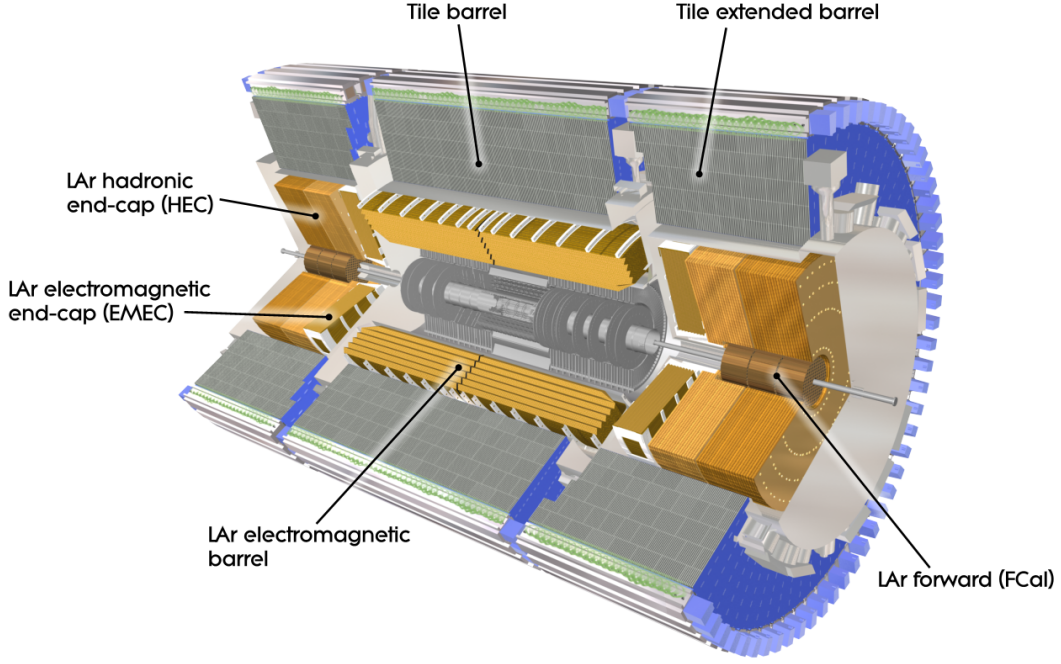


Figure 3.7: The cat-away view of the calorimeter system

The energy deposit in LAr calorimeter is estimated from values of these five points (yellow circles) by comparing with sampling model.

The LAr calorimeter is composed of three layers. As features of each layer; (1) the 1st layer has high granularity ($\Delta\eta \times \Delta\phi = 0.0031 \times 0.0245$) along η to identify the electron or photon in addition to determine the direction of the particles; (2) the 2nd layer is long distance along r ($\sim 16X_0$: X_0 is radiation length) and measures the most of energy deposit of the particles; (3) the 3rd layer identifies the electrons, photons or the hadrons by estimating the ratio of energy deposit between 2nd layer and 3rd layer. Total thickness of the LAr calorimeter module is $22X_0$ - $30X_0$ in $0 < |\eta| < 0.8$ and $24X_0$ - $33X_0$ in $0.8 < |\eta| < 1.3$, on the other hand thickness is approximately 2λ for hadron interaction length λ . Figure 3.10 shows the radiation length X_0 as a function of η in each LAr layer.

Energy resolution estimated by test beam is

$$\frac{\sigma_E}{E} = \frac{10\%}{\sqrt{E [\text{GeV}]}} \oplus 0.7\%. \quad (3.2.2)$$

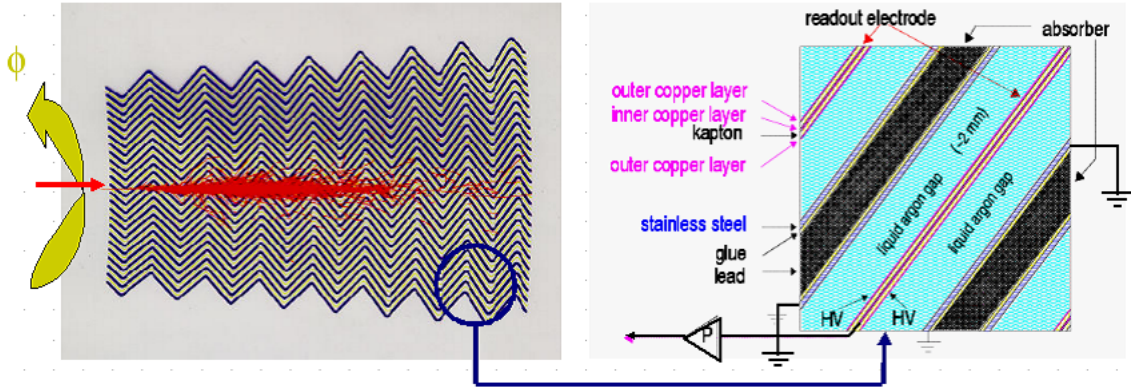


Figure 3.8: Shower shape in LAr calorimeter and fine structure of it.

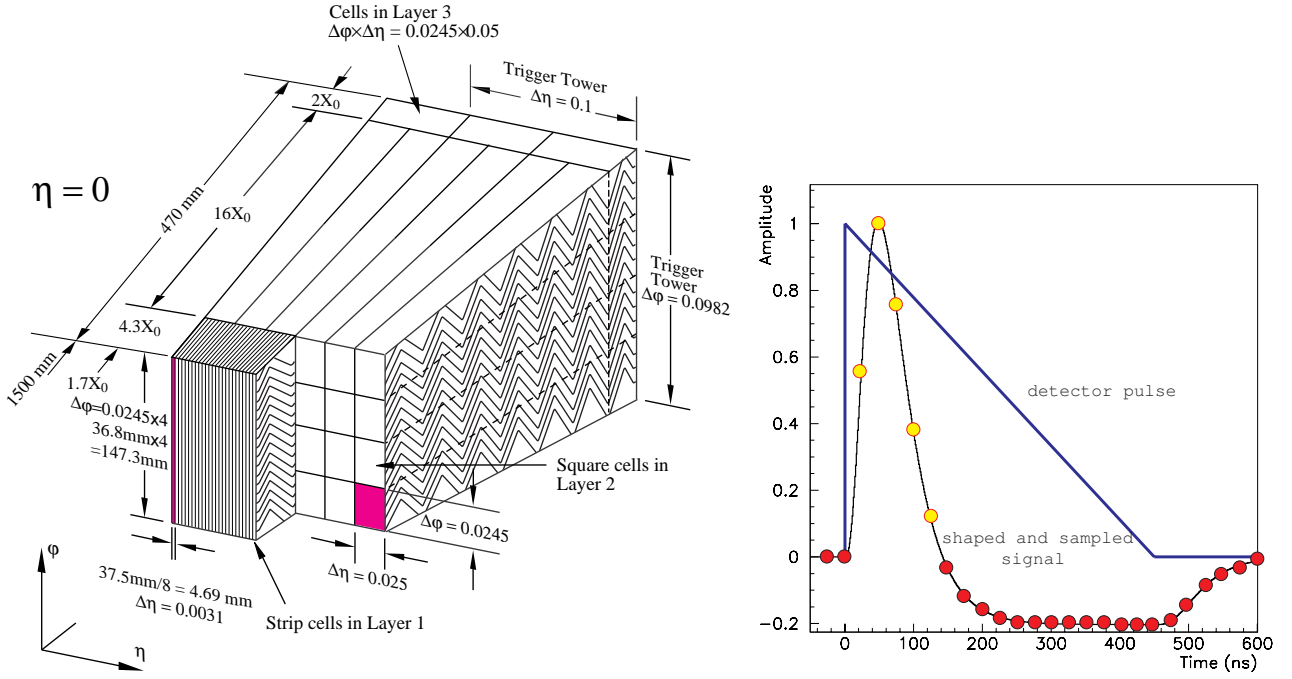


Figure 3.9: A sketch of LAr barrel module (left) and the raw and converted signal shape of LAr (right).

Hadron Calorimeter

Two type technology are applied to hadron calorimeter, Tile technology in barrel region and LAr technology in end-cap and forward regions. The LAr technology is mentioned at the previous section but the absorber is different from the electromagnetic calorimeter. Because many radiated particles fly along beam axis, copper is used in end-cap calorimeter and the first layer of forward calorimeter to optimize energy resolution and remove heat, while tungsten is used in the second and third layer of forward calorimeter to contain and minimize lateral spread of hadronic shower.

In barrel region, the tile calorimeters cover in $|\eta| < 1.7$ with inner radius of 2.28 m and outer radius of 4.45 m. This calorimeter consists of three layers and the cells of size of $\Delta\eta \times \Delta\phi = 0.1 \times 0.1$ in the first and second layer, 0.2×0.1 in the third layer which measure the energy deposit independently. The schema of a module and segmentation of the tile calorimeter are shown in right of Figure 3.11 and Figure 3.12. Iron is used for the sampling absorber, then total thick of tile calorimeter is 9.7λ approximately. Distribution of λ as a function of η is shown in the left of Figure 3.11. Hadronic shower is detected by scintillators which are installed in the

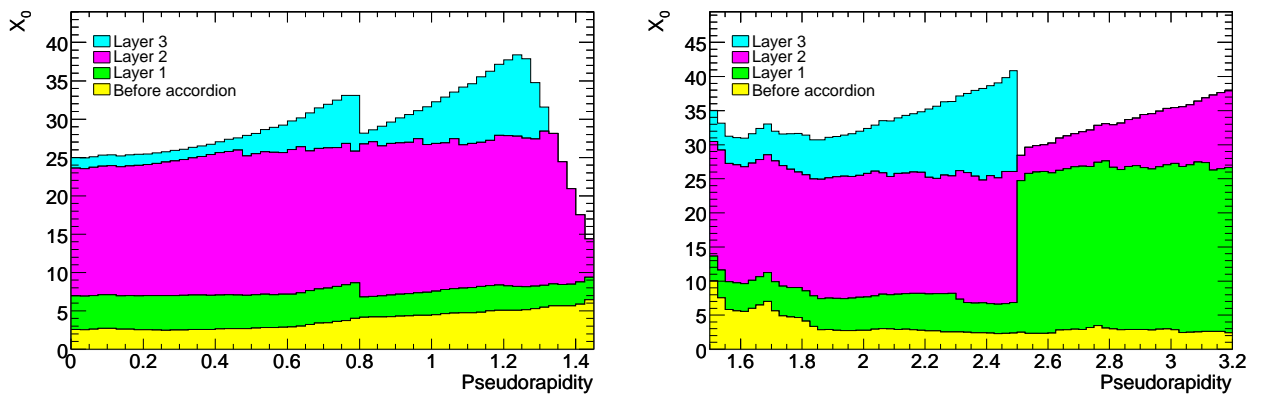


Figure 3.10: The cumulative amount of material in the unit of radiation length X_0 for the electromagnetic calorimeter in the barrel region (left) and end-cap region (right).

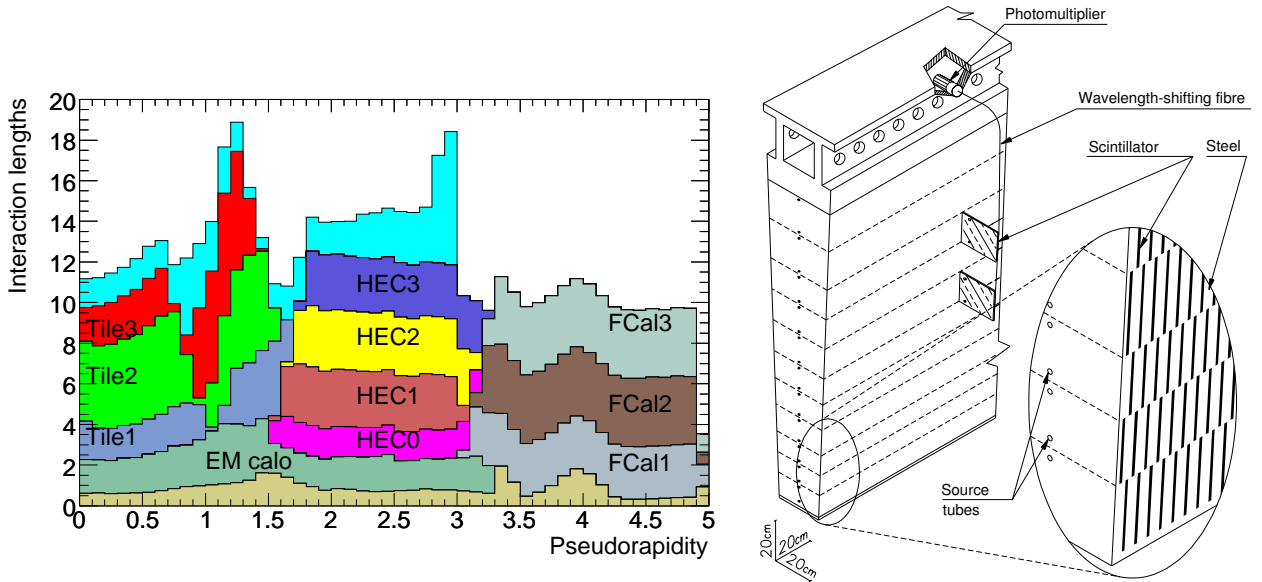


Figure 3.11: Left : Cumulative amount of material in unit of interaction length λ_0 for electromagnetic calorimeter, hadronic calorimeter and total amount of material in front of the first active layer of the Muon spectrometer ($|\eta| < 3.0$). Right : Schematic of module of tile calorimeter

absorber scintillator lights are collected to the PMT through the wavelength shifting fibres. Energy resolutions estimated by the test beam are given by

$$\frac{\sigma_E}{E} = \frac{60\%}{\sqrt{E} [\text{GeV}]} \oplus 6\%. \quad (\text{Tile Calorimeter}) \quad (3.2.3)$$

$$\frac{\sigma_E}{E} = \frac{70\%}{\sqrt{E} [\text{GeV}]} \oplus 6\%. \quad (\text{Endcap Hadron Calorimeter}) \quad (3.2.4)$$

$$\frac{\sigma_E}{E} = \frac{100\%}{\sqrt{E} [\text{GeV}]} \oplus 10\%. \quad (\text{Forward Hadron Calorimeter}) \quad (3.2.5)$$

In tile calorimeter, cluster energy is measured in EM scale which is estimated by taking electron incidences to calorimeter. The EM scale is validated by using muon events in Combined Test Beam (CTB) results to compare with a result of cosmic ray in Appendix D.

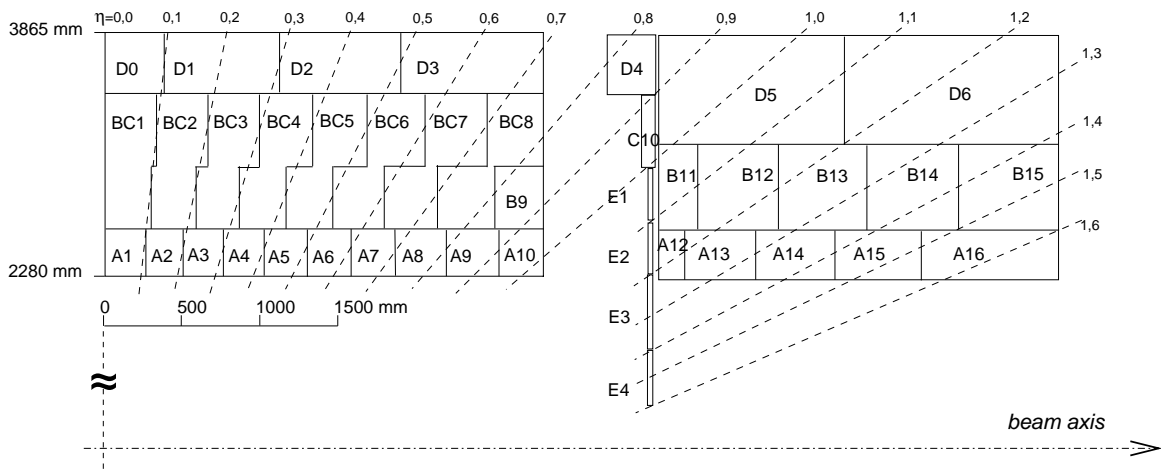


Figure 3.12: Segmentation of tile calorimeter modules in center (left) and extended barrels (right)

3.2.5 Muon Spectrometer (MS)

Muon Spectrometer consists of four detectors, Monitored Drift Tubes (MDT), Cathode Strip Chambers (CSC), Thin Gap Chambers (TGC) and Resistive Plate Chambers (RPC). Purpose of MDT and CSC are precise tracking, meanwhile that of TGC and RPC are firing triggers, providing the bunch-crossing identification, well-defined p_T thresholds and measuring the muon coordinate in the direction orthogonal to that determined by the precision-tracking chambers. Conceptual layout of muon spectrometer is shown in Figure 3.13 and each detector is described in following sections.

Monitored Drift Tubes (MDT)

The MDT consists of three to eight layers of drift tubes and its diameter is 29.97 mm. The layer size is 1-2 m in width and 1-6 m in length. The layout of MDT module is shown in Figure 3.14. Alignment system which consists of a set of four optical alignment laser monitors and calibrates the MDT position two times in a day. The MDT achieves an average resolution of $80 \mu\text{m}$ per tube or $35 \mu\text{m}$ per chamber. Therefore for a track crossing three MDT chambers, a sagitta resolution is expected $\Delta S = 45 \mu\text{m}$ corresponding to the momentum resolution $\Delta p/p = \Delta S \times p [\text{TeV}] / 500 \mu\text{m}$.

Cathode Strip Chamber (CSC)

Because a limitation of safe operation of the MDT is about 150 Hz/cm^2 , CSC which is multi-proportional chamber with radially-oriented wires are set up in end-cap region instead of the MDT. Layout of CSC is shown in Figure 3.14. The safe operation limit of CSC is up to 1000 Hz/cm^2 . As the beam test, position resolution is estimated $45\text{-}60 \mu\text{m}$ at 1 kHz/cm^2 , while signal inefficiency increases up to 4-10%.

Thin Gap Chamber (TGC)

TGC is one of muon trigger chamber, thus requirements with TGC are; (1) fast and coarse tracking information to be used in high level trigger stage; (2) bunch-crossing identification; (3) robustness against noise due to neu-

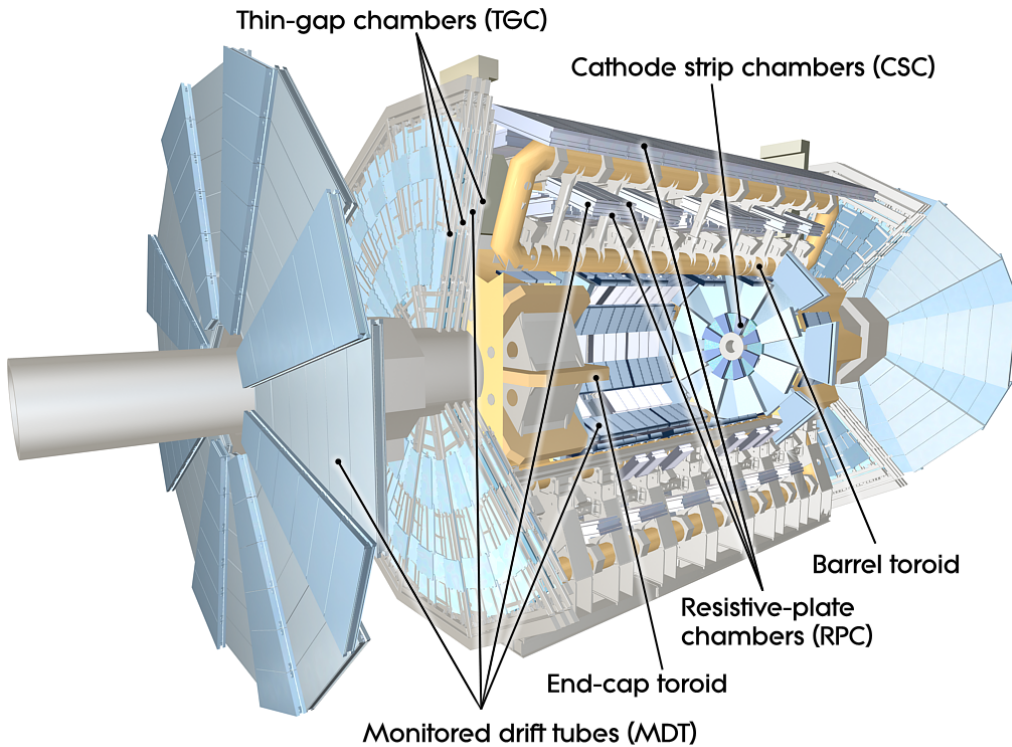


Figure 3.13: Cut-away view of ATLAS muon system

fire the trigger for the low p_T muon ($6 < p_T < 9$ GeV) meanwhile that of large lever provides the high p_T muon trigger ($9 < p_T < 35$ GeV). The RPC consists of two plate holding with distance of 2 mm. The RPC is operated in two modes, avalanche mode and stream mode. In the high background environment the avalanche mode is offered to receive the high rate signal. At the nominal operating the signal width is about 5 ns and signal inefficiency is smaller than 1%.

3.2.6 Trigger System

The ATLAS trigger system is performed in three stages, Level-1 (L1), Level-2 (L2) and Event Filter (EF). The structure of trigger system is shown in Figure 3.16. At the L1 trigger, the signal of detectors are selected by the electronics. The electrons, photons, muons, jets, τ leptons decaying into hadron and large E_T^{miss} and total p_T candidates are searched for by L1 trigger. The L2 is seeded by the Regions of Interest (RoI) where the L1 trigger has identified the candidates and reconstructs it quickly and roughly by using trigger algorithm. The EF uses off-line analysis procedures on fully-built events to further select events to reduce event rates. The trigger rates are 75 kHz, 3.5 kHz and 200 Hz at L1, L2 and EF trigger, respectively.

3.2.7 Luminosity Detector

An accurate measurement of luminosity is very important to determine sensitivity for signatures of new phenomena. For the luminosity measurements, the first a set of detectors calculates the luminosity on a bunch-by-bunch by using either event or hit counting algorithm. The second, it infers the total luminosity (summed over all bunches) by monitoring detector currents which is sensitive to average particle rate over longer time scales.

Although there are many detectors to measure the luminosity, six detectors; (1) inner detectors; (2) MBTS; (3) BCM; (4) LUCID; (5) tile calorimeter; (6) forward calorimeter are employed for the measurement in 2011.

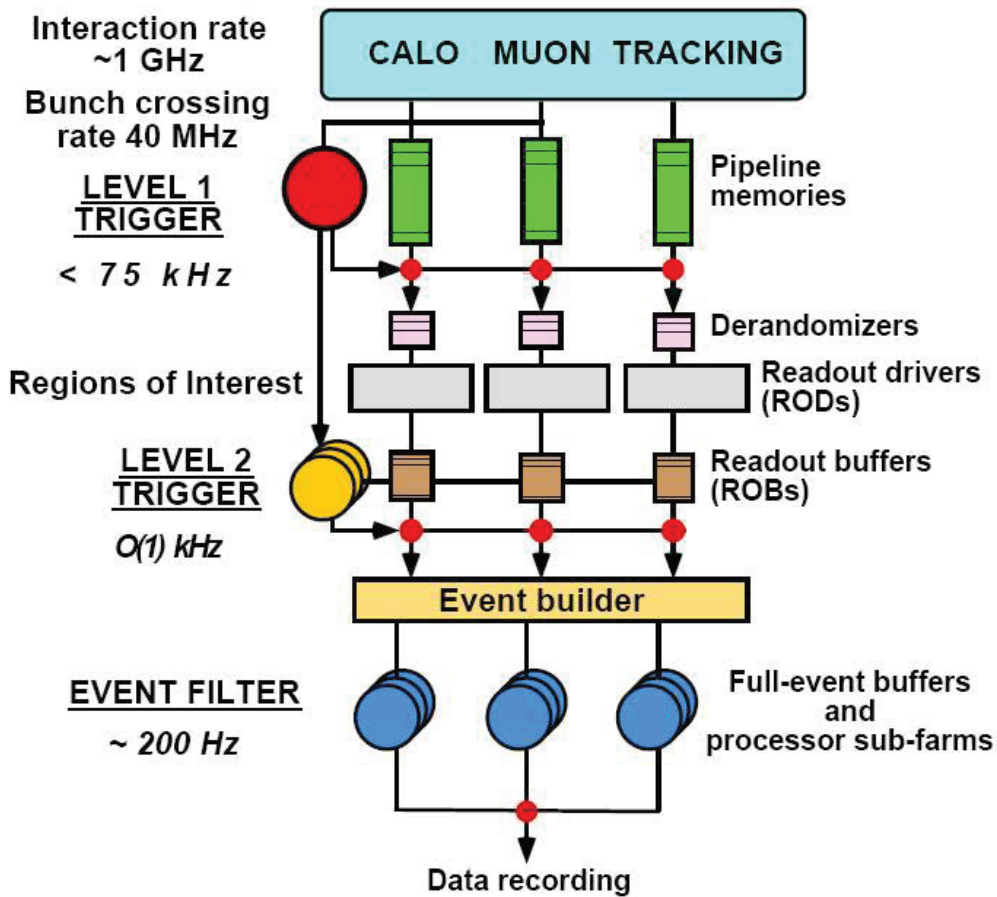


Figure 3.16: ATLAS Trigger system

The inner detectors are used to detect the vertices produced in inelastic pp interactions. For both tile and forward calorimeters, the luminosity is assumed to be linearly proportional to the observed current after correcting for pedestals in non-collision backgrounds. Therefore the integrated luminosity can be estimated by measuring the current in such calorimeters.

This section provides descriptions of MBTS, BCM and LUCID.

MBTS (Minimum Bias Trigger Scintillator)

At low instantaneous luminosity ($L < 10^{33} \text{cm}^{-2}\text{s}^{-1}$), ATLAS is equipped with segmented scintillator counters, the MBTS, located at $z = \pm 365$ cm from the nominal interaction point, and covering $2.09 < |\eta| < 3.84$. Main purpose of the MBTS is to provide a trigger on minimum collision activity during a pp bunch crossing. Light emitted by the scintillators is collected by wavelength-shifting optical fibers and guided to photomultiplier tubes. The MBTS signals, after being shaped and amplified, are fed into leading-edge discriminators and sent to the ATLAS trigger system. Figure 3.17 shows the schematic and photo of MBTS.

BCM (Beam Condition Monitor)

The BCM consists of four small diamond sensors, approximately 1 cm^2 in cross section, arranged around the beam pipe in a cross pattern on each side of the interaction point, at distance of 184 cm. The BCM is a fast device originally designed to monitor background levels and issue beam-abort requests when beam losses start to risk damaging the ATLAS detectors. The fast readout of the BCM also provides a bunch-by-bunch luminosity signal at $|\eta| = 4.2$ with a time resolution of $\simeq 0.7$ ns. The horizontal and vertical pairs of BCM detectors are read out separately, leading to two independent luminosity measurements. Figure 3.18 shows the picture of BCM.

LUCID (LUMinosity measurement using Cherenkov Integrating Detector)

LUCID consists of sixteen aluminium tubes surrounding the beam pipe and pointing the interaction point. Length and diameter of tubes are 1.5 m and 15 mm, and each tube is filled with C_4F_{10} gas at a constant pressure of 1.2-1.4 bar providing a Cherenkov threshold of 2.8 GeV for pions and 10 MeV for electrons. Two LUCID are placed in each end-cap region at a distance of 17 m from the interaction point and radial distance of 10 cm from the beam line, covering the pseudo-rapidity range $5.6 < |\eta| < 6.0$. The Cherenkov photons created by charged particles in the gas are reflected by the tube walls until they reach photomultiplier tubes (PMTs) situated at the back end of the LUCID tubes. Additional Cherenkov photons are produced in the quartz window separating the aluminium tubes from the PMTs. The Cherenkov light created in the gas typically produces 60-70 photoelectrons per incident charged particles, while the quartz window adds another 40 photoelectrons to the signal. If one of LUCID PMTs produces a signal over a preset threshold ($\simeq 15$ photoelectrons), a “hit” is recorded for that tube in that bunch crossing. LUCID hit pattern is processed by a custom-built electronics card which contains Field Programmable Gate Array (FPGAs) that can be programmed with different luminosity

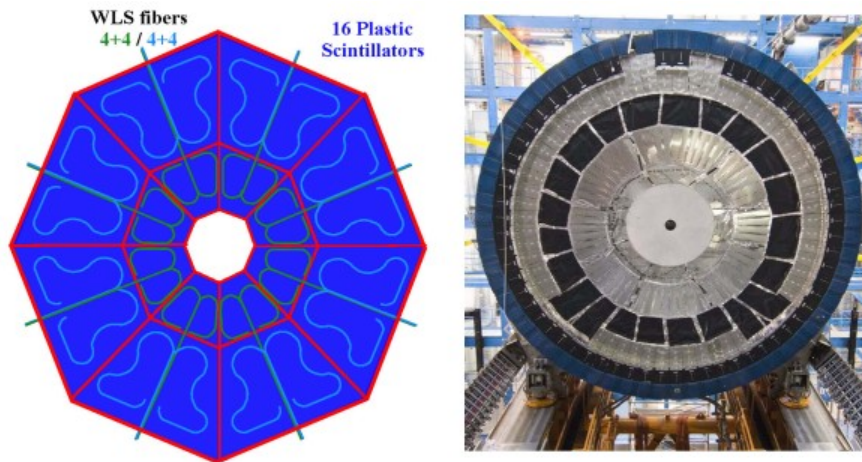


Figure 3.17: Schematic (left) and photo (right) of MBTS.

algorithms and provide separate luminosity measurements for each LHC bunch crossing. Figure 3.19 shows the pictures of LUCID.

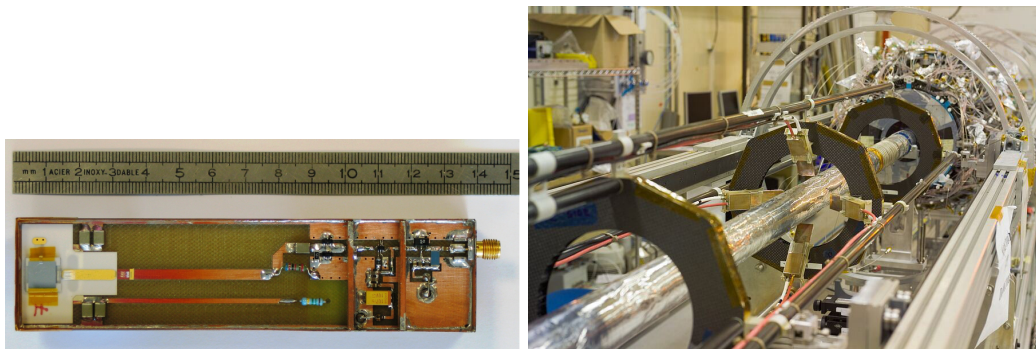


Figure 3.18: Top view of a BCM module in left picture, showing the diamond sensors (left side of picture), HV supply and signal-transmission lines, two amplification stages and signal connector (right side of picture). Close-up view one BCM station in right picture installed at 184 cm from the center of the pixel detector, which can be seen at the far end of the picture.

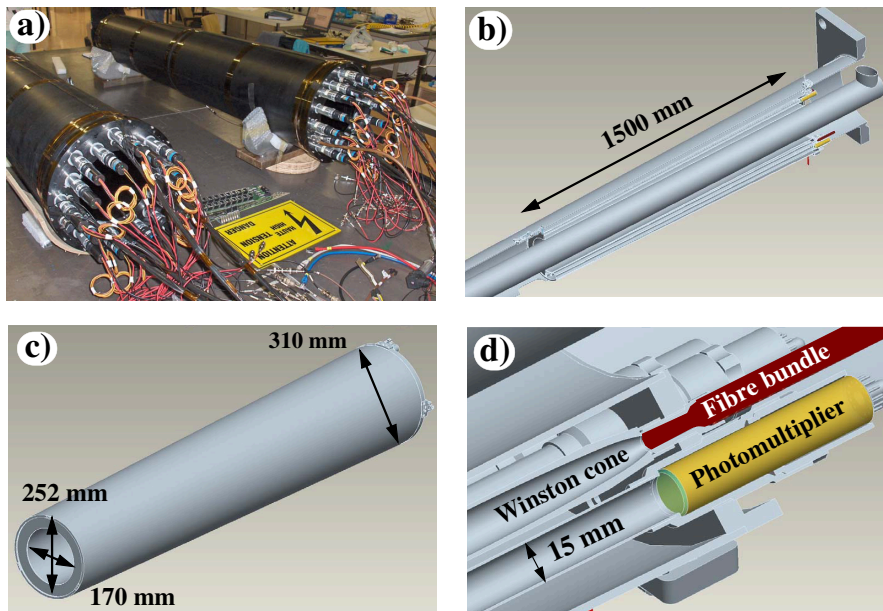


Figure 3.19: (a) Picture of the two LUCID vessels fully assembled and ready to be installed in ATLAS; (b) Sketch of LUCID integrated in the cone supporting the beam pipe; (c) Design of the gas vessel; (d) Expanded view of the readout area showing the coupling between the 15 mm diameter Cherenkov tubes and the photomultiplier tubes.

Chapter 4

Data and Monte Carlo samples

In 2011, collected data was 4.7 fb^{-1} as available integrated luminosity and new particles search is carried out by using the data. Background and signal events are estimated by using Monte Carlo (MC) samples corresponding to the ATLAS detector conditions. This section describes the 2011 data and MC samples with its detector conditions during data taking and corresponding simulation configurations.

4.1 2011 Data

In 2011 year, LHC had been operated without any fatal problems and total luminosity of $5.2 \pm 0.2 \text{ fb}^{-1}$ is obtained in proton-proton collisions at center-of-mass energy $\sqrt{s} = 7 \text{ TeV}$. The 2011 data is separated into four term by taking into account LHC and ATLAS conditions. The integral luminosity, beginning and end of each term and the detector configuration are described as follows. The detector configurations are installed into geometry on simulation.

1. B2 - D7 ($\int Ldt = 194.9 \text{ pb}^{-1}$, 22/3/2011 - 29/4/2011)
Corresponding $\sim 3\%$ of data, 54 dead pixel modules, 7 dead b-layer modules and 5 dead modules in the tile calorimeter in this term.
2. E1 - H4 ($\int Ldt = 1036.7 \text{ pb}^{-1}$, 30/4/2011 - 28/6/2011)
In this term, 6 dead module in the LAr calorimeter, 6 dead modules in tile calorimeter, 56 dead pixel modules and 7 dead b-layer modules.

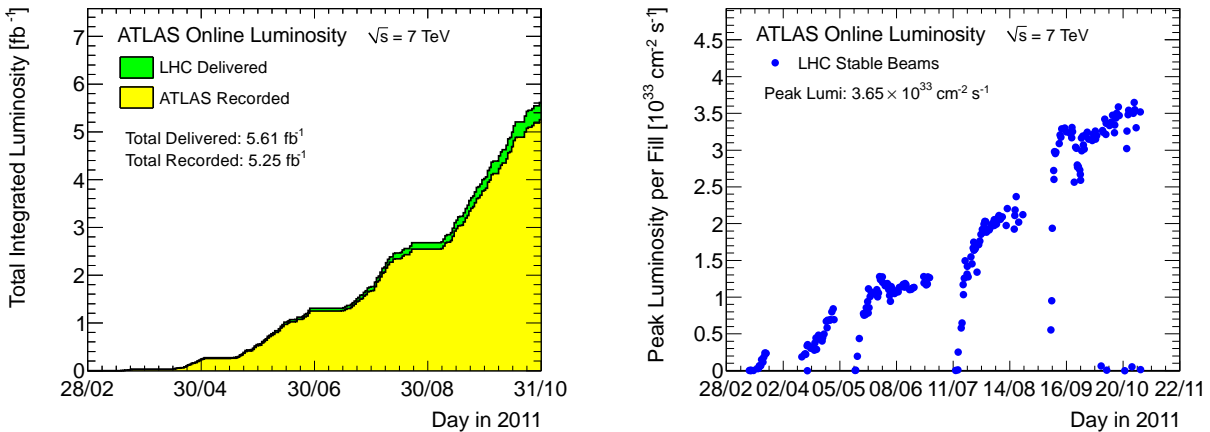


Figure 4.1: Total integrated luminosity (left) and peak luminosity per day (right) in 2011. The five term corresponds to five blocks and blanks between each term are corresponding to stopping beam due to maintenance. The first term corresponds to calibration run and the last four terms are employed for this analysis and described in Section 4.1.

3. I1 - K6 ($\int Ldt = 1287.9 \text{ pb}^{-1}$, 13/7/2011 - 22/8/2011)
The 2 modules in LAr calorimeter are dead, 7 dead modules in tile calorimeter, 62 dead pixel modules and 10 dead b-layer modules.
4. L1 - M10 ($\int Ldt = 2674.4 \text{ pb}^{-1}$, 7/9/2011 - 25/10/2011)
The 2 modules in LAr calorimeter are dead, 9 dead modules in tile calorimeter, 63 dead pixel modules and 10 dead b-layer modules.

Figure 4.1 shows total integrated luminosity (left) and peak luminosity (right) in 2011. During blanks between each term in the figures, technical maintenances were applied to LHC and ATLAS, therefore performances of LHC and ATLAS were improved after blanks.

4.2 Monte Carlo (MC) Samples

MC simulation samples are performing important roles to understand the data. This section describes how to generate the simulated samples and which samples are used.

4.2.1 Generations of Monte Carlo Samples

A simulation process is categorized into two part, event generation and detector simulation. Generators calculate decay branches until the particles become stable and also four vector of these decay particles. After that, the stable particles are handed off to the detector simulation and interact with the detector material. The detector simulation calculates the hit positions in the track detectors and the energy deposits in the calorimeter cells, and the electric output signals of detectors by using the hit positions and energy deposits. After the detector simulation, the data and MC samples are treated equally by using the same reconstruction algorithm.

For the event generation, various generators are prepared to correspond with properties of the events. In this section, the event generation is described in focusing on ALPGEN generator because W +jets and $t\bar{t}$ MC samples as dominant backgrounds are generated by this generator.

Event Generation

Event generator takes charge of processes from proton collision to emission of the stable decayed particles. The processes are classified into three types, a matrix element calculation, a parton shower process and hadronization. Figure 4.2 shows a concept of the processes from proton collisions to hadronization on the MC level. The processes are explained as follows.

1. Matrix element calculation
ALPGEN generates hard-processes using leading order calculation. The generator produces partons whose energy scale is larger than factorization scale μ_F in the collision proton. The other partons whose energy are smaller than μ_F are treated by Parton Distribution Function (PDF). Coupling constant α_s are defined by a renormalization scale μ_R which is usually the same value as the factorization scale μ_F . The μ_R is set to its hard process energy scale, e.g. $\mu_R^2 = m_W^2 + (p_T^W)^2$ in the W +jets events and $\mu_R^2 = m_t^2 + (p_T^t)^2$ in $t\bar{t}$ events. In element matrix calculations, ALPGEN includes additional partons in the matrix element, then cross sections are calculated in each additional parton bin. ALPGEN samples are labeled by the number of partons as Np0, Np1, \dots , Np5.
2. Parton shower
Parton shower program evolves partons generated in the matrix element. The process is introduced virtuality Q^2 defined by transfer momentum $Q^2 = -q^2$. Parton in hard-process emits parton shower until the $|Q^2|$ falls down at $|Q_0^2|$.
3. Hadronization
After the parton shower, hadronization proceeds by using all partons which are evolved by the parton shower and the soft gluons coming from partons below the factorization scale. The partons are combined with the neighbor partons to be color singlet. The color singlet hadrons are handed to the detector simulation.

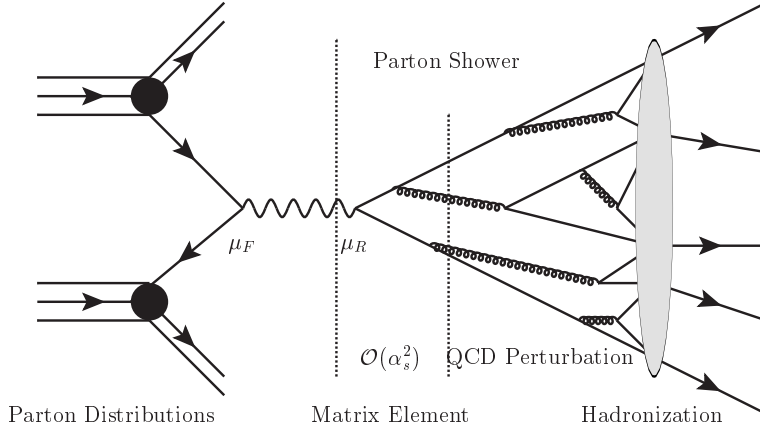


Figure 4.2: Procedure of event generation.

To populate the phase space not taken care of by the matrix element generator, it is necessary to interface the matrix element generator with a parton shower program like PYTHIA and HERWIG. Because it is possible for a parton generated by parton shower program to proceed in phase space where the matrix element calculation already covers. To avoid this, MLM matching scheme described below is applied to these events.

The partons in the matrix element are generated above a given p_T threshold $p_T > p_T^{min}$. The showered events (before hadronization) are processed with a cone algorithm, defined by E_T^{min} and R_{jet} which are energy threshold for the cone jet and angle distance thresholds between the cone jets, respectively. Usually $E_T^{min} = 20$ GeV and $R_{jet} = 0.7$ are employed. Then the partons from the matrix element calculation are matched to jets and for every parton, the jet with the smallest $\Delta R(jet, parton)$ is selected. If $\Delta R(jet, parton)$ is smaller than R_{jet} , the parton is considered as matched.

ALPGEN generator calculates the cross sections in each number of parton independently. After the diagrams drawing and cross section calculations are finalized, the events are generated to follow the diagrams. The events generated by ALPGEN which is leading order (LO) generator are corrected by using k-factor which is ratio of LO cross section to next-to-leading order (NLO) cross section. Figure 4.3 shows a example of the relation between the LO, NLO and next-to-next-leading order (NNLO) cross section as a function of the renormalization scale. The ratio becomes constant depending the renormalization scale μ_R . The higher order cross sections are reliable but it takes large time to calculate the complicated matrix elements. The k-factors compensate the cross section with the higher order contributions.

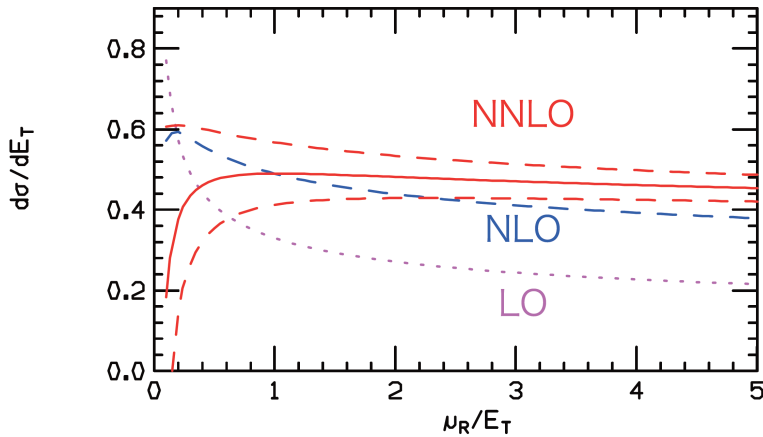


Figure 4.3: Cross section of the leading order, next-to-leading order, next-to-next-leading order calculation as a function of the renormalization scale. Single jet inclusive distribution at $E_T = 100$ GeV, appropriate for Run I of the Tevatron. Theoretical predictions are shown at LO (dotted magenta), NLO (dashed blue) and NNLO (red). Since the full NNLO calculation is not complete, three plausible possibilities are shown [39].

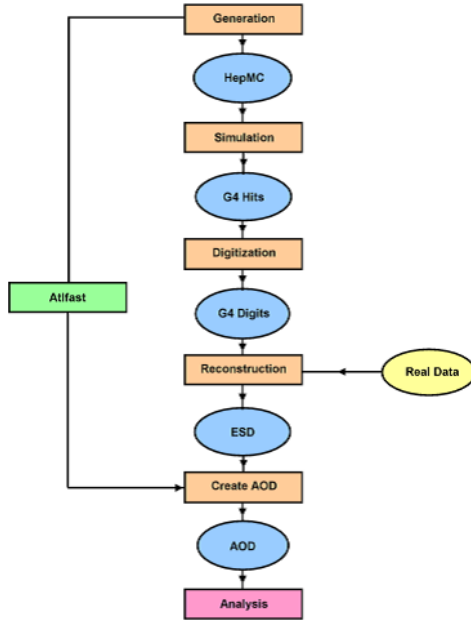


Figure 4.4: Sketch of flow for generation of Monte Carlo samples from event generation to analysis.

Detector Simulation

The simulation of the detector response is performed by the simulation tool kit GEANT4. The hit position and time in the track detectors and the energy deposit in the calorimeters are simulated (so-called simulation) and these information is converted into signals of the detector (so-called digitization). Finally the simulated detector signals are processed in the same way as the data and reconstructed to objects (so-called reconstruction). The reconstructed simulation samples are treated the same as real data and the information of objects, hit positions and calorimeter energy deposits and so on are stored into data files named ESD (Event Summary Data) or AOD (Analysis Object Data). In analysis the necessary information are taken out from the data files.

The flow chart of MC sample generations described above are drawn and summarized in Figure 4.4.

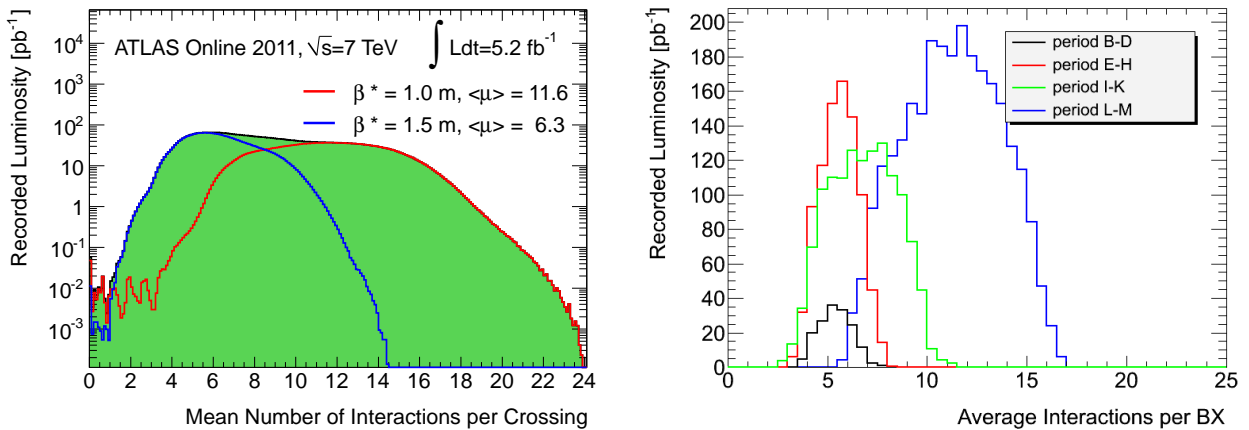


Figure 4.5: Average number of interactions per bunch crossing for the measurement in the data derived in period B-K (left-blue) and L-M (left-red), and different setups of minimum-bias events in MC simulation in terms (right).

Pile-up

The peak instantaneous luminosity delivered by LHC has increased from $L = 2.0 \times 10^{32} \text{ cm}^{-2}\text{s}^{-1}$ in 2010 to $L = 3.6 \times 10^{33} \text{ cm}^{-2}\text{s}^{-1}$ by the end of 2011. This increase results from both an increased instantaneous luminosity delivered per bunch crossing and significant increase in the total number of bunches colliding. The average number of interactions per bunch crossing $\langle\mu\rangle$ has also increased from $\langle\mu\rangle \sim 6.3$ to $\langle\mu\rangle \sim 11.6$, and maximum inelastic interactions per bunch crossing is approximately 24.

All simulated samples are generated with a range of simulated minimum-bias interactions overlaid on the hard-scattering event to account for the multiple proton-proton interactions in the same beam crossing. The minimum-bias interactions are called “pile-up”. Figure 4.5 shows the measurement of average number of interactions per bunch crossing (left) and number of simulated minimum-bias events per bunch crossing contained into the simulated events.

4.2.2 Monte Carlo Samples

Background samples employed in this analysis are generated by ALPGEN, HERWIG, MC@NLO and PYTHIA. Especially the ALPGEN generator is important since the W +jets and $t\bar{t}$ events are produced by this generator. The dibosons and single top events are generated by the HERWIG and MC@NLO, respectively. Generators, cross sections and order of calculations are summarized in Table 4.2. The features of these samples are explained simply below.

W +jets and Z +jets Samples

The W +jets events are dominant background for the one lepton channel analysis. The events are generated by a valence quark and a anti-quark derived from a gluon split, vice versa. Figure 4.6 show the diagrams of W +jets and W event associated with heavy flavor jets. Z +jets events are produced in the same manner as W +jets events.

$t\bar{t}$ and single top Samples

The secondary dominant background processes are $t\bar{t}$ events, especially the semi-leptonic decay. This has higher jet multiplicity compared to the W +jets events. Single top events are also considered. The top quark events can be enhanced by using b -tagging. The decay processes of $t\bar{t}$ and single top are shown in Figure 4.7.

Dibosons Samples

The dibosons contaminations are smaller than W +jets and $t\bar{t}$ events. The diagrams of s -channel and t -channel dibosons events are shown in Figure 4.8.

Signal Samples

The signal Monte Carlo samples are generated by the HERWIG and MADGRAPH. The generator and the order of calculations are shown in Table 4.2.

Term	Period	Run Number	Date	$\int Ldt[\text{pb}^{-1}]$ Record	$\int Ldt[\text{pb}^{-1}]$ Available
1st	B2 – D7	178044 – 180481	22-Mar-2011 – 29-Apr-2011	195.0	112.7
2nd	E1 – H4	180614 – 184169	30-Apr-2011 – 28-Jun-2011	1036.7	948.6
3rd	I1 – K6	185353 – 187815	13-Jul-2011 – 22-Aug-2011	1287.9	1154.3
4th	L1 – M10	188902 – 191933	07-Sep-2011 – 30-Oct-2011	2674.4	2431.4
Total	B2 – M10	177531 – 191933	2011-Mar-13 – 2011-Oct-30	5194.0	4713.1

Table 4.1: Term and integral luminosity of ATLAS data preparation in 2011.

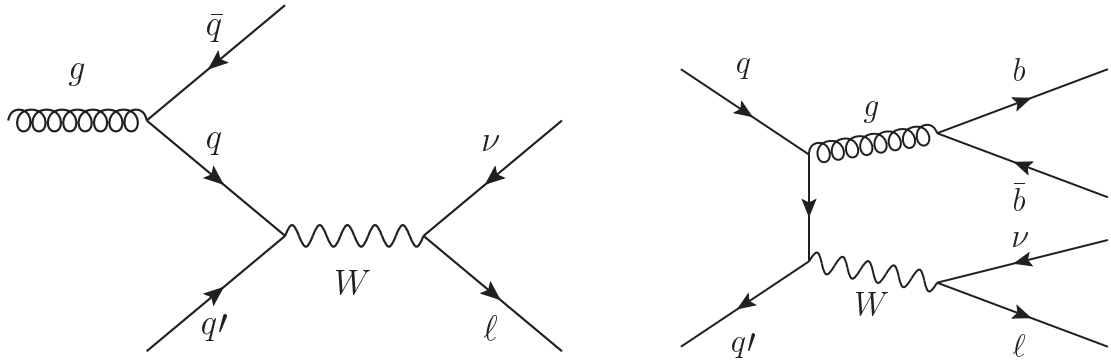


Figure 4.6: Diagrams of the W +jets and W +bb samples.

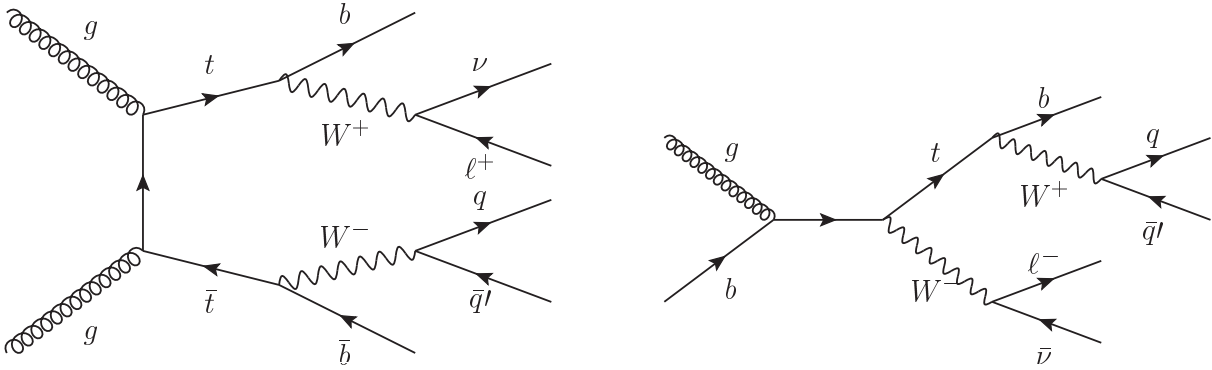


Figure 4.7: Diagrams of the $t\bar{t}$ samples (left) and single top sample (right).

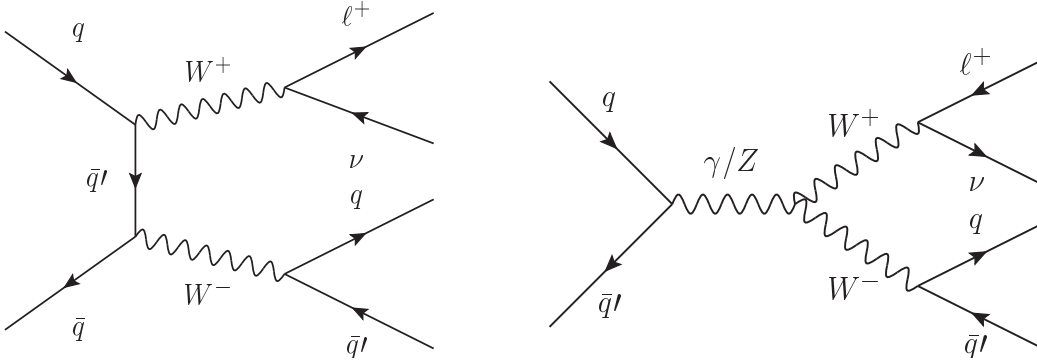


Figure 4.8: Diagrams of the dibosons samples. The left figure shows the t -channel (left) and the right figure shows the s -channel (right) dibosons event

Physics process	Generator	Cross section (pb)	Calculation accuracy
$t\bar{t}$	ALPGEN 2.13 [40]	166.8	LO×K
$W(\rightarrow l\nu) + \text{jets}$	ALPGEN 2.13 [40]	10460	LO×K
$W(\rightarrow l\nu) + b\bar{b} + \text{jets}$	ALPGEN 2.13 [40]	130	LO×K
$W(\rightarrow l\nu) + c\bar{c} + \text{jets}$	ALPGEN 2.13 [40]	360	LO×K
$W(\rightarrow l\nu) + c + \text{jets}$	ALPGEN 2.13 [40]	1100	LO×K
$Z/\gamma^*(\rightarrow \ell\ell) + \text{jets} (m_{\ell\ell} > 40 \text{ GeV})$	ALPGEN 2.13 [40]	1070	LO×K
$Z/\gamma^*(\rightarrow \ell\ell) + \text{jets} (10 \text{ GeV} < m_{\ell\ell} < 40 \text{ GeV})$	ALPGEN 2.13 [40]	3970	LO×K
$Z/\gamma^*(\rightarrow \ell\ell) + b\bar{b} + \text{jets} (m_{\ell\ell} > 40 \text{ GeV})$	ALPGEN 2.13 [40]	10.3	LO×K
Single-top (t -chan)	MC@NLO 4.01 [41]	7.0	NLO
Single-top (s -chan)	MC@NLO 4.01 [41]	0.5	NLO
Single-top (Wt -chan)	MC@NLO 4.01 [41]	15.7	NLO
WW	HERWIG 6.5.20 [42]	44.9	NLO
$WZ/\gamma^* (m_{Z/\gamma^*} > 60 \text{ GeV})$	HERWIG 6.5.20 [42]	18.5	NLO
$Z/\gamma^*Z/\gamma^* (m_{Z/\gamma^*} > 60 \text{ GeV})$	HERWIG 6.5.20 [42]	5.96	NLO

Signal Samples	Generator	Region	Calculation
Simplified SUSY	MADGRAPH5 [43]	$200 \leq m_{\tilde{g}} \leq 1200 \text{ GeV}$	NLO+NNL
UED	HERWIG++ 2.5.2 [40]	$300 \leq 1/R \leq 1150 \text{ GeV}$ $2 \leq \Lambda R \leq 40$	NLO

Table 4.2: Simulated background and signal event samples used in this analysis, with the corresponding production cross sections. The notation LO×K indicates that the process is calculated at leading-order and corrected by a factor derived from the ratio of LO to NLO cross sections for a closely related process. The $t\bar{t}$, W +light-jets and Z +light-jets samples are normalized using the inclusive cross sections; the values shown for the W +light-jets and Z +light-jets samples are for a single lepton flavor. The single-top cross sections are listed for a single lepton flavor in the s - and t -channels.

Chapter 5

Object Definition

In this chapter, definitions of used objects and kinematics variables by using electron, muon, jet and E_T^{miss} are described. Reconstruction algorithms and performance of each object are described in Appendix B.

5.1 Electron

Electrons are reconstructed with the clusters in the electromagnetic calorimeter matching with charged tracks. These reconstructed electrons are refined through two steps. First, *medium* identification algorithm is applied to the reconstructed electrons as preselection by using shower shape and strip-based cut in first layer of LAr calorimeter to separate from pion processes. In addition the preselected electrons are required to be isolated with any jets $\Delta R(e, jets) > 0.4$. The preselected electrons are employed for rejection against noise events and scale factor estimation.

Second, the preselected electrons are required to pass signal selection criteria by using $\text{ptcone20} < 0.1 \times p_T^e$ and *tight* identification algorithm which requires larger ratio of number of high-threshold hits to total number of hits in TRT than a threshold. The ptcone20 is described in Section 5.5. The signal electrons are employed for event selections.

The definitions of preselected and signal electrons are summarized in Table 5.1. The reconstruction and identification algorithm, and their qualities are explained in Appendix B.

5.2 Muon

Muons are reconstructed from combined tracks between inner detector and muon spectrometer. The analysis employs STACO muons and segment tagged muons as follows; 1) the STACO muons are reconstructed by using combined good track in both inner detector and muon spectrometer; 2) the segment tagged muons are reconstructed from a good track in inner detector and a segment reconstructed in muon spectrometer layer.

Similarly to the electrons, the reconstructed muons are selected through two steps, preselected and signal muon selection criteria. The preselected muons are refined by requiring additional inner track qualities and an isolation with $\Delta R(\mu, jets) > 0.4$. The selected muons are required $\text{ptcone20} < 1.8$ GeV. The definition of preselected and signal muon is tabled in Table 5.2 and reconstruction and performance are described in Appendix B

5.3 Jet

Jets are reconstructed by using clusters in the electromagnetic and the hadronic calorimeters and Anti- k_T 4Topo algorithm with size parameter $\Delta R = 0.4$ [44–46]. The clusters are merged as long as

$$d_{iB} < d_{ij} = \min\left(1/k_{Ti}^2, 1/k_{Tj}^2\right) \cdot \Delta_{ij}^2 / (0.4)^2, \quad (5.3.1)$$

where k_T is a transverse momentum of clusters, Δ_{ij} is an angle distance between a cluster i and other cluster j and d_{iB} is calculated by its own cluster. The energy of clusters are given by EM scale in the jet reconstruction.

The EM scale is given by using the detector responses corresponding to electron energy in test beam. The momentum of jet is calibrated by using jet energy scale (JES) measured in test beam and jet-photon measurements and so on.

The reconstructed jets are classified into the preselected jets with $p_T > 20$ GeV and $|\eta| < 2.5$. The jets are also selected by jet vertex fraction (JVF) which is a fraction of tracks coming from a primary vertex to total momentum of tracks associated with the jet as following,

$$\text{JVF}(jet_i, vertex_j) = \frac{\sum_k p_T(track_k^{jet_i}, vertex_j)}{\sum_n \sum_l p_T(track_l^{jet_i}, vertex_n)}, \quad (5.3.2)$$

where the $vertex_j$ is selected from the primary vertex where the associated track p_T sum is the highest in the event. Schematic of jet vertex and distribution of the jet vertex fraction are shown in Figure 5.1. For jets, it is required that the jet vertex fraction is larger than 0.75.

The b -tagged jets are identified by using JetFitterCombNN algorithm. The algorithm is a combination of JetFitterComb algorithm which identifies b -jets, c -jets and light flavor jets by using information of primary vertex, secondary vertex and particle trajectories, and IP3D algorithm which is based on a likelihood ratio between the transverse impact parameter d_0/σ_{d_0} and longitudinal impact parameter z_0/σ_{z_0} . Operating point of 1.8 is used for the b -tagging where efficiency of b -jets is 60% and rejection factor of light flavor is 200-400, and 7-10 for the charm jets.

The criteria is shown in Table 5.3 and the jet reconstruction algorithm and performance are described in Appendix B.

5.4 Missing Transverse Energy E_T^{miss}

E_T^{miss} is defined with vectorial sum of the reconstructed objects in each event. The following objects are used to calculate E_T^{miss} .

- Electron
Reconstructed electrons satisfy $p_T > 10$ GeV and *medium* selection criteria.
- Muon
STACO muons are applied to isolation with respect to the selected jets by using $\Delta R(\mu, jets) > 0.3$.

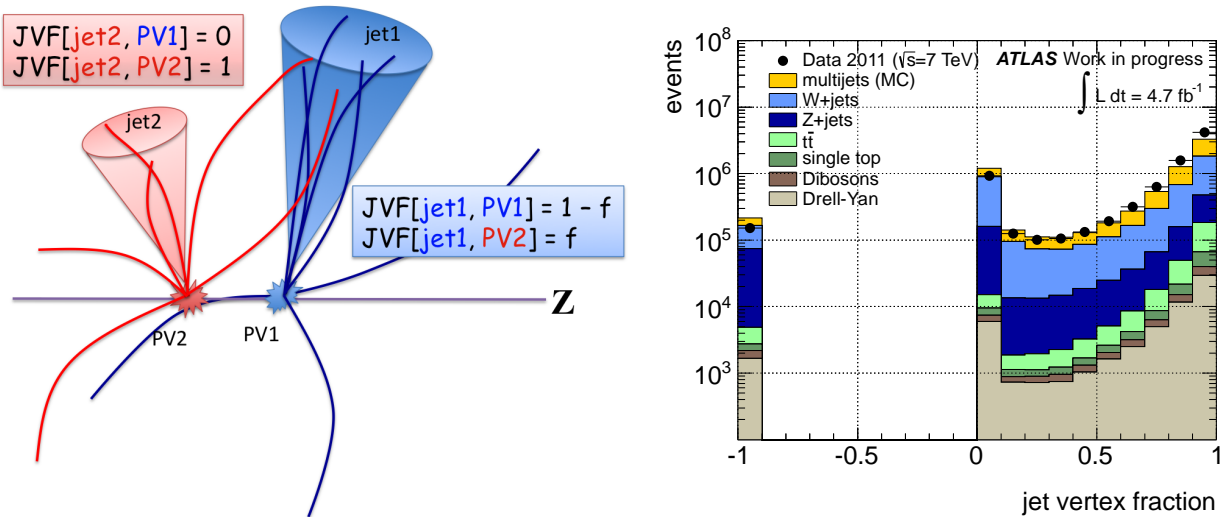


Figure 5.1: Depiction of jet vertex fraction discriminant (left) and distribution of its variable (right). JVF=-1 events are that tracks associated with jet pass through $|\eta| > 2.5$ region where the inner track detectors do not exist.

	hard electron		soft electron	
	preselected	signal	preselected	signal
p_T	$p_T > 10$ GeV	$p_T > 25$ GeV	$p_T > 7$ GeV	$7 < p_T < 25$ GeV
η	$ \eta^{\text{clust}} < 2.47$		$0 < \eta^{\text{clust}} < 1.37, 1.52 < \eta^{\text{clust}} < 2.47$	
Algorithm	Electron		Electron	
Quality Isolation	<i>medium</i>	<i>tight</i> $\text{ptcone20}/p_T < 0.10$	<i>medium</i>	<i>tight</i> $\text{ptcone20}/p_T < 0.10$
Overlap Removal	$\Delta R(e, jets) < 0.2$ and $\Delta R(e, jets) > 0.4$			

Table 5.1: Definition of electron selection criteria.

	hard muon		soft muon	
	preselected	signal	preselected	signal
p_T	$p_T > 10$ GeV	$p_T > 20$ GeV	$p_T > 6$ GeV	$6 < p_T < 20$ GeV
η	$ \eta < 2.40$		$ \eta < 2.40$	
Algorithm	STACO or segment-tagged muon		STACO or segment-tagged muon	
Isolation	—	$\text{ptcone20} < 1.8$ GeV	—	$\text{ptcone20} < 1.8$ GeV
Inner Detector Track Quality	number of pixel hits + number of crossed dead pixel sensors > 1 number of SCT hits + number of crossed dead SCT sensors ≥ 6 number of pixel holes + number of SCT holes < 3 \geq one b-layer hit when it can be expected if $ \eta < 1.9$ then $n_{\text{TRT}} > 5$ and $n_{\text{TRT}}^{\text{outliers}} < 0.9n_{\text{TRT}}$ if $ \eta < 1.9$ and $n_{\text{TRT}} > 5$ then $n_{\text{TRT}}^{\text{outliers}} < 0.9n_{\text{TRT}}$			
Overlap Removal	$\Delta R(\mu, jets) > 0.4$			

Table 5.2: Definition of muon selection criteria. The number of hole is lack of hit on the layers along the track. n_{TRT} is the total number of TRT hits, and $n_{\text{TRT}}^{\text{outlier}}$ is number of TRT hits not using for track reconstruction.

	preselected	select	b-jet
p_T	$p_T > 20$ GeV	$p_T > 25$ GeV	$p_T > 25$ GeV
η	$ \eta < 2.5$		
Algorithm	Antik _T , $\Delta R < 0.4$, TopoCluster		
Jet Vertex Fraction	—	JVF > 0.75	
Overlap Removal	$\Delta R(e, jets) > 0.2$		
b-tag Algorithm	—	—	JetFitterCombNN

Table 5.3: Definition of jet and b -jet selection criteria. Algorithm of JetFitterCombNN are described in Appendix B.

- Jet

Jets are formed from topoclusters by using Anti- k_T Topo algorithm with size parameter $\Delta R = 0.4$ calibrated by the EM+JES scale (the topocluster and Anti- k_T Topo algorithm are described in Appendix B). Transverse momentum of the jets is required to be larger than 20 GeV.

- Cell-out

Cell-out term is formed from all topocluster in the calorimeter not to belong to any other objects (electrons, muons and jets). Energy scale is calibrated by the EM scale.

These terms are expressed as following formula

$$E_x^{\text{miss}} = -\sum E_x^e - \left(\sum E_x^{\text{calo},\mu}\right) - \sum p_x^\mu - \sum E_x^{\text{jet}} - \sum E_x^{\text{Cell-out}} \quad (5.4.1)$$

$$E_y^{\text{miss}} = -\sum E_y^e - \left(\sum E_y^{\text{calo},\mu}\right) - \sum p_y^\mu - \sum E_y^{\text{jet}} - \sum E_y^{\text{Cell-out}} \quad (5.4.2)$$

and the E_T^{miss} is described as follow

$$E_T^{\text{miss}} = \sqrt{(E_x^{\text{miss}})^2 + (E_y^{\text{miss}})^2} \quad (5.4.3)$$

5.5 Definitions of variables

Products by cascade decay from SUSY particles are detected as leptons, jets or E_T^{miss} . To reduce the background or enhance the signal yield, some variables are defined as follows

- Transverse momentum : $p_T = \sqrt{(p_x)^2 + (p_y)^2}$

The transverse momentum is the momentum on the r - ϕ plane and this momentum is conserved in the proton-proton collisions.

- Transverse mass : $m_T = \left(|p_T^\nu| + |p_T^\ell|\right)^2 - (p_T^\nu + p_T^\ell)^2 = \sqrt{2 \cdot p_T^\ell \cdot E_T^{\text{miss}} [1 - \cos(\Delta\phi(\ell, E_T^{\text{miss}}))]}$

This variable is reconstructed by using transverse momentum of a lepton p_T^ℓ and E_T^{miss} .

- Effective mass : $m_{\text{eff}} = \sum p_T^\ell + \sum p_T^{\text{jet}} + E_T^{\text{miss}}$

m_{eff} is composed of scalar sum of p_T with leptons and jets and E_T^{miss} , thus m_{eff} corresponds to the all products originating from SUSY particles decay. Two different versions of the effective mass are considered. One is $m_{\text{eff}}^{\text{inc}}$ based on all selected jets. The other m_{eff} only uses the number of jets that are required as a minimum in a given signal selection. For example, in 2-jets soft lepton signal region, only two jets are used in m_{eff} .

- Angle distance : $\Delta R(a, b) = \sqrt{(\eta_a - \eta_b)^2 + (\phi_a - \phi_b)^2}$

The $\Delta R(a, b)$ means the angle distance between an object a and an object b .

- ptcone

The ptcone is sum of momentum of tracks within the cone ΔR along trajectory of selected electron or muon, and subtracted its electron or muon momentum. The cone size is determined to optimize for each analysis. In this analysis the ptcone20 whose cone size is $\Delta R = 0.2$ is employed. The leptons after applying the ptcone are named isolation leptons.

- Invariant mass $m_{\ell\ell}$

Invariant mass is calculated by using dileptons events. The formula is

$$m_{\ell\ell} = \left(E_T^{\ell_{1\text{st}}} + E_T^{\ell_{2\text{nd}}}\right)^2 - |\mathbf{p}^{\ell_{1\text{st}}} + \mathbf{p}^{\ell_{2\text{nd}}}|^2 \quad (5.5.1)$$

- Generated W boson p_T and Z boson p_T : generated p_T^W and generated p_T^Z

The transverse momentum of the generated W and Z boson which are generated particles on the generator level employs the transverse momentum calculated by the event generator.

- Reconstructed W boson p_T and Z boson p_T : p_T^W and p_T^Z

On the data and reconstructed MC objects, the transverse momentum of W boson p_T^W and Z boson p_T^Z are obtained from transverse momentum of lepton p_T^ℓ and missing transverse energy E_T^{miss} . The p_T^W is calculated by using the vectorial sum of four momentum with the a lepton and E_T^{miss} . As well, the p_T^Z is calculated by using the vectorial sum of four momentum with the two leptons. The formula is as follows.

$$(p_T^W)^2 = (p_x^W)^2 + (p_y^W)^2 = (p_x^\ell + E_x^{\text{miss}})^2 + (p_T^\ell + E_y^{\text{miss}})^2. \quad (5.5.2)$$

$$(p_T^Z)^2 = (p_x^Z)^2 + (p_y^Z)^2 = (p_x^{\ell_{1\text{st}}} + p_x^{\ell_{2\text{nd}}})^2 + (p_y^{\ell_{1\text{st}}} + p_y^{\ell_{2\text{nd}}})^2. \quad (5.5.3)$$

Chapter 6

Event Selection

Optimization of selection and event cleaning are described in this chapter. One lepton channel analysis requires the exact one electron or muon isolated with jets. A tau lepton is not identified but the electron and muon coming from tau decay is identified as a prompt-lepton.

The signal region is optimized for the degenerate SUSY model and the UED model by using low p_T lepton which corresponds to an electron with $6 < p_T^{e_{1st}} < 25$ GeV and a muon with $6 < p_T^{\mu_{1st}} < 20$ GeV. Analysis using such lepton is called “soft lepton channel”. Also “hard lepton channel” analysis employs a $p_T^{e_{1st}} > 25$ GeV electron or a $p_T^{\mu_{1st}} > 20$ GeV muon. Although the hard lepton channel is optimized to MSUGRA model, results of the channel are combined with that of the soft lepton channel and it improves sensitivity to the degenerate models. Signal region is also required to have large E_T^{miss} and jet multiplicity because of a production of heavy particles and cascade decays in SUSY or UED models.

In this chapter, event selections which remove events triggered by coherent noise or cosmic rays are described. After that, the signal regions are determined to be optimized by using a significance. The end of this chapter, expected significance for the degenerate SUSY model on $m_{\tilde{g}}-m_{\text{LSP}}$ plane and UED model on $1/R-\Lambda R$ plane are shown.

6.1 Event Cleaning

Calorimeter burst and data with bad status of detectors should be removed as follows. Non-collision data, for example cosmic ray, are also eliminated by applying some technic written below.

Good Runs Lists :

The ATLAS detectors are monitored to preserve data qualities. Data in bad status of ATLAS detector and combined performance are flagged to corresponding luminosity block, which is a data block for approximately a minute.

Bad Jet Cleaning :

Noise in calorimeters makes mismeasurement of jet energy and E_T^{miss} . In general, a localized cluster can be regarded as noise since the clusters derived from particles deposit the energy in some calorimeter cells. To remove noise, the events as following are eliminated.

- HEC spike noise
Energy fraction in HEC is larger than 0.5 or negative energy in jet is larger than 60 GeV.
- EM coherent noise
Energy fraction in electromagnetic calorimeter is larger than 0.95 in $|\eta| < 2.8$.
- Non-collision background and cosmic
Maximum energy fraction in one calorimeter layer is larger than 0.99 in $|\eta| < 2.0$.

LAr Hole Veto :

From April 30th 2011, some plate controllers of LAr calorimeter of $-0.1 < \eta < 1.5$, $-0.9 < \phi < -0.5$ have been broken due to an electric power problem. Jets passing through this region are considered to be misreconstructed.

To deal with the hole, events where missing energy exceeds a threshold is discarded. The estimation of missing energy is

$$E = \sum_{\text{jets in hole}} p_T^{\text{jet}} (1 - f_{E_{\text{cell}}}) \left[\frac{1}{1 - f_{E_{\text{jet}}}} - 1 \right] \cos(\phi_{\text{jet}} - \phi_{E_T^{\text{miss}}}) \quad (6.1.1)$$

where $f_{E_{\text{cell}}}$ and $f_{E_{\text{jet}}}$ are fraction of the jet energy corrected by using the neighbor cells assuming the same energy density and jet shape comparing with simulation after jet reconstruction, respectively. If $E > 10$ GeV and $E > 0.1 \cdot E_T^{\text{miss}}$, the event is rejected.

Primary Vertex :

To ensure the event coming from not non-collision event or cosmic ray but a hard process, primary vertex where sum of momentum of tracks from the vertex is the most energetic is required to have at least five tracks in the event.

Cosmic Muon and Bad Muon :

Events which contain muons like cosmic ray or muons interfering with E_T^{miss} are rejected. The cosmic-like muons are identified by using the muon trajectory as $|z_0| > 1.0$ mm and $|d_0| > 0.2$ mm. On the other hand, non-isolated muon tracks in muon spectrometer are rarely used to calculate E_T^{miss} term. These events are called ‘‘bad muon events’’ and removed by applying $\sigma(q/p)/|(q/p)| > 0.2$ to muons.

Electron Crack Veto (only soft electrons) :

In crack region of LAr calorimeter ($1.37 < |\eta| < 1.52$), quantities of sampling material are smaller. MC predictions are good modeling for hard electrons however the MC predictions are not in agreement with data for soft electrons in this region. Therefore the events where the soft electrons entering the crack region are rejected.

6.2 Trigger

The hard electron channel, hard muon channel and soft lepton channel are required the electron trigger, muon trigger and transverse missing energy trigger, respectively. p_T threshold of reconstructed objects are determined that each trigger efficiency becomes a plateau. Trigger algorithm is described in following.

- Electron trigger
The electron trigger algorithm requires the $p_T^e > 20$ GeV in earlier 2011, and $p_T^e > 22$ GeV in later 2011 to correspond to instantaneous luminosity increasing. Figure 6.1 (top-left) shows the electron trigger efficiency of trigger with p_T^e threshold at 22 GeV in trigger algorithm and the plateau of efficiencies are from $p_T^e > 25$ GeV. Therefore the electrons are required $p_T^e > 25$ GeV.
- Muon trigger
The muon trigger algorithm requires muons with $p_T > 18$ GeV in earlier 2011. In later 2011, the muon trigger requires a jet with $p_T > 10$ GeV at the level-1 trigger additionally. Figure 6.1 (bottom) show the muon trigger efficiencies of trigger p_T^μ threshold at 18 GeV in barrel region and end-cap region. The plateau of trigger efficiency of muon p_T is from 20 GeV.
- Missing transverse energy E_T^{miss} trigger
 E_T^{miss} trigger is applied to the soft lepton channel. E_T^{miss} trigger algorithm requires $E_T^{\text{miss}} > 60$ GeV on event filter level, but level-2 trigger algorithm requires $E_T^{\text{miss}} > 40$ GeV in early 2011, $E_T^{\text{miss}} > 45$ GeV in middle 2011 and $E_T^{\text{miss}} > 55$ GeV in later 2011, respectively. E_T^{miss} trigger efficiency becomes plateau at 180 GeV for all E_T^{miss} trigger conditions. Figure 6.1 (top-right) shows the E_T^{miss} trigger efficiencies for the $E_T^{\text{miss}} > 40$ GeV at level 2 trigger. When the soft lepton channel is analyzed, $E_T^{\text{miss}} > 180$ GeV is required.

The discrepancy of efficiencies for both electron and muon trigger between observed data and MC events are corrected by taking scale factors of trigger efficiency. On the other hand, since the efficiency of E_T^{miss} trigger shows almost 100% and no discrepancy between data and MC in the plateau region, the scale factors for E_T^{miss} trigger are not needed.

6.3 Signal Region

Before optimizations for signal regions, features of the degenerate model and MSUGRA are discussed. The features of the signal model is described below.

- Degenerate SUSY model and UED

As mentioned already in Section 2.2, for the degenerate model the momentum and energy of decay products are small due to small mass difference in cascade decays. Meanwhile the p_T of leading jet and E_T^{miss} are expected to become large. That is because the production of large mass particles need a large transfer momentum Q^2 . To generate the large transfer momentum, the collision parton emits ISR jet with high p_T and the ISR jet is detected as a high p_T leading jet. Consequently, E_T^{miss} is detected in opposite direction to the leading jet with the approximately same energy as leading jet p_T .

- MSUGRA (large $m_{1/2}$ region)

In the high $m_{1/2}$ region the squark production is dominant compared to the gluino production since $m_{\tilde{q}} < m_{\tilde{g}}$. In the region, the m_{eff} approximately corresponding to the squark mass are heavier and the jet multiplicity tend to be a bit smaller than the gluino productions because a squark immediately decays into the chargino.

- MSUGRA (large m_0 region)

In the high m_0 region the gluino production is dominant compared to the squark production because of $m_{\tilde{g}} < m_{\tilde{q}}$. In the region the gluino decays through the virtual squarks thus the jet multiplicity tends to be higher.

To consider these points, the three analysis channel are provided as follows,

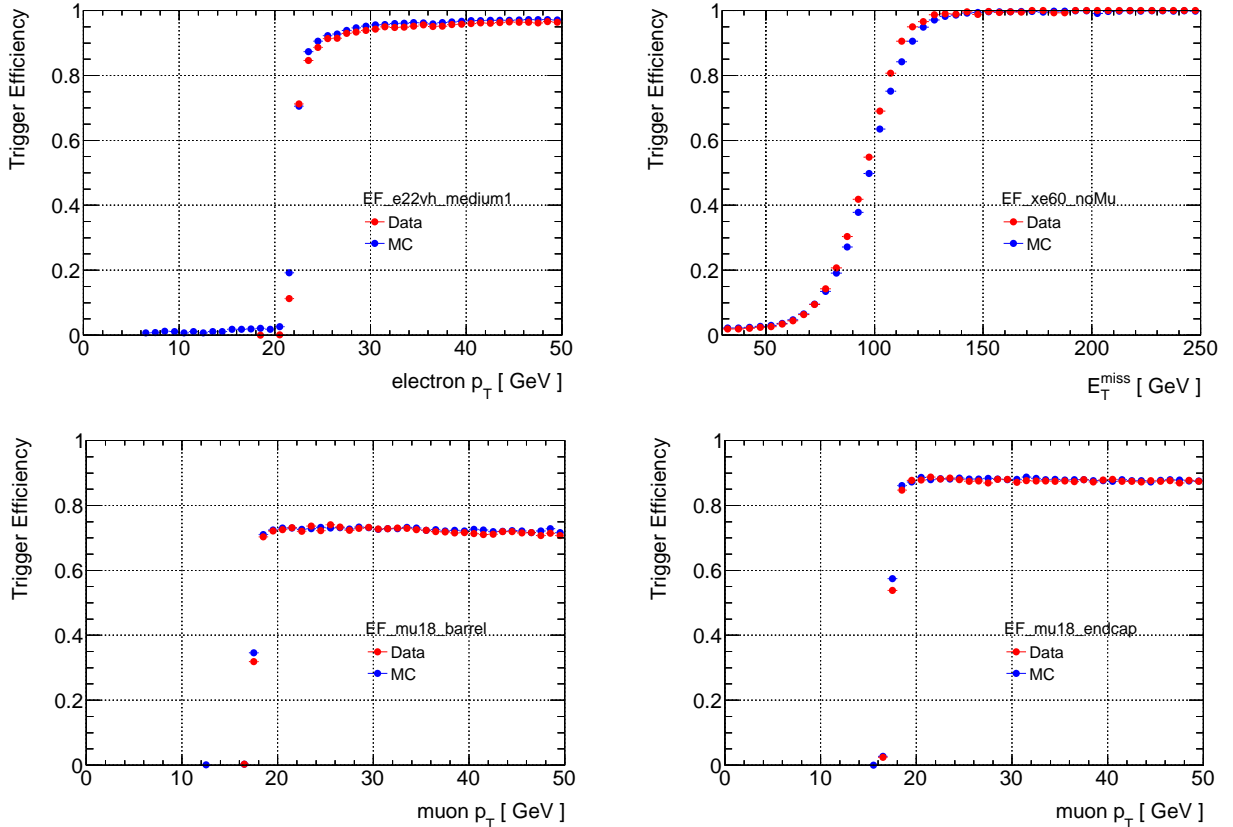


Figure 6.1: Efficiency of electron trigger (top-left), E_T^{miss} trigger (top-right), muon trigger in barrel region (bottom-left) and muon trigger in end-cap region (bottom-right) as a function of p_T of each object. Only statistical uncertainty is quoted by bi-nominal.

	soft lepton	hard lepton 3 jets	hard lepton 4 jets
Trigger	Missing E_T	lepton trigger	
N^ℓ	=1	=1	=1
$p_T^{\ell_{1st}}$	[7,25]([6,20])	> 25 (20) GeV	> 25 (20) GeV
$p_T^{\ell_{2nd}}$	< 7 (6) GeV	< 10 GeV	< 10 GeV
N^{jet}	≥ 2	≥ 3	≥ 4
$p_T^{jet_{1st}}$	> 130, 25 GeV	> 100, 25, 25 GeV	> 80, 80, 80, 80 GeV
$p_T^{jet_{4th}}$	—	< 80 GeV	—
E_T^{miss}	> 250 GeV	> 250 GeV	> 250 GeV
m_T	> 100 GeV	> 100 GeV	> 100 GeV
m_{eff}^{inc}	—	> 1200 GeV	> 800 GeV
E_T^{miss}/m_{eff}	> 0.3	> 0.3	> 0.2

Table 6.1: Definition of the selection criteria of each signal region. The p_T selections for lepton is given for electron (muon).

- Soft lepton (2-jets) channel
Exact soft one isolated electron or muon + ≥ 2 jets + E_T^{miss} (for the degenerate model).
- Hard lepton (3-jets) channel
Exact one isolated electron or muon + ≥ 3 jets + E_T^{miss} (for the MSUGRA high $m_{1/2}$ region).
- Hard lepton (4-jets) channel
Exact one isolated electron or muon + ≥ 4 jets + E_T^{miss} (for the MSUGRA high m_0).

The 3-jets and 4-jets hard lepton channels are analyzed to combine with soft lepton channel and improve the sensitivity to the degenerate models.

6.3.1 Degenerate Model

Optimization of the signal region for the degenerate model is described in this section. The distributions of representative variables for the analysis with some cuts applied which is described following are shown in Figure 6.2 and Figure 6.3. The figures show leading jet $p_T^{jet_{1st}}$ and second leading jet $p_T^{jet_{2nd}}$, jet multiplicity N^{jet} , m_T , E_T^{miss} and E_T^{miss}/m_{eff} for the Standard Model background and both simplified SUSY and UED signals by using MC predictions. The signal points drawn in these figures are $(m_{\tilde{g}}, m_{LSP}) = (425 \text{ GeV}, 345 \text{ GeV})$, $(425 \text{ GeV}, 185 \text{ GeV})$ and $(515 \text{ GeV}, 35 \text{ GeV})$ for the SUSY, on the other hand $1/R = 550, 700, 850 \text{ GeV}$ which ΛR is fixed at $\Lambda R = 10$ and $1/R = 700 \text{ GeV}$ varying $\Lambda R = 2, 10, 40$ for the UED model. p_T cut ($7 < p_T^{e_{1st}} < 25 \text{ GeV}$ or $6 < p_T^{\mu_{1st}} < 20 \text{ GeV}$) for lepton, $N^{jet} \geq 2$ and $E_T^{miss} > 180 \text{ GeV}$ cuts are applied to all figures in Figure 6.2 and Figure 6.3.

The optimization begins with $N^{jet} \geq 2$ and $E_T^{miss} > 180 \text{ GeV}$.

- The first, jet multiplicity distribution is shown in Figure 6.2 (top-left) and Figure 6.3 (top-left). The figure shows the tighter mass degenerate models (e.g. $m_{\tilde{g}} = 425 \text{ GeV}$ at $m_{LSP} = 345 \text{ GeV}$ for SUSY and $1/R = 700 \text{ GeV}$ at $\Lambda R = 2$ for UED) tend to be small jet multiplicity, although the peak of the distribution of $\Lambda R \sim 10$ is held around 3-5. Thus the signal region is required jet multiplicity $N^{jet} \geq 2$.
- The second, distribution of leading jet p_T with the $N^{jet} \geq 2$ cut applied are shown in Figure 6.2 (top-right) and Figure 6.3 (top-right). Peaks of total background and each signal parameter are located around $p_T^{jet_{1st}} \sim 150 \text{ GeV}$. The leading jet p_T is cut at 130 GeV.
- The third, distribution of second leading jet p_T to which the above cuts are applied is shown in Figure 6.2 (middle-left) and Figure 6.3 (middle-left). The peak of tighter degenerate models are below 25 GeV. In addition, the distribution of signals are softer than that of background. Therefore the second leading jet p_T cut is set to 25 GeV.

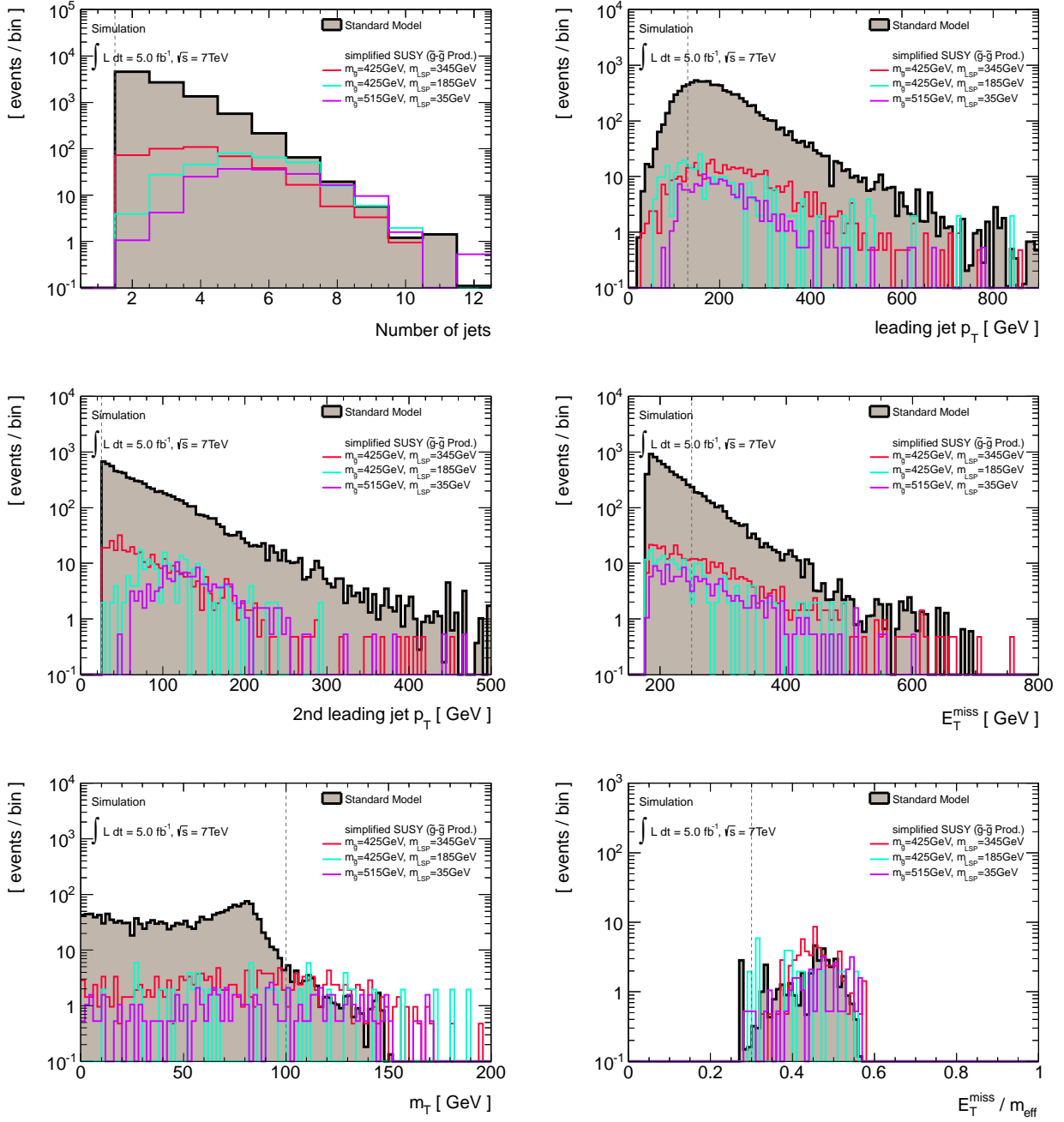


Figure 6.2: Distributions with the Standard Model background and simplified SUSY of jet multiplicity (top-left), leading jet p_T (top-right), second leading jet p_T (middle-left), E_T^{miss} (middle-right), m_T (bottom-left) and $E_T^{\text{miss}}/m_{\text{eff}}$ (bottom-right) to which are applied jet multiplicity $N^{\text{jet}} \geq 2$, lepton p_T cut ($7 < p_T < 25$ GeV, $6 < p_T^{\mu_{1\text{st}}} < 20$ GeV), $E_T^{\text{miss}} > 180$ GeV cut and additional cut described in the text in detail, respectively. The dashed line shows the border of the signal region.

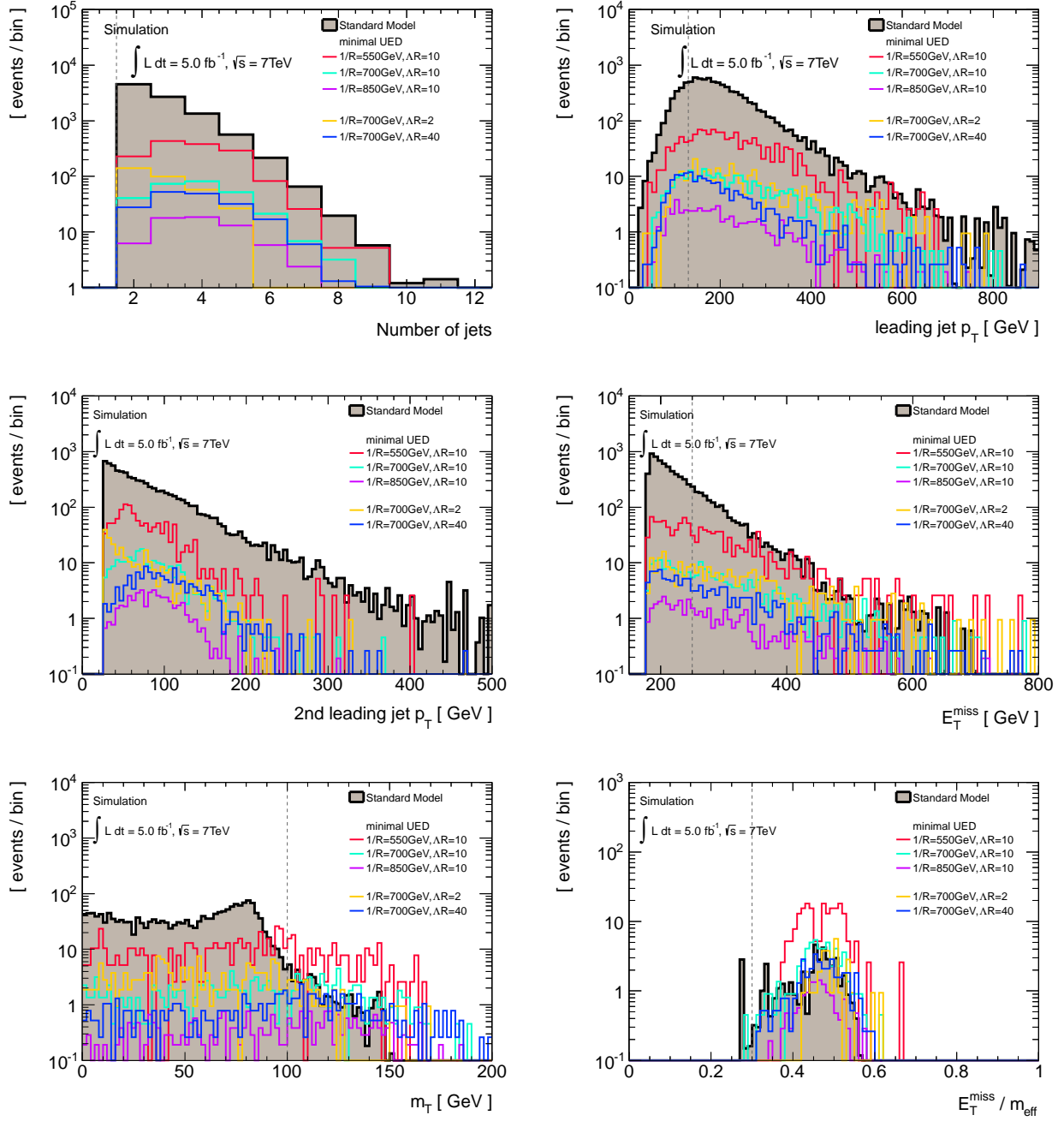


Figure 6.3: Distributions with the Standard Model background and UED model of jet multiplicity (top-left), leading jet p_T (top-right), second leading jet p_T (middle-left), E_T^{miss} (middle-right), m_T (bottom-left) and $E_T^{\text{miss}}/m_{\text{eff}}$ (bottom-right) to which are applied jet multiplicity $N^{\text{jet}} \geq 2$, lepton p_T cut ($7 < p_T < 25$ GeV, $6 < p_T^{\mu_{1\text{st}}} < 20$ GeV), $E_T^{\text{miss}} > 180$ GeV cut and additional cut described in the text in detail, respectively. The dashed line shows the border of the signal region.

- The fourth, E_T^{miss} distribution are shown in Figure 6.2 (middle-right) and Figure 6.3 (middle-right). E_T^{miss} distribution of signals become harder than the background, this indicates that a tight E_T^{miss} cut increases the sensitivity of signal events. In this analysis the E_T^{miss} cut is set to 250 GeV since the larger than 250 GeV cut decreases the statistic of signal events.
- The fifth, m_T distribution are shown in Figure 6.2 (bottom-left) and Figure 6.3 (bottom-left). $m_T > 100$ GeV cut is applied to the signal region. The W +jets and $t\bar{t}$ events are decreased by taking this cut significantly.
- Finally, $E_T^{\text{miss}}/m_{\text{eff}}$ distribution is shown in Figure 6.2 (bottom-right) and Figure 6.3 (bottom-right). The component of m_{eff} are almost E_T^{miss} and leading jet p_T , and the amount of E_T^{miss} is approximately the same as leading jet p_T in the degenerate models. Therefore the signal events concentrate to $E_T^{\text{miss}}/m_{\text{eff}} \sim 0.5$ and width of the signal distribution is narrower than that of background distribution. $E_T^{\text{miss}}/m_{\text{eff}} > 0.3$ cut is applied to the signal region.

The definition of the signal region for soft lepton channel is described as following.

1. Exact one soft lepton ($7 < p_T^{e_{1st}} < 25$ GeV or $6 < p_T^{\mu_{1st}} < 20$ GeV) is required.
2. The leading jet $p_T^{jet_{1st}} > 130$ GeV is required.
3. The jet multiplicity and p_T are required $N^{jet} \geq 2$ and $p_T^{jet} > 25$ GeV, respectively.
4. The missing transverse energy $E_T^{\text{miss}} > 250$ GeV.
5. The transverse mass $m_T > 100$ GeV to remove the W +jets events.
6. The ratio of E_T^{miss} to m_{eff} is larger than 0.3 : $E_T^{\text{miss}}/m_{\text{eff}} > 0.3$.

The selection criteria for the degenerate scenario is tabled in Table 6.1 as the soft lepton channel.

6.3.2 MSUGRA High $m_{1/2}$ Region

The high $m_{1/2}$ region are dominated the squark pair production ($m_{\tilde{g}}^2 \sim 2.6m_{1/2}^2$ and $m_{\tilde{q}}^2 \sim m_0^2 + 6m_{1/2}^2$), thus the jet multiplicity is larger than that of background and the m_{eff} is larger. The signal region for high $m_{1/2}$ is determined as 3-jets channel as follows.

1. Exact one hard lepton ($p_T^{e_{1st}} > 25$ GeV or $p_T^{\mu_{1st}} > 20$ GeV) is required.
2. The leading jet $p_T^{jet_{1st}} > 100$ GeV is required.
3. The jet multiplicity $N^{jet} \geq 3$ with $p_T^{jet} > 25$ GeV.
4. The 4th leading jet transverse momentum is required $p_T^{jet_{4th}} < 80$ GeV due to orthogonal with 4-jets channel.
5. The missing transverse energy $E_T^{\text{miss}} > 250$ GeV.
6. The transverse mass $m_T > 100$ GeV to remove the W +jets events.
7. The ratio of E_T^{miss} to m_{eff} as $E_T^{\text{miss}}/m_{\text{eff}} > 0.3$.
8. The effective mass $m_{\text{eff}} > 1200$ GeV.

6.3.3 MSUGRA High m_0 Region

In the high m_0 region, the jet multiplicity is higher than the distribution in high $m_{1/2}$ region due to the gluino pair production dominant. In this region the produced gluino mass is smaller than the squark mass, then the required m_{eff} cut is 800 GeV which is smaller than the 3-jets channel. This signal region is determined as follows.

1. Exact one hard lepton ($p_T^{e_{1st}} > 25$ GeV or $p_T^{\mu_{1st}} > 20$ GeV) is required.
2. The jet multiplicity $N^{jet} \geq 4$ with $p_T^{jet} > 80$ GeV.

3. The missing transverse energy $E_T^{\text{miss}} > 250$ GeV.
4. The transverse mass $m_T > 100$ GeV to remove the W +jets events.
5. The ratio of E_T^{miss} to m_{eff} as $E_T^{\text{miss}}/m_{\text{eff}} > 0.2$.
6. The effective mass $m_{\text{eff}} > 800$ GeV.

6.4 Expected Significance

Expected significances in the three signal regions are estimated. In this section, a simple likelihood ratio is employed to estimate the significance value. The likelihood function is defined as

$$L(\mu) = \frac{(\mu s + b)^n}{n!} e^{-(\mu s + b)} \quad (6.4.1)$$

where the s , b , n and μ are number of signal, number of background, total number of events $n = \mu s + b$ and signal strength, respectively. The number of events of background-only samples and background-plus-signal samples are described by using signal strength $\mu = 0$ and $\mu = 1$, respectively. Then the significance of signal-plus-background hypothesis to background-only hypothesis $\text{med}[Z_0|\mu = 1]$ can be written by using the likelihood ratio as following.

$$\begin{aligned} \text{med}[Z_0|\mu = 1] &= \sqrt{q_0} = \sqrt{-2 \log \frac{L(\mu = 0)}{L(\mu = 1)}} \\ &= \sqrt{2 \left(n \log \frac{n}{b} + b - n \right)} \\ &= \sqrt{2 \left[(s + b) \log \left(1 + \frac{s}{b} \right) - s \right]}. \end{aligned} \quad (6.4.2)$$

The significance corresponding to the exclusion limit of 95% confidence level indicates $\text{med}[Z_0|\mu = 1] = 1.64$ and the significance of discovery corresponding to 5σ is $\text{med}[Z_0|\mu = 1] = 5.00$, respectively.

Figure 6.5 shows the expected significance and exclusion limits in each signal region by MC prediction for the simplified SUSY model and UED model. These plots imply the soft lepton channel is optimized for the diagonal region i.e. degenerate region for the simplified SUSY model. The exclusion region of 3-jets and 4-jets channel extend the high $m_{\tilde{g}}$.

The distributions of ratio of significance in soft lepton signal region to that in 3-jets hard lepton signal region and 4-jets hard lepton signal region are shown in Figure 6.4. The figures show that the soft lepton signal region is more sensitive to the region where mass spectrum is degenerated than the hard lepton signal regions which is optimized for MSUGRA. The factors become approximately two to three in the region.

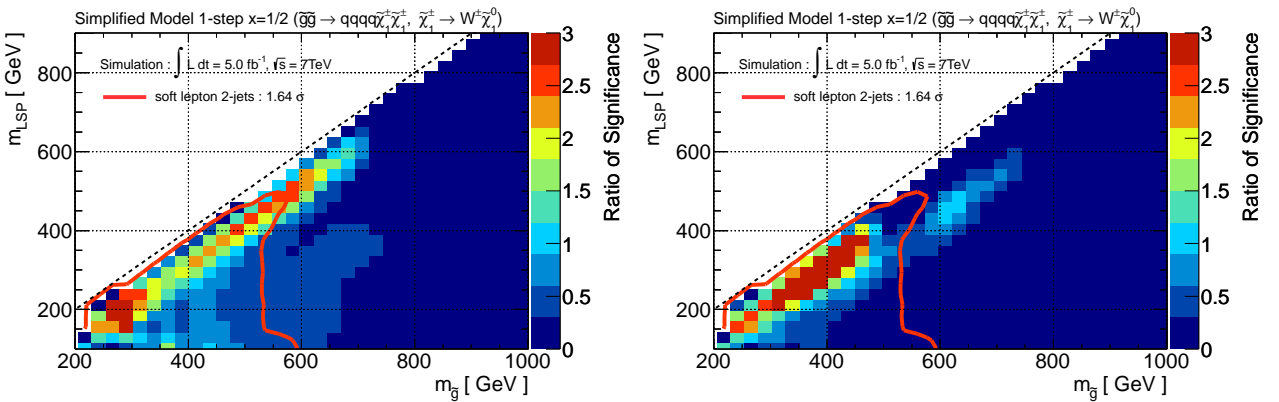


Figure 6.4: Ratio of significance of 2-jets soft lepton signal region to that of 3-jets hard lepton signal region (left) and 4-jets hard lepton signal region (right), respectively, with simplified SUSY model in $m_{\tilde{g}}-m_{\text{LSP}}$ plane.

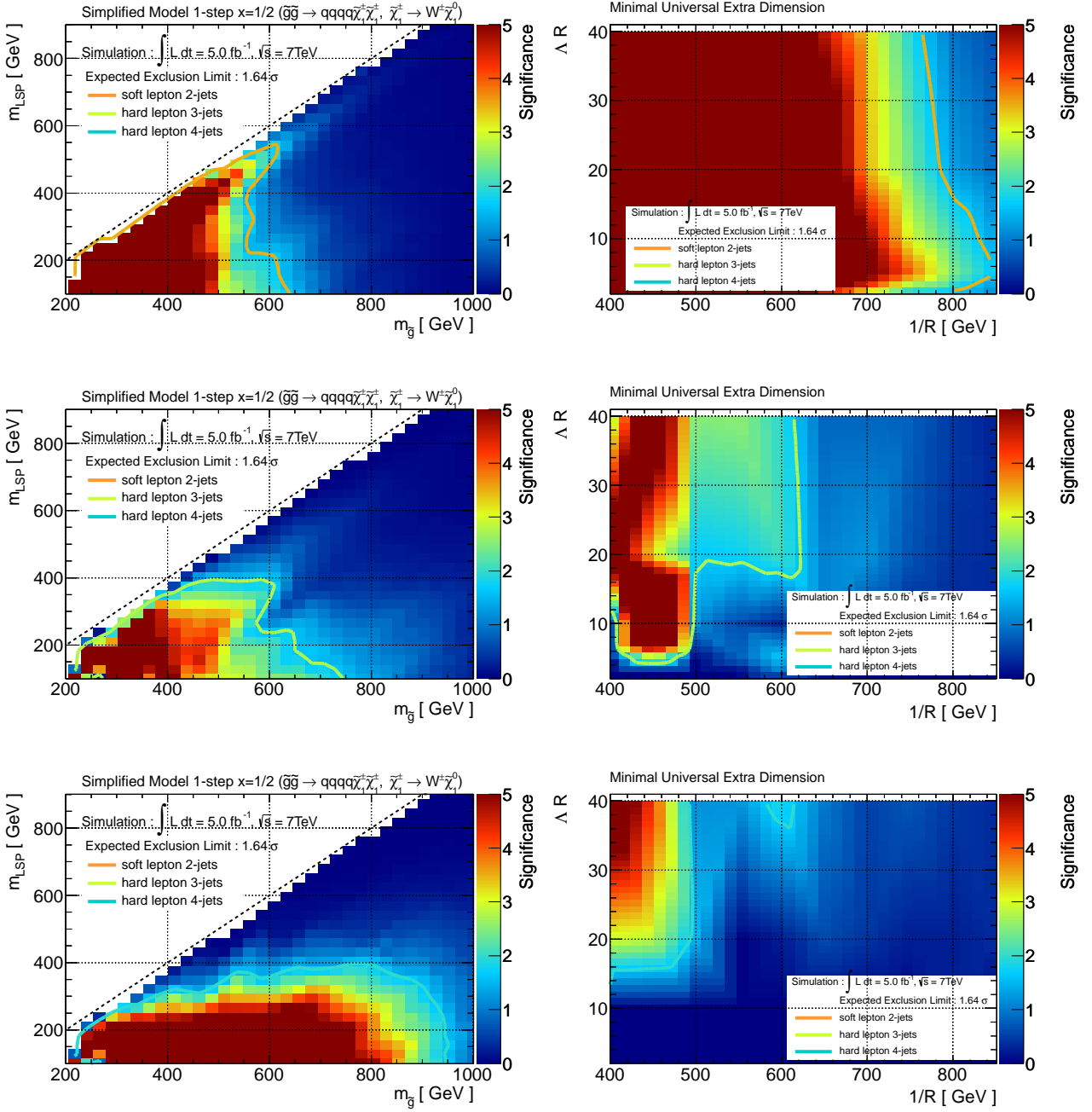


Figure 6.5: Expected exclusion limits estimated by MC. The left figures are shown the significance of the simplified SUSY model as functions of $m_{\tilde{g}}$ and m_{LSP} . The right figures are shown the significance of the UED model as functions of $1/R$ and ΛR . The top figures are results of soft lepton channel, the middle are hard lepton 3 jets channel and the bottom figures are hard lepton 4 jets channel.

Chapter 7

Background Estimation

This chapter describes how to estimate the background contribution in the signal regions. The dominant backgrounds are leptonic decays in W +jets processes and semi-leptonic decays in $t\bar{t}$ processes. Other small background processes considered are Z +jets, single-top, dibosons and multijets.

For the W +jets and $t\bar{t}$ events as dominant background, both shape and normalization of distributions are corrected by using distributions in each control region where the background events are enhanced. In shape correction, the events of generated W and Z bosons are reweighted to fit to the data in p_T distribution of reconstructed Z boson assuming that W and Z bosons have a common set of corrections. The normalizations are corrected to fit the W +jets and $t\bar{t}$ events to observed data in control regions.

The multijets events become background when a jet or a lepton coming from heavy flavor decay is misidentified as lepton coming from a primary vertex. These misreconstructed and non-prompt leptons are called misidentified leptons. Since the misidentified lepton event is not well modeled in simulation, the distributions of the misidentified lepton events are estimated by using the data. A matrix method, which is one of data-driven methods, is employed to estimate the multijets events background.

For the single-top and dibosons events, these MC samples are used to estimate the distributions for each process without any corrections because their contributions are small.

Figure 7.1 shows control regions, validation regions and signal region. The definitions of the W +jets and $t\bar{t}$ control regions are described in Table 7.1. The first, data-driven estimation for the multijets events are performed and the estimation is extrapolated into all control regions. The second, the shape corrections by the generated W and Z boson events are performed. Finally the normalization factors are obtained to fit

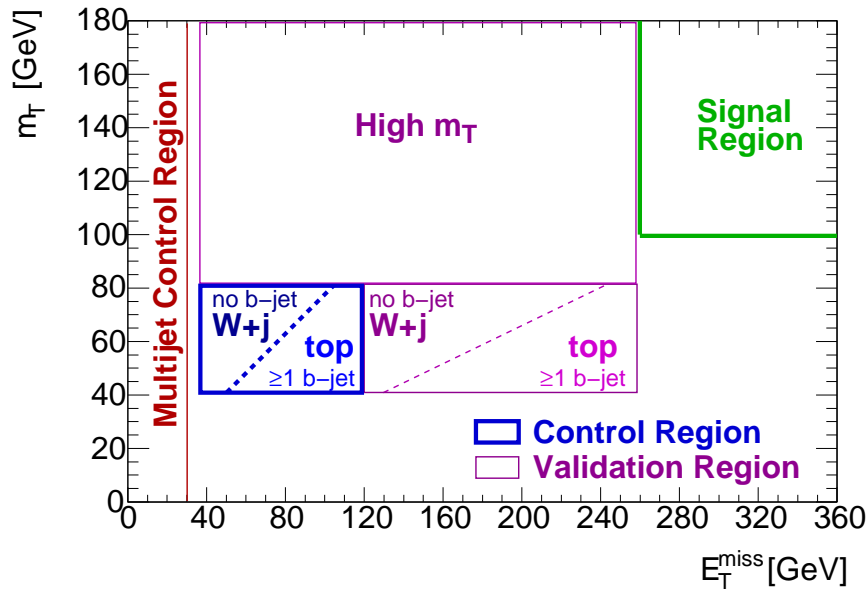


Figure 7.1: Illustration of control regions, validation regions and signal regions in $E_T^{\text{miss}}-m_T$ plane.

	hard lepton		soft lepton	
	$W+\text{jets}$	$t\bar{t}$	$W+\text{jets}$	$t\bar{t}$
N^ℓ	=1	=1	=1	=1
p_T^ℓ	> 25 (20) GeV	> 25 (20) GeV	> [7,25]([6,20]) GeV	[7,25]([6,20]) GeV
N^{jet}	≥ 3	≥ 3	≥ 2	≥ 2
p_T^{jet}	> 80, 25, 25 GeV	> 80, 25, 25 GeV	> 130, 25 GeV	> 130, 25 GeV
$N^{b\text{-jet}}$	= 0	≥ 1 (within 3 jets)	= 0	≥ 1 (within 2 jets)
E_T^{miss}	$40 < E_T^{\text{miss}} < 150$ GeV	$40 < E_T^{\text{miss}} < 150$ GeV	$180 < E_T^{\text{miss}} < 250$ GeV	$180 < E_T^{\text{miss}} < 250$ GeV
m_T	$40 < m_T < 80$ GeV	$40 < m_T < 80$ GeV	$40 < m_T < 80$ GeV	$40 < m_T < 80$ GeV
$m_{\text{eff}}^{\text{inc}}$	$m_{\text{eff}}^{\text{inc}} > 500$ GeV	$m_{\text{eff}}^{\text{inc}} > 500$ GeV	—	—

Table 7.1: Definitions of selection criteria of $W+\text{jets}$ and $t\bar{t}$ control regions in both hard lepton and soft lepton channel. The p_T selections without (with) parentheses is given for electron (muon).

the $W+\text{jets}$ and $t\bar{t}$ events to observed data in jet multiplicity distributions. The normalization factors are determined for each number of partons individually and used for the background estimations in the signal region. The estimated background events are extrapolated into the validation regions and signal regions. In validation regions, the corrected background distributions are cross-checked by comparing with observed data. The same way is applied to the signal regions, and the excess of observed data over background expectations is checked.

7.1 Multijets Background

Multijets events become a background due to misidentified leptons. Three major sources of such misidentified leptons are considered; 1) a process of neutral hadron associated with charged particles; 2) a photon conversion to an electron; and 3) a heavy flavor process when a real lepton appears as a decay product of hadrons in jets but is sufficiently isolated. Such objects are collectively referred to as misidentified leptons. The multijets background in the signal region and in both $W+\text{jets}$ and $t\bar{t}$ control regions is measured from data following a matrix method.

The multijets background from the all sources (but separated by lepton flavor) is determined collectively. The events are enhanced in control samples by relaxing selection criteria for signal leptons and required the several kinematics. The selection criteria for signal leptons and its relaxed selection criteria are called tight and loose selection criteria, respectively. The definitions are summarized in Table 7.2. Defining $N_{\text{obs}}^{\text{pass}}$ and $N_{\text{obs}}^{\text{fail}}$ as the number of events in such a loose sample passing or failing the final lepton selection criteria, and defining N_{real} and N_{misid} as the number of real leptons and the number of misidentified leptons, the following equations hold

$$\begin{aligned} N_{\text{obs}}^{\text{pass}} &= \epsilon_{\text{real}} N_{\text{real}}^{\text{loose}} + \epsilon_{\text{misid}} N_{\text{misid}}^{\text{loose}}, \\ N_{\text{obs}}^{\text{fail}} &= (1 - \epsilon_{\text{real}}) N_{\text{real}}^{\text{loose}} + (1 - \epsilon_{\text{misid}}) N_{\text{misid}}^{\text{loose}}, \end{aligned} \quad (7.1.1)$$

where ϵ_{real} is the relative identification efficiency for real leptons, and ϵ_{misid} is the misidentification efficiency for misidentified leptons as defined by using the number of leptons passing the loose selection criteria $N_{\text{obs}}^{\text{loose}}$ and tight selection criteria $N_{\text{obs}}^{\text{tight}}$ as follows

$$\epsilon_{\text{real}} = \frac{N_{\text{real}}^{\text{tight}}}{N_{\text{real}}^{\text{loose}}}, \quad \epsilon_{\text{misid}} = \frac{N_{\text{misid}}^{\text{tight}}}{N_{\text{misid}}^{\text{loose}}}. \quad (7.1.2)$$

Solving the equations leads to

$$N_{\text{misid}}^{\text{pass}} = \epsilon_{\text{misid}} N_{\text{misid}}^{\text{loose}} = \frac{N_{\text{obs}}^{\text{fail}} - (1/\epsilon_{\text{real}} - 1) N_{\text{obs}}^{\text{pass}}}{1/\epsilon_{\text{misid}} - 1/\epsilon_{\text{real}}}. \quad (7.1.3)$$

This equation indicates the number of misidentified leptons passing the signal lepton selection criteria $N_{\text{misid}}^{\text{pass}}$ can be estimated from the numbers of $N_{\text{obs}}^{\text{pass}}$ and $N_{\text{obs}}^{\text{fail}}$ in interesting regions and efficiencies ϵ_{real} and ϵ_{misid} .

	loose selection	tight selection
electron	preselection · <i>medium</i> identification	signal selection · <i>tight</i> identification · $ptcone20/p_T < 0.1$
muon	preselection —	signal selection · $ptcone20 < 1.8$ GeV

Table 7.2: Definition of loose electron (muon) and tight electron (muon) in multijets background estimation.

In the efficiency measurements, one control sample for real leptons and three control samples for misidentified leptons are prepared. The ϵ_{real} is measured from data by using a sample of $Z \rightarrow \ell\ell$ decays. For the misidentified leptons, the efficiency measurements are performed by three control samples as high p_T electrons, high p_T muons and soft leptons control sample to enhance the multijets events.

The measurements of ϵ_{real} and ϵ_{misid} are described in following sections.

7.1.1 Identification Efficiency for Real Leptons

The identification efficiency for real leptons is measured by using $Z \rightarrow \ell\ell$ events as a control sample. In the measurement of the identification efficiency, a tag-and-probe method is employed. The method requires one tagged lepton in the control sample passing the tight selection criteria and one probe lepton satisfying the loose selection criteria. The efficiency is calculated by taking a ratio of the number of probe leptons passing the tight selection criteria to the number of all probe leptons. The selection criteria for this control sample are defined as follows

- The events must be fired by the electron or muon trigger.
- The events contain at least two leptons isolated with jets : $\Delta R(\ell, jets) > 0.4$.
- The two leptons satisfy opposite charge, same flavor and loose selection criteria.
- The invariant mass of the two leptons lies the Z mass window ($80 < m_{\ell\ell} < 100$ GeV).
- $E_T^{\text{miss}} < 30$ GeV.
- One lepton satisfies the tight selection criteria and matches the corresponding trigger object.

Figure 7.2 shows the p_T distributions of the probe leptons, the probe leptons satisfying the tight selection criteria and the identification efficiencies, respectively. The figures indicate the contaminations of the other processes in the control sample are negligible ($< 1\%$). The efficiencies for electrons and muons are measured to be $\epsilon_{\text{real}} \sim 70\text{-}95\%$ depending on p_T and $|\eta|$, and 97% , respectively.

7.1.2 Misidentification Efficiency for Electrons in High p_T Region ($p_T^e > 25$ GeV)

The control sample of misidentified electrons with high p_T ($p_T^e > 25$ GeV) is collected as the multijets events that consist of one misidentified electron and at least one jet. E_T^{miss} in multijets events tend to be small since the events do not have the undetected objects. Selection criteria for the control sample is defined as follows.

- The events must be fired by the electron trigger.
- The events contain the probe electron isolated with jets : $\Delta R(e, jets) > 0.4$.
- $E_T^{\text{miss}} < 30$ GeV.
- At least one jet with $p_T^{\text{jet}} > 25$ GeV.

Since the multijets events are not modeled well, the events are estimated from difference between the observed data and real electron events predicted by MC simulations. In estimation of the real electron distribution, MC prediction except multijets events are assumed to consist of real electrons and be good modeled but their cross sections have 20% uncertainty.

Difference of the efficiency between components of misidentified electrons are assigned as additional systematic uncertainty. The efficiencies of each component of misidentified electrons are predicted by using MC

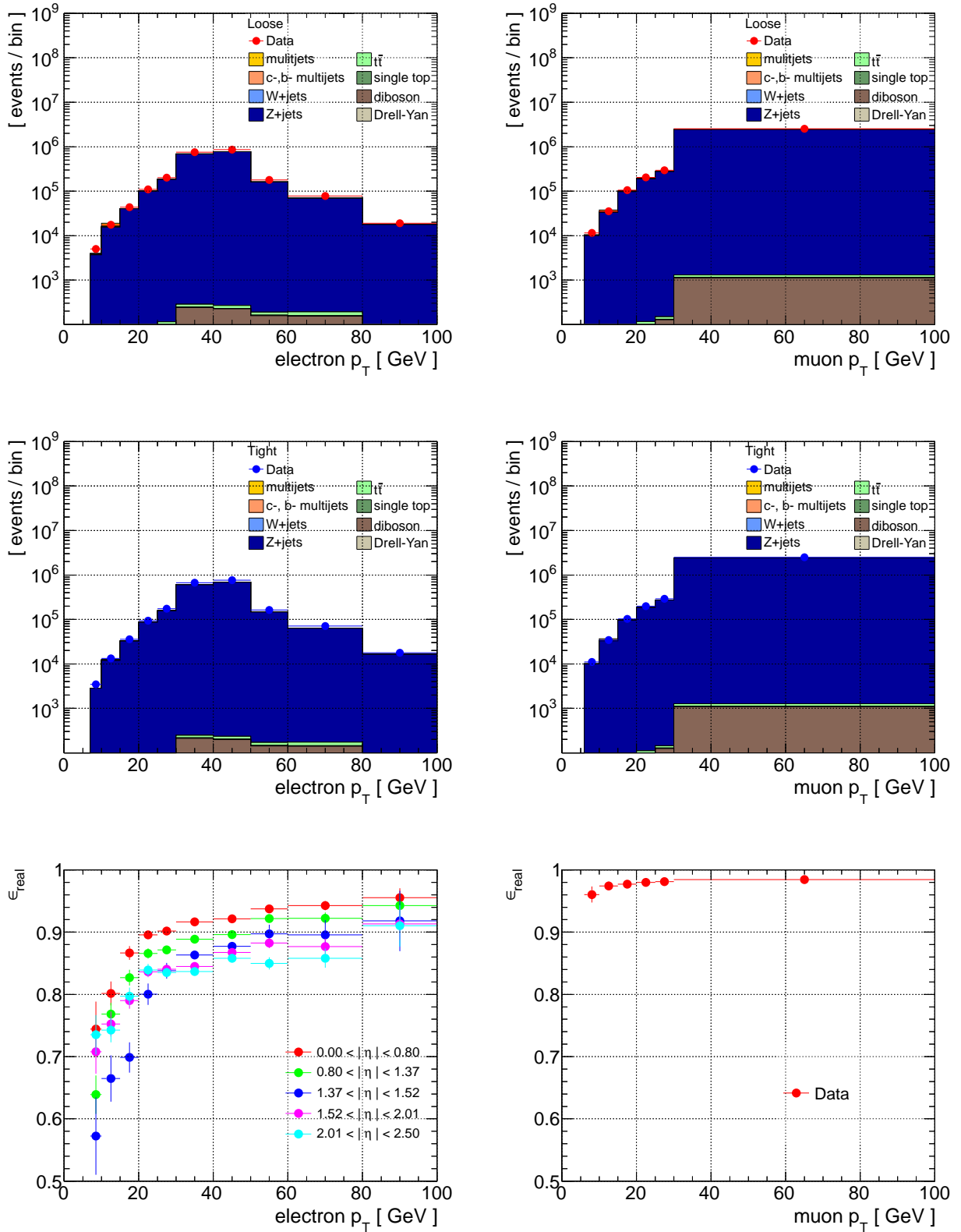


Figure 7.2: Distribution of p_T of probe leptons satisfying loose selection criteria (top), p_T of probe leptons satisfying tight selection criteria (middle) and identification efficiencies ϵ_{real} (bottom) in data and MC for the electron channel (left) and muon channel (right).

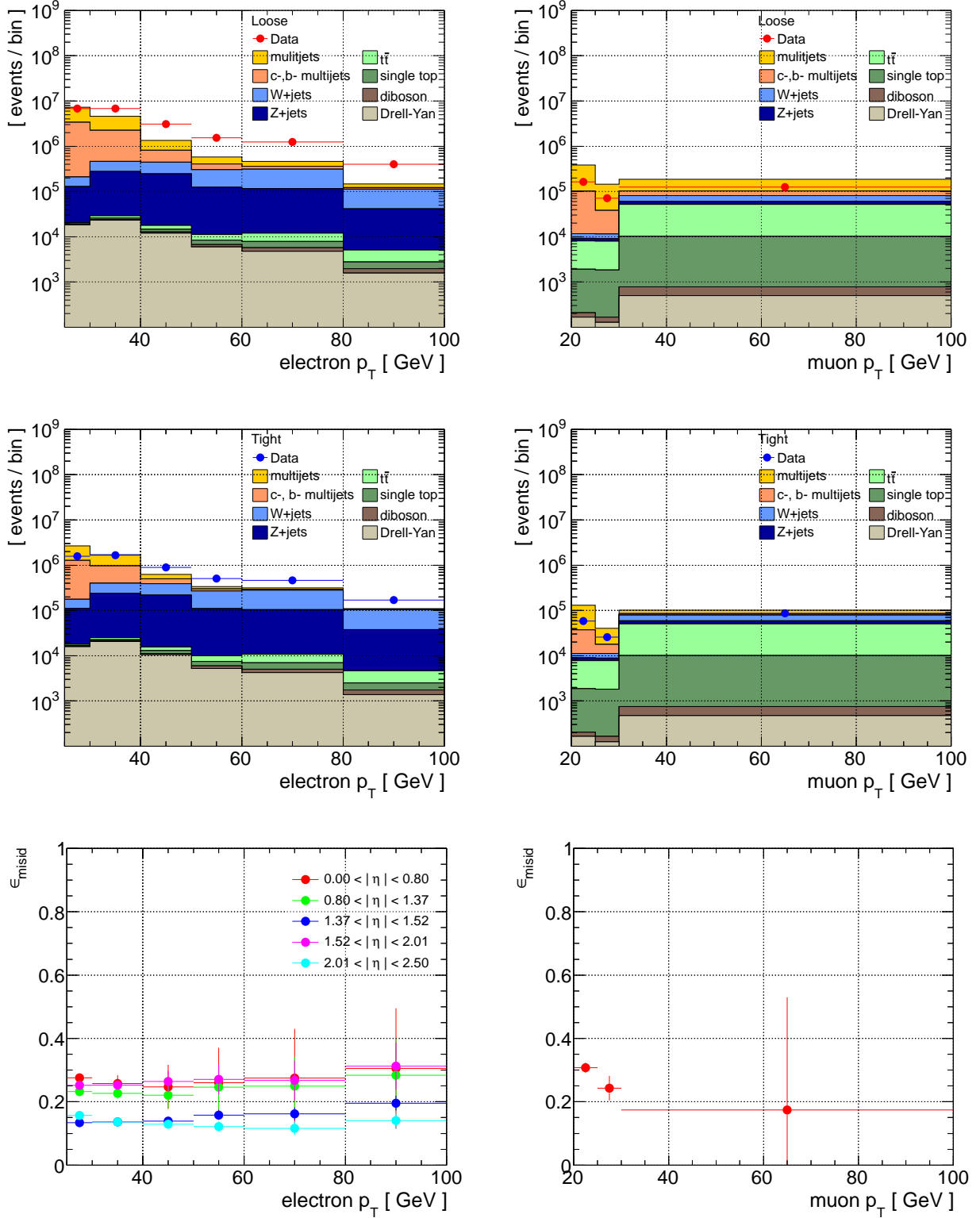


Figure 7.3: Distribution of p_T of leptons passing the loose selection criteria (top), p_T of leptons passing the tight selection criteria (middle) and the misidentification efficiencies (bottom) in the control samples for high p_T electrons (left) and high p_T muons (right). The multijets events are estimated by subtracting MC events except multijets MC events from data since the multijets MC events are not reliable and MC events except multijets MC events consist of real leptons. 20% uncertainty is assigned to cross sections of real lepton events. Total of statistical and systematic uncertainties are quoted as error bars.

events as $34 \pm 1\%$ for hadron process, $20 \pm 3\%$ for photon conversion events and $37 \pm 1\%$ for heavy flavor events, respectively (the errors are quoted only statistical uncertainty). Additional systematic uncertainty of 10% for the misidentification efficiency is therefore assigned as absolute value.

The p_T distribution of the probe electrons, that of the probe electrons satisfying the tight selection criteria and the misidentification efficiency are shown in Figure 7.3. The misidentification efficiency for the high p_T electrons is measured to be $\epsilon_{\text{misid}} \sim 11\text{-}32\%$ with uncertainty 1-8% depending on p_T and $|\eta|$.

For the events containing at least one b -jet in the control sample, the misidentification efficiency is $\sim 10\%$ higher than that of nominal control sample. This efficiency is shown in Figure 7.4 and used for the estimation of multijets events in the $t\bar{t}$ control region.

7.1.3 Misidentification Efficiency for Muon in High p_T Region ($p_T^\mu > 20$ GeV)

Since a dominant component in the misidentified muon events is the heavy flavor process, the trajectories of such muons do not point to the primary vertex. The events are expected to have at least two heavy flavor jets, thus the selection criteria for the control sample are defined as follows,

1. The events must be fired by the muon trigger.
2. The events contain exact one probe muon satisfying the loose selection criteria and $|d_0/\sigma_{d_0}| > 5$.
3. The probe muons are isolated with jets : $\Delta R(\mu, jets) > 0.4$.
4. The events contain at least one jet with $p_T > 60$ GeV.

The d_0 is a transverse impact parameter with respect to the primary vertex and σ_{d_0} is a standard deviation of transverse impact parameter. The $p_T^{\text{jet}} > 60$ GeV is required to avoid a bias due to muon trigger algorithm requiring a jet with $p_T > 10$ GeV at level-1 trigger. In the multijets events measurement, the real muon events predicted by simulations are subtracted from the distribution in the control sample as well as the efficiency measurement for misidentified electrons. The p_T distributions for the probe muon before and after tight selection applied and the misidentification efficiency ϵ_{misid} are shown in Figure 7.3. The efficiency is measured to be $\epsilon_{\text{misid}} \sim 25\text{-}36\%$ with an uncertainty 3-25% depending on p_T .

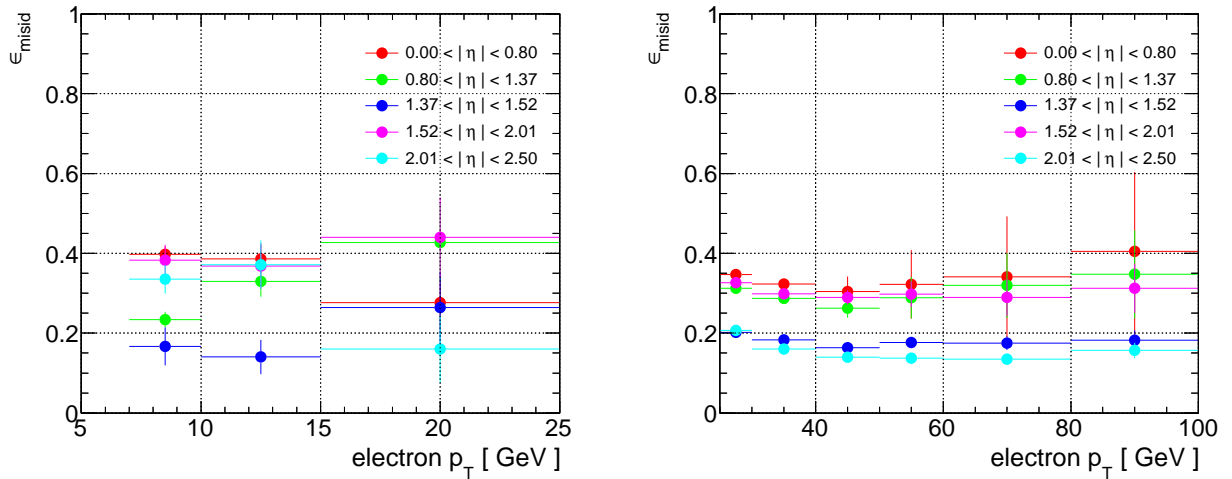


Figure 7.4: Misidentification efficiency for low p_T electrons (left) and high p_T electrons (right) in at least one b -jets events ($N^{b\text{-jet}} \geq 1$) in the control samples. The multijets events are estimated by subtracting MC events except multijets MC events from data since the multijets MC events are not reliable and MC events except multijets MC events consist of real leptons. 20% uncertainty is assigned to cross sections of real lepton events. Total of statistical and systematic uncertainties are quoted as error bars.

7.1.4 Misidentification Efficiencies for Low p_T Leptons ($7 < p_T^e < 25$ GeV or $6 < p_T^\mu < 20$ GeV)

For the measurement of misidentification efficiency in low p_T region, the events containing two misidentified leptons are collected as control samples to avoid the trigger bias, and the tag-and-probe method is applied to the sample in the efficiency measurement. To enhance the misidentified leptons, the first the tagged lepton is required to fail to the tight selection criteria. Since the dileptons events are contaminated by Z and J/ψ events, invariant mass and charge combination are required to enhance the misidentified lepton events. Figure 7.5 shows the distributions of invariant mass with same sign and opposite sign under the failure in the tight selection criteria for the tagged leptons. In the figures, the two peaks around $m_{\ell\ell} = 3$ GeV and 90 GeV consist of J/ψ and Z events. Therefore the requirements of $m_{\ell\ell} > 10$ GeV and $|m_{\ell\ell} - m_Z| > 25$ GeV are added.

The selection criteria for the control sample is determined as follows.

- The events must be fired by the electron or muon trigger.
- The events contain at least two leptons isolated with jets : $\Delta R(\ell, jets) > 0.4$.
- The relation between two leptons is required for same sign and same flavor.
- The invariant mass lies $m_{\ell\ell} > 10$ GeV and $|m_{\ell\ell} - m_Z| > 25$ GeV.
- The tagged lepton fails to the tight selection criteria and the probe lepton satisfies the loose selection criteria.

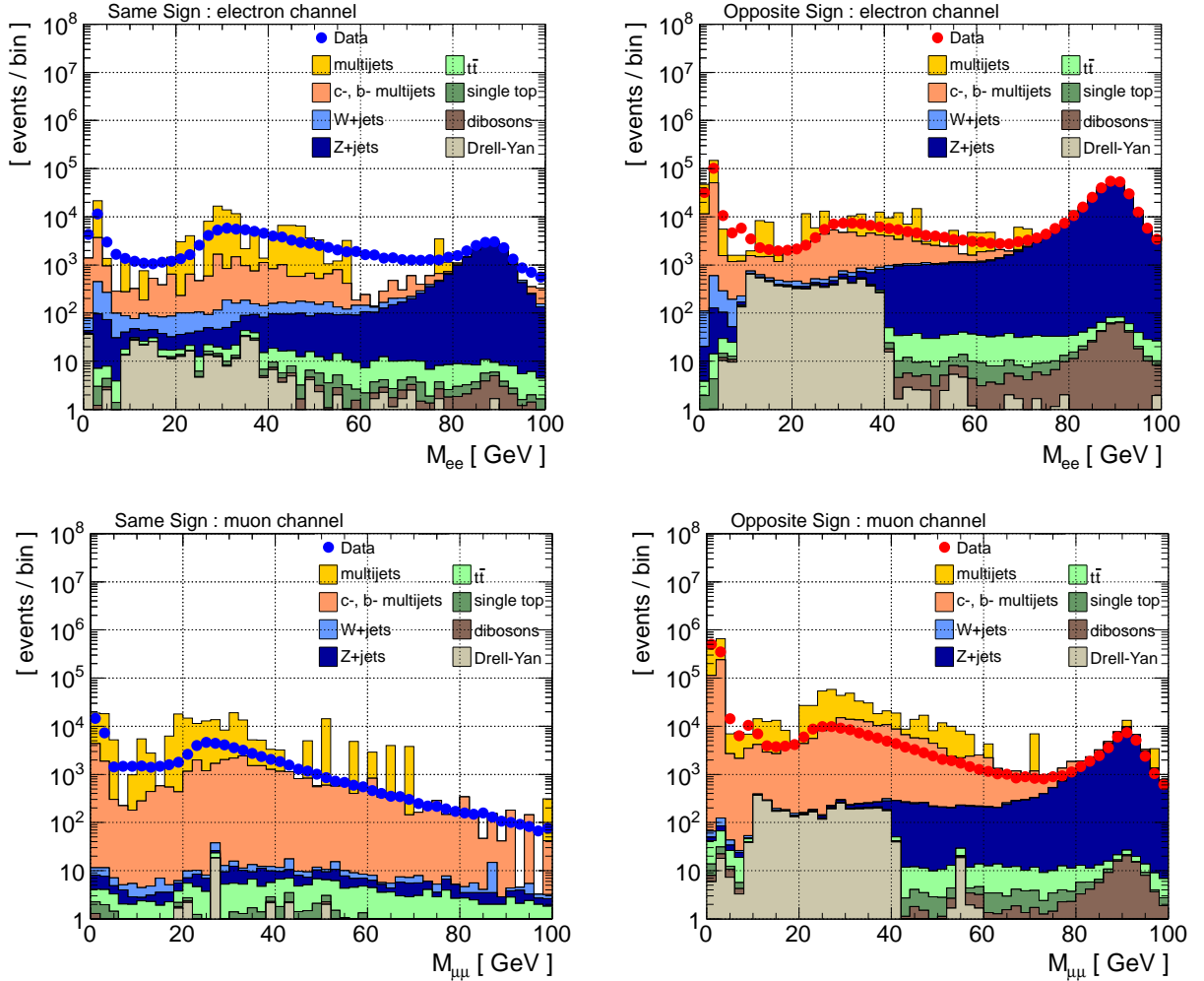


Figure 7.5: Distributions of the invariant mass $m_{\ell\ell}$ in the control sample of electrons (top) and the muons (bottom) with the same sign (left) and the opposite sign (right) requirement, respectively.

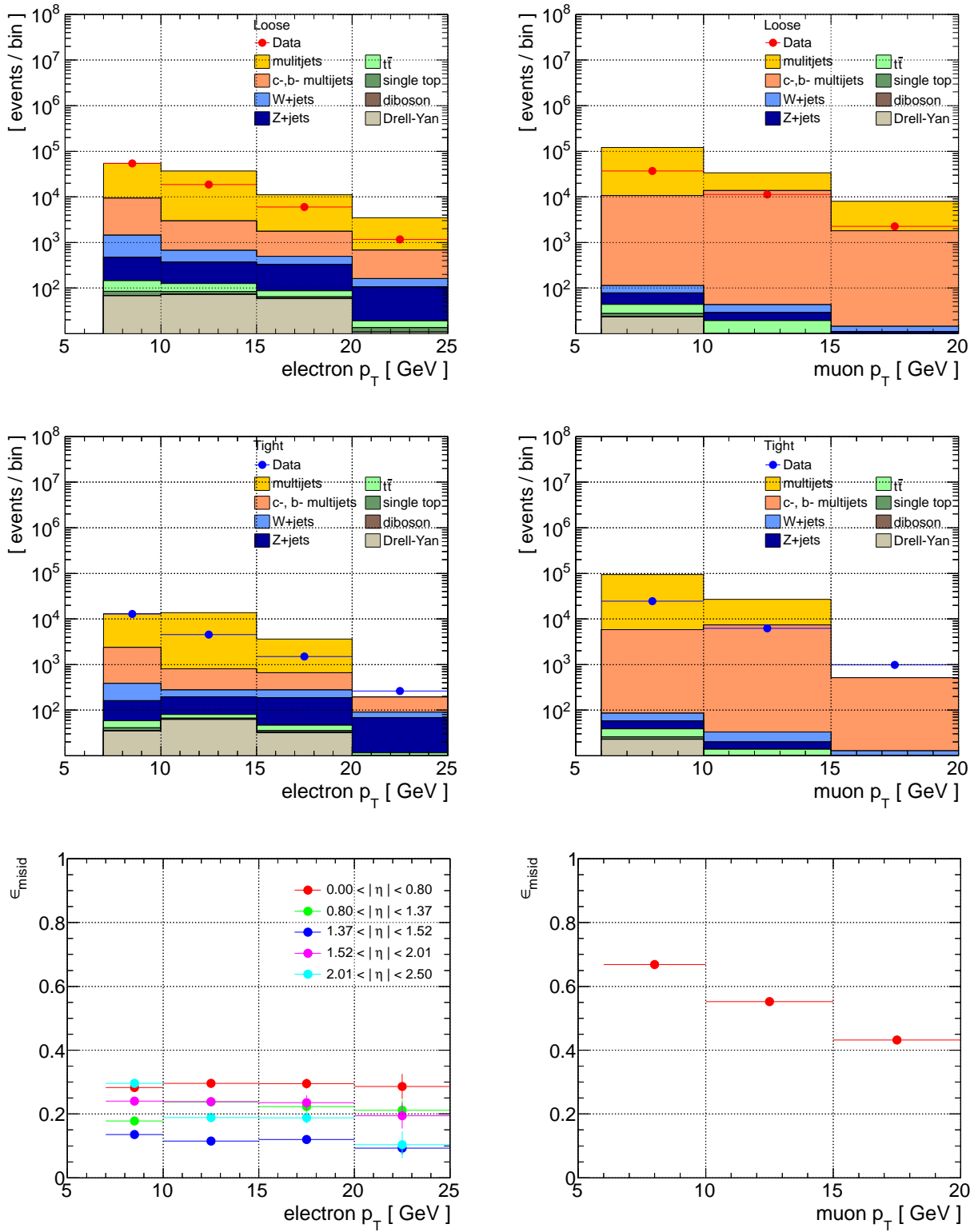


Figure 7.6: Distribution of p_T for probe leptons passing the loose selection criteria (top), p_T for the probe leptons passing tight selection criteria (middle) and the misidentification efficiencies ϵ_{misid} (bottom) in the control samples for low p_T electrons (left) and muons (right). The misidentification efficiencies are estimated by subtracting real lepton events predicted by MC.

p_T distributions of probe leptons, probe leptons satisfying the tight selection criteria and the misidentification efficiencies ϵ_{misid} in the control samples for the low p_T leptons are shown in Figure 7.6, respectively. The same method is applied to the electrons and the muons. The efficiencies are measured to be $\epsilon_{\text{misid}} \sim 10\text{-}30\%$ with the uncertainty $\lesssim 6\%$ depending on the electron p_T and $|\eta|$, and $\epsilon_{\text{misid}} \sim 44\text{-}66\%$ with the uncertainty $\lesssim 6\%$ depending on the muon p_T . The uncertainty of 10% derived from the difference of component is added to the efficiency of low p_T electrons as well as the high p_T electrons. The misidentified efficiency for low p_T electrons in the events containing at least one b -jets is shown in Figure 7.4.

7.2 W +jets and $t\bar{t}$ Background

The dominant source of background are leptonic decays for the W +jets and the products of the semi-leptonic decay for $t\bar{t}$. To obtain better modeling of background events, following corrections is applied to the simulated samples of the dominant background,

1. Correction with the shape of distributions for W +jets and Z +jets events.
2. Correction with the normalization factors for W +jets, Z +jets and $t\bar{t}$ events.

For the shape correction, p_T of the both generated Z bosons and reconstructed Z bosons are used. The generated Z boson events are reweighted based on a comparison of data with simulation depending on the p_T of reconstructed Z boson in a control sample enriched in Z +jets events. The same correction factor is applied to W production because of an assumption that the process is similar to the Z +jets process. After the shape correction, normalizations of the dominant backgrounds are corrected. The relative normalization of the ALPGEN samples (W +jets, Z +jets and $t\bar{t}$) is adjusted by comparing the jet multiplicity distribution in data versus simulation in all control regions. Both control region of W +jets and $t\bar{t}$ samples are defined in Table 7.1. The control regions are chosen to enhance the W +jets and $t\bar{t}$ events by requiring $40 < m_T < 80$ GeV and $40 < E_T^{\text{miss}} < 150$ GeV, and similar jet cut to the signal regions. A common set of corrections is obtained for the W +jets and Z +jets samples, and a set of corrections is obtained for semi-leptonic leptonic $t\bar{t}$ decays.

First, this section describes a way of fit, second the shape correction and the normalization correction are described.

7.2.1 Fit Configurations

Fit results are obtained by using a likelihood function. The likelihood function consists of two parameter type. One is a signal strength μ which is a scale factor of cross section of interesting sample for example a signal process. The other is a nuisance parameter θ which determines deviation of probable density function in calculation of the most probable value. The systematic uncertainties are treated as the nuisance parameters.

The likelihood function proceeds through two steps to calculate the most probable values for signal strength and nuisance parameters. First, the likelihood functions are performed by inserting the signal strength and nuisance parameters into a Poisson function in each bin of the histograms. A product of the likelihood functions L as following is used to calculate the signal strength

$$L = \prod_{c \in \text{channels}} \prod_{b \in \text{bins}} \text{Pois}(n_{cb} | \nu_{cb}) \cdot G(\text{Lumi} | \lambda, \Delta_{\text{Lumi}}) \prod_{\theta \in \text{syst}} P_{\theta}(a_{\theta} | \alpha_{\theta}), \quad (7.2.1)$$

where n_{cb} and ν_{cb} are number of observed events and expected events in each histogram bin b in each channel c . The λ is luminosity parameter for a given sample, thus $G(\text{Lumi} | \lambda, \Delta_{\text{Lumi}})$ determines overall normalization within the uncertainty of luminosity Δ_{Lumi} . The $P_{\theta}(a_{\theta} | \alpha_{\theta})$ is a constraint term describing an auxiliary measurement a_{θ} that constrains the nuisance parameter α_{θ} . The constraint is given by Gaussian function where the width is obtained from discrepancy between nominal distribution and distributions after applying $\pm 1\sigma$ uncertainties.

The Poisson function Pois are described by using observed number of events n_i and expected number of events $\nu = \mu s_i + b_i$,

$$\text{Pois}(\mu) = \frac{(\mu s_i + b_i)^{n_i}}{n_i!} e^{-(\mu s_i + b_i)}, \quad (7.2.2)$$

where s_i and b_i are number of signal events and background events in each bin i . The most probable value for signal strength $\hat{\mu}$ is given by maximizing the likelihood function.

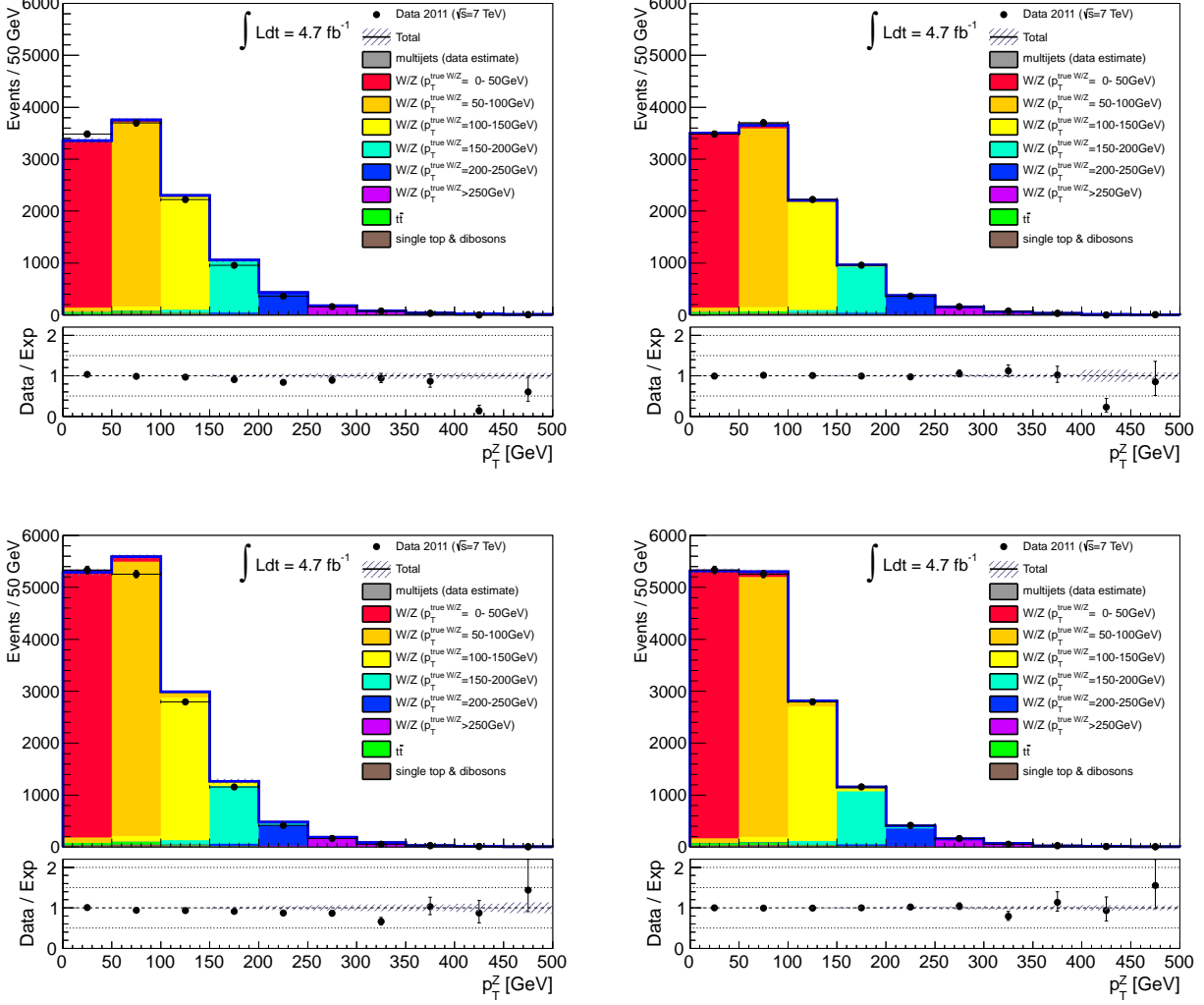


Figure 7.7: Distribution of reconstructed p_T^Z in the shape correction control sample for the electron channel (top) and muon channel (bottom), and before the generated p_T^Z fitting (left) and after the generated p_T^Z fitting (right).

Next, the covariance matrix V_{jk} is calculated from the likelihood function as follow

$$V_{jk}^{-1} = -E \left[\frac{\partial^2 \ln L}{\partial \theta_j \partial \theta_k} \right], \quad (7.2.3)$$

where the E means a expectation value of deviations of L . Here the signal strength and nuisance parameters are treated equally, then θ contains the signal strength. The covariance matrix shows the correlation between the nuisance parameters, and the correlation constrains uncertainties. The uncertainties are estimated from the covariance matrix by varying the nuisance parameters θ as following

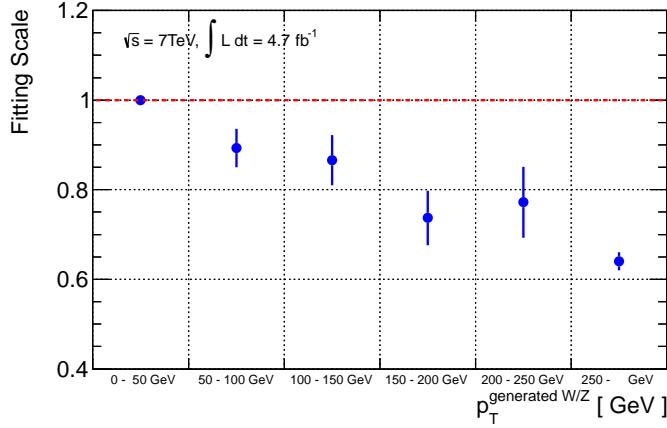
$$\Delta \theta_l = \sum_{j,k}^l \Delta \theta_j V_{jk}^{-1} \Delta \theta_k, \quad (7.2.4)$$

where $\Delta \theta$ is the value of difference from $-\frac{1}{2}\sigma$ to $+\frac{1}{2}\sigma$ with each nuisance parameter θ .

The fit configurations are described in Appendix C in more detail.

7.2.2 Shape Correction

To correct the shape, the simulated events of W +jets and Z +jets are reweighted by using the generated vector bosons. Common correction factors for the W +jets and Z +jets events are obtained from a $Z \rightarrow \ell\ell$ sample



Generated p_T^Z bin	scale factor
$0 < p_T^Z < 50$ GeV	1.0
$50 < p_T^Z < 100$ GeV	0.893 ± 0.043
$100 < p_T^Z < 150$ GeV	0.866 ± 0.056
$150 < p_T^Z < 200$ GeV	0.737 ± 0.061
$200 < p_T^Z$	0.772 ± 0.079

Figure 7.8: Fitting results for p_T^Z reweighting as a function of generated p_T .

number of parton bin	W/Z +jets	$t\bar{t}$
$N_p = 0$	1.0 ± 0.2	0.72 ± 0.18
$N_p = 1$	1.0 ± 0.2	1.15 ± 0.10
$N_p = 2$	1.22 ± 0.13	1.10 ± 0.17
$N_p = 3$	0.85 ± 0.07	0.94 ± 0.06
$N_p = 4$	0.97 ± 0.06	0.94 ± 0.06
$N_p = 5$	0.68 ± 0.25	0.94 ± 0.06

Table 7.3: Fitting results with normalization factors for the W +jets and $t\bar{t}$ events in each number of parton bin.

because the process of W +jets events are similar to that of Z +jets and the Z sample can reduce the dependence on a jet energy scale uncertainty. The control sample is defined as follows.

- At least two leptons $N^\ell \geq 2$ satisfy opposite charge and same flavor.
- Leading lepton and second leading lepton are required $p_T^{\ell_{1st}} > 25$ GeV and $p_T^{\ell_{2nd}} > 10$ GeV, respectively.
- Invariant mass for the dileptons event lies Z mass window $81 < m_{\ell\ell} < 101$ GeV.
- At least two jets $N^{jet} \geq 2$ are required.
- The second leading jet is larger than $p_T^{jet_{2nd}} > 50$ GeV.
- $E_T^{miss} < 50$ GeV.

The transverse momentum of the generated Z on the simulation p_T^Z is utilized to estimate the correction factors. The generated p_T^Z distribution for the sample is separated into five bins, with the first four bins stepped by 50 GeV from 0 GeV to 200 GeV and the last bin integrated above 200 GeV. The reconstructed p_T^Z distribution for the simulated samples in the control sample is fitted to the data by reweighting the generated Z boson events. Likelihood function is performed in the fit, and the most probable values give the correction factors. Source of uncertainties as input are jet energy scale and renormalization scale, both are described in detail in Chapter 8. Figure 7.7 shows the distribution of the reconstructed p_T^Z before and after reweighting by the generated Z events. The correction factors obtained from the reweighting are shown in Figure 7.8.

7.2.3 Normalizations

After the shape correction, the W +jets and $t\bar{t}$ events are normalized in the W +jets and $t\bar{t}$ control regions. The normalization factors are measured as the ratio of the normalization obtained from the fit results to the normalization predicted by the theoretical cross section. The factors are evaluated in each number of parton.

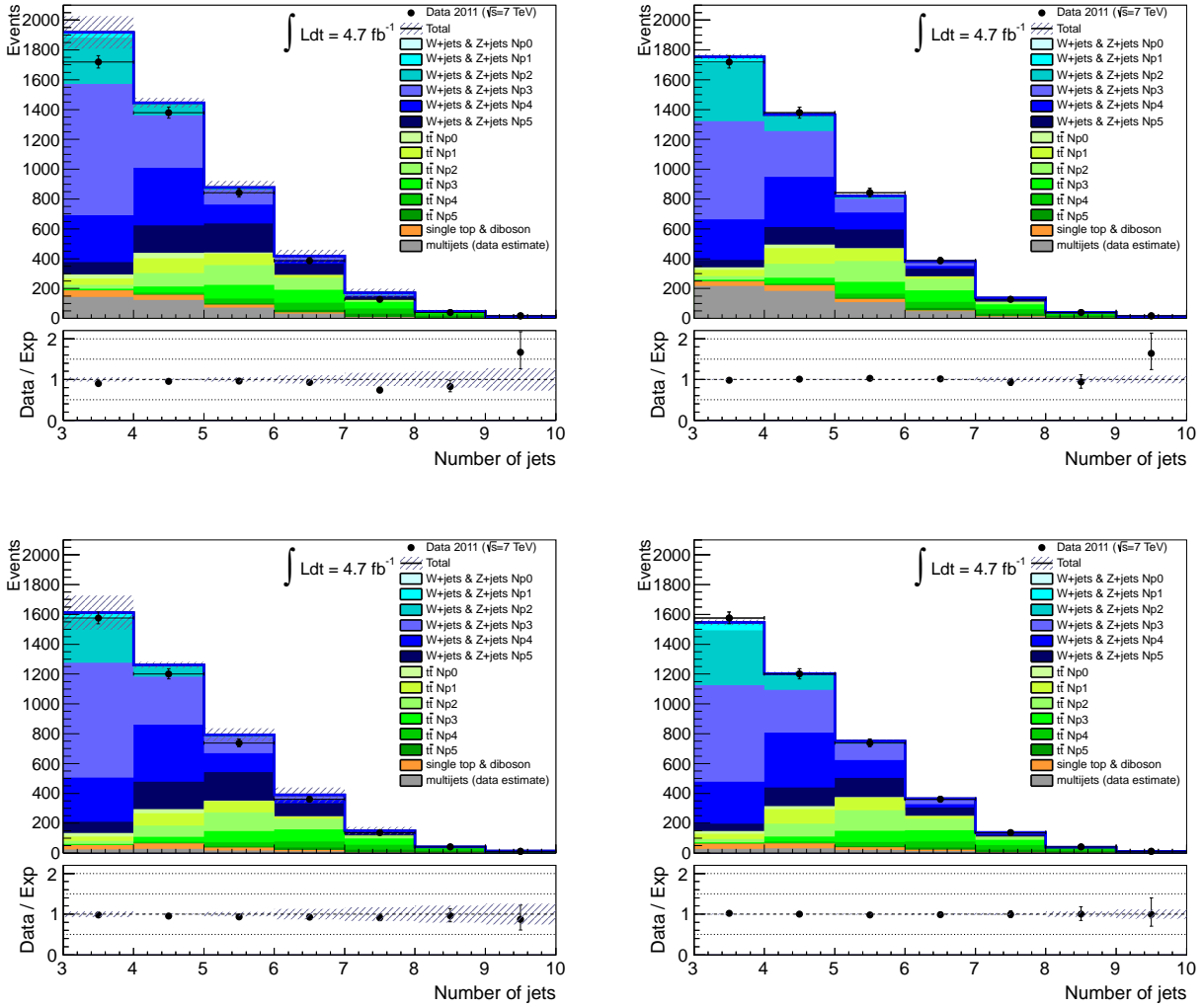


Figure 7.9: Distribution of the number of jets in the W +jets control region for the electron channel (top) and muon channel (bottom) before normalization (left) and after normalization (right).

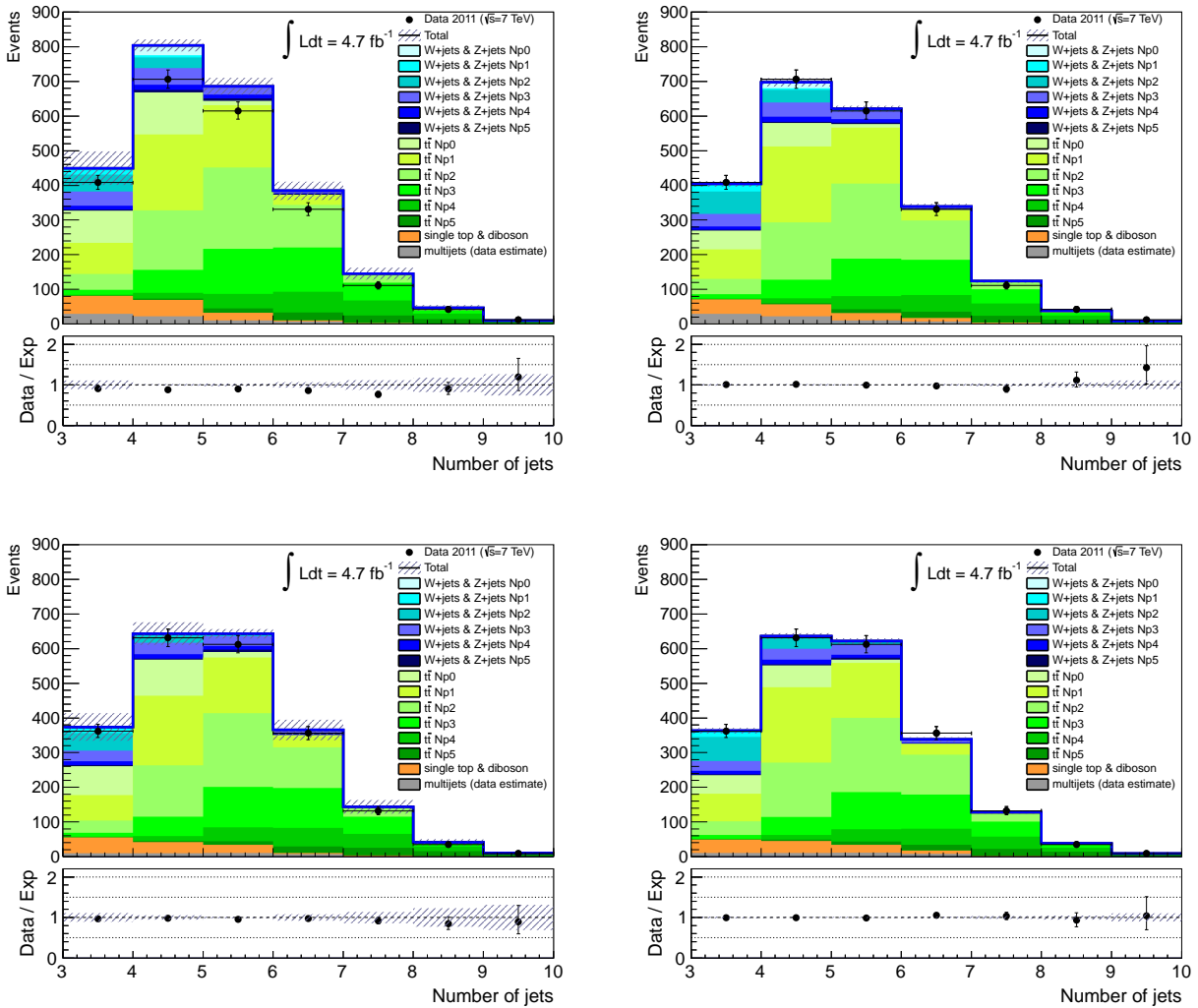


Figure 7.10: Distribution of the number of jets in the $t\bar{t}$ control region for the electron channel (top) and muon channel (bottom) before normalization (left) and after normalization (right).

Control region channel	W +jets (hard lepton)		$t\bar{t}$ (hard lepton)	
	electron	muon	electron	muon
Observed events	4510	4064	2225	2137
Fitted bkg events	4511.2 ± 67.7	4053.5 ± 61.8	2231.2 ± 40.9	2133.4 ± 39.4
Fitted $t\bar{t}$ events	1073.9 ± 75.6	1043.7 ± 79.7	1740.7 ± 51.4	1701.8 ± 53.6
Fitted W +jets & Z +jets events	2762.5 ± 104.0	2813.0 ± 99.7	308.1 ± 37.7	281.8 ± 31.8
Fitted other bkg events	100.0 ± 13.4	94.6 ± 12.3	109.5 ± 14.7	109.1 ± 16.0
Fitted multijets events	574.8 ± 111.7	102.2 ± 55.6	73.0 ± 38.0	40.7 ± 33.1
MC exp. SM events	4887.3 ± 713.5	4262.2 ± 647.9	2525.7 ± 434.4	2220.7 ± 393.1
MC exp. $t\bar{t}$ events	1154.0 ± 147.7	1006.6 ± 138.9	2012.4 ± 350.2	1816.7 ± 339.7
MC exp. W +jets & Z +jets events	3241.9 ± 632.2	3069.3 ± 589.3	315.9 ± 126.0	257.6 ± 106.4
MC exp. other bkg events	110.7 ± 23.4	99.5 ± 22.6	124.1 ± 32.0	108.5 ± 34.2
Data-driven multijets events	380.8 ± 111.7	86.8 ± 55.6	73.3 ± 38.0	37.9 ± 33.1

Control region channel	W +jets (soft lepton)		$t\bar{t}$ (soft lepton)	
	electron	muon	electron	muon
Observed events	633	1092	131	200
Fitted bkg events	641.0 ± 21.7	1093.4 ± 28.5	130.4 ± 9.8	197.5 ± 12.0
Fitted $t\bar{t}$ events	37.3 ± 4.6	68.7 ± 5.9	70.2 ± 6.1	108.9 ± 7.2
Fitted W +jets & Z +jets events	576.5 ± 20.3	966.7 ± 35.4	34.9 ± 4.1	50.8 ± 6.0
Fitted other bkg events	13.1 ± 1.7	15.9 ± 2.3	11.8 ± 1.7	17.6 ± 2.4
Fitted multijets events	14.1 ± 13.0	42.1 ± 26.3	13.5 ± 10.1	20.2 ± 11.3
MC exp. SM events	679.3 ± 154.2	1091.5 ± 300.2	125.7 ± 42.2	212.8 ± 78.9
MC exp. $t\bar{t}$ events	44.3 ± 16.0	72.5 ± 25.7	78.8 ± 34.0	122.6 ± 50.3
MC exp. W +jets & Z +jets	597.0 ± 169.0	961.5 ± 277.9	30.3 ± 16.5	50.0 ± 26.7
MC exp. other bkg events	14.2 ± 5.6	21.0 ± 6.4	11.2 ± 4.0	19.5 ± 5.7
Data-driven multijets events	23.9 ± 13.0	36.4 ± 26.3	5.4 ± 10.1	20.7 ± 11.3

Table 7.4: Number of events in control regions. The fit results of background (Fit) consist of the data-driven multijets and simulated backgrounds. The inputs to the fit (MC) consist of multijets and nominal expectations from simulation normalized to theoretical cross sections are also shown. The errors shown are the statistical plus systematic uncertainties.

	W +jets	hard lepton $t\bar{t}$	High m_T	soft lepton
N^ℓ	=1	=1	=1	=1
p_T^ℓ	> 25 (20) GeV	> 25 (20) GeV	> 25 (20) GeV	[7,25]([6,20])
N^{jet}	≥ 3	≥ 3	≥ 3	≥ 2
p_T^{jet}	> 80, 25, 25 GeV	> 80, 25, 25 GeV	> 80, 25, 25 GeV	> 130, 25 GeV
N^{b-jet}	= 0	≥ 1 (within 3 jets)	—	—
E_T^{miss}	$150 < E_T^{\text{miss}} < 250$ GeV	$150 < E_T^{\text{miss}} < 250$ GeV	$40 < E_T^{\text{miss}} < 250$ GeV	$180 < E_T^{\text{miss}} < 250$ GeV
m_T	$40 < m_T < 80$ GeV	$40 < m_T < 80$ GeV	$m_T > 100$ GeV	$80 < m_T < 100$ GeV
$m_{\text{eff}}^{\text{inc}}$	$m_{\text{eff}}^{\text{inc}} > 500$ GeV	$m_{\text{eff}}^{\text{inc}} > 500$ GeV	$m_{\text{eff}}^{\text{inc}} > 500$ GeV	—

Table 7.5: Definitions of the selection criteria of each validation region. The p_T selections for lepton is given for electron (muon).

The fit is implemented in following conditions.

- The samples of W +jets associated with the heavy flavor process share the same normalization factors as the light flavor samples in each bin of parton numbers.
- The Z +jets background associated with both light and heavy flavor process are scaled by the common normalization factors to the W +jets samples in the same parton bin.
- Larger than three parton bins ($N_p^{t\bar{t}} \geq 3$) for the $t\bar{t}$ samples are merged due to a small statistics.
- Normalization factors for the W +jets background in zero and one parton bins ($N_p^{W+jets} = 0$ and $N_p^{W+jets} = 1$) are fixed at a unity due to the small contributions, and 20% uncertainty are assigned to the cross sections.
- The factors of the other backgrounds are fixed at a unity and 20% uncertainty is assigned to the cross sections.

The normalization factors are measured by fitting the backgrounds to data in a jet multiplicity distribution in both W +jets and $t\bar{t}$ control regions. Uncertainties as input for the fit are described in Section 8.1 and Section 8.2. The measured normalization factors are shown in Table 7.3. The jet multiplicity distribution in W +jets and $t\bar{t}$ control regions before and after fit by applying both shape corrections and normalization factors are shown in Figure 7.9 and Figure 7.10. In addition, the number of events as fit results in each control region are summarized in Table 7.4.

7.3 Validation Regions

The background correction is cross-checked by counting the number of events in validation regions, situated between the control regions and the signal regions. Distributions in the validation regions are corrected by taking the shape corrections and normalization factors in the control regions referred to Figure 7.8 and Table 7.3. The definitions of validation regions are described in Table 7.5 and depicted on $E_T^{\text{miss}}-m_T$ plane in Figure 7.1.

E_T^{miss} distribution in soft lepton, W +jets and $t\bar{t}$ validation regions are shown in Figure 7.12 (electron channel) and Figure 7.13 (muon channel). The fit results in both the validation regions are shown in Table 7.6. Pull results which is difference between observed and predicted number of events divided by total uncertainty are also shown in Figure 7.11. The distributions before fit are overestimated in the validation regions, and the shape correction decreases the distributions at high E_T^{miss} region. The pull result shows $\chi^2/\text{NDOF} = 4.12/4 = 1.03$ in electron channel, $\chi^2/\text{NDOF} = 1.67/4 = 0.42$ in muon channel and $\chi^2/\text{NDOF} = 5.79/8 = 0.72$ in combined channel. The results are equivalent to probabilities of 39%, 80% and 67% in chi-square statistic, respectively. The table and pull results show the background estimation corrected by the scale factors are reasonably in agreement with the observed data in each validations region.

Validation region channel	W +jets (hard lepton)		$t\bar{t}$ (hard lepton)	
	electron	muon	electron	muon
Observed events	1068	1019	499	427
Fitted bkg events	1001.1 ± 51.8	1015.2 ± 36.6	465.5 ± 23.2	456.9 ± 18.5
Fitted $t\bar{t}$ events	248.9 ± 15.9	239.5 ± 15.8	366.4 ± 18.2	350.3 ± 18.0
Fitted W +jets & Z +jets events	719.1 ± 41.6	739.3 ± 38.8	67.4 ± 9.7	76.4 ± 8.5
Fitted other bkg events	31.3 ± 4.1	31.8 ± 4.3	31.4 ± 4.7	26.3 ± 3.7
Fitted multijets events	1.8 ± 23.4	4.6 ± 11.6	0.3 ± 12.2	3.8 ± 5.8
MC exp. SM events	1144.1 ± 211.7	1120.2 ± 197.2	558.1 ± 107.7	491.1 ± 93.8
MC exp. $t\bar{t}$ events	280.5 ± 53.6	242.6 ± 44.4	447.6 ± 90.9	386.5 ± 77.7
MC exp. W +jets & Z +jets events	826.3 ± 211.5	842.2 ± 181.1	70.6 ± 33.8	73.7 ± 32.1
MC exp. other bkg events	35.4 ± 10.0	30.7 ± 8.4	39.6 ± 11.3	27.1 ± 8.5
Data-driven multijets events	1.8 ± 23.4	4.6 ± 11.6	0.3 ± 12.2	3.8 ± 5.8

Validation region channel	High m_T		soft lepton	
	electron	muon	electron	muon
Observed events	7692	7075	295	463
Fitted bkg events	7413.8 ± 547.6	7095.4 ± 135.4	337.1 ± 23.7	490.8 ± 27.0
Fitted $t\bar{t}$ events	3127.5 ± 121.8	3100.6 ± 115.7	65.3 ± 5.0	77.0 ± 5.2
Fitted W +jets & Z +jets events	3619.7 ± 108.0	3728.8 ± 114.2	246.6 ± 14.3	380.3 ± 16.1
Fitted other bkg events	231.0 ± 29.5	230.0 ± 29.6	11.8 ± 1.6	16.1 ± 2.1
Fitted multijets events	435.5 ± 525.7	35.9 ± 85.3	13.4 ± 16.3	17.5 ± 20.4
MC exp. SM events	8002.2 ± 888.2	7396.1 ± 835.8	342.4 ± 95.5	479.2 ± 137.1
MC exp. $t\bar{t}$ events	3376.1 ± 476.0	3198.4 ± 476.6	69.5 ± 26.2	80.9 ± 30.2
MC exp. W +jets & Z +jets events	3961.9 ± 721.1	3925.5 ± 718.4	247.1 ± 87.7	363.6 ± 122.5
MC exp. other bkg events	228.7 ± 65.2	236.2 ± 38.7	12.4 ± 4.3	17.1 ± 6.1
Data-driven multijets events	435.5 ± 525.7	35.9 ± 85.3	13.4 ± 16.3	17.5 ± 20.4

Table 7.6: Number of events in validation regions. The fit results of background (Fit) consist of the data-driven multijets and simulated backgrounds. The inputs to the fit (MC) consist of multijets and nominal expectations from simulation normalized to theoretical cross sections are also shown. The errors shown are the statistical plus systematic uncertainties.

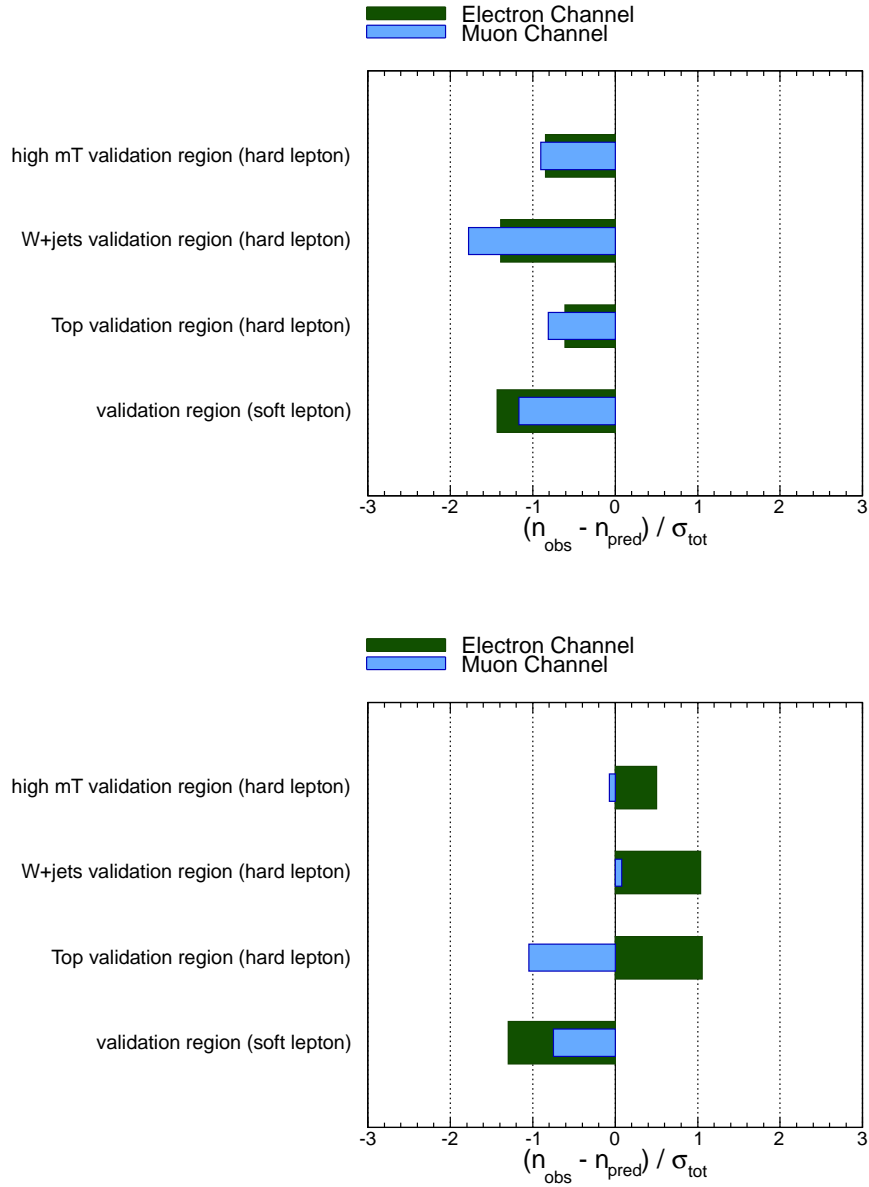


Figure 7.11: Summary of fitting results in validation regions before correction (top) and after correction (bottom). Difference between the observed and predicted number of events divided by the total uncertainty is shown. For the corrected distributions, χ^2/NDOF of the pull results are $\chi^2/\text{NDOF} = 4.12/4 = 1.03$ (probability of 39%) in electron channel, $\chi^2/\text{NDOF} = 1.67/4 = 0.42$ (probability of 80%) in muon channel and $\chi^2/\text{NDOF} = 5.79/8 = 0.72$ (probability of 67%) in combined channel.

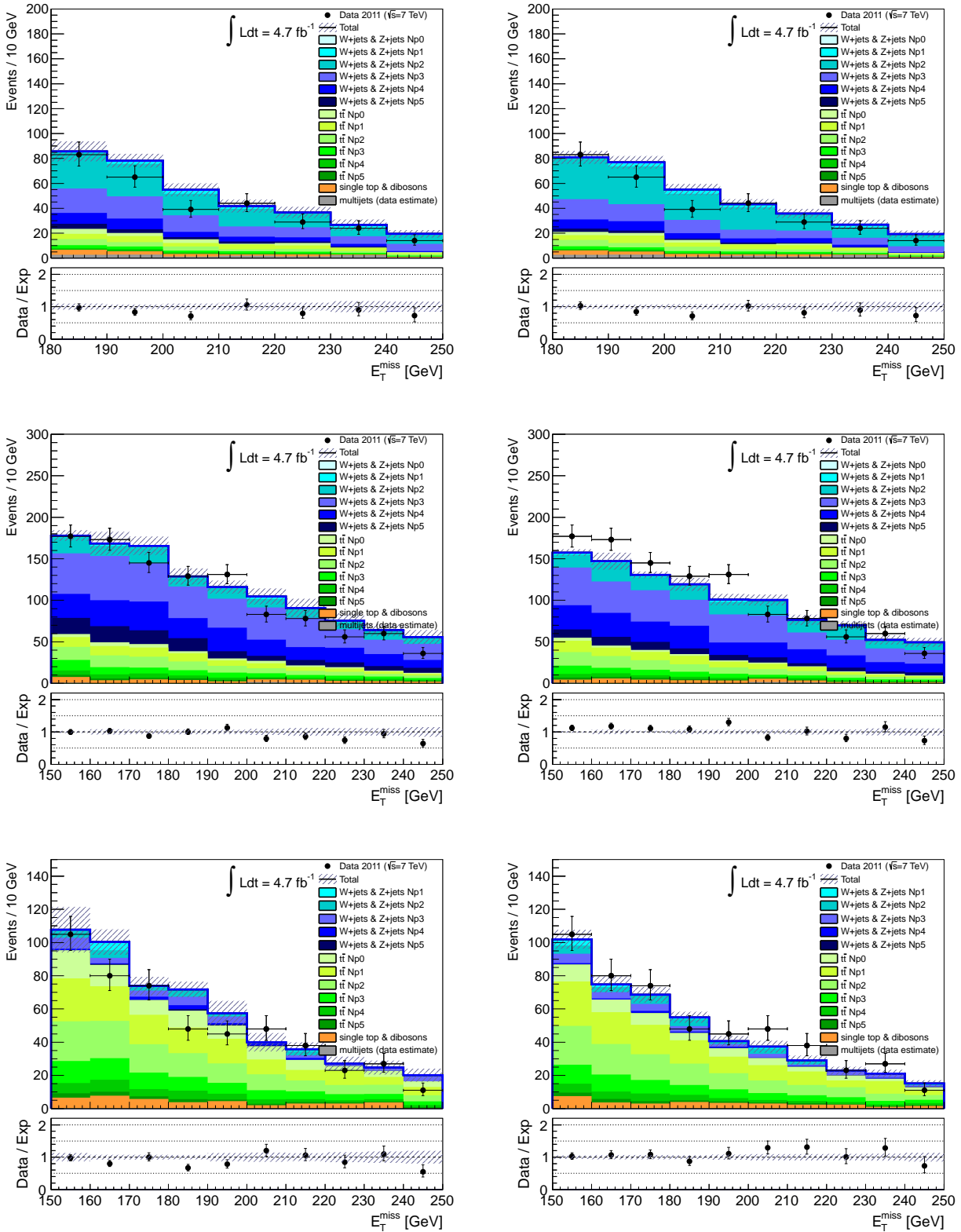


Figure 7.12: Distributions of the E_T^{miss} in the soft lepton (top), W +jets (middle) and $t\bar{t}$ (bottom) validation region for the electron channel before (left) and after (right) corrections.

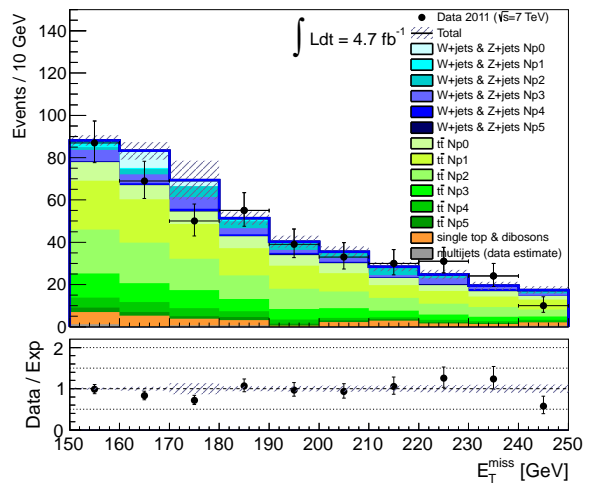
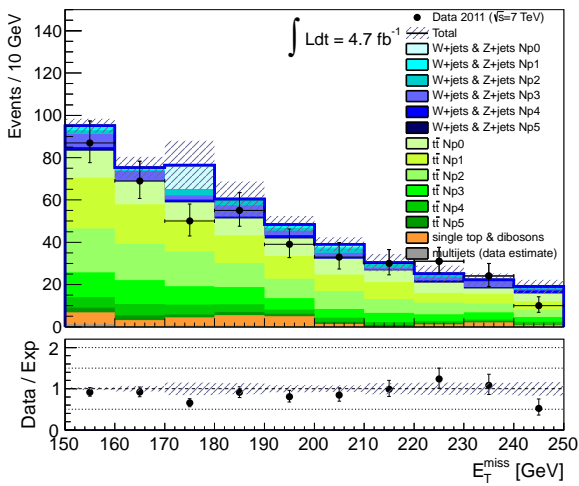
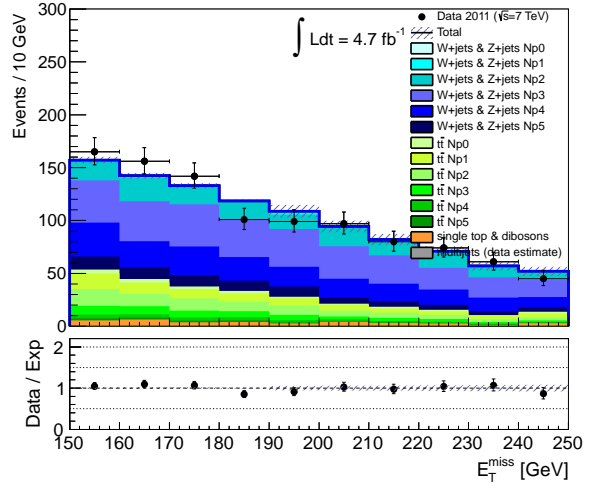
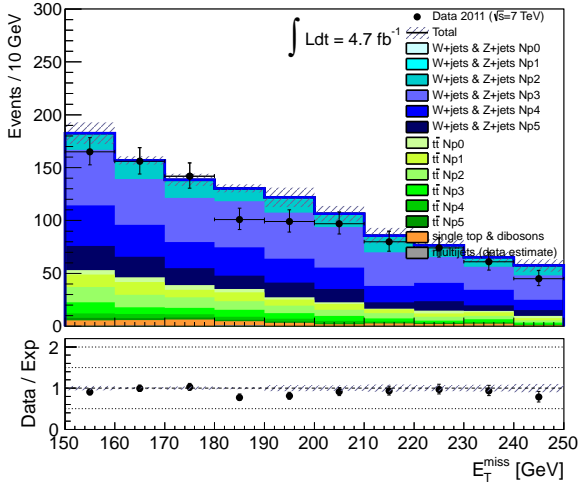
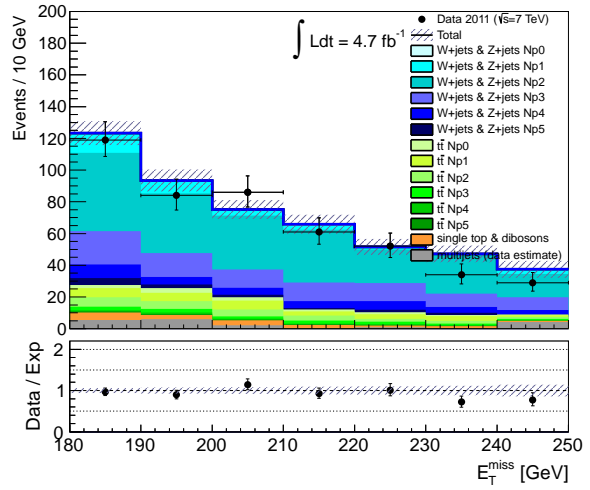
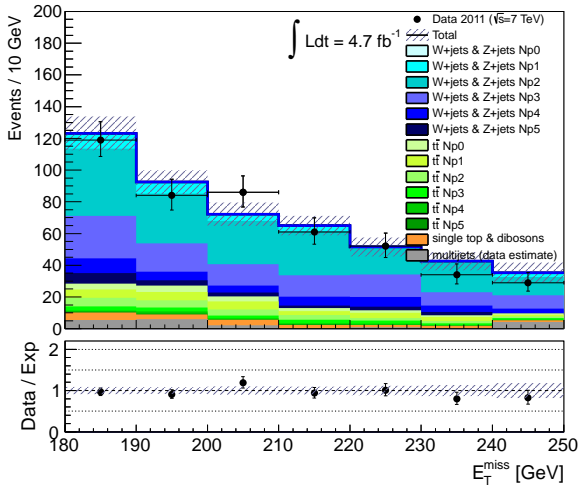


Figure 7.13: Distributions of the E_T^{miss} in the soft lepton (top), W +jets (middle) and $t\bar{t}$ (bottom) validation region for the muon channel before (left) and after (right) corrections.

Chapter 8

Uncertainties

The systematic uncertainties of energy scales and momentum resolutions with leptons and jets are measured in beam tests and collision data in detail. The scale factors which correct the MC distributions to agree with data have the systematic uncertainties as well. Cross sections and distributions for the simulated samples have theoretical uncertainties derived from modeling and parameters of generators.

In fitting with the background estimation, the uncertainties give widths where the most probable value can be fitted. For the some of uncertainties, the shape of distributions after applying $\pm 1\sigma$ uncertainties are different from that of nominal distribution. As an example, Figure 8.1 shows jet multiplicity distribution for nominal and obtained by applying $\pm 1\sigma$ jet energy scale uncertainties to jets with $40 < p_T < 100$ GeV and with $p_T > 100$ GeV in W +jets control region. These uncertainties are inputted in bin by bin so that the background expectations can be described well by varying the shape of distributions. Therefore the uncertainties are classified into varying shape and not varying shape. The uncertainties not varying shape are treated as varying the normalization. In the following sections the uncertainties are summarized and categorized into varying shape labeled [shape] or varying normalization labeled [normalization].

The systematic uncertainties are substituted into the likelihood function (Equation 7.2.1) as nuisance parameters. The input values of each uncertainties in this chapter are shown. The output from the covariance matrix (Equation 7.2.3) are shown in Table 8.3.

8.1 Systematic Uncertainties

Uncertainties of hit positions and energy scales are measured and propagated to the uncertainties of momentum and energy. The uncertainties with the scale factors of efficiencies for lepton identifications and triggers are also measured. Estimation method of systematic uncertainties are described in Appendix B. This section lists and explains the considered systematic uncertainties. The values of uncertainties written in each item below

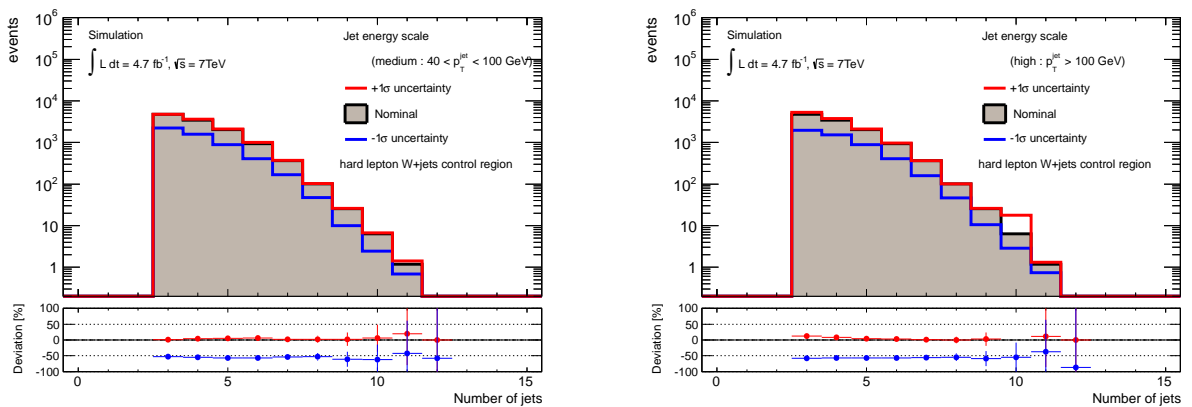


Figure 8.1: Jet multiplicity distributions of nominal and after applying $\pm 1\sigma$ jet energy scale uncertainties. Jet energy scale uncertainty is applied to jets with $40 < p_T < 100$ GeV (left) and jets with $p_T > 100$ GeV (right).

are estimated from deviations with the number of events between nominal distribution and distribution after applying $\pm 1\sigma$ uncertainties in control regions.

- Jet energy scale [shape]
Jet energy scale is the most dominant source of the uncertainties. The uncertainty increases at both large and small jet p_T , and the origin of uncertainty depends on the jet p_T . The uncertainty originating from calorimeter response is dominant in large p_T region while not only it but also modeling of generator affect the uncertainty in small p_T region. Figure B.10 shows the component of uncertainty in detail. Thus when the uncertainty is applied to jets, jets are binned into three region, $p_T^{jet} < 40$ GeV, $40 < p_T^{jet} < 100$ GeV and $p_T^{jet} > 100$ GeV, respectively. The jet energy scale uncertainty is applied to jets in each p_T^{jet} bin independently to shift $\pm 1\sigma$. The uncertainty is estimated as $\sim \pm 25\%$.
- E_T^{miss} cell-out [shape]
The energy scale uncertainty of cell-out cluster are derived from the dead materials and mismodeling of shower shape in calorimeters on the simulation. The uncertainty contributes to the overall cell-out E_T^{miss} term. The numbers of events in control regions is increased or decreased $\sim 1\%$ from that of nominal distribution when $\pm 1\sigma$ uncertainties are applied to the nominal distribution.
- E_T^{miss} pile-up uncertainty [shape]
To reduce the pile-up contaminations, a cut-off is set for topocluster energy. This E_T^{miss} pile-up uncertainty is derived from the mismodeling with the dead material and the shower shape of soft jets. The numbers of events in control regions varies $\sim 1\%$ from that of nominal distribution when $\pm 1\sigma$ uncertainties are applied to the nominal distribution.
- Electron energy scale uncertainty [normalization]
The electron energy scale uncertainty is estimated by using $Z \rightarrow ee$ events. The energy scale measurement is affected from an imperfect knowledge of the material in front of the electromagnetic calorimeter and different response between the high E_T and low E_T electron measurement. The value of this uncertainty is about 1%.
- Muon momentum resolution uncertainty (with inner detector) [normalization]
The muon momentum resolution uncertainty in inner detector tracks is estimated by using $Z \rightarrow \mu\mu$ events. Difference of the Z peak fitting results by using a Gaussian function between data and MC simulation are dealt as systematic uncertainty. The value is measured about 1%.
- Muon momentum resolution uncertainty (with muon spectrometer) [normalization]
The muon momentum resolution uncertainty with the muon spectrometer track is estimated as well as the inner detector. The value is measured about 1%.
- Trigger efficiency uncertainty [normalization]
The efficiencies of electron trigger and muon trigger are not modeled by the MC simulation completely thus the trigger efficiencies are corrected by the scale factors measured $Z \rightarrow \ell\ell$ events in depending on the p_T and η . The uncertainty is measured as about 2%. The efficiency of E_T^{miss} trigger is estimated as almost 100% above $E_T^{miss} > 180$ GeV both data and MC simulation, thus uncertainty of E_T^{miss} trigger efficiency is not applied to the soft lepton channel.
- Lepton scale factor uncertainty [normalization]
The efficiencies of electron and muon identification are also not modelled by the MC simulation completely, thus the identification efficiencies are corrected by the scale factors measured $Z \rightarrow \ell\ell$ events in depending on p_T and η . The uncertainty is measured as about 2%.
- Luminosity uncertainty [normalization]
The luminosity uncertainty is measured 3.7% derived from a bunch current measurement [47,48]. Method of luminosity measurement and source of uncertainty are described in detail in Appendix B.
- b -tagging efficiency uncertainty [normalization]
The b -tagging is employed when it is separated into the W +jets control region and the $t\bar{t}$ control region. The uncertainty of b -tagging scale factor with no b -jets are applied to the events in W +jets control region, while the uncertainty of b -tagging scale factor with b -jets are applied to the events in $t\bar{t}$ control region. About 9% uncertainty in $t\bar{t}$ control region and 5% in W +jets control region are given.

		Hard lepton control region						
sample	N^{jet}	= 3	= 4	= 5	= 6	= 7	= 8	= 9
$t\bar{t}$	-1σ	-0.1%	-0.1%	-0.1%	-2%	-5%	-0.1%	-10%
$t\bar{t}$	$+1\sigma$	+8%	+5%	+0.3%	+0.1%	+0.1%	+0.4%	+0.1%
W +jets	-1σ	-0.1%	-2%	-0.1%	-0.1%	-0.1%	-0.1%	-0.1%
W +jets	$+1\sigma$	+0.1%	+0.1%	+0.6%	+6%	+20%	+2%	+6%

		Soft lepton control region					
sample	N^{jet}	= 2	= 3	= 4	= 5	= 6	= 7
$t\bar{t}$	-1σ	-0.1%	-0.1%	-1%	-2%	-4%	-0.1%
$t\bar{t}$	$+1\sigma$	+0.3%	+4%	+0.1%	+0.1%	+0.1%	+11%
W +jets	-1σ	-0.1%	-4%	-10%	-14%	-12%	-0.1%
W +jets	$+1\sigma$	+3%	+0.1%	+0.1%	+0.1%	+0.1%	+3%

		signal region		
sample	N^{jet}	3-jets hard lepton	4-jets hard lepton	2-jets soft lepton
$t\bar{t}$		$\pm 12\%$	$\pm 16\%$	$\pm 2\%$
W +jets		$\pm 19\%$	$\pm 8\%$	$\pm 30\%$

Table 8.1: MLM matching uncertainty for individual jet bin in hard lepton control regions, soft lepton control regions and signal regions.

- Fitting uncertainty [shape]

The scale factors of shape and normalization corrections contain the uncertainty. Since variations derived from renormalization and factorization scale uncertainties mostly affect the shape and normalizations, the energy scale uncertainties in generators are replaced by the uncertainties of fit in the corrections of shape and normalization of the individual light parton bins. The values are tabled in Figure 7.8 and Table 7.3.

- Multijets events uncertainty [normalization]

For the multijets background estimated by data-driven method, the systematic uncertainty of cross section of real lepton events predicted by the simulation is assumed as 20%. In subtraction of the real lepton events from observed data, the uncertainty propagates to the multijets distribution. The uncertainty amounts to 15% in soft lepton control regions, on the other hand 1% for hard lepton control regions.

8.2 Theoretical Uncertainties

Some background and signal estimations are performed by using the simulated events, therefore the modeling of generator is important. The parameters in the generator are tuned with collected data at Tevatron and LHC. In this section, the uncertainties with modeling or parameters for the generators are summarized.

- Renormalization and factorization scale uncertainty [normalization]

The MC samples are generated with renormalization and factorization scale Q_0 defined as following

$$Q_0^2 = m_W^2 + \sum_{\text{partons}} (m^2 + p_T^2) \quad (8.2.1)$$

for W +jets event and it is given by

$$Q_0^2 = \sum_{\text{partons}} (m^2 + p_T^2) \quad (8.2.2)$$

for $t\bar{t}$ event. The factorization and renormalization scale uncertainty is estimated from the deviation of samples in which the energy scale is changed upward $2|Q_0|$ and downward $0.5|Q_0|$.

- MLM matching [shape]

To avoid parton overlap between the different number of parton sample, the MLM matching is applied. The MLM matching is described in Section 4.2.1. In this analysis, the $p_T^{min} = 15$ GeV, $E_T^{min} = p_T^{min} + 5$ GeV = 20 GeV and $R_{jet} = 0.7$ are employed.

When the threshold p_T^{min} is varied, the number of jets, p_T^{jet} distributions and the cross sections are affected. Deviations from default sample with $p_T^{min} = 15$ GeV to the samples with $p_T^{min} = 20$ GeV and 30 GeV in each jet multiplicity bin in control regions and signal region are assigned as the MLM matching uncertainty. The amounts are shown in Table 8.1.

- Parton shower and hadronization [normalization]

The difference of parton shower and hadronization model leads to the different distributions. The uncertainty is obtained from the difference of distributions between PYTHIA and HERWIG as the interfaces. One of the difference between these generators is a given energy scale Q which determines probability of parton emission, PYTHIA uses $Q^2 \sim m^2$ where m is a mass of generated particle, HERWIG uses $Q^2 \sim E^2\theta^2$ where E and θ are an energy and an open angle for branching particles. The different is fitted to a linear function in m_{eff} and E_T^{miss} distributions. Figure 8.2 shows m_{eff} distribution of $t\bar{t}$ events generated and the difference between HERWIG and PYTHIA. After fitting, the fit function extrapolates from the control region to the signal region as follows

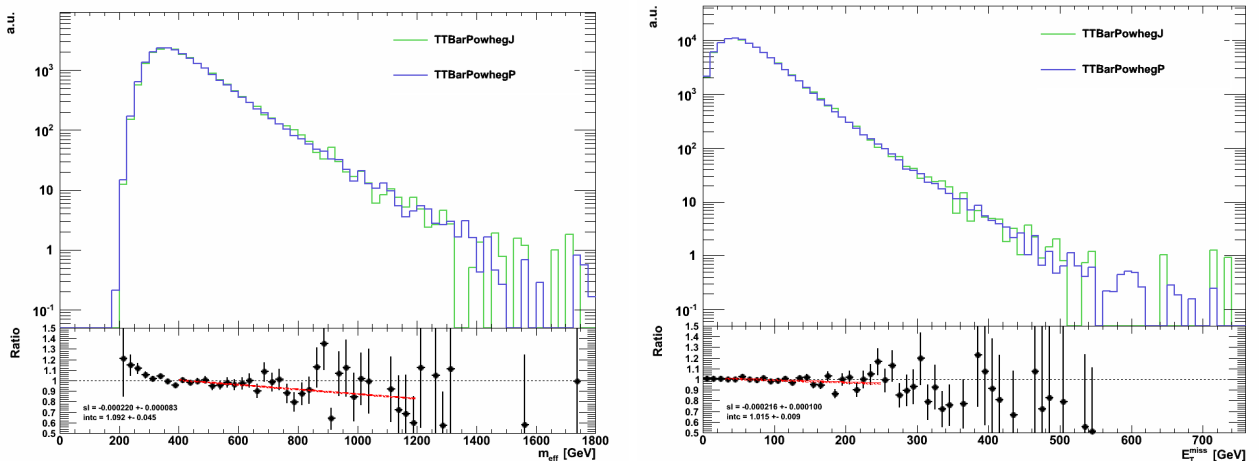
$$\Delta_{Had}(\%) = \pm a_{E_T^{miss}} \times [E_T^{miss}(x_2) - E_T^{miss}(x_1)], \quad (8.2.3)$$

$$\Delta_{Had}(\%) = \pm a_{m_{eff}} \times [m_{eff}(x_2) - m_{eff}(x_1)], \quad (8.2.4)$$

where the $E_T^{miss}(x_1)$ and $m_{eff}(x_1)$ are the thresholds of the control regions, and $E_T^{miss}(x_2)$ and $m_{eff}(x_2)$ are thresholds of signal regions. Therefore in the 3-jets, 4-jets hard lepton channel and soft lepton channel, $m_{eff}(x_1) = 500$ GeV and $m_{eff}(x_2) = 1200$ GeV, $m_{eff}(x_1) = 500$ GeV and $m_{eff}(x_2) = 800$ GeV and $E_T^{miss}(x_1) = 180$ GeV and $E_T^{miss}(x_2) = 250$ GeV are substituted into above equation, respectively. Δ_{Had} are estimated as 0.7% for W +jets events and 1.5% for $t\bar{t}$ events in both control and signal regions.

- Cross section of W and Z associated with heavy flavour [shape]

For the heavy flavor quark production associated with W and Z boson, the cross section is not well known. The cross section of $Wb\bar{b}$, $Wc\bar{c}$ and Wc events whose diagram is shown in Figure 4.6 are measured in $t\bar{t}$ charge asymmetry analysis to extract the events from data [49]. The uncertainties of $Wb\bar{b}$ and $Wc\bar{c}$ cross



	W +jets and Z +jets	$t\bar{t}$
m_{eff}	$a = -0.0177$	$a = -0.0220$
E_T^{miss}	$a = 0.0111$	$a = -0.0216$

Figure 8.2: Difference of hadronization interface. Top figures show distribution of the effective mass (left) and the E_T^{miss} (right) in the three jet selection for $t\bar{t}$ events generated with HERWIG (green) and PYTHIA (blue). Bottom table shows fit results of the difference and coefficient a .

section are estimated as 32% and that of Wc is 47%. For $Zb\bar{b}$ events the uncertainty of cross section is estimated as 25%.

- Cross section of single-top and dibosons [normalization]

The single-top and dibosons events are estimated by taking the simulated events. The cross sections are treated as 20% uncertainty assigned.

8.3 Signal Cross Section Uncertainties

The cross sections of supersymmetry models are calculated by the two tools, “NLL-fast” and “Prospino”. The NLL-fast computes the hadron production cross sections including next-to-leading order SUSY QCD corrections which calculates the gluon or quark radiation by gluon loops and the virtual diagram involving squark and gluino loops separately and add a re-summation of soft gluon emissions at next-to-leading logarithmic. Prospino calculates the cross sections of pair production for supersymmetric particles at next-to-leading order (NLO). The two tools calculate the uncertainties by using some parton density function (PDF) sets and varying both factorization and the renormalization scale Q_0 . The estimation for theoretical uncertainty is described as following.

8.3.1 Factorization and Renormalization Scale Uncertainty

The cross section calculation adopts the same value $Q_0^2 = (m_k + m_l)^2$ for both factorization and renormalization scale where k or l is squark or gluino mass contributing to the pair production. The cross section uncertainty derived from the scale is estimated by taking into account the difference of cross section by shifting the $|Q_0|$ from $|0.5Q_0|$ to $|2Q_0|$. For the UED model, this uncertainty Δ_{α_s} is obtained by using PYTHIA and the value is given as 9%.

8.3.2 PDF Uncertainty

CTEQ and MSTW PDF sets contain one central PDF value for the lightest five quarks and five anti-quarks and one gluon and 22 variations which span the range of the uncertainties coming from the experimental errors. This gives another 44 PDFs (up and down variations). The PDF uncertainty is estimated from the difference of cross sections between nominal PDF set and each PDF set as follows,

$$\Delta_{\text{PDF}}^{\text{up}} = \sqrt{\sum_{\text{PDF sample}} \{\max[w_{\text{up}} - w_0, w_{\text{down}} - w_0, 0]\}^2} \quad (8.3.1)$$

$$\Delta_{\text{PDF}}^{\text{down}} = \sqrt{\sum_{\text{PDF sample}} \{\max[w_0 - w_{\text{up}}, w_0 - w_{\text{down}}, 0]\}^2} \quad (8.3.2)$$

$$(8.3.3)$$

where the w_{up} and w_{down} are the PDF weight with cross sections of upward and downward at 90% confidence level of each PDF samples respectively, and w_0 is nominal weight. It is employed to the CTEQ6.6 [50] and MSTW2008 [51] as the PDF set. The upward and downward uncertainties are determined by either PDF set which gives larger uncertainty than the other.

8.3.3 ISR Uncertainty

The $E_{\text{T}}^{\text{miss}}$ trigger is applied to the soft lepton channel, this $E_{\text{T}}^{\text{miss}}$ is generated by the recoil of neutrino or neutralino against ISR jet. Thus the ISR jet uncertainty is critical for the soft lepton channel. The ISR uncertainty estimation employs the MADGRAPH generator. The value is obtained from distributions which is generated to vary the energy scale of parton emission from $|0.5Q|$ up to $|2Q|$, where $|Q|$ is nominal value of energy scale for the transfer momentum. Figure 8.3 shows the nominal distribution of leading jet p_{T} for UED events and that of distributions after applying $\pm 1\sigma$ ISR uncertainties. The discrepancy from the nominal

distribution is from -10% to +20%. The uncertainty of simplified SUSY model is given as following [52]

$$\Delta_{\text{ISR}} = \left(1 - \frac{m_{\text{diff}}}{300\text{GeV}}\right) \cdot \text{Norm} \quad (8.3.4)$$

$$\text{Norm} = \begin{cases} \sqrt{(0.25)^2 + (0.10)^2} + \left(1.0 - \frac{m_{\tilde{g}} - 200\text{GeV}}{100\text{GeV}}\right) \cdot 0.25 & (m_{\tilde{g}} < 300\text{GeV}) \\ \sqrt{(0.25)^2 + (0.10)^2} & (m_{\tilde{g}} > 300\text{GeV}) \end{cases} \quad (8.3.5)$$

$$m_{\text{diff}} = m_{\tilde{g}} - m_{\text{LSP}} \quad (8.3.6)$$

8.3.4 Combined Uncertainty

The combined theoretical uncertainty of simplified SUSY model and UED model are estimated as the quadratic summation of scale uncertainty and PDF uncertainty as follows

$$\Delta = \sqrt{\Delta_{\alpha_s}^2 + \Delta_{\text{PDF}}^2 + \Delta_{\text{ISR}}^2} \quad (8.3.7)$$

The estimated uncertainties of gluino pair production and squark pair production are shown in Figure 8.4.

8.4 Total Uncertainties Estimations

Contributions from uncertainties listed above to the signal regions are estimated in each signal region. The estimation employs the likelihood function (Equation 7.2.1) and covariance matrix (Equation 7.2.3), and the uncertainties listed in Section 8.1-8.2 are substituted into the functions as nuisance parameters. The systematic uncertainties as inputs are shown in Table 8.2. Number of events in each component of uncertainties and total uncertainty in each signal region as outputs of the covariance matrix are shown in Table 8.3. Correlations between nuisance parameters in covariance matrix constrain the uncertainties, therefore the values of outputs in Table 8.3 are smaller than those of inputs.

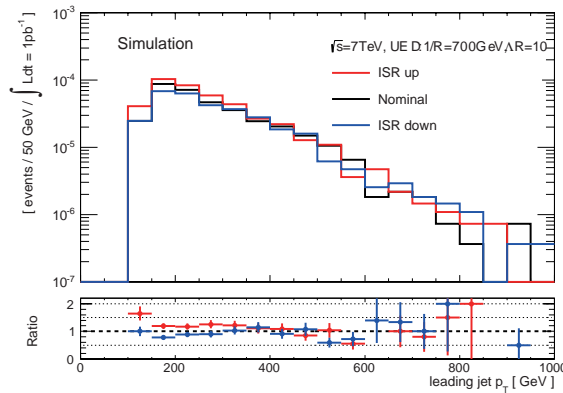


Figure 8.3: Distribution of leading jet p_T for nominal and the distributions after applying $\pm 1\sigma$ ISR uncertainties for UED signal events at $1/R = 700$ GeV and $\Delta R = 10$.

Inputs to covariance matrix

Signal region channel	hard lepton 3-jets		hard lepton 4-jets		soft lepton 2-jets	
	electron	muon	electron	muon	electron	muon
Total statistical ($\sqrt{N_{\text{obs}}}$)	± 1.41	± 1.00	± 2.00	± 1.41	± 3.32	± 3.74
Total background systematic	± 1.98	± 0.95	± 1.92	± 1.11	± 3.79	± 5.64
Jet energy scale ($p_T^{jet} < 40$ GeV)	± 0.72	± 0.08	± 1.18	± 0.36	± 0.17	± 0.14
Jet energy scale ($40 < p_T^{jet} < 100$ GeV)	—	± 0.07	± 0.35	± 0.50	± 0.14	± 0.02
Jet energy scale ($p_T^{jet} > 100$ GeV)	± 1.58	± 0.35	± 0.72	± 0.57	± 0.22	± 0.47
E_T^{miss} cell-out	± 0.14	± 0.06	± 0.13	± 0.30	± 0.24	± 0.09
E_T^{miss} pile-up	± 0.24	± 0.06	± 0.49	± 0.21	± 0.31	± 0.02
Electron energy scale (hard electron)	± 0.18	—	± 0.11	—	—	—
Electron energy scale (soft electron)	—	—	—	—	—	—
Hard muon energy resolution (Inner Detector)	—	± 0.07	—	± 0.05	—	—
Soft muon energy resolution (Inner Detector)	—	—	—	—	—	± 0.05
Hard muon energy resolution (Muon Spectrometer)	—	± 0.06	—	± 0.05	—	—
Soft muon energy resolution (Muon Spectrometer)	—	—	—	—	—	—
Trigger Efficiency (electron)	± 0.01	—	± 0.03	—	—	—
Trigger Efficiency (muon)	—	± 0.11	—	± 0.13	—	—
Lepton scale factor (hard electron)	± 0.03	—	± 0.07	—	—	—
Lepton scale factor (hard muon)	—	± 0.01	—	± 0.01	—	—
Lepton scale factor (soft electron)	—	—	—	—	± 0.54	—
Lepton scale factor (soft muon)	—	—	—	—	—	± 0.02
p_T^Z weight (0 - 50 GeV)	—	± 0.02	—	± 0.05	—	—
p_T^Z weight (50 - 100 GeV)	—	—	—	—	—	± 0.05
p_T^Z weight (100 - 150 GeV)	—	—	—	—	—	± 0.02
p_T^Z weight (150 - 200 GeV)	± 0.11	± 0.15	± 0.12	—	± 0.41	± 0.71
$t\bar{t}$ Np0 normalization	—	—	—	—	± 0.08	± 0.27
$t\bar{t}$ Np1 normalization	—	—	± 0.01	—	± 0.06	± 0.07
$t\bar{t}$ Np2 normalization	± 0.05	± 0.02	± 0.09	± 0.10	± 0.23	± 0.19
$t\bar{t}$ Np3 normalization	± 0.04	± 0.05	± 0.15	± 0.12	± 0.13	± 0.14
W +jets Np2 normalization	—	—	—	—	± 0.27	± 0.83
W +jets Np3 normalization	± 0.12	± 0.05	—	—	± 0.26	± 0.18
W +jets Np4 normalization	—	± 0.11	± 0.04	—	± 0.11	± 0.11
W +jets Np5 normalization	—	± 0.24	± 0.21	± 0.21	—	± 0.62
Multijets (3-jets electron signal region)	± 0.38	—	—	—	—	—
Multijets (4-jets electron signal region)	—	—	± 0.38	—	—	—
Multijets (2-jets electron signal region)	—	—	—	—	± 2.45	—
Multijets (2-jets muon signal region)	—	—	—	—	—	± 2.43
MLM matching ($t\bar{t}$ events)	—	—	—	—	—	—
MLM matching (W +jets events)	—	—	—	—	—	—
Hadronization ($t\bar{t}$ events)	± 0.11	± 0.08	± 0.50	± 0.32	± 0.09	± 0.08
Hadronization (W +jets events)	± 0.23	± 0.38	± 0.14	± 0.03	± 1.65	± 3.15
W/Z +jets Heavy Flavor	± 0.34	—	± 0.41	—	± 0.26	± 0.70
W +jets Np0 cross section	—	—	—	—	—	—
W +jets Np1 cross section	—	—	± 0.18	—	—	—
single top & dibosons cross sections	—	± 0.04	± 0.08	± 0.02	± 0.10	± 0.02
MC statistical uncertainty	± 0.67	± 0.70	± 0.81	± 0.44	± 2.14	± 3.67

Table 8.2: Number of events as inputs derived from systematic uncertainties as inputs on background estimates in the signal regions. Uncertainties not written are negligible.

Outputs from covariance matrix

Signal region channel	hard lepton 3-jets		hard lepton 4-jets		soft lepton 2-jets	
	electron	muon	electron	muon	electron	muon
Total statistical ($\sqrt{N_{\text{obs}}}$)	± 1.41	± 1.00	± 2.00	± 1.41	± 3.32	± 3.74
Total background systematic	± 0.81	± 0.75	± 0.96	± 0.50	± 3.29	± 4.45
Jet energy scale ($p_{\text{T}}^{jet} < 40$ GeV)	± 0.21	± 0.01	± 0.53	± 0.06	± 0.08	± 0.04
Jet energy scale ($40 < p_{\text{T}}^{jet} < 100$ GeV)	—	± 0.01	± 0.09	± 0.09	± 0.01	—
Jet energy scale ($p_{\text{T}}^{jet} > 100$ GeV)	± 0.08	± 0.13	± 0.17	± 0.11	± 0.02	± 0.01
$E_{\text{T}}^{\text{miss}}$ cell-out	± 0.01	± 0.02	± 0.05	± 0.03	± 0.07	± 0.02
$E_{\text{T}}^{\text{miss}}$ pile-up	± 0.02	± 0.04	± 0.11	± 0.07	± 0.28	—
Electron energy scale (hard electron)	± 0.02	—	± 0.02	—	—	—
Electron energy scale (soft electron)	—	—	—	—	—	—
Hard muon energy resolution (Inner Detector)	—	—	—	—	—	—
Soft muon energy resolution (Inner Detector)	—	—	—	—	—	± 0.05
Hard muon energy resolution (Muon Spectrometer)	—	—	—	—	—	—
Soft muon energy resolution (Muon Spectrometer)	—	—	—	—	—	—
Trigger Efficiency (electron)	± 0.01	—	± 0.02	—	—	—
Trigger Efficiency (muon)	—	± 0.04	—	± 0.03	—	—
Lepton scale factor (hard electron)	± 0.02	—	± 0.04	—	—	—
Lepton scale factor (hard muon)	—	—	—	—	—	—
Lepton scale factor (soft electron)	—	—	—	—	± 0.35	—
Lepton scale factor (soft muon)	—	—	—	—	—	± 0.01
p_{T}^Z weight (0 - 50 GeV)	—	± 0.02	—	± 0.01	—	—
p_{T}^Z weight (50 - 100 GeV)	—	—	—	—	—	± 0.05
p_{T}^Z weight (100 - 150 GeV)	—	—	—	—	—	± 0.02
p_{T}^Z weight (150 - 200 GeV)	± 0.06	± 0.08	± 0.04	—	± 0.41	± 0.71
$t\bar{t}$ Np0 normalization	—	—	—	—	± 0.04	—
$t\bar{t}$ Np1 normalization	—	—	± 0.01	—	± 0.06	± 0.07
$t\bar{t}$ Np2 normalization	± 0.03	± 0.02	± 0.07	± 0.06	± 0.23	± 0.19
$t\bar{t}$ Np3 normalization	± 0.03	± 0.02	± 0.12	± 0.09	± 0.12	± 0.14
W +jets Np2 normalization	—	—	—	—	± 0.25	± 0.82
W +jets Np3 normalization	± 0.07	± 0.03	—	—	± 0.18	± 0.13
W +jets Np4 normalization	—	± 0.07	—	—	± 0.08	± 0.08
W +jets Np5 normalization	—	± 0.04	± 0.13	± 0.12	—	± 0.27
Multijets (3-jets electron signal region)	± 0.38	—	—	—	—	—
Multijets (4-jets electron signal region)	—	—	± 0.38	—	—	—
Multijets (2-jets electron signal region)	—	—	—	—	± 2.45	—
Multijets (2-jets muon signal region)	—	—	—	—	—	± 2.43
MLM matching ($t\bar{t}$ events)	—	—	—	—	—	—
MLM matching (W +jets events)	—	—	—	—	—	—
Hadronization ($t\bar{t}$ events)	± 0.08	± 0.08	± 0.15	± 0.11	± 0.06	± 0.06
Hadronization (W +jets events)	± 0.10	± 0.19	± 0.05	± 0.02	± 0.04	± 0.09
W/Z +jets Heavy Flavor	± 0.17	—	± 0.20	—	± 0.11	± 0.51
W +jets Np0 cross section	—	—	—	—	—	—
W +jets Np1 cross section	—	—	± 0.01	—	—	—
single top & dibosons cross sections	—	± 0.02	± 0.02	—	± 0.06	± 0.01
MC statistical uncertainty	± 0.67	± 0.70	± 0.81	± 0.44	± 2.14	± 3.67

Table 8.3: Number of events derived from systematic uncertainties as outputs on background estimates in the signal regions. Uncertainties not written are negligible. The uncertainties are constrained by taking the covariance matrix.

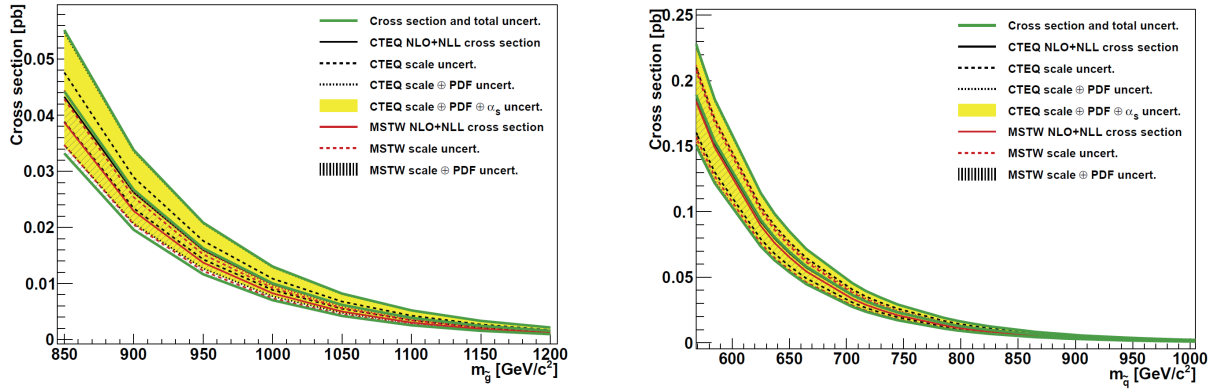


Figure 8.4: Cross section for $\tilde{g}\text{-}\tilde{g}$ pair (left) and $\tilde{q}\text{-}\tilde{q}$ pair (right) production and associated uncertainty derived from parton density function and renormalization scale [53].

Chapter 9

Results

In this chapter, the signals of physics beyond the Standard Model are searched for by using the observed data and background estimations. Distributions before corrections in signal regions are shown in Figure 9.1 (simplified SUSY with $m_{\tilde{g}} = 665$ GeV and $m_{\text{LSP}} = 585$ GeV) and Figure 9.2 (UED with $1/R = 900$ GeV and $\Lambda R = 10$). The distributions after the shape and normalization corrections in each signal region are shown in Figure 9.3. The fit results in signal regions are also shown in Table 9.1.

We can conclude discovery and exclusion by testing background-only hypothesis and signal-plus-background hypothesis, respectively. To summarize the outcome of such a search one quantifies the level of agreement of the observed data with a given hypothesis H by computing a p -value, i.e. a probability, under assumption of H , of finding data of equal or greater incompatibility with the predictions of H . In following sections, the test results of background-only and signal-plus-background hypotheses with simplified SUSY and UED models are described.

9.1 Testing the background-only hypothesis

In order to evaluate how well the observed data agree with the background prediction and find an excess of events originating from new physics, a statistical test is performed. For the hypothesis test with a given signal

Signal region channel	3-jets hard lepton		4-jets hard lepton		2-jets soft lepton	
	electron	muon	electron	muon	electron	muon
Observed events	2	1	4	2	11	14
Fitted bkg events	1.7 ± 0.8	2.2 ± 0.7	3.7 ± 1.0	2.1 ± 0.5	14.0 ± 3.3	18.9 ± 4.4
Fitted $t\bar{t}$ events	0.5 ± 0.2	0.5 ± 0.2	2.3 ± 0.5	1.7 ± 0.4	4.1 ± 0.7	4.0 ± 0.8
Fitted W +jets & Z +jets events	0.8 ± 0.4	1.6 ± 0.5	0.9 ± 0.3	0.3 ± 0.1	5.6 ± 0.9	11.2 ± 2.3
Fitted other bkg events	0.0 ± 0.0	0.1 ± 0.1	0.2 ± 0.1	0.0 ± 0.0	0.5 ± 0.1	0.1 ± 0.0
Fitted multijets events	0.3 ± 0.4	0.0 ± 0.0	0.3 ± 0.4	0.0 ± 0.0	3.8 ± 2.5	3.6 ± 2.5
MC exp. SM events	2.4 ± 3.0	2.8 ± 1.2	5.6 ± 3.2	2.5 ± 1.3	14.2 ± 4.5	18.0 ± 7.9
MC exp. $t\bar{t}$ events	0.9 ± 0.6	0.6 ± 0.3	3.1 ± 1.4	2.0 ± 1.2	4.3 ± 1.5	3.8 ± 1.4
MC exp. W +jets & $t\bar{t}$ events	1.2 ± 2.6	2.0 ± 1.3	1.7 ± 2.0	0.4 ± 0.4	5.5 ± 3.1	10.5 ± 5.0
MC exp. other bkg events	0.0 ± 0.1	0.2 ± 0.2	0.4 ± 0.6	0.1 ± 0.6	0.5 ± 0.2	0.1 ± 0.1
Data-driven multijets events	0.3 ± 0.4	0.0 ± 0.0	0.3 ± 0.4	0.0 ± 0.0	3.8 ± 2.5	3.6 ± 2.5

Table 9.1: Number of events in signal regions. The fit results of background (Fit) consist of the data-driven multijets and simulated backgrounds. The inputs to the fit (MC) consist of multijets and nominal expectations from simulation normalized to theoretical cross sections are also shown. The errors shown are the statistical plus systematic uncertainties.

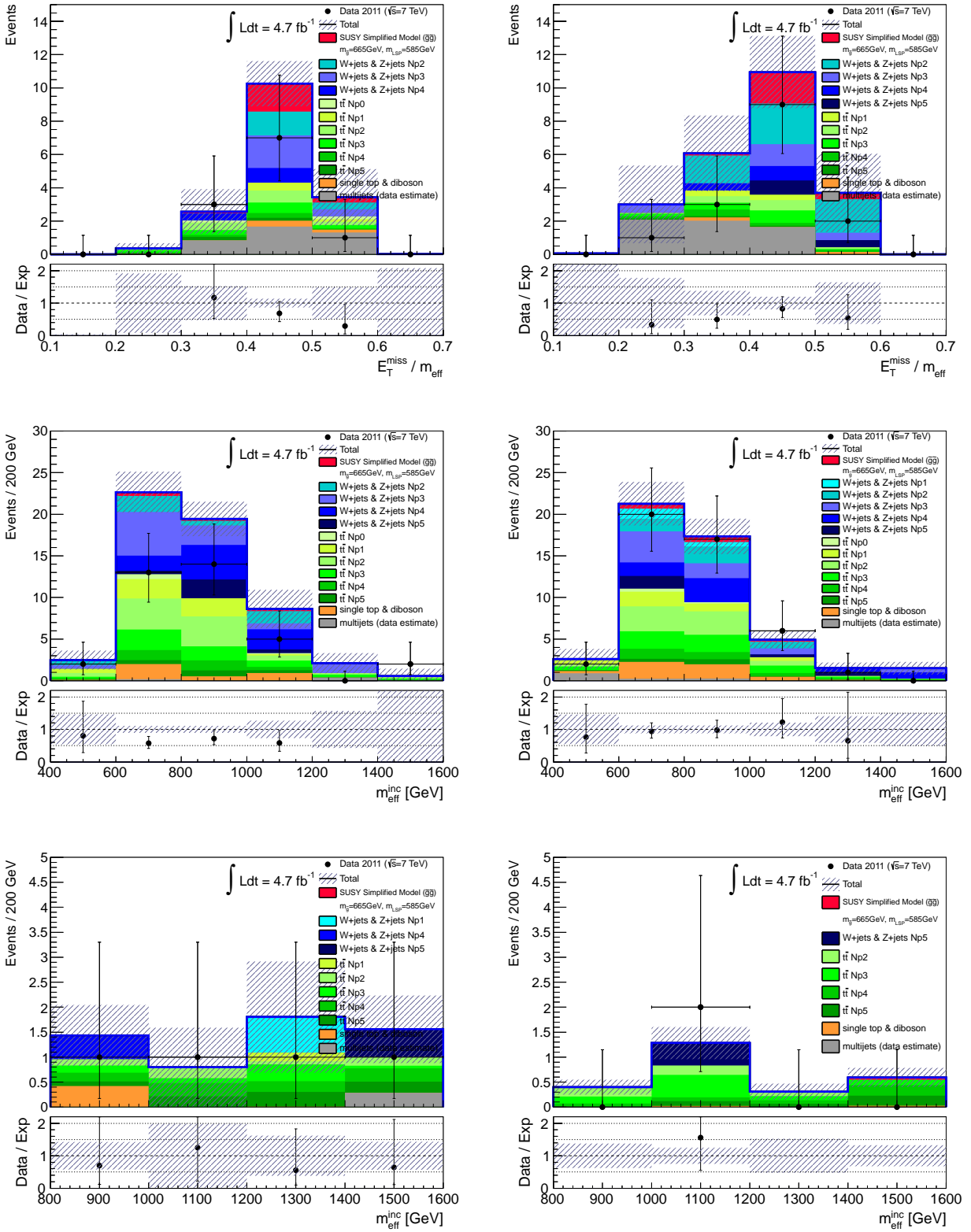


Figure 9.1: Distribution of the $E_T^{\text{miss}}/m_{\text{eff}}$ in soft lepton signal region (top), and m_{eff} in 3-jets hard lepton (middle) and 4-jets hard lepton (bottom) signal region in electron channel (left) and muon channel (right) before shape and normalization corrections. The contribution of simplified SUSY with $m_{\tilde{g}} = 665 \text{ GeV}$ and $m_{\text{LSP}} = 585 \text{ GeV}$ is also shown.

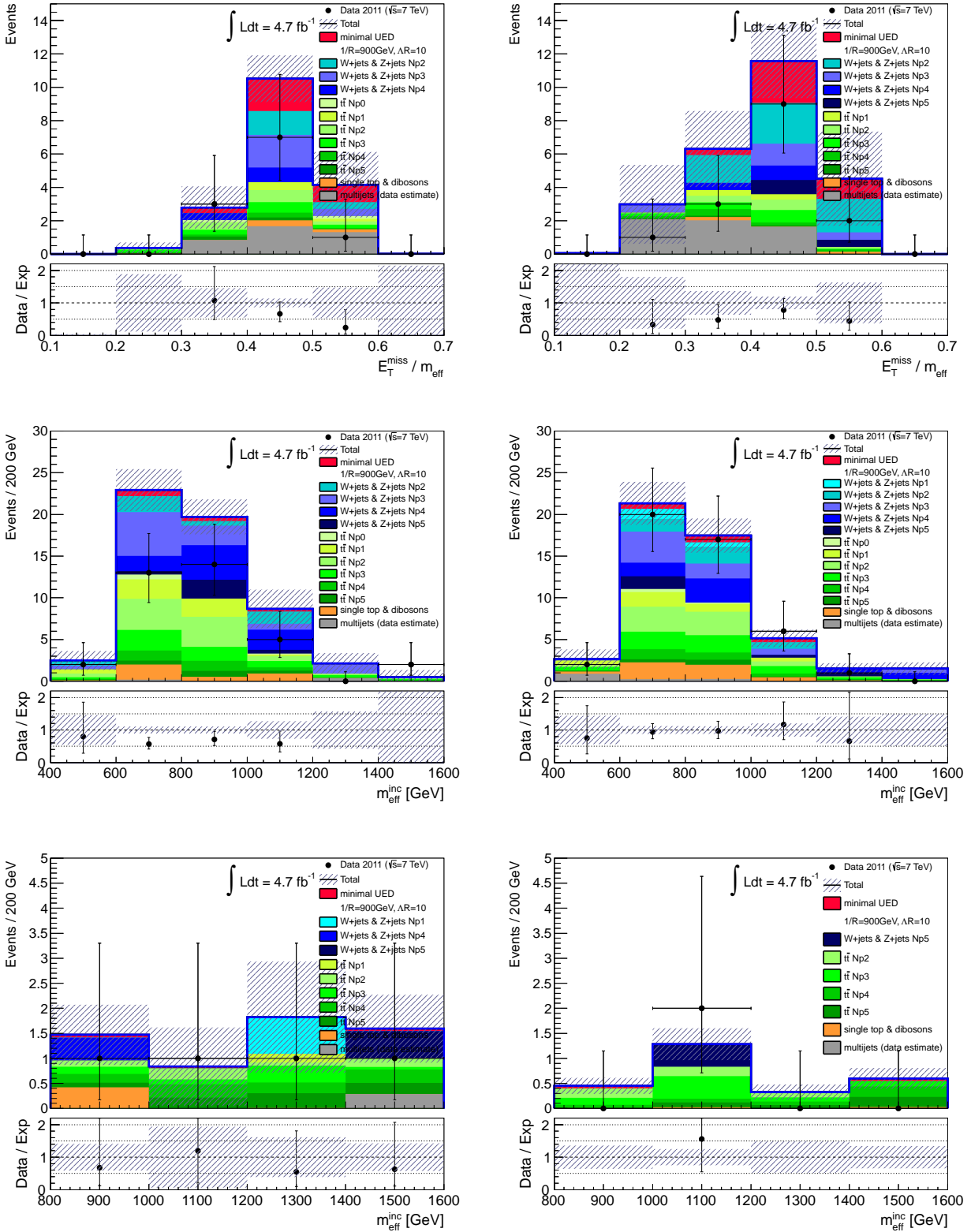


Figure 9.2: Distribution of the $E_T^{\text{miss}}/m_{\text{eff}}$ in soft lepton signal region (top), and m_{eff} in 3-jets hard lepton (middle) and 4-jets hard lepton (bottom) signal region in electron channel (left) and muon channel (right) before shape and normalization corrections. The contribution of UED with $1/R = 900 \text{ GeV}$ and $\Lambda R = 10$ is also shown.

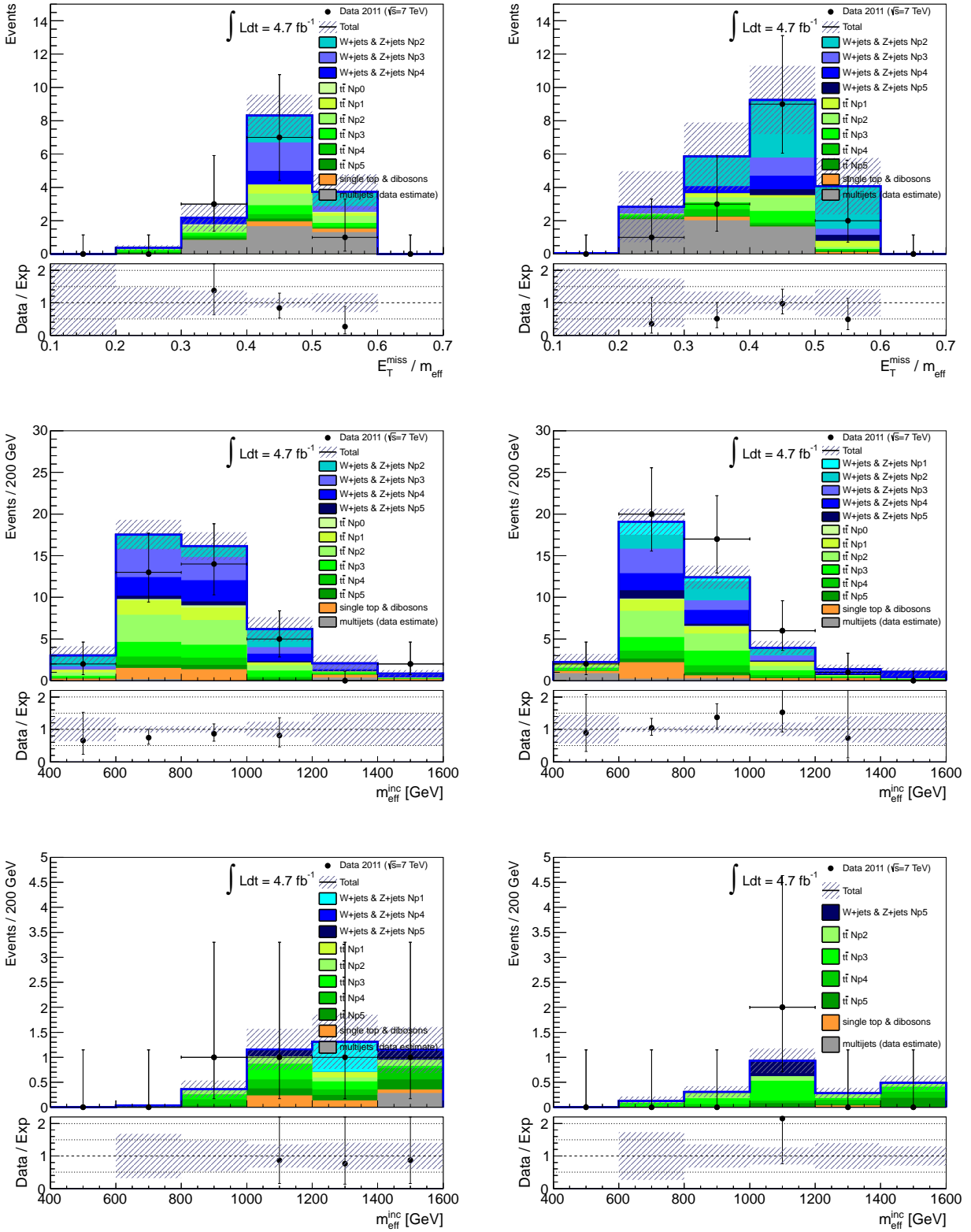


Figure 9.3: Distribution of the $E_T^{\text{miss}}/m_{\text{eff}}$ in soft lepton signal region (top), and m_{eff} in 3-jets hard lepton (middle) and 4-jets hard lepton (bottom) signal region in electron channel (left) and muon channel (right) after the shape and normalization corrections.

Signal region	$\langle\epsilon\sigma\rangle_{\text{obs}}^{95}$ [fb]	S_{obs}^{95}	S_{exp}^{95}	CL _b
hard electron 3-jets	0.96	4.5	$4.2^{+2.2}_{-1.5}$	0.57
hard muon 3-jets	0.94	4.4	$4.4^{+2.2}_{-1.2}$	0.50
hard electron 4-jets	1.22	5.8	$5.3^{+2.6}_{-1.3}$	0.63
hard muon 4-jets	1.30	6.1	$6.2^{+2.4}_{-1.4}$	0.47
soft electron	1.92	9.0	$10.6^{+4.3}_{-2.8}$	0.31
soft muon	2.34	11.0	$12.2^{+4.9}_{-1.2}$	0.21

Table 9.2: 95% CL upper limits on the visible cross-section ($\langle\epsilon\sigma\rangle_{\text{obs}}^{95}$) and on the observed (S_{obs}^{95}) and expected (S_{exp}^{95}) number of signal events for the various signal regions. The last column indicates the CL_b value.

model with μ , a test statistics

$$\lambda(\mu) = \frac{L(\mu, \hat{\theta})}{L(\hat{\mu}, \hat{\theta})}, \quad (9.1.1)$$

is used, where $L(\hat{\mu}, \hat{\theta})$ is the maximized likelihood function by taking $\hat{\theta}$ and $\hat{\mu}$. The quantity $\hat{\theta}$ denotes the nuisance parameter of that maximizes L for the specified μ . The numerator of this ratio is called profile likelihood function, and is a function of μ . Since the signal strength must not have a negative value, the test statistics is then given by

$$\tilde{q}_{\mu} = \begin{cases} -2 \ln \lambda(\mu) & (\hat{\mu} \leq \mu) \\ 0 & (\hat{\mu} > \mu) \end{cases} = \begin{cases} -2 \ln \frac{L(\mu, \hat{\theta}(\mu))}{L(0, \hat{\theta}(0))} & (\hat{\mu} < 0), \\ -2 \ln \frac{L(\mu, \hat{\theta}(\mu))}{L(\hat{\mu}, \hat{\theta}(\hat{\mu}))} & (0 \leq \hat{\mu} \leq \mu), \\ 0 & (\hat{\mu} > \mu). \end{cases} \quad (9.1.2)$$

The p_{b} -value of the background-only hypothesis is calculated by integrating the probability density distribution of the test statistics with null signal in the range from $\tilde{q}_{\mu=0, \text{obs}}$ to infinity:

$$p_{\text{b}} = \int_{\tilde{q}_{\mu=0, \text{obs}}}^{\infty} f(\tilde{q}_{\mu=0} | \mu = 0) d\tilde{q}_{\mu=0}. \quad (9.1.3)$$

Distributions of background-only hypothesis in the signal regions are already shown Figure 9.3. Model independent limit on the visible cross section derived from the observations in the signal regions are also measured. A μ scan in the soft electron signal region is shown Figure 9.4 and it gives the upper limits on both observed and expected 95% CL_s of non-standard-model event in the signal regions. The number of non-standard-model signal events at 95% CL, S_{obs}^{95} , S_{exp}^{95} are derived using the CL_s. The limits are divided by integral luminosity to obtain the limits on visible cross sections $\langle\epsilon\sigma\rangle_{\text{obs}}^{95}$. The CL_b are taken at the same signal strength as the 95% CL_s. The results in each signal region are shown in Table 9.2. These results show the CL_b \sim 20-60%, thus the observed data is consistent with the background-only hypothesis.

9.2 Exclusion Limit

In the absence of a signal, specific models of new physics are included by comparing signal-plus-background hypothesis with the observed data. The p-value of the signal-plus-background hypothesis is calculated as follows:

$$p_{\text{s+b}} = \int_{\tilde{q}_{\mu=1, \text{obs}}}^{\infty} f(\tilde{q}_{\mu=1} | \mu = 1) d\tilde{q}_{\mu=1}. \quad (9.2.1)$$

The confidence level of exclusion CL_s is given by using the $p_{\text{s+b}}$ as $\text{CL}_{\text{s+b}} = 1 - p_{\text{s+b}}$ and $\text{CL}_{\text{s}} = \text{CL}_{\text{s+b}} / (1 - \text{CL}_{\text{b}})$. The CL_s is given by scanning the signal strength μ of specific signal model. Figure 9.5 shows the scan result

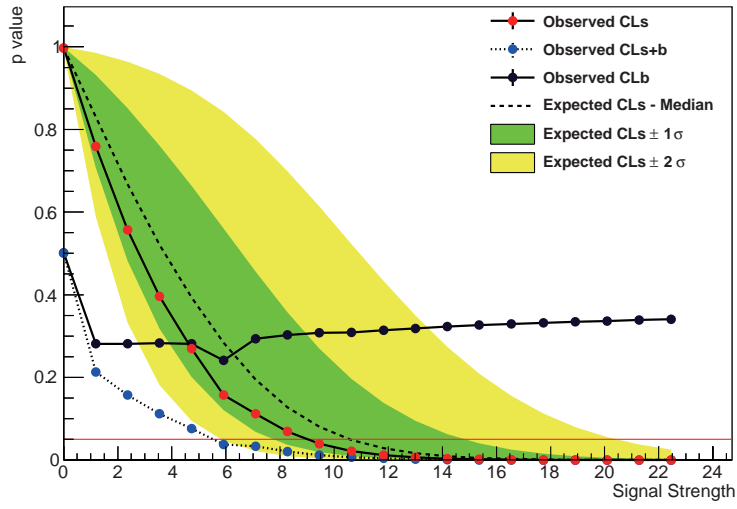


Figure 9.4: Scan results for signal strength μ with CL_s , CL_{s+b} and CL_b for observed and expected with non-standard-model signal in soft electron signal region.

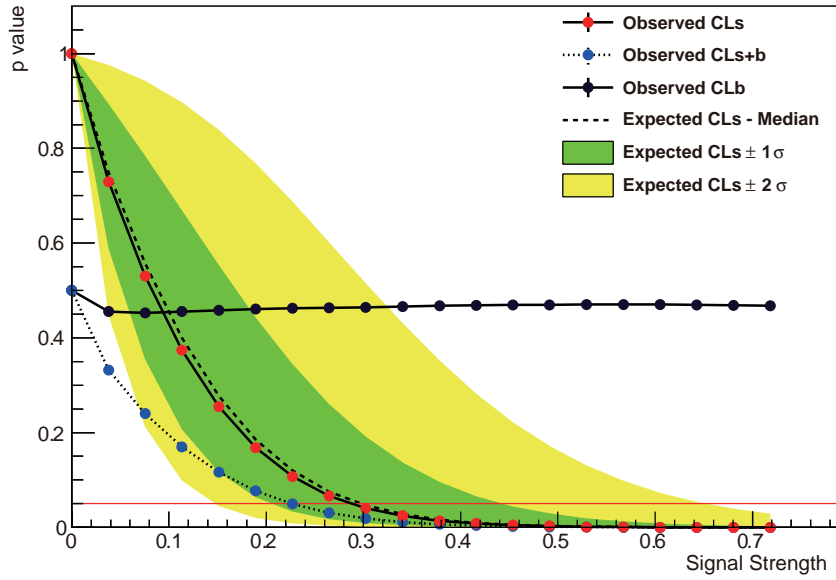


Figure 9.5: Scan results for signal strength μ with CL_s , CL_{s+b} and CL_b for observed and expected with UED model at $1/R = 700$ GeV and $\Delta R = 10$

for UED model at $1/R = 700$ GeV and $\Lambda R = 10$. Both normalizations of dominant background and signal strength μ are re-fitted in both control regions and signal regions simultaneously corresponding to the scanning signal strength. When the signal strength μ at 95% CL_s is less than 1.0, we conclude that the signal model is excluded.

In the calculation of the upper limit on the cross-section for a given signal model, the total theoretical uncertainty of the signal model described in Section 8.3 is treated as increasing and decreasing the signal cross sections upward and downward $\pm 1\sigma$, respectively. The results are treated as the $\pm 1\sigma_{\text{theory}}$ observed limits. In following sections, the exclusion limits at 95% CL_s for simplified SUSY model (\tilde{g} - \tilde{g} pair production) and UED model are shown.

Simplified SUSY model (\tilde{g} - \tilde{g} Pair Production)

The results of searching for degenerate SUSY model with simplified SUSY model are shown in Figure 9.6. The three figures show the exclusion limits at 95% CL_s for the soft lepton channel, the hard lepton channel and combination of soft lepton and hard lepton channel.

In the diagonal region along the dashed line where the mass spectrums are degenerated, $m_{\tilde{g}}$ space below ~ 300 GeV in degenerate mass region were already excluded in 2011 summer results (Figure 2.1). The below figures indicate that $m_{\tilde{g}} \sim 540$ GeV and $m_{LSP} \sim 450$ GeV in degenerated mass region and $m_{\tilde{g}} \sim 970$ GeV and $m_{LSP} \sim 100$ GeV in large mass difference region are excluded at 95% CL_s .

In mass degenerated region as $(m_{\tilde{g}} - m_{LSP})/m_{\tilde{g}} \sim 10\%$, the exclusion limit of the soft lepton channel ($m_{\tilde{g}} \sim 460$ GeV) advances compared to that of hard lepton channel $m_{\tilde{g}} \sim 400$ GeV. The combined result excludes a point at $m_{\tilde{g}} \sim 540$ GeV and $m_{LSP} \sim 450$ GeV for simplified SUSY model. About 250 GeV in $m_{\tilde{g}}$ space is improved in the degenerate region from the 2011 summer results.

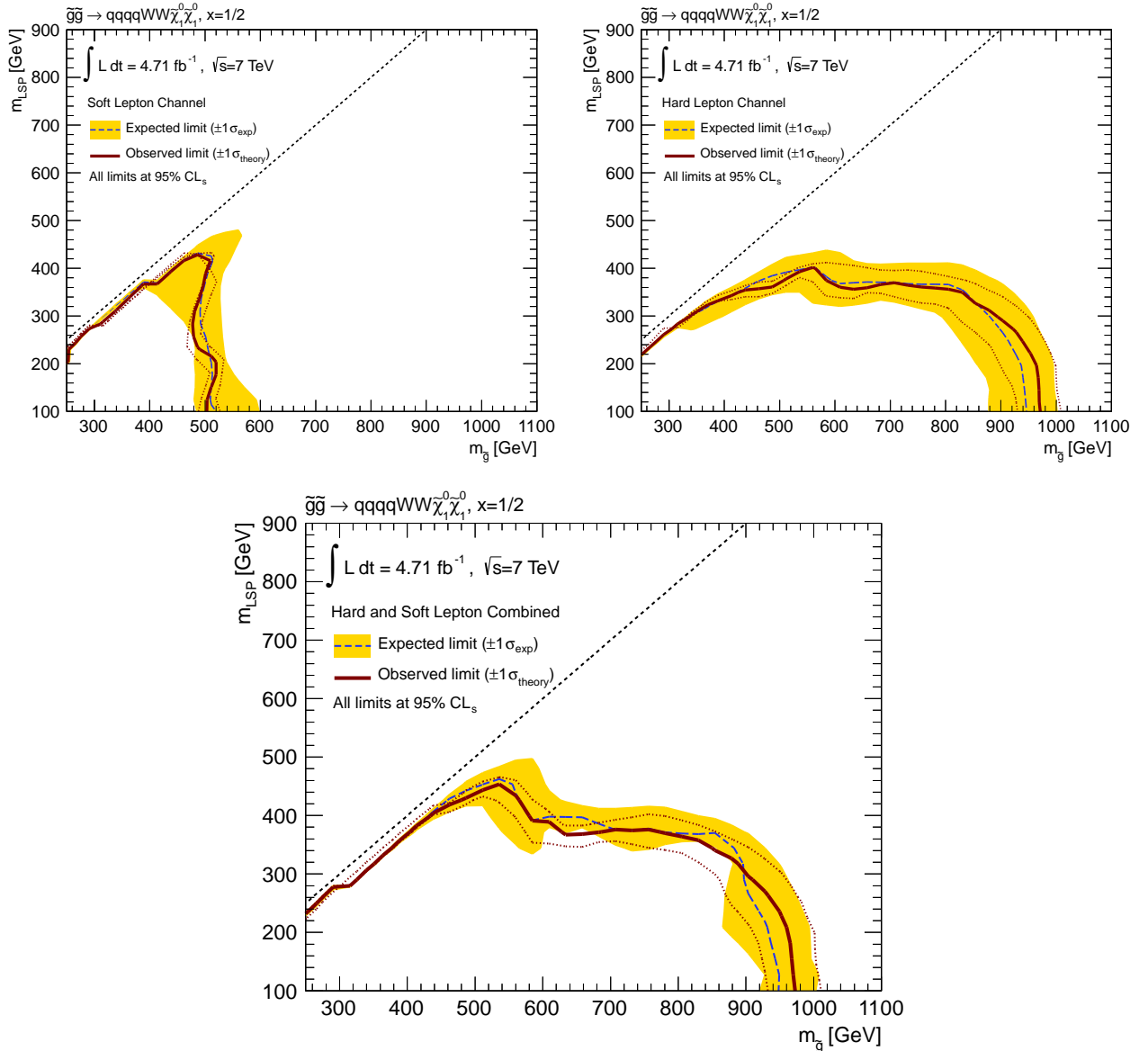


Figure 9.6: Exclusion regions at 95% CL_s upper limits in simplified SUSY model in gluino pair production with $X = (m_{\tilde{\chi}_1^\pm} - m_{\tilde{\chi}_1^0})/(m_{\tilde{g}} - m_{\tilde{\chi}_1^0}) = 1/2$ samples for the soft lepton channel (top-left), hard lepton channel (top-right) and combined results (bottom), respectively.

Universal Extra Dimensions

The exclusion limits of UED model for the soft lepton channel, the hard lepton channel and the combination of both channels are shown in Figure 9.7 on $1/R$ - ΛR plane.

For UED model, the degree of mass degenerate ($m_{\text{KKgluon}} - m_{\text{KKphoton}}$)/ m_{KKgluon} are less than 25% in the considered ΛR region ($\Lambda R = 2$ -40). Within the degree, the soft lepton channel contributes to the exclusion limits greatly. The exclusion limits at 95% CL reaches $1/R \sim 840$ GeV at $\Lambda R = 5$ in the soft lepton channel, although the exclusion limit of hard lepton channel reaches $1/R \sim 630$ GeV at $\Lambda R = 5$. At large ΛR region ($\Lambda R \sim 40$) corresponding to the large degree of mass degenerate, the hard lepton channel gets sensitivity to the model however it is more sensitive for soft lepton channel than that of hard lepton channel in this region.

The combination result excludes the $1/R$ space above 800 GeV, especially the space of $1/R \sim 840$ GeV at $\Lambda R = 5$ is excluded. The upper limit in a space of $1/R = 830$ GeV at $\Lambda R = 20$ is more impressive result than Tevatron results which had excluded the model in $1/R$ parameter space below 280 GeV. This analysis improves the upper limit greatly.

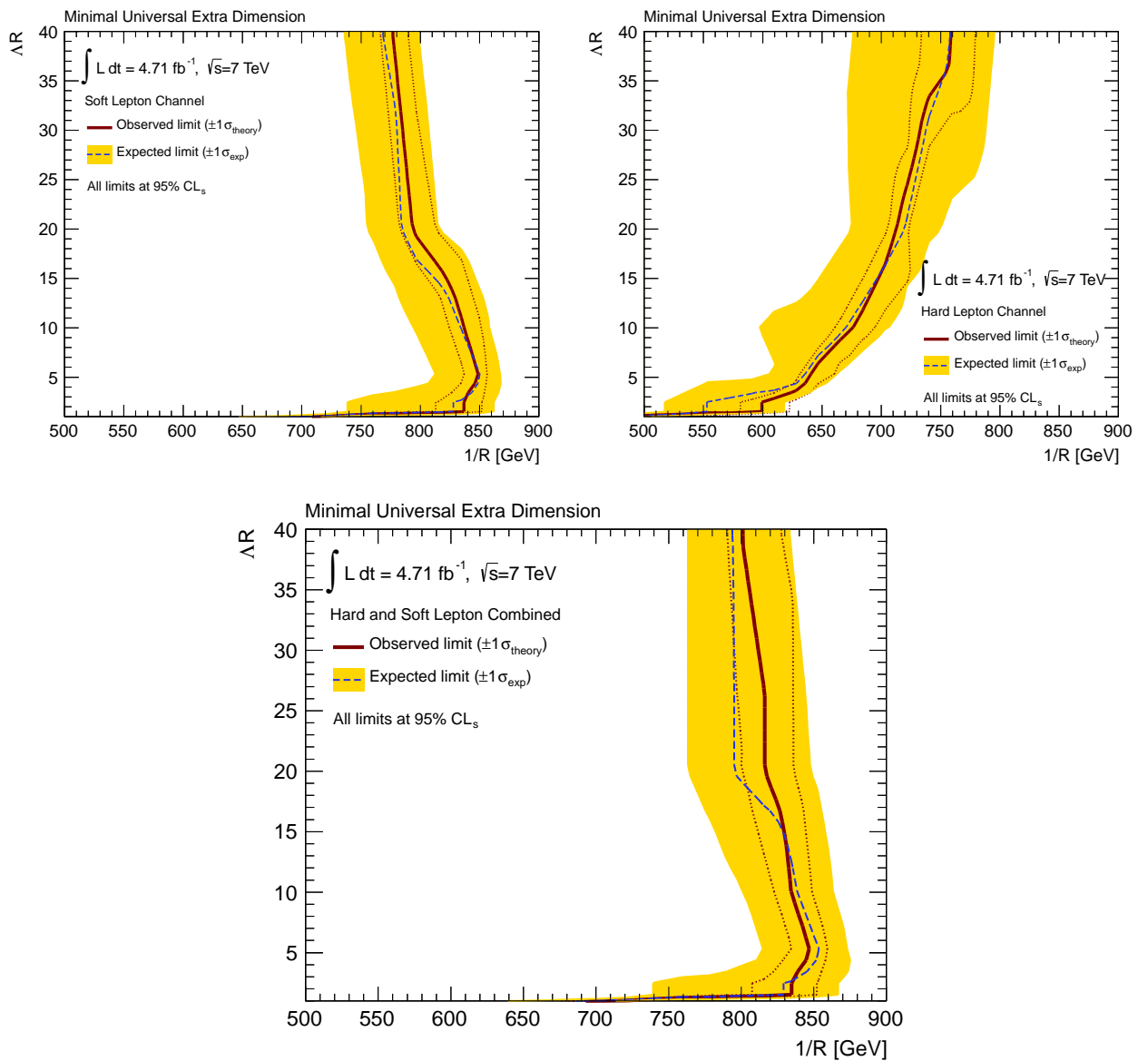


Figure 9.7: Exclusion regions at 95% CL_s upper limits in UED model for soft lepton channel (top-left), hard lepton channel (top-right) and combined results (bottom), respectively.

9.3 Summary and Prospects

In both the soft lepton and hard lepton signal regions, the expected background with the Standard Model is consistent with the observed data. The signal excesses are not observed with integrate luminosity of 4.7 fb^{-1} . The test of background-only hypothesis gives the 95% upper limits on the invisible cross sections, number of signal events and CL_b in each signal region.

For the test of background-plus-signal hypothesis, exclusion upper limits at 95% CL_s are estimated for the simplified SUSY and the UED models. The results of hard lepton channel, soft lepton channel and combination of these channel are summarized in Figure 9.8. The observed upper limits of these results are overlaid in the figures. The results show that only soft lepton channel is sensitive to the new physics in small degree space of degenerate $(m_{\tilde{g}} - m_{\text{LSP}})/m_{\tilde{g}}$ or $(m_{\text{KKgluon}} - m_{\text{KKphoton}})/m_{\text{KKgluon}} \lesssim 15\%$. Approximately from 15% to 25% of the degree, the soft lepton channel is more sensitive to such models than the hard lepton channel. For UED model, the result of soft lepton channel is significantly more better than that of hard lepton channel in all ΔR space since the degree of degenerate whose values are from $\sim 5\%$ ($\Delta R = 2$) to $\sim 25\%$ ($\Delta R = 40$) is smaller than the general SUSY models.

In 2012 run, LHC operates at center-of-mass energy of 8 TeV and integral luminosity is expected to reach to 20 fb^{-1} . Cross sections of SUSY and UED model in 8 TeV are calculated to be approximately twice larger than that of 7 TeV. The increasing cross section and integral luminosity improve about five times significance of the models than the 2011 data. Predicted upper limits in 2012 for simplified SUSY model and UED model reach $m_{\tilde{g}} \sim 700 \text{ GeV}$ in degenerated region and $1/R \sim 950 \text{ GeV}$, respectively. It is possible to discover the degenerate SUSY model or UED model in more higher mass region.

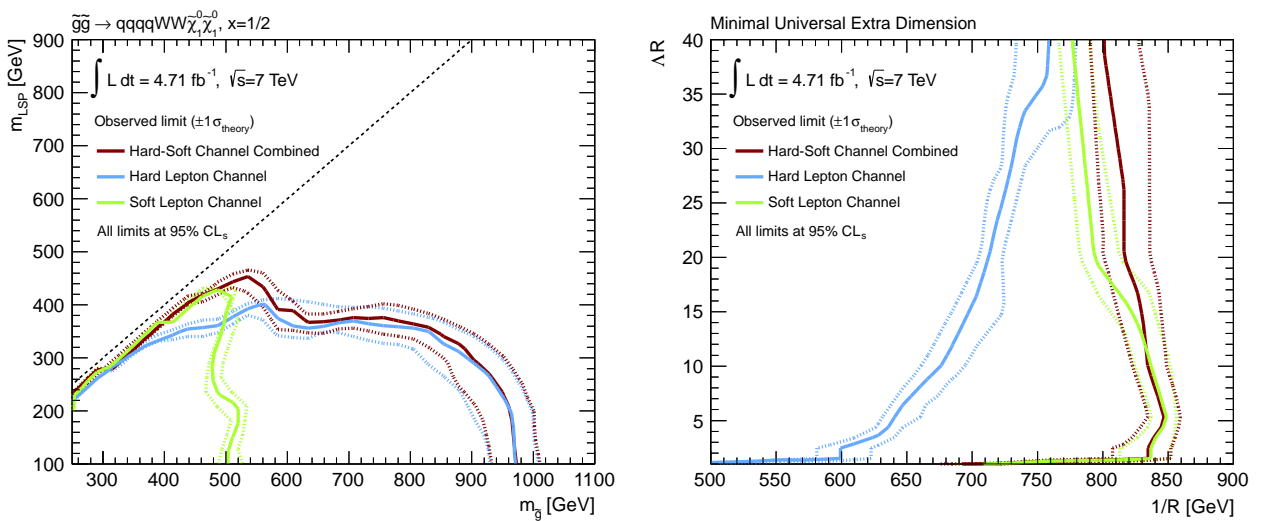


Figure 9.8: Exclusion regions for simplified $\tilde{g}\text{-}\tilde{g}$ production SUSY model and UED in the hard lepton channel (blue), the soft lepton (green) channel and the combined results (red).

Chapter 10

Conclusion

This analysis searches for physics beyond the Standard Model with degenerate mass spectrum in final states containing one isolated lepton, jets and E_T^{miss} . The interesting models are supersymmetry (SUSY) and universal extra dimensions (UED) where mass difference between the heaviest and lightest particles in the model are approximately less than 30%. In addition, a high p_T lepton channel for MSUGRA search is also employed for the analysis to increase the sensitivity to the degenerate models. The collected data in 2011 corresponding to an integrated luminosity of 4.7 fb^{-1} and center-of-mass energy of 7 TeV are used for the analysis.

The signal region is optimized for the best significance with integrated luminosity with 5.0 fb^{-1} . The selection criteria of signal region for the degenerate model are determined by using low p_T one lepton and at least two jets coming from cascade decay, and large E_T^{miss} originating from neutralino $\tilde{\chi}_1^0$ or KK-photon, and high p_T leading jet due to initial state radiation. The signal region is expected to have approximately twice sensitivity of MSUGRA search in region where the mass spectrum is degenerated.

The background estimations are performed by fitting to observed data in control regions. The W +jets, Z +jets and $t\bar{t}$ events as dominant background are estimated by using simulated samples. These events are fitted the simulated events to observed data in p_T^Z space for shape correction and in control regions where such events are enriched for normalization correction.

The multijets events are estimated by data-driven method which decomposes the leptons satisfying signal selection criteria into real leptons and misidentified leptons by using efficiencies of real leptons and misidentified leptons. In the efficiency measurements, dileptons events are employed to avoid a trigger bias and some selections are applied to the events to enhance the real or misidentified lepton events. The multijets events are measured by applying the efficiencies to the number of observed leptons satisfying and failing the signal selection criteria.

The results show that the observed data are in agreement with the Standard Model expectations and there are no evidences of the beyond standard models. The \tilde{g} - \tilde{g} pair production of simplified SUSY model is excluded in degenerate mass region where the $m_{\tilde{g}}$ and m_{LSP} are below approximately 540 GeV and 450 GeV at 95% CL. In addition, UED model is excluded below 840 GeV in $1/R$ space at $\Delta R = 5$ at 95% CL. For these models, the result of soft lepton channel contributes greatly compared to that of hard lepton channel which targets MSUGRA model.

Acknowledgements

I would like to express my deepest appreciation to Prof. Shoji Asai for giving me many idea and knowledge about the experiments. He supports my research life.

Prof. Naoko Kanaya, Prof. Koji Terashi and Prof. Shimpei Yamamoto, they teach me very kindly and professionally. I'm the most grateful to them.

Staff members of International Center for Elementary Particle Physics (ICEPP) in the university of Tokyo and ATLAS-JAPAN, Prof. Tatsuo Kawamoto, Prof. Junichi Tanaka, Prof. Osamu Jinnouchi, Prof. Yousuke Kataoka, Prof. Susumu Oda, Dr. Taiki Yamamura, Dr. Tatsuya Masubuchi, Dr. Koji Nakamura and Dr. Takashi Yamanaka, they support and advise me on the analysis.

Member of SUSY in strong production in one and more leptons channel, Prof. Moritz Backes, Prof. David Côté, Prof. Mark Hohlfeld, Prof. Max Baak, Prof. Aleksej Koutsman, Prof. George Redlinger, Prof. Marie-Helene Genest, Dr. Xin Chen, Dr. Meyer Carsten, Dr. Matthias Lungwitz, Ms. Jeanette Miriam Lorentz, Prof. Renaud Brunelière, Dr. Otilia Anamaria Docu, Dr. Julian Maurer, they help and teach me greatly. I would like to express my gratitude to them.

In tile calorimeter group, Prof. Claudio Santoni and Dr. Zhili Weng teach me how to estimate performance of tile calorimeter. I am very grateful to them.

I deeply appreciate for staffs and students in ICEPP, Prof. Tomio Kobayashi, Prof. Hiroshi Sakamoto, Prof. Tetsuro Mashimo, Prof. Yoshizumi Inoue, Prof. Toshio Nanba, Prof. Tomoaki Nakamura, Prof. Kenji Mishima, Prof. Tomohiko Tanabe, Prof. Akira Ishida, Dr. Taikan Suehara, Dr. Hidetoshi Otono, Dr. Takayuki Yamazaki, Mr. Nagataka Matsui, and Mr. Hideyuki Oide, Mr. Ryo Katayama, and graduated students Mr. Junichi Okamura and Mr. Yoshihumi Takeichi.

I would like to thank students of ICEPP as Mr. Ginga Akimoto, Mr. Yuya Azuma, Mr. Kohei Kessoku, Mr. Yoichi Ninomiya, Mr. Yuichi Sasaki, Mr. Shingo Kazama, Mr. Keisuke Yoshihara, Mr. Yohei Yamaguchi and Mr. Akira Miyazaki, and members of ATLAS-JAPAN as Dr. Yasuyuki Okumura, Dr. Yuta Takahashi, Dr. Takashi Hayakawa, Mr. Takeshi Domae, Mr. Minoru Hirose, Mr. Yu Suzuki, Mr. Takayuki Kanno, Mr. Satoshi Hasegawa, Mr. Tatsuma Meguro, Mr. Matt King, Mr. Ljiljana Morvaj, Mr. Toyonobu Okuyama, Mr. Wataru Okamura, Ms. Katarina Bendtz, Mr. Takuya Nobe, Mr. Ryo Nagai, Mr. Jun Wakabayashi.

I am thankful to Dr. Takashi Kubota, Dr. Keigo Imai, Ms. Konomi Sakamoto Ms. Asuka Suzuki, Mr. Tsuyoshi Maeda, Mr. Yusuke Okuno and Mr. Kouzou Mizunuma they supported and encouraged me when I enrolled in the graduated school.

My deepest appreciation goes to secretaries in department of physics and ICEPP, Ms. Kuniko Kono, Ms. Masako Shiota, Ms. Yoko Takemoto, Ms. Akiko Miyazono, Ms. Yoshie Teduka, Ms. Megumi Suzuki, Ms. Cheiko Morita, Ms. Naoko Kataoka and Ms. Ritsuko Anbiru.

I would like to thank Ms. Geraldine Donaldson, Ms. Esther Lutz Donaldson and Mr. John Donaldson who teach English and take care of me.

Finally, I thank my family, Yukio Yamaguchi, Miyoko Yamaguchi, Tatsuya Yamaguchi, Yuka Yamaguchi, Yoshiki Yamaguchi and Keiko Yamaguchi.

Appendix A

MSUGRA and UED Mass Spectrum

A.1 MSUGRA

A.1.1 Gauginos Mass

The gaugino masses m_i and coefficients b_i are given by the one-loop renormalization group equations in MSSM from the Equation 1.3.2,

$$\beta_{m_i} = \frac{d}{dt} m_i = \frac{1}{8\pi^2} b_i g_i^2 m_i \quad (i = 1, 2, 3) \quad (\text{A.1.1})$$

where m_1 , m_2 and m_3 are the mass of bino, wino and gluino, respectively. It implies the three ratios m_i/g_i^2 are constant,

$$\frac{m_1}{g_1^2} = \frac{m_2}{g_2^2} = \frac{m_3}{g_3^2} = \frac{m_{1/2}}{g_G^2}. \quad (\text{A.1.2})$$

Then

$$m_3 = \frac{\alpha_3}{\alpha} m_2 \sin^2 \theta_W = \frac{3}{5} \frac{\alpha_3}{\alpha} m_1 \cos^2 \theta_W, \quad (\text{A.1.3})$$

where θ_W is Weinberg angle. This implies the relation between the gauginos near the TeV scale roughly

$$m_1 : m_2 : m_3 \sim 1 : 2 : 6. \quad (\text{A.1.4})$$

A.1.2 Neutralinos Mass

The neutralino mass part of the Lagrangian is described by using gauge-eigenstate wave function $\phi^0 = (\tilde{B}, \tilde{W}^0, \tilde{H}_d^0, \tilde{H}_u^0)$ as following

$$\mathcal{L}_{\text{neutralino-mass}} = -\frac{1}{2} (\phi^0)^T \mathbf{M}_{\tilde{\chi}^0} \phi^0 + c.c., \quad (\text{A.1.5})$$

where

$$\mathbf{M}_{\tilde{\chi}^0} = \begin{pmatrix} M_1 & 0 & -\cos \beta \sin \theta_W m_Z & \sin \beta \sin \theta_W m_Z \\ 0 & M_2 & \cos \beta \cos \theta_W m_Z & -\sin \beta \cos \theta_W m_Z \\ -\cos \beta \sin \theta_W m_Z & \cos \beta \cos \theta_W m_Z & 0 & -\mu \\ \sin \beta \sin \theta_W m_Z & -\sin \beta \cos \theta_W m_Z & -\mu & 0 \end{pmatrix}. \quad (\text{A.1.6})$$

This mass matrix $\mathbf{M}_{\tilde{\chi}^0}$ can be diagonalized by a unitary matrix \mathbf{N} to obtain the mass eigenstates

$$\tilde{\chi}^0_i = \mathbf{N}_{ij} \psi_j^0, \quad (\text{A.1.7})$$

so that

$$\mathbf{N}^* \mathbf{M} \mathbf{N}^{-1} = \begin{pmatrix} m_{\tilde{\chi}_1^0} & 0 & 0 & 0 \\ 0 & m_{\tilde{\chi}_2^0} & 0 & 0 \\ 0 & 0 & m_{\tilde{\chi}_3^0} & 0 \\ 0 & 0 & 0 & m_{\tilde{\chi}_4^0} \end{pmatrix}. \quad (\text{A.1.8})$$

If $m_Z \ll |\mu \pm M_1|, |\mu \pm M_2|$, then the neutralino mass eigenstates are nearly bino-like $\tilde{\chi}_1^0 \sim \tilde{B}$, wino-like $\tilde{\chi}_2^0 \sim \tilde{W}$ and higgsino-like $\tilde{\chi}_3^0, \tilde{\chi}_4^0 \sim (\tilde{H}_u^0 \pm \tilde{H}_d^0)/\sqrt{2}$, with the mass eigenvalues,

$$m_{\tilde{\chi}_1^0} = m_1 - \frac{m_Z^2 \sin \theta_W (m_1 + \mu \sin 2\beta)}{\mu^2 - m_1^2} + \dots, \quad (\text{A.1.9})$$

$$m_{\tilde{\chi}_2^0} = m_2 - \frac{m_W^2 (m_2 + \mu \sin 2\beta)}{\mu^2 - m_2^2} + \dots, \quad (\text{A.1.10})$$

$$m_{\tilde{\chi}_3^0}, m_{\tilde{\chi}_4^0} = |\mu| - \frac{m_Z^2 (I - \sin 2\beta) (\mu + m_1 \cos^2 \theta_W + m_2 \sin^2 \theta_W)}{2(\mu + m_1)(\mu + m_2)} + \dots, \quad (\text{A.1.11})$$

$$= |\mu| - \frac{m_Z^2 (I + \sin 2\beta) (\mu - m_1 \cos^2 \theta_W - m_2 \sin^2 \theta_W)}{2(\mu - m_1)(\mu - m_2)} + \dots. \quad (\text{A.1.12})$$

The m_1 and m_2 are set to positive and real, and μ is assumed to be real number with sign $I = \pm 1$.

A.1.3 Charginos Mass

The chargino mass spectrum is estimated on the analogue to neutralino. The gauge-eigenstate wave function $\phi^\pm = (\tilde{W}^+, \tilde{H}_u^+, \tilde{W}^-, \tilde{H}_d^-)$, the chargino mass terms in the Lagrangian are

$$\mathcal{L}_{\text{chargino-mass}} = -\frac{1}{2} (\phi^\pm)^T M_{\tilde{\chi}^\pm} \phi^\pm + c.c., \quad (\text{A.1.13})$$

where 2×2 block form,

$$M_{\tilde{\chi}^\pm} = \begin{pmatrix} 0 & \mathbf{X}^T \\ \mathbf{X} & 0 \end{pmatrix}, \quad \text{with } \mathbf{X} = \begin{pmatrix} m_2 & gv_u \\ gv_d & \mu \end{pmatrix} = \begin{pmatrix} m_2 & \sqrt{2} \sin \beta m_W \\ \sqrt{2} \cos \beta m_W & \mu \end{pmatrix}. \quad (\text{A.1.14})$$

The 2×2 matrices \mathbf{U} and \mathbf{V} relate to the mass eigenstates are introduced

$$\begin{pmatrix} \tilde{\chi}_1^\pm \\ \tilde{\chi}_2^\pm \end{pmatrix} = \mathbf{V} \begin{pmatrix} \tilde{W}^\pm \\ \tilde{H}_u^\pm \end{pmatrix}, \quad \begin{pmatrix} \tilde{\chi}_1^\mp \\ \tilde{\chi}_2^\mp \end{pmatrix} = \mathbf{U} \begin{pmatrix} \tilde{W}^\mp \\ \tilde{H}_d^\mp \end{pmatrix}. \quad (\text{A.1.15})$$

There are the eigenvalues of the 4×4 matrix $M_{\tilde{\chi}^\pm}^\dagger M_{\tilde{\chi}^\pm}$, or equivalently the eigenvalues of $\mathbf{X}^\dagger \mathbf{X}$

$$\mathbf{V} \mathbf{X}^\dagger \mathbf{X} \mathbf{V}^{-1} = \mathbf{U}^* \mathbf{X} \mathbf{X}^\dagger \mathbf{U}^T = \begin{pmatrix} m_{\tilde{\chi}_1^\pm}^2 & 0 \\ 0 & m_{\tilde{\chi}_2^\pm}^2 \end{pmatrix}. \quad (\text{A.1.16})$$

The solutions of this matrix is

$$m_{\tilde{\chi}_1^\pm} = m_2 - \frac{m_Z^2 (m_2 + \mu \sin 2\beta)}{\mu^2 - m_2^2} + \dots \quad (\text{A.1.17})$$

$$m_{\tilde{\chi}_2^\pm} = |\mu| + \frac{m_Z^2 I (m_2 + \mu \sin 2\beta)}{\mu^2 - m_2^2} + \dots \quad (\text{A.1.18})$$

A.1.4 Squark and Slepton Mass

The same type squarks and sleptons have the same quantum state, electric charge and color, thus the scalar particles are mixed in the family. Then squarks and sleptons are separated into four groups, the up-type squarks ($\tilde{u}_L, \tilde{c}_L, \tilde{t}_L, \tilde{u}_R, \tilde{c}_R, \tilde{t}_R$), down-type squarks ($\tilde{d}_L, \tilde{s}_L, \tilde{b}_L, \tilde{d}_R, \tilde{s}_R, \tilde{b}_R$), charged sleptons ($\tilde{e}_L, \tilde{\mu}_L, \tilde{\tau}_L, \tilde{e}_R, \tilde{\mu}_R, \tilde{\tau}_R$) and sneutrino ($\tilde{\nu}_e, \tilde{\nu}_\mu, \tilde{\nu}_\tau$).

The squarks and sleptons mass are determined by taking the contributions K_1, K_2, K_3 from each renormalization group running coupling proportional to the gaugino masses. The squared masses of scalar particles can

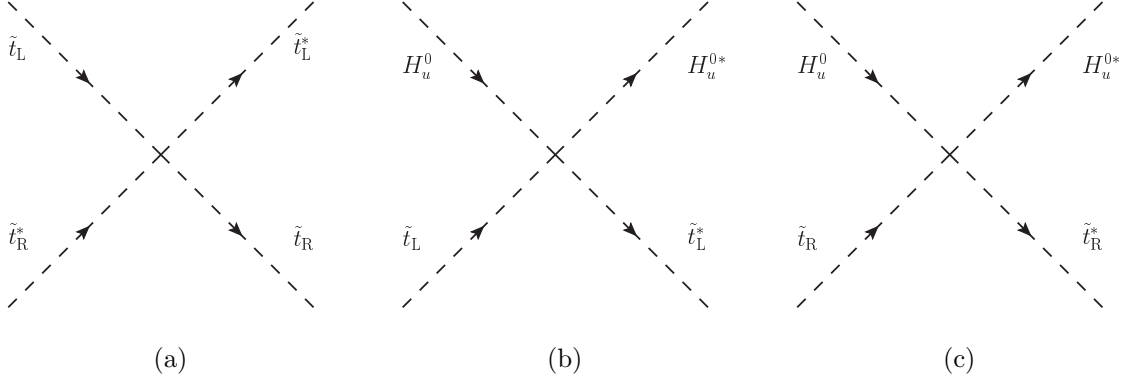


Figure A.1: Some of the scalar interactions with strength proportional to y_t^2 .

be approximated as following,

$$m_Q^2 = m_0^2 + K_3 + K_2 + \frac{1}{36}K_1, \quad (\text{A.1.19})$$

$$m_u^2 = m_0^2 + K_3 + \frac{4}{9}K_1, \quad (\text{A.1.20})$$

$$m_d^2 = m_0^2 + K_3 + \frac{1}{9}K_1, \quad (\text{A.1.21})$$

$$m_L^2 = m_0^2 + K_2 + \frac{1}{4}K_1, \quad (\text{A.1.22})$$

$$m_{\tilde{t}}^2 = m_0^2 + K_1. \quad (\text{A.1.23})$$

The K_i are estimated by integrating the running coupling from the grand unification scale Q_G to the squark or slepton mass under consideration Q , around TeV scale,

$$\begin{pmatrix} K_1 \\ K_2 \\ K_3 \end{pmatrix} = \begin{pmatrix} 3/5 \\ 3/4 \\ 4/3 \end{pmatrix} \times \frac{1}{2\pi^2} \int_{\log Q}^{\log(Q_G)} dt g_i^2(t) |m_i(t)|^2 \sim \begin{pmatrix} 0.35m_{1/2}^2 \\ 0.5m_{1/2}^2 \\ (4.5 - 6.5)m_{1/2}^2 \end{pmatrix}. \quad (i = 1, 2, 3) \quad (\text{A.1.24})$$

Besides the renormalization group effects, the electroweak symmetry breaking contributes to the squarks and sleptons hyperfine mass splitting. Each squark and slepton ϕ are given as the contribution Δ_ϕ ,

$$\Delta_\phi = \frac{1}{2} (T_{3\phi}g_1^2 - Y_\phi g_2^2) (v_d^2 - v_u^2) = (T_{3\phi} - Q_\phi \sin^2 \theta_W) m_Z^2 \cos 2\beta, \quad (\text{A.1.25})$$

where $T_{3\phi}$, Y_ϕ and Q_ϕ are the third component of weak isospin, the weak hypercharge and the electric charge of the left-handed chiral supermultiplet to which ϕ belongs, respectively.

For the squarks and sleptons in the third generation, these particles are affected from the Yukawa coupling of the scalar particles. Figure A.1 indicates the $m_{\tilde{t}}$ terms are contributed from Figure A.1 (b) and (c) as $y_t^2 \tilde{H}_u^{0*} \tilde{H}_u^0 \tilde{t}_L^* \tilde{t}_L$ and $y_t^2 \tilde{H}_u^{0*} \tilde{H}_u^0 \tilde{t}_R^* \tilde{t}_R$. The scalar potential like Figure A.1 (a) contributes the stop mass as $-\mu^* y_t \tilde{t} \tilde{t} \tilde{H}_d^{0*}$. These terms are expressed as the squark mass matrix for the stop squarks in the gauge-eigenstate basis $(\tilde{t}_L, \tilde{t}_R)$ which is given by

$$\mathcal{L}_{\text{stop-mass}} = -(\tilde{t}_L^*, \tilde{t}_R^*) \mathbf{m}_{\tilde{t}}^2 \begin{pmatrix} \tilde{t}_L \\ \tilde{t}_R \end{pmatrix}, \quad (\text{A.1.26})$$

where

$$\mathbf{m}_{\tilde{t}}^2 = \begin{pmatrix} m_Q^2 + m_{\tilde{t}}^2 + \Delta_{\tilde{u}_L} & v(a_t^* \sin \beta - \mu y_t \cos \beta) \\ v(a_t \sin \beta - \mu^* y_t \cos \beta) & m_q^2 + m_{\tilde{t}}^2 + \Delta_{\tilde{u}_R} \end{pmatrix}, \quad (\text{A.1.27})$$

and the a_t is a running coupling strength of top quark. This matrix is diagonalized by taking a unitary matrix to give mass-eigenstates

$$\begin{pmatrix} \tilde{t}_1 \\ \tilde{t}_2 \end{pmatrix} = \begin{pmatrix} \cos \theta_{\tilde{t}} & \sin^* \theta_{\tilde{t}} \\ \sin \theta_{\tilde{t}} & \cos \theta_{\tilde{t}} \end{pmatrix} \begin{pmatrix} \tilde{t}_L \\ \tilde{t}_R \end{pmatrix} \quad (\text{A.1.28})$$

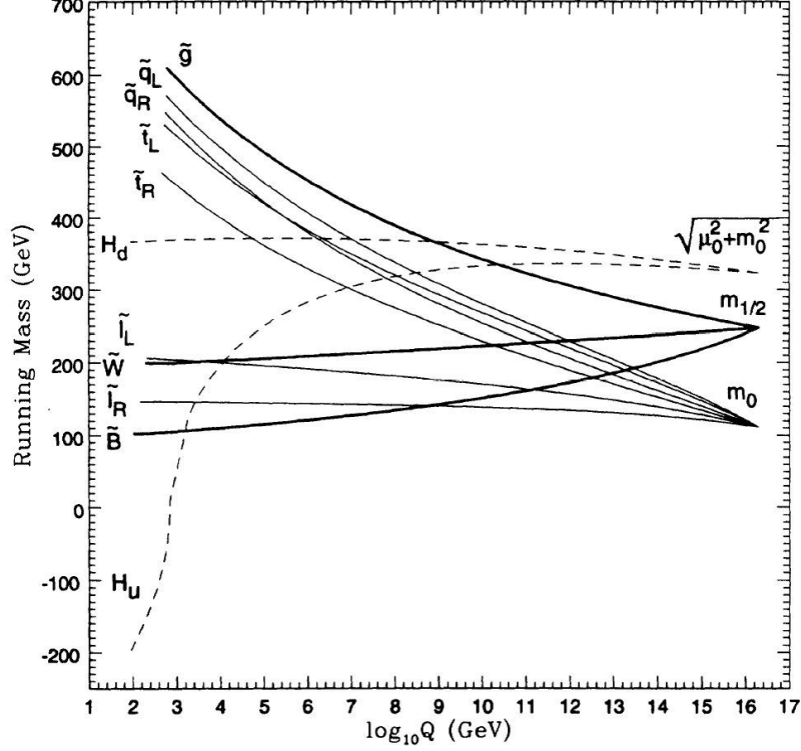


Figure A.2: The coupling constant of standard model and SUSY MSSM model as a function of the energy scale.

The \tilde{t}_1 is made the lightest squark of all due to the \tilde{t}_R .

Similarly squared-mass matrices for scalar bottom quark and scalar tau lepton are

$$\mathbf{m}_b^2 = \begin{pmatrix} m_Q^2 + \Delta_{\tilde{d}_L} & v(a_b^* \sin \beta - \mu y_b \cos \beta) \\ v(a_b^* \sin \beta - \mu^* y_b \cos \beta) & m_{\tilde{q}}^2 + \Delta_{\tilde{d}_R} \end{pmatrix}, \quad (\text{A.1.29})$$

$$\mathbf{m}_\tau^2 = \begin{pmatrix} m_L^2 + \Delta_{\tilde{\tau}_L} & v(a_\tau^* \cos \beta - \mu y_\tau \sin \beta) \\ v(a_\tau^* \cos \beta - \mu^* y_\tau \sin \beta) & m_{\tilde{\tau}}^2 + \Delta_{\tilde{\tau}_R} \end{pmatrix}. \quad (\text{A.1.30})$$

The mixing between the left-handed and right-handed is determined by taking the $\tan \beta$. When the $\tan \beta$ is given as the large value, the mixing is larger, and the lighter squarks and sleptons of third generation are tended to be the lightest supersymmetric particle (LSP).

Figure A.2 shows the running group evolution of squarks, sleptons and gaugino mass on MSUGRA which the used parameters are $m_0 = 200$ GeV, $m_{1/2} = 600$ GeV, $\tan \beta = 10$ and $\text{sign}(\mu) = +$. The plot indicates the colored particles are weighted heavier meanwhile the weak and hypercharge particles are lightened in decreasing the energy scale to TeV scale. The $(\mu^2 + m_0^2)^{1/2}$ term runs to the negative potential because of the effects of the large top Yukawa coupling and this provokes electroweak symmetry breaking.

A.2 minimal UED

At tree-level, the mass of minimal UED model particles are contributed from the n -th Kaluza-Klein excitation and the Standard Model particles as follows

$$m_{X^n}^2 = \frac{n^2}{R^2} + m_{X^0}^2 + \delta m_{X^n}, \quad (\text{A.2.1})$$

where X^n is the n -th Kaluza-Klein excitation, X^0 is the Standard Model particle and R is the compactification scale, respectively.

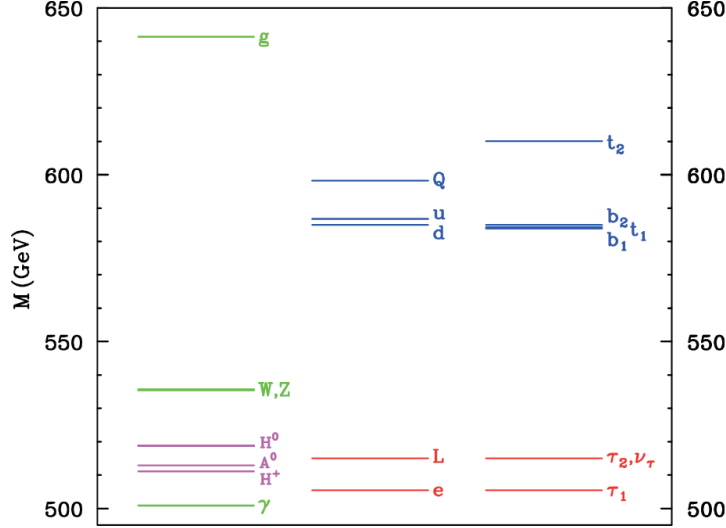


Figure A.3: Spectrum of first level Kaluza-Klein states, including the effective of radiative corrections and boundary terms. A compactification scale of $1/R = 500$ GeV, Higgs mass of 115 GeV and cut-off scale of $\Lambda R = 20$. [54]

The radiative corrections to KK masses should be considered with the loop diagram transverse around the extra dimension, called bulk loop, and the brane-localized kinetic terms which appear on the orbifold boundaries. These contributions are given by

$$\begin{aligned}
\delta(m_{B^{(n)}}^2) &= \frac{g'^2}{16\pi^2 R^2} \left(\frac{-39}{2} \frac{\zeta(3)}{\pi^2} - \frac{n^2}{3} \ln \Lambda R \right), \\
\delta(m_{W^{(n)}}^2) &= \frac{g^2}{16\pi^2 R^2} \left(\frac{-5}{2} \frac{\zeta(3)}{\pi^2} + 15n^2 \ln \Lambda R \right), \\
\delta(m_{g^{(n)}}^2) &= \frac{g_3^2}{16\pi^2 R^2} \left(\frac{-3}{2} \frac{\zeta(3)}{\pi^2} + 23n^2 \ln \Lambda R \right), \\
\delta(m_{Q^{(n)}}) &= \frac{n}{16\pi^2 R^2} \left(6g_3^2 + \frac{27}{8}g^2 + \frac{1}{8}g'^2 \right) \ln \Lambda R, \\
\delta(m_{u^{(n)}}) &= \frac{n}{16\pi^2 R^2} (6g_3^2 + 2g'^2) \ln \Lambda R, \\
\delta(m_{d^{(n)}}) &= \frac{n}{16\pi^2 R^2} \left(6g_3^2 + \frac{1}{2}g'^2 \right) \ln \Lambda R, \\
\delta(m_{L^{(n)}}) &= \frac{n}{16\pi^2 R^2} \left(\frac{8}{27}g^2 + \frac{9}{8}g'^2 \right) \ln \Lambda R, \\
\delta(m_{e^{(n)}}) &= \frac{n}{16\pi^2 R^2} \frac{9}{2}g'^2 \ln \Lambda R.
\end{aligned} \tag{A.2.2}$$

Here $\zeta(3) \sim 1.2020 \dots$ is the third zeta function and Λ is the cut-off scale and the g_i are gauge coupling constants (see Section 1.3.2).

After the KK modes of the W and Z bosons acquire masses by eating the fifth components of the gauge fields and Higgs KK modes, four scalar states remain at each KK level. These modes have masses given by

$$\begin{aligned}
m_{H_n^0}^2 &= \frac{n^2}{R^2} + m_h^2 + \delta m_{H_n}^2, \\
m_{H_n^\pm}^2 &= \frac{n^2}{R^2} + m_W^2 + \delta m_{H_n}^2, \\
m_{A_n^0}^2 &= \frac{n^2}{R^2} + m_Z^2 + \delta m_{H_n}^2,
\end{aligned} \tag{A.2.3}$$

where the radiative and boundary term corrections are given by

$$\delta m_{H_n}^2 = \frac{n^2}{16\pi^2 R^2} \left(3g^2 + \frac{3}{2}g'^2 - 2\lambda_H \right) \ln \Lambda R + \bar{m}_H^2. \quad (\text{A.2.4})$$

where the λ_H is the Higgs quartic coupling and \bar{m}_H^2 is the boundary mass term for the Higgs mode. Finally, the additional contribution from the top quark Yukawa coupling yields:

$$\begin{aligned} \delta_{h_t}(m_{Q_3^{(n)}}) &= \frac{n}{R} \left(-\frac{3h_t^2}{64\pi^2} \ln \frac{\Lambda^2}{\mu^2} \right), \\ \delta_{h_t}(m_{t^{(n)}}) &= \frac{n}{R} \left(-\frac{3h_t^2}{32\pi^2} \ln \frac{\Lambda^2}{\mu^2} \right). \end{aligned} \quad (\text{A.2.5})$$

An example of UED mass spectrum at first level is shown in Figure A.3 whose parameters are a compactification scale of $1/R = 500$ GeV, Higgs mass of 120 GeV and cut-off scale of $\Lambda R = 20$. The one-loop radiative correction and boundary terms are included.

Appendix B

Performance

In this section, the object definitions and their performance are described.

B.1 Electron

B.1.1 Electron Reconstruction

The electrons are reconstructed by using a track in inner detectors and a cluster in the electromagnetic (EM) calorimeter. The reconstruction algorithm runs through five steps as follows [55]

1. Cluster search

It looks for a longitudinal tower in the EM calorimeter with total transverse energy $E_T > 2.5$ GeV in a window size 3×5 in unit of $\Delta\eta \times \Delta\phi = 0.025 \times 0.025$.

2. Track matching

Reconstructed tracks are extrapolated from their last measurement point to the second layer of the EM calorimeter. A distance between the track impact point and seed cluster is smaller than $\Delta\eta < 0.5$ and $\Delta\phi < 0.1$.

3. Cluster rebuilt

The seed cluster is rebuilt by using a new window size of 3×7 in barrel region or 5×5 in end-cap region.

4. Energy determination

The cluster energy is determined by summing the energy deposit from four parts; (1) in material in front of calorimeters; (2) in the cluster; (3) outside of cluster as lateral leakage; (4) beyond EM calorimeter as longitudinal leakage. These four terms are parameterized as a function of the measured cluster energies in the pre-sampler detector and the three EM calorimeter layers based on simulation.

5. Four momentum calculation

The four momentum of the electron is computed by using the final cluster and the best matching track.

The efficiency of electron reconstruction is expected to be $\sim 95\%$ at $E_T = 5$ GeV and 100% for the electrons with >15 GeV derived from W and Z decays in MC simulations.

The loss of acceptance causes due to rejections for bad clusters to keep electron object quality, for example failures of readout from boards, high voltage problems and isolated cell expected to be noise. The value and the uncertainty with loss of acceptance are measured to be about 6% and 0.4% per electron, respectively.

B.1.2 Electron Identification

The electron identification which relies on a cut-based selection and separates the electron candidates into isolated or non-isolated signal electrons, background electrons and jets faking electrons. The identification is classified into three categories, “*loose*”, “*medium*” and “*tight*”. The *loose* selection requires a narrow shower shape in the middle layer of EM calorimeter and a small hadronic leakage in tile calorimeters. The *medium* selection is defined by taking variables of shower width in the first layer of the EM calorimeter, track quality and tighter track-cluster matching. The *tight* selection satisfies the number of high-threshold hits in TRT, b-layer hits to reject photon conversion events and ratio of the cluster energy to the track momentum E/p . The

Type	Description	Name
<i>loose</i> selection		
Acceptance	$ \eta < 2.47$	
Hadronic leakage	Ratio of E_T in the first layer of the hadronic calorimeter to E_T of the EM cluster (used over the range $ \eta < 0.8$ and $ \eta > 1.37$)	R_{had1}
	Ratio of E_T in the hadronic calorimeter to E_T of the EM cluster (used over the range $ \eta < 0.8$ and $ \eta > 1.37$)	R_{had}
Middle layer of EM calorimeter	Ratio the energy in 3×7 cells over the energy in 7×7 cells centered at the electron cluster position	R_{eta}
	Lateral shower width, $\sqrt{(\sum E_i \eta_i^2) / (\sum E_i) - ((\sum E_i \eta_i) / (\sum E_i))^2}$, where E_i is the energy and η_i is the pseudo-rapidity of cell i and the sum is calculated within a window of 3×5 cells	$w_{\eta 2}$
<i>medium</i> selection (includes loose)		
Strip layer of EM cluster	Shower width, $\sqrt{(\sum E_i (i - i_{\text{max}})^2) / (\sum E_i)}$, where i runs over all strips in a window of $\Delta\eta \times \Delta\phi \approx 0.0625 \times 0.2$, corresponding typically to 20 strips in η , and i_{max} is the index of the highest-energy strip	w_{stot}
	Ratio of the energy difference between the largest and second largest energy deposits in the cluster over the sum of these energies	E_{ratio}
Track quality	Number of hits in the pixel detector (≥ 1)	n_{pixel}
	Number of total hits in the pixel and SCT detectors (≥ 7)	n_{Si}
	Transverse impact parameter ($ d_0 < 5$ mm)	d_0
Track-cluster matching	$\Delta\eta$ between the cluster position in the strip layer and the extrapolated track ($\Delta\eta < 0.01$)	$\Delta\eta$
<i>tight</i> selection (includes medium)		
Track-cluster matching	$\Delta\phi$ between the cluster position in the middle layer and the extrapolated track ($\Delta\phi < 0.02$)	$\Delta\phi$
	Ratio of the cluster energy to the track momentum	E/p
	Tighter $\Delta\eta$ requirement ($ \Delta\eta < 0.005$)	$\Delta\eta$
Track quality	Tighter transverse impact parameter requirement ($ d_0 < 1$ mm)	d_0
TRT	Total number of hits in the TRT	n_{TRT}
	Ratio of the number of high-threshold hits to the total number of hits in the TRT	f_{HT}
Conversions	Number of hits in the b-layer (≥ 1)	n_{BL}
	Veto electron candidates matched to reconstructed photon conversions	

Table B.1: Definition of variables used for *loose*, *medium* and *tight* electron identification cuts

definition of each category is summarised in Table B.1. The three categories are expected to be powerful jet rejections as 500, 5000 and 50000 for *loose*, *medium* and *tight*, respectively, based on the MC study.

B.1.3 Electron Energy Scale

The energy scale in EM calorimeter (EM scale) is derived from beam test measurement. The total uncertainty of this energy scale is 3%, and the most of uncertainty comes from LAr absolute temperature normalisation in the test beam cryostat.

The energy calibration for electrons is divided into three steps [56, 57]:

1. The raw signal from each cell as ADC counts is converted into a deposit energy using the electronic calibration in the EM calorimeter.
2. MC-based calibration corrects the cluster energy with an energy loss due to absorption in dead materials and leakage outside of the cluster.

3. The in-situ calibration by using $Z \rightarrow ee$ decays, alternatively $W \rightarrow e\nu$ and $J/\psi \rightarrow ee$ events, determines the energy scale.

In this section, only the EM scale calibration by using the in-situ measurement is described.

The miscalibration is parameterized by using residual calibration constants α_i (i is given by each $\Delta\eta \times \Delta\phi$ region) and the α_i is defined as

$$E^{\text{mean}} = E^{\text{true}} (1 + \alpha_i), \quad (\text{B.1.1})$$

where E^{true} is the true electron energy, E^{mean} is the measured electron energy after the MC-based energy scale correction. The α_i is estimated by fitting the Z mass peak of MC to that of data on an invariant mass distribution to shift the calibration constant α_i in each $\Delta\eta \times \Delta\phi$ region. The α_i estimation uses the log-likelihood function as following

$$-\ln L = \sum_{i,j} \sum_{k=1}^{N_{ij}^{\text{events}}} \left[-\ln L_{ij} \left(\frac{m_k}{1 + \frac{\alpha_i + \alpha_j}{2}} \right) \right], \quad (\text{B.1.2})$$

where the indices i and j denote the regions with one of electrons from $Z \rightarrow ee$ decaying in region i and the other in region j , N_{ij}^{events} is the total number of selected Z decays, m_k is the measured dielectrons invariant mass. The L_{ij} is the probability density function quantifying the compatibility with the line-shape of Z invariant mass distribution in MC simulation. The calibration constants are given by minimizing the $-\ln L$ in each region.

The considered uncertainties contributing to the calibration constant are (1) Additional materials in front of the calorimeter which is not accounted for in MC-based calibration ($\sim 2\%$); (2) low E_T electrons due to difference of calibration constant between using the Z events and J/ψ events (1% with $E_T \leq 10$ GeV electron decreasing linearly to 0% for $E_T = 20$ GeV); (3) pre-sampler detector energy scale whose uncertainty is measured by comparing the electron energy extracted from $W \rightarrow e\nu$ events in data with that of MC simulation (0-1.4%). The other uncertainties are extremely small (0-0.5%).

The calibration constants as a function of E_T in $0 < |\eta| < 0.6$ and $1.52 < |\eta| < 1.8$ are shown in Figure B.1.

B.1.4 Electron Energy Resolution

The electron energy resolution can be described

$$\frac{\sigma_E}{E} = \frac{a}{\sqrt{E}} \oplus \frac{b}{E} \oplus c, \quad (\text{B.1.3})$$

where a , b and c are the sampling term, noise term and constant term, respectively. The resolutions are estimated by using the $Z \rightarrow ee$ events and comparing data with MC samples. We can assume that the sampling term are good modeling within a 10% uncertainty in simulation, and the contribution from noise term is negligible in high

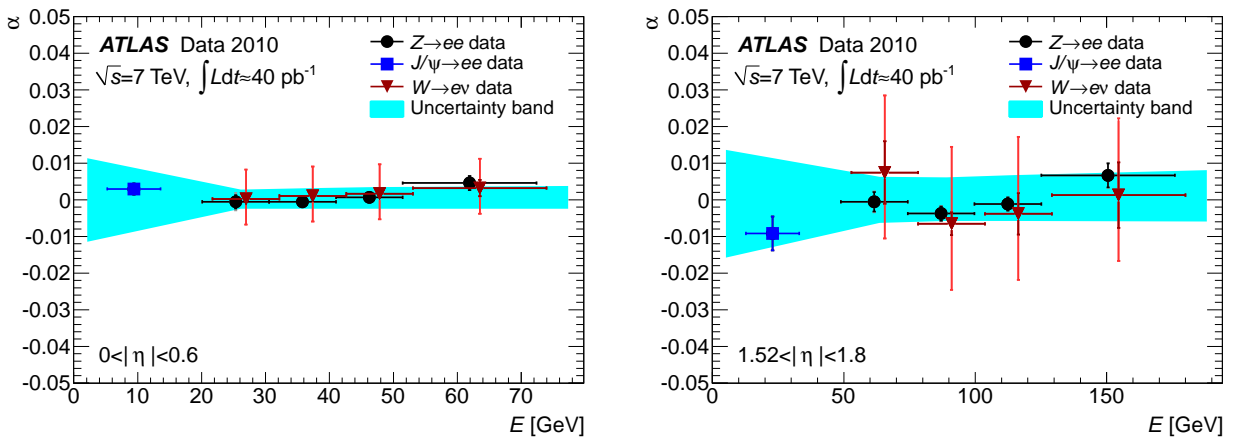


Figure B.1: Correction factors of the electron energy scale as a function of E_T in $Z \rightarrow ee$ and $J/\psi \rightarrow ee$ events.

energy scale. Moreover, the constant term can be cancel out at first order of those terms. These assumptions can indicate a formula

$$c_{\text{data}} = \sqrt{2 \cdot \left[\left(\frac{\sigma}{m_Z} \right)_{\text{data}}^2 - \left(\frac{\sigma}{m_Z} \right)_{\text{MC}}^2 \right] + c_{\text{MC}}^2}, \quad (\text{B.1.4})$$

where m_Z is Z mass calculated in the dielectrons events, σ is the Gaussian component of the experimental resolution and $c_{\text{data(MC)}}$ is effective constant term of data (MC). The resolutions $\sigma_{\text{data(MC)}}$ are estimated by fitting the invariant mass distribution of data and simulation in the 80-100 GeV by Breit-Wigner convolved with a Crystal Ball function. In the fit, the Breit-Wigner width is fixed to measured Z width and the experimental resolution is determined by the Crystal Ball function. Figure B.2 shows the fitting results with Z mass peak both data and MC in barrel and end-cap region. The value of c_{MC} used in the MC simulation is 0.5%, thus the c_{data} is calculated 1-3% by using the Equation B.1.4 and results in Figure B.2. The systematic uncertainty is estimated 0.4-1.5% in an assumption that the sampling term increases by 10% in simulation. The contribution from discrepancy of the constant term between data and MC compensates for electron energy in the MC simulation.

B.1.5 Electron Scale Factors

In order to ensure the electron distribution on MC, we estimate the efficiencies both data and MC and the distributions of MC samples are corrected for the discrepancy of the efficiencies. The total efficiency ϵ and the correction factor (or scale factor) ϵ_{sf} are

$$\epsilon = \epsilon_{\text{event}} \cdot \epsilon_{\text{reco}} \cdot \epsilon_{\text{id}} \cdot \epsilon_{\text{trig}} \cdot \epsilon_{\text{iso}}, \quad (\text{B.1.5})$$

$$\epsilon_{\text{sf}} = \frac{\epsilon_{\text{data}}}{\epsilon_{\text{MC}}}, \quad (\text{B.1.6})$$

where ϵ_{event} is the efficiency of pre-selection cuts e.g. noise suppression. The ϵ_{reco} is reconstruction efficiency that algorithm finds both an EM cluster and a charged track, and the objects are reconstructed to an electron. The ϵ_{id} , ϵ_{trig} and ϵ_{iso} are the identification efficiency relative to the reconstructed electrons, the trigger efficiency with respect to all reconstructed and identified electron, and the isolation efficiency relative to the identified electrons, respectively. The ϵ_{data} and ϵ_{MC} are total efficiencies of data and MC, respectively.

These efficiencies are estimated by using the $Z \rightarrow ee$, $W \rightarrow e\nu$ and $J/\psi \rightarrow ee$ events and the scale factor is estimated in each $\Delta E_T \times \Delta \eta$ region. In order to obtain the clean and unbiased sample of electrons, the scale factor is measured by using a tag-and-probe method [58] [59]. This method assumes the events lying on the Z (or J/ψ) mass window are coming from Z (or J/ψ) decay, thus both electrons can be regarded as true electrons. In the case, the one of them so-called ‘‘tagged electron’’ satisfies the tight criteria and isolation, the other electron so-called ‘‘probe electron’’ is used to measure the efficiency after the background subtraction. The tagged electron for the $Z \rightarrow ee$ and $J/\psi \rightarrow ee$ events is defined:

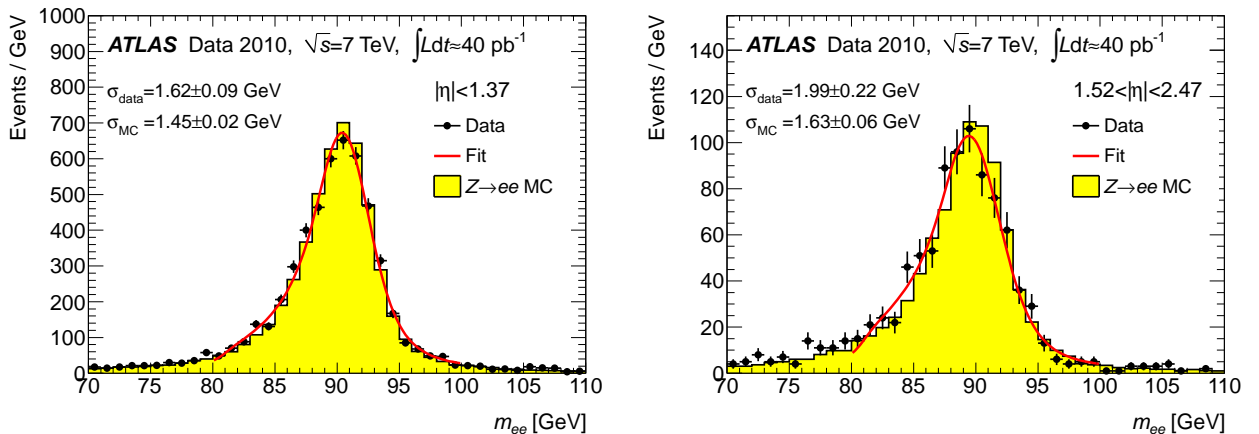


Figure B.2: Distributions of invariant mass and correction factor of the electron energy resolution as a function of η in $Z \rightarrow ee$ and $J/\psi \rightarrow ee$ events.

- The tagged electron matches the corresponding trigger object.
- The tagged electron satisfies the tight selection criteria.
- The tagged electron is required to have $E_T > 20$ GeV.

On the other hand the probe electron is basically defined:

- The charge of probe electron is opposite to tagged electron for the $Z \rightarrow ee$ and $J/\psi \rightarrow ee$ events.
- The E_T of probe electron is $E_T > 15$ GeV for $Z \rightarrow ee$ and $W \rightarrow e\nu$ events, $E_T > 4$ GeV for $J/\psi \rightarrow ee$ events.

The other definitions corresponding to each efficiency measurement are applied to the probe electrons. The trigger efficiency are measured by taking the ratio of the number of probe electrons matching the trigger object in $\Delta R < 0.15$ to total number of probe electrons. In the identification efficiency, the probe electrons which consist of a EM calorimeter cluster and matching track are checked to passing the *medium* or *tight* selection criteria.

The background estimation for the efficiency measurement is fitted by exponential, Landau function and distribution of same sign sample in the side-band of Z or J/ψ peaks. The signal events are modeled either by a Breit-Wigner distribution convolved with a parameterization of the low mass tail, by a Crystal Ball function, or by a template obtained from MC simulation. The background subtraction becomes a dominant source of a systematic uncertainty. The uncertainties of each efficiency are estimated by varying the background subtraction, for example the signal window and the electron definition.

Figure B.3 shows the identification efficiency of each selection criteria and Figure B.4 shows the scale factor of tight electrons except the trigger efficiency. The MC distributions are corrected by these scale factors.

B.2 Muon

B.2.1 Muon Reconstruction

Track Reconstruction in Inner Detectors

A inner detector tracks are reconstructed by using NEWT algorithm [60]. This algorithm covers the two sequences; (1) inside-out track reconstruction; and (2) outside-in tracking. A kink track reconstruction is also deployed common tracking tool, but is not particular to an approach of this algorithm.

- Inside-out sequence

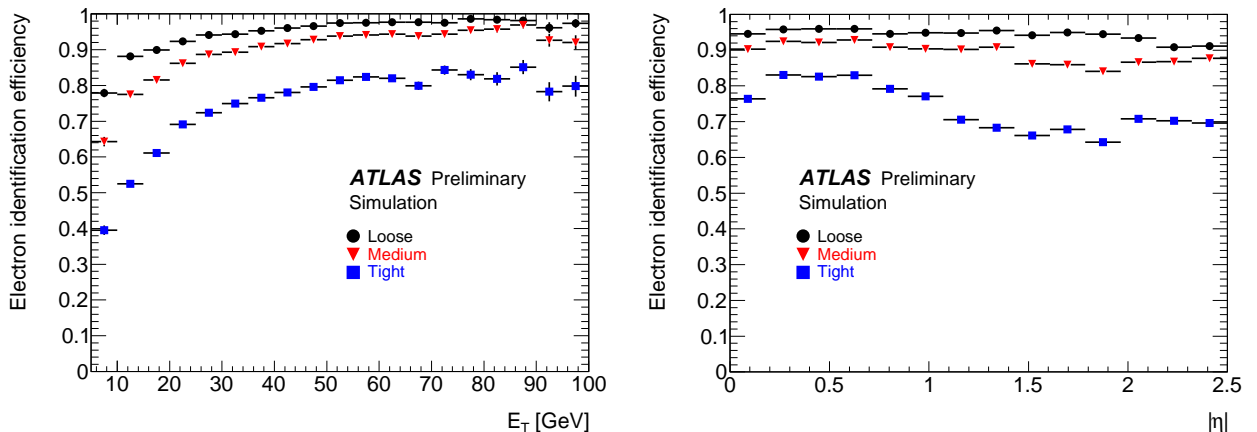


Figure B.3: Efficiency of the electron identification as a function of E_T and $|\eta|$ for the *loose*, *medium* and *tight* in $Z \rightarrow ee$ channel.

1. Global track seeding

The primary inner detector pattern recognition starts with seeding in the inner silicon tracker (Pixel and SCT) and finds hits toward the outer border of the inner detector. The track seed is created as three-dimensional representation and a window search through the direction of track seed is applied. Hits on the inner detector elements within the windows are collected and judged whether these hits are added to the track candidate by using a simplified Kalman filtering.

2. Ambiguity solving

In order to reject the fake tracks, the track candidates are scored with respect to the disposal of hits in Pixel and SCT. In general, each hit associated with the track leads to a better score value to favor fully reconstructed track rather than small segments. Currently, a hit-pattern based scoring and a maximum likelihood approach are available.

3. TRT track extension

The track (segment) is extended from the silicon detectors into the outer TRT. The track passing the ambiguity solving is used as an input to find compatible sets of TRT measurements that is further processed as candidate of extension. The silicon-only track is not modified, then the association of the TRT hits is a pure extension. Two concrete implementations of the track extension tool exist:

- The standard implementation follows a classical approach starting to find hits through track extrapolation.
- A second implementation is based on an extension of the standard Kalman filter formalism

• Outside-in sequence

The tracks coming from secondary vertices or photon conversions may not be reconstructed by inside-out sequence due to lack of silicon hits. In outside-in sequence, track segments are identified by using a standard Hough transform mechanism which is an extraction technique, while a dedicated association tool prevents hits that have already been assigned to tracks in the inside-out procedure to be used again. The TRT segments are followed back into the silicon detectors.

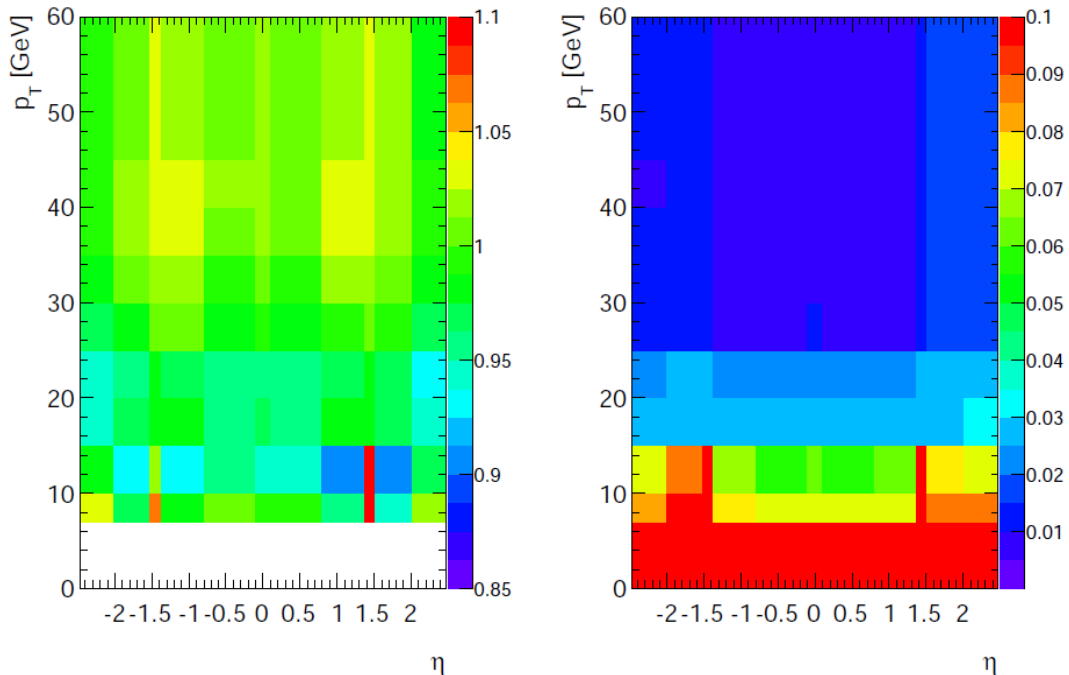


Figure B.4: Value and uncertainty of scale factor and the uncertainty for the electrons as functions of E_T and η .

Track Reconstruction in Muon Spectrometer

1. Identification of region of activity (ROA) in the muon system through the muon trigger systems (RPC/TGC). The regions of activity (ROA) defined the size as roughly $\Delta\eta \times \Delta\phi = 0.4 \times 0.4$ are required at least one hit in RPC and TGC. The ROA becomes a seed for the muon segments and tracks.
2. Reconstruction of the local segments in each muon station in these ROA.
A straight track segment is formed by combining with the hits in multi-layers of the same MDT station. The pair of hits in two multi-layers is required and points to the interaction point loosely to suppress background hits. A track segment is validated by requiring its quality factor χ^2 to be small sufficiently. The definition of quality factor χ^2 is described in Equation B.2.1.
3. Combination of segments of different muon stations to form muon track candidates using three-dimensional tracking in the magnetic field.
Tracks are seeded from the segments with a first estimation of the momentum deduced from the position and direction of the segment. These segments are extrapolated to the other stations with its relaxed momentum. If some matching segments exist, the extrapolated tracks are fitted to perform more accurate estimation of the momentum. In the fitting procedure, only one segment is kept per crossed station and a candidate track has at least two segments.
4. Global track fit of the muon track candidates through the full detector systems using individual hit information.
The global fit is performed with starting from the best fitting tracks by using raw information (i.e. TDC values) to suppress the δ -rays, gamma and neutron background. The procedure estimates the likelihood of the candidate tracks and selects more good tracks among all hits a priori belonging to the track from the bad track which are too far from the reconstructed path of the muon. Finally, the fit including matter is performed by using Kalman filter method.

Muon Track Reconstruction

The muon reconstruction employs three different algorithm, Muonboy, MuTag and STACO, as follow [61]. This analysis employs the STACO muons and MuTag muons.

1. Standalone reconstruction (Muonboy)
The muon candidates are reconstructed by using the segments and tracks in only the muon spectrometer. These standalone tracks are extrapolated to the primary vertex.
2. Tagged muon (MuTag)
The Tagged muons are reconstructed by the hit information in the inner detector and matching with a segment (not track) in the muon spectrometer to ensure the muon candidate. This reconstruction is prepared for the low p_T muons since these muons lost most of their energy in the calorimeters and their trajectories in the muon spectrometer are difficult to reconstruct. This algorithm runs after the STACO.
3. Combined reconstruction (STACO)
The candidate tracks are combined with a inner track and a muon spectrometer track. The combined track is estimated as follow. Suppose i -th measured hit position m_i , the error e_i of the position and the position on the fitting track $M_{\vec{p}}$ to minimize the distance between the hit position and the fitting track whose vector is \vec{p} . The likelihood parameter \vec{p} is evaluated by the function,

$$\chi^2(\vec{p}) = \sum_i \frac{(m_i - M_i(\vec{p}))^2}{e_i^2}. \quad (\text{B.2.1})$$

If the \vec{p}_0 minimizing χ^2 at χ_0^2 is defined, the χ^2 can be described around the minimum of χ^2

$$\chi^2(\vec{p}) = \chi_0^2 + (\vec{p}_0 - \vec{p})^T W_0 (\vec{p}_0 - \vec{p}), \quad (\text{B.2.2})$$

where the weight W_0 serves to evaluate the errors and correlations of the \vec{p}_0 . Now the likelihood function of the fitting track estimated by the inner detector and muon spectrometer is

$$\chi^2(\vec{p}) = \sum_i^{\text{ID}} \frac{(m_i - M_i(\vec{p}))^2}{e_i^2} + \sum_j^{\text{MS}} \frac{(m_j - M_j(\vec{p}))^2}{e_j^2}. \quad (\text{B.2.3})$$

This function can be written as

$$\chi^2(\vec{p}) = (\chi_0^{\text{ID}})^2 + (\chi_0^{\text{MS}})^2 + (\vec{p}_0^{\text{ID}} - \vec{p})^T W^{\text{ID}} (\vec{p}_0^{\text{ID}} - \vec{p}) + (\vec{p}_0^{\text{MS}} - \vec{p})^T W^{\text{MS}} (\vec{p}_0^{\text{MS}} - \vec{p}). \quad (\text{B.2.4})$$

The combined track satisfies the below equations,

$$(W^{\text{ID}} + W^{\text{MS}}) \vec{p}_0 = W^{\text{ID}} \vec{p}_0^{\text{ID}} + W^{\text{MS}} \vec{p}_0^{\text{MS}}, \quad (\text{B.2.5})$$

$$W_0 = W^{\text{ID}} + W^{\text{MS}}. \quad (\text{B.2.6})$$

Then,

$$\chi_0^2 = (\chi_0^{\text{ID}})^2 + (\chi_0^{\text{MS}})^2 + (\chi^{\text{match}})^2, \quad (\text{B.2.7})$$

$$(\chi^{\text{match}})^2 = (\vec{p}_0^{\text{ID}} - \vec{p}_0^{\text{MS}})^T (W^{\text{ID}-1} + W^{\text{MS}-1})^{-1} (\vec{p}_0^{\text{ID}} - \vec{p}_0^{\text{MS}}) \quad (\text{B.2.8})$$

The track of combined muon is reconstructed by minimizing the χ^{match} .

B.2.2 Muon Momentum Resolution

The muon momentum resolution measurement is estimated by applying the Z mass fitting. The dimuons invariant mass distribution is obtained from the muon momentum estimated by the inner detector (ID) and the muon spectrometer (MS), separately. The Z mass shape line is fitted by the double Gaussian function modeling the detector resolution as follow

$$f(x) = A \frac{1}{x^2} + B \frac{(x^2 - \bar{x}^2)}{(x^2 - \bar{x}^2)^2 + \sigma_x^2 \bar{x}^2} + C \frac{x^2}{(x^2 - \bar{x}^2)^2 + \sigma_x^2 \bar{x}^2}, \quad (\text{B.2.9})$$

where x indicates the reconstructed dimuons invariant mass $m_{\mu\mu}$, the A , B , C and σ_x are fixed parameters determined from the MC dimuons invariant mass distribution. The only fitted parameter is \bar{x} and this results are shown in Figure B.5 for the inner detector and the muon spectrometer separately. The discrepancy between data and MC in Figure B.5 becomes the correction factor and the factors are applied to the muon momentum on simulation.

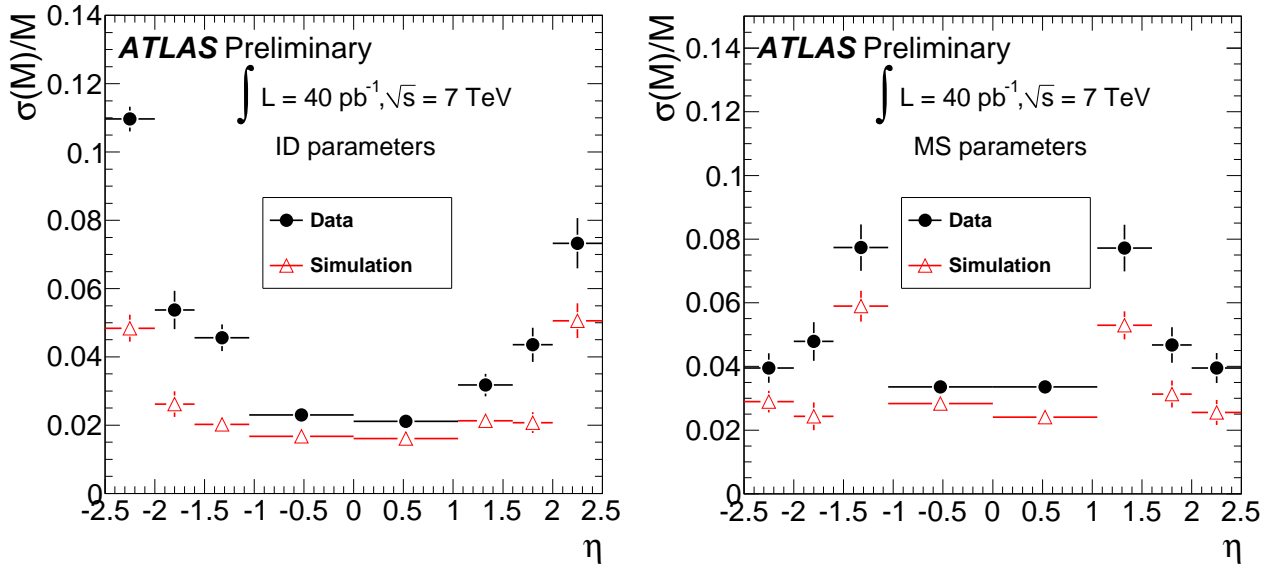


Figure B.5: The muon momentum resolution as a function of η for the inner detector (left) and muon spectrometer (right).

B.2.3 Muon Reconstruction Efficiency and Scale Factor

The muon reconstruction efficiency and isolation efficiency are estimated by using the tag-and-probe method and Z events as well as the electrons in Section B.1.5 [62]. The events lie in the Z mass window ($|m_Z - m_{\mu\mu}| < 10$ GeV) and the tagged muons are selected from combined muons and required for $p_T > 20$ GeV and isolation ($\sum_{tracks} p_T^{ID}/p_T < 0.2, \Delta R < 0.4$). The inner track muons are employed for probe muons and the muons satisfy the $p_T > 20$ GeV and coming from the same vertex to tagged muons. The J/ψ events are fitted by Gaussian function and the background are described by second-order polynomial function. These functions are estimated by using a χ^2 fit simultaneously. The probe muons are required the combined or segment tagged muon reconstructed by the STACO muon algorithm.

The systematic uncertainties are derived from the both signal and background shape given by fit functions. The results [63] for low p_T muons are obtained from the J/ψ events and shown in the bottom two plots in Figure B.6 and scale factors are shown in Table B.2. The trigger efficiency is also shown in Figure B.7 [64].

B.3 Jet

B.3.1 Jet Reconstruction

The jets are reconstructed by so-called “anti- k_T ” jet algorithm. As the input seeds, the topological clusters are created event by event.

Topological Cluster

The topological clusters (topocluster) are generated through three steps to suppress the noise [44].

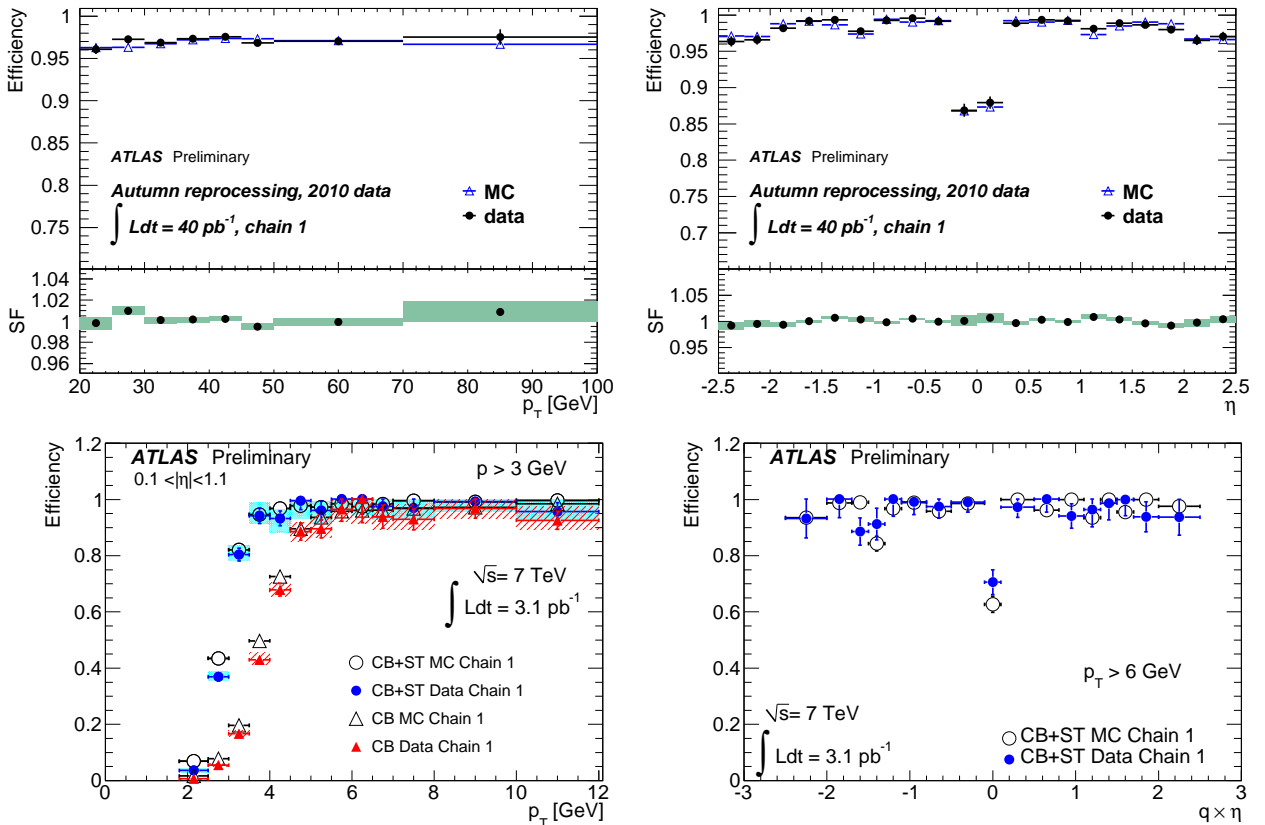


Figure B.6: Efficiencies and correction scale factor of the muon as a function of p_T (top-left) and η (top-right) for the high p_T muon and efficiencies of the low p_T muon as a function of p_T (bottom-left) and η (bottom-right) in $Z \rightarrow \mu\mu$ and $J/\psi \rightarrow \mu\mu$ events.

Algorithm	$ \eta $	scale factor
Combined Muon	0.0-0.1	1.022 ± 0.084 (stat.) $^{+0.025}_{-0.042}$ (syst.)
	0.1-1.1	0.973 ± 0.018 (stat.) $^{+0.022}_{-0.001}$ (syst.)
	1.1-1.3	0.909 ± 0.050 (stat.) $^{+0.025}_{-0.007}$ (syst.)
	1.3-2.0	0.951 ± 0.023 (stat.) $^{+0.037}_{-0.075}$ (syst.)
	2.0-2.5	0.976 ± 0.056 (stat.) $^{+0.040}_{-0.013}$ (syst.)
Inner Track + Segment Muon	0.0-0.1	0.958 ± 0.155 (stat.) $^{+0.009}_{-0.019}$ (syst.)
	0.1-1.1	0.989 ± 0.017 (stat.) $^{+0.015}_{-0.001}$ (syst.)
	1.1-1.3	1.024 ± 0.046 (stat.) $^{+0.015}_{-0.020}$ (syst.)
	1.3-2.0	0.970 ± 0.024 (stat.) $^{+0.036}_{-0.066}$ (syst.)
	2.0-2.5	0.976 ± 0.050 (stat.) $^{+0.040}_{-0.013}$ (syst.)

Table B.2: Scale factors for the efficiency with respect to the combined muon and the inner track plus segment muon for $|\eta| < 2.5$ and $p_T > 6$ GeV.

1. The topological cluster algorithm finds the $|E_{\text{cell}}| > 4\sigma_{\text{cell}}$ cell as a seed, where σ_{cell} is the RMS of energy distribution of random events in each calorimeter cell (typically $\sigma_{\text{cell}} \sim 40$ MeV).
2. Neighbor cells of the seed are added if the cell satisfies $|E_{\text{cell}}| > 2\sigma_{\text{cell}}$ until no nearest-neighbor cell has $|E_{\text{cell}}| > 2\sigma_{\text{cell}}$.
3. Finally all nearest-neighbor cells surrounding the cluster are added to the cluster. These three steps are executed to direction of 3D (r, η, ϕ) . In case the cluster energy is negative, the jet algorithm rejects such clusters.

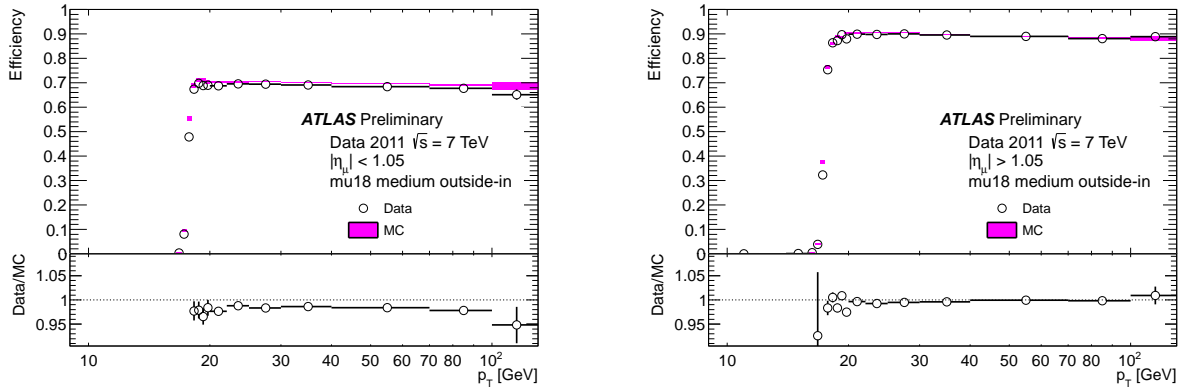


Figure B.7: Trigger efficiencies and scale factors of the muon as a function of p_T in barrel region (left) and end-cap region (right).

Anti k_T jet algorithm

The jet algorithm estimates the distance between clusters and merges if the distances are nearer than a certain threshold [45] [46]. The distance d_{ij} between the i -th and j -th jet cluster is calculated by

$$d_{ij} = \min(k_{Ti}^{2p}, k_{Tj}^{2p}) \frac{\Delta_{ij}^2}{R^2} \quad (\text{B.3.1})$$

$$d_{iB} = k_{Ti}^{2p} \quad (\text{B.3.2})$$

where k_T , Δ_{ij} are the transverse momentum of the topocluster and distance $\Delta_{ij}^2 = (\eta_i - \eta_j)^2 + (\phi_i - \phi_j)^2$, respectively. The cluster is merged until $d_{iB} < d_{ij}$. The topocluster reconstruction is illustrated in Figure B.8. ATLAS usually employs the $R = 0.4$ and $p = -1$ called "anti- k_T " jet algorithm.

B.3.2 Jet Energy Scale Uncertainty

The jet response in a calorimeter is smaller than that of electron and photon with the same energy because the some of hadronic interaction, for example the nuclear excitation and slow neutrons, are invisible. Typical value of the ratio of energy deposit of hadron in calorimeter to that of electron is $e/h \sim 1.3$. In off-line reconstruction, the visible cluster energies are calculated by using the EM scale and the jet energy in the EM scale is factored by the jet energy scale (JES). The jet energy scale is estimated by comparing the energy deposit of the truth particle with that of the reconstructed particle $\langle R \rangle = \langle E_{\text{calo}}^{\text{EM+JES}} / E_{\text{truth}} \rangle$ or $\langle R \rangle = \langle p_T^{\text{jet}} / p_T^{\text{truth}} \rangle$ on the MC simulations [65]. Figure B.9 show the average of jet energy scale correction as a function of jet transverse momentum p_T and pseudo-rapidity, respectively.

The ratio $\langle R \rangle$ is included the uncertainties derived from several effects, for example the dead material not considering on the simulations and modeling of calorimeter response with single particle. These contributions are concluded as follows

1. The each source of uncertainty is calculated in each p_T^{jet} and η bin.

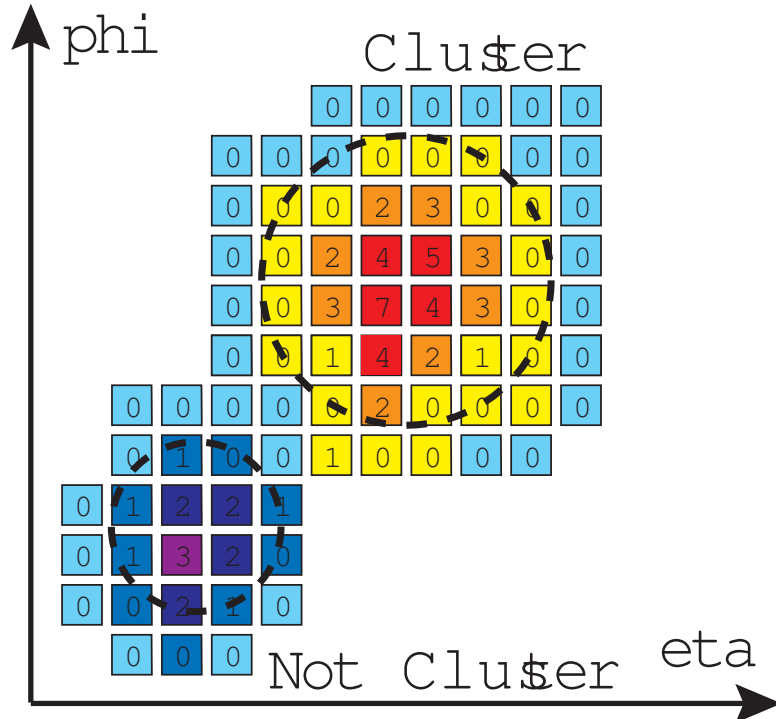


Figure B.8: Schematic of the algorithm of topological cluster.

2. The deviations Δ_{JES} is estimated from $\langle R_{\text{var}} \rangle$ of each source and the nominal ratio $\langle R_{\text{nom}} \rangle$ as follows

$$\Delta_{\text{JES}}(p_{\text{T}}^{\text{jet}}, |\eta|) = \left| 1 - \frac{\langle R_{\text{var}}(p_{\text{T}}^{\text{jet}}, |\eta|) \rangle}{\langle R_{\text{nom}}(p_{\text{T}}^{\text{jet}}, |\eta|) \rangle} \right| \quad (\text{B.3.3})$$

3. The largest Δ_{JES} is selected from the jet energy (E) or jet transverse momentum (p_{T})

$$\Delta_{\text{JES}}(p_{\text{T}}^{\text{jet}}, |\eta|) = \max \left(\Delta_{\text{JES}}^E(p_{\text{T}}^{\text{jet}}, |\eta|), \Delta_{\text{JES}}^{p_{\text{T}}}(p_{\text{T}}^{\text{jet}}, |\eta|) \right) \quad (\text{B.3.4})$$

4. Estimate the total uncertainties to add the all contributions.

This jet energy scale uncertainty is validated by the in-situ techniques like these

- Direct transverse momentum balance between a jet and a photon ($\sim 1.5\%$ uncertainty) [66].
- Photon balance using the missing transverse momentum $E_{\text{T}}^{\text{miss}}$ ($\sim 1\%$ uncertainty) [66].
- Balance between a high p_{T} jet recoiling against one or more lower p_{T} jets ($\sim 4\%$ uncertainty) [67].
- Comparison of jet calorimeter energy to the momentum carried by tracks associated to a jet ($\sim 3\%$ uncertainty) [68].

The total jet energy scale uncertainty in barrel region ($0.3 < |\eta| < 0.8$) shows the left of Figure B.10 and the right of B.10 shows the uncertainty in the end-cap region.

B.3.3 b -tag algorithm

The jets derived from the b -quark have the second vertex because the average of flight length of b -hadron is about $\ell \sim 500 \mu\text{m}$. There are some b -tagging algorithm, this analysis uses “JetFitterCombNN” algorithm [69] which is combined with the “JetFitter” algorithm and “IP3D” algorithm by using artificial neural network techniques with Monte Carlo simulated training samples and additional variables describing the topology of the decay chain. The IP3D algorithm is based on the likelihood ratio between the transverse impact parameter d_0/σ_{d_0} and longitudinal impact parameter z_0/σ_{z_0} . The feature of JetFitter algorithm is assuming the c -hadrons decay on the b -hadron flight direction and looking for the both b -hadron and c -hadron decay points.

The JetFitter algorithm needs the jet information (the position of b -hadron and c -hadron decay), vertex information (mass and energy fraction reconstructed by tracks). The variables of jet information are introduced as follows,

$$\vec{d} = (x_{\text{PV}}, y_{\text{PV}}, z_{\text{PV}}, \phi, \theta, d_1, d_2, \dots, d_N) \quad (\text{B.3.5})$$

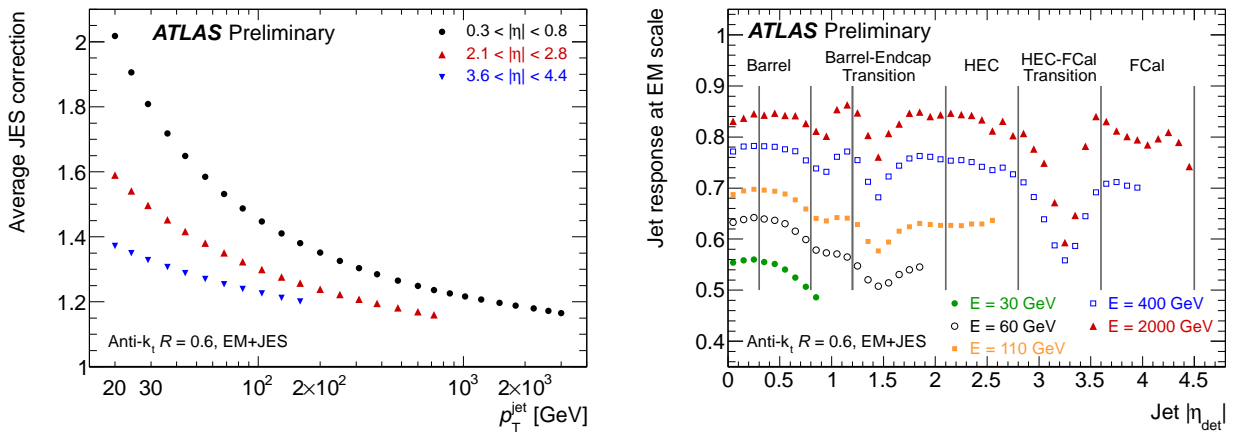


Figure B.9: Average of jet energy scale correction as a function of calibrated jet p_{T} in three η region (left) and simulated jet energy response at the electromagnetic energy scale as a function of EM+JES calibrated jet energy and η .

where (x_{PV}, y_{PV}, z_{PV}) is position at a primary vertex, ϕ, θ are direction of the track and d_i are distance from the primary vertex to the intersection between the d_i -th track and b -hadron flight axis. This \vec{d} and these vertices have following variables

- Mass
the invariant mass of all charged particle tracks associating with the decay chain.
- Energy Fraction
the fraction of energy of these particles divided by the sum of the energies of all charged particles matched to the jet.
- Flight length significance $d/\sigma(d)$
the weighted average position divided by their errors of the displaced vertices.

The category of decay topology is defined to avoid the correlation between the flavors by the following.

1. Number of vertices with at least two tracks.
2. Total number of tracks at these vertices.
3. Number of additional single track vertices on the b -hadron flight axis.

The likelihood function is formed by these variables as follow

$$L^{b,c,l} = \sum_{\text{category}} \text{coeff} \cdot PDF_{\text{category}}(\text{mass}) \cdot PDF_{\text{category}}(\text{EnergyFraction}) \cdot PDF_{\text{category}}(d/\sigma(d)) \quad (\text{B.3.6})$$

The three different flavors (b , c and light flavor) are parameterized separately. The coefficient coeff is estimated by using the JetFitter variable \vec{d} in a given flavor and each PDF has been already predicted by MC which is shown in Figure B.13.

Finally the likelihood ratio of IP3D and JetFitter are multiplied and the b -tag weight is estimated by applying the neural network results. Figure B.11 (right) shows a distribution of the output of the JetFitterCombNN algorithm for observed data and simulated data. In this analysis, the operating point at 1.8 is applied where the b -tagging efficiency is about 60%. Figure B.12 show the rejection power for the light and charm flavor jets, and the 60% of b -tagging efficiency indicates ~ 500 and ~ 7 rejection power for light flavour and charm jets, respectively.

B.3.4 b -tagging Efficiency and Scale Factor

The b -tagging efficiency is estimated by two method, “ p_T^{rel} method” and “System8 method”.

The p_T^{rel} is defined as the muon momentum transverse to the direction combined with muon and jet. The templates p_T^{rel} distribution of light-flavour jets, c -jets and b -jets before and after b -tagging by using MC are

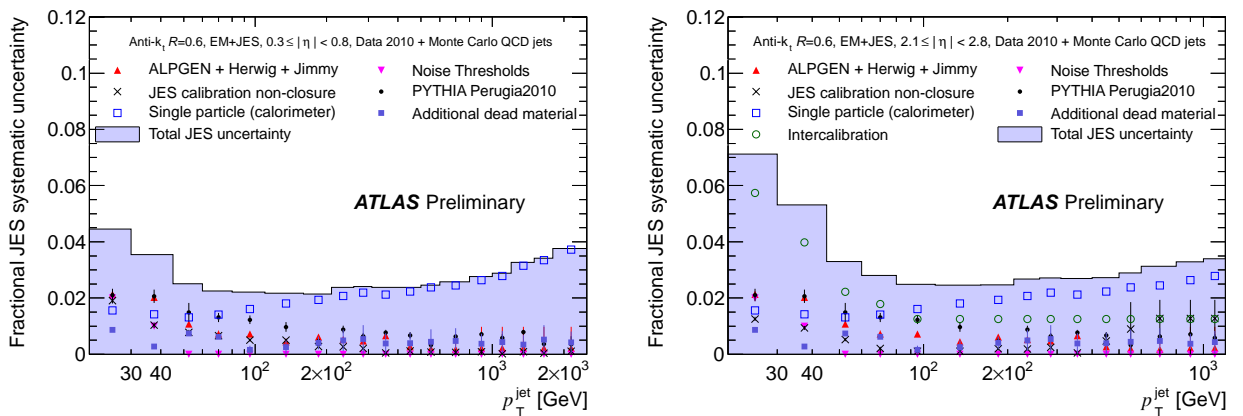


Figure B.10: Distributions of the jet energy scale uncertainties as a function of jet p_T in barrel region ($0.3 < |\eta| < 0.8$) and end-cap region ($2.1 < |\eta| < 2.8$).

prepared and fitted to data to obtain the fraction of each quark component. Figure B.14 shows p_T^{rel} distribution before and after b -tagging. The b -tagging efficiency ϵ_b^{data} is defined as

$$\epsilon_b^{\text{data}} = \frac{f_b^{\text{tag}} \cdot N^{\text{tag}}}{f_b \cdot N} \cdot C, \quad (\text{B.3.7})$$

where f_b and f_b^{tag} are the fractions of b -jets before and after b -tagging to p_T^{rel} samples and N and N^{tag} are the total number of jets and the number of b -tagged jets in those samples. The factor C is a correction factor for the efficiency for the biases coming from difference of modeling between data and MC. The scale factor for b -tagging efficiency is measured as $\epsilon_{\text{SF}} = \epsilon_b^{\text{data}} / \epsilon_b^{\text{MC}}$

The System8 method uses three uncorrelated selection criteria and estimates the b -jet and non b -jet efficiencies, and the number of real b -jets and non b -jets in the samples to pass each of three selection criteria. The three selection criteria are

- The lifetime tagging criteria
- The muon $p_T^{rel} \leq 700$ MeV
- An opposite-jet with $p_T > 10$ GeV, $|\eta| < 2.5$ and $\pi - |\Delta\phi_{jj}| < 1$ where $\Delta\phi_{jj}$ is azimuth difference between selection jet and opposite side jet. The opposite jet is required for the b -tagging by the secondary vertex with $L/\sigma(L) > 1$.

The eight equations are described as follows

$$\begin{aligned} n &= n_b & + & n_{cl}, \\ p &= p_b & + & p_{cl}, \\ n^{LT} &= \epsilon_b^{LT} n_b & + & \epsilon_{cl}^{LT} n_{cl}, \\ p^{LT} &= \alpha_6 \epsilon_b^{LT} p_b & + & \alpha_4 \epsilon_{cl}^{LT} p_{cl}, \\ n^{MT} &= \epsilon_b^{MT} n_b & + & \epsilon_{cl}^{MT} n_{cl}, \\ p^{MT} &= \alpha_5 \epsilon_b^{MT} p_b & + & \alpha_3 \epsilon_{cl}^{MT} p_{cl}, \\ n^{LT,MT} &= \alpha_1 \epsilon_b^{LT} \epsilon_b^{MT} n_b & + & \alpha_2 \epsilon_{cl}^{LT} \epsilon_{cl}^{MT} n_{cl}, \\ p^{LT,MT} &= \alpha_7 \alpha_6 \alpha_5 \epsilon_b^{LT} \epsilon_b^{MT} p_b & + & \alpha_8 \alpha_4 \alpha_3 \epsilon_{cl}^{LT} \epsilon_{cl}^{MT} p_{cl}. \end{aligned} \quad (\text{B.3.8})$$

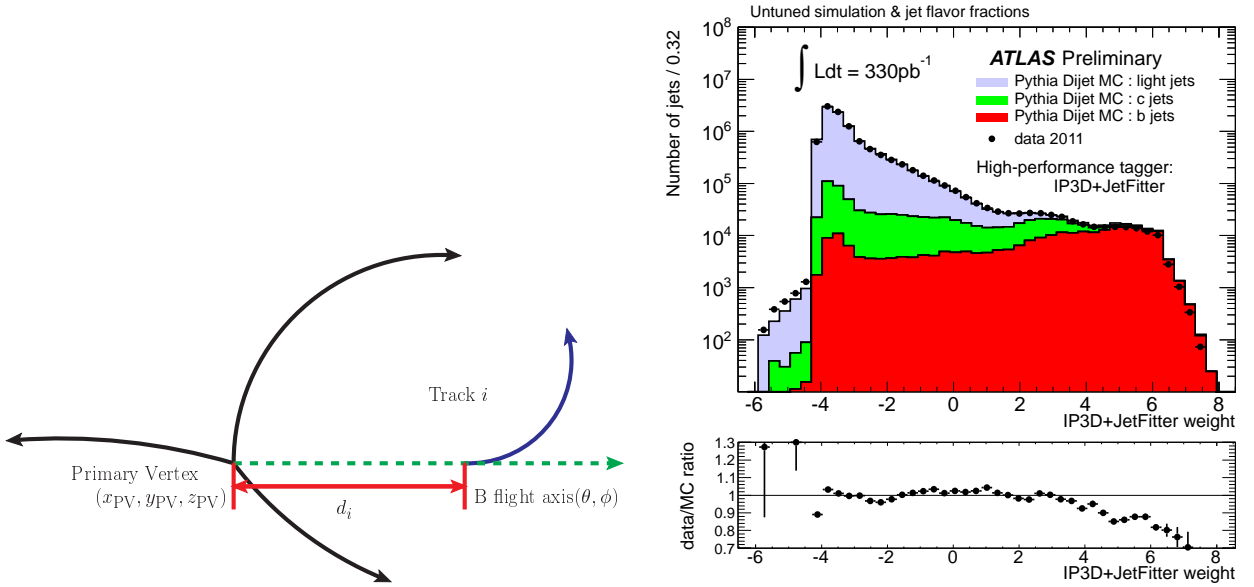


Figure B.11: Schematic of the relation between the primary vertex and secondary vertex about b -jets (left) and distribution of b -tagged jets as a function of operating point of combination of IP3D and JetFitterComb algorithms

In these equations, the superscript LT and MT mean the lifetime tagging and soft muon tagging, respectively. The n and p are the number of events of the sample with applied or without applied opposite-jet correction. The b and cl mean b -jet and non- b flavour jet (c, s, d, u, g), respectively. The correction factor α_i are

$$\begin{aligned}
\alpha_1 &= \epsilon_b^{LT,MT,n} / (\epsilon_b^{LT,n} \epsilon_b^{MT,n}), & \alpha_2 &= \epsilon_{cl}^{LT,MT,n} / (\epsilon_{cl}^{LT,n} \epsilon_{cl}^{MT,n}), \\
\alpha_3 &= \epsilon_{cl}^{MT,p} / \epsilon_{cl}^{MT,n}, & \alpha_4 &= \epsilon_{cl}^{LT,p} / \epsilon_{cl}^{LT,n}, \\
\alpha_5 &= \epsilon_b^{MT,p} / \epsilon_b^{MT,n}, & \alpha_6 &= \epsilon_b^{LT,p} / \epsilon_b^{LT,n}, \\
\alpha_7 &= \epsilon_b^{LT,MT,p} / (\epsilon_b^{LT,n} \epsilon_b^{MT,p}), & \alpha_8 &= \epsilon_{cl}^{LT,MT,p} / (\epsilon_{cl}^{LT,p} \epsilon_{cl}^{MT,p}).
\end{aligned} \tag{B.3.9}$$

The b -tagging efficiency and light flavor efficiency are estimated by resolving these equations. For the efficiency, the source of systematic uncertainties are considered as modeling of b - and c -production, b -Hadron direction modeling, b -quark fragmentation and so on. The combined efficiency of p_T^{rel} method with system8 method are estimated by applying the maximum likelihood method in each jet p_T bin. The likelihood function is expressed as follows

$$L = L'(\kappa_1 | \hat{\kappa} (1 + \Delta\kappa_1^{syst1} \lambda^{syst1} + \Delta\kappa_1^{syst2} \lambda^{syst2}), \Delta\kappa_1^{stat}) \times \tag{B.3.10}$$

$$L'(\kappa_2 | \hat{\kappa} (1 + \Delta\kappa_2^{syst1} \lambda^{syst1} + \Delta\kappa_2^{syst2} \lambda^{syst2}), \Delta\kappa_1^{stat}) \times \tag{B.3.11}$$

$$L'(\lambda^{syst1} | 0, 1) \times L'(\lambda^{syst2} | 0, 1), \tag{B.3.12}$$

where the $\hat{\kappa}$ is the combined b -tagging scale factor when each measurement of κ_i corresponds $i = 1$ to the p_T^{rel} method and $i = 2$ to System8 method, the $\Delta\kappa$ means the width of uncertainties and λ expresses the how much standard deviations the systematic uncertainties are shifting. The $(\lambda^{syst} | 0, 1)$ term are constrained to the factor of uncertainties between zero to one. The scale factors estimated by this method are shown in Figure B.15.

B.4 Missing Transverse Energy E_T^{miss}

Because the energy and the momentum are preserved in the transverse plane, the unbalance of energy in this plane indicates the total energy of invisible objects [70]. The missing transverse energy E_T^{miss} consists of four components as follows

- Electron
Reconstructed electrons satisfy $p_T > 10$ GeV and *medium* selection criteria.

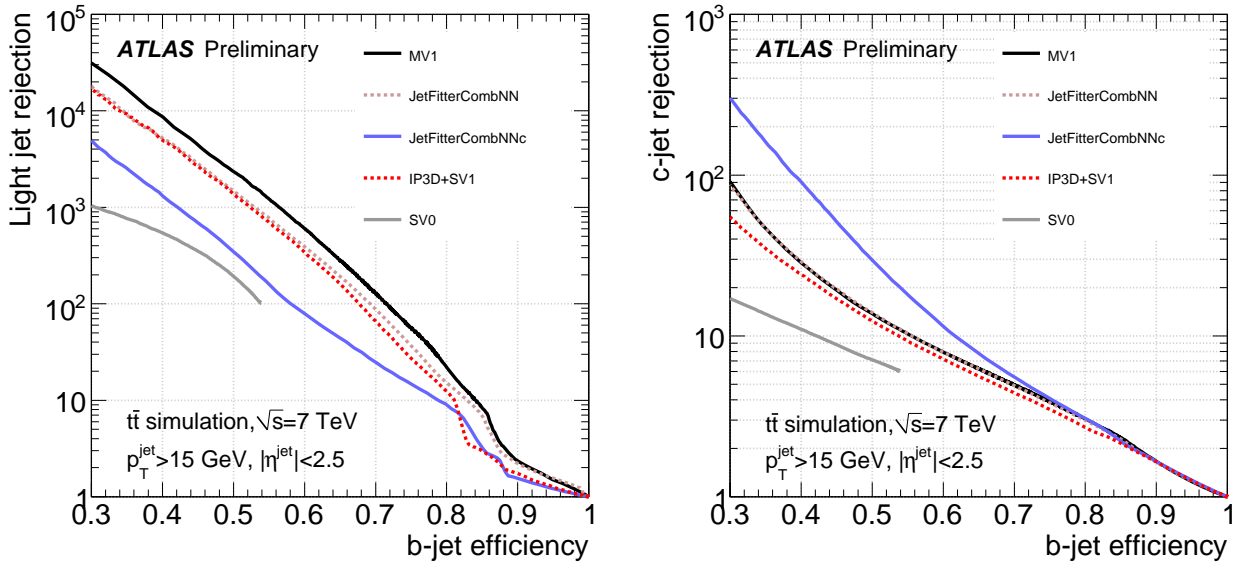


Figure B.12: Light flavour jet rejection (left) and c -hadron jet rejection as a function of the b -tag efficiency for the each b -tag algorithm based on $t\bar{t}$ MC samples.

- Muon
STACO muon applied the isolation cut satisfy the out of $\Delta R > 0.3$ cone with selected jets.
- Jet
Jet seeded the topocluster jet and applied size parameter $\Delta R = 0.4$ AntiKtTopo algorithm with calibration by the EM+JES scale. The transverse momentum is larger than $p_T > 20$ GeV.
- Cell Out
The Cell Out term is formed from all topocluster in the calorimeter not to belong to the any other objects. This energy scale is calibrated by the EM scale.

The E_T^{miss} is calculated by below formulas

$$E_x^{\text{miss}} = -\sum E_x^e - \left(\sum E_x^{\text{calo},\mu}\right) - \sum p_x^\mu - \sum E_x^{\text{jet}} - \sum E_x^{\text{CellOut}} \quad (\text{B.4.1})$$

$$E_y^{\text{miss}} = -\sum E_y^e - \left(\sum E_y^{\text{calo},\mu}\right) - \sum p_y^\mu - \sum E_y^{\text{jet}} - \sum E_y^{\text{CellOut}} \quad (\text{B.4.2})$$

$$E_T^{\text{miss}} = \sqrt{(E_x^{\text{miss}})^2 + (E_y^{\text{miss}})^2}. \quad (\text{B.4.3})$$

In these formulas, the energy deposit terms of muon in calorimeter $E_{x,y}^{\text{calo},\mu}$ are depended on the qualification of the muon. When its muon is isolated with jets i.e. the angular distance $\Delta R(\mu, \text{jets})$ is further than 0.3, the energy deposit in the calorimeters is used to calculate the muon momentum, then the $E_{x,y}^{\text{calo},\mu}$ term is not added. On the other hand overlapped muon with jets $\Delta R(\mu, \text{jets}) < 0.3$ can not resolved the energy deposit

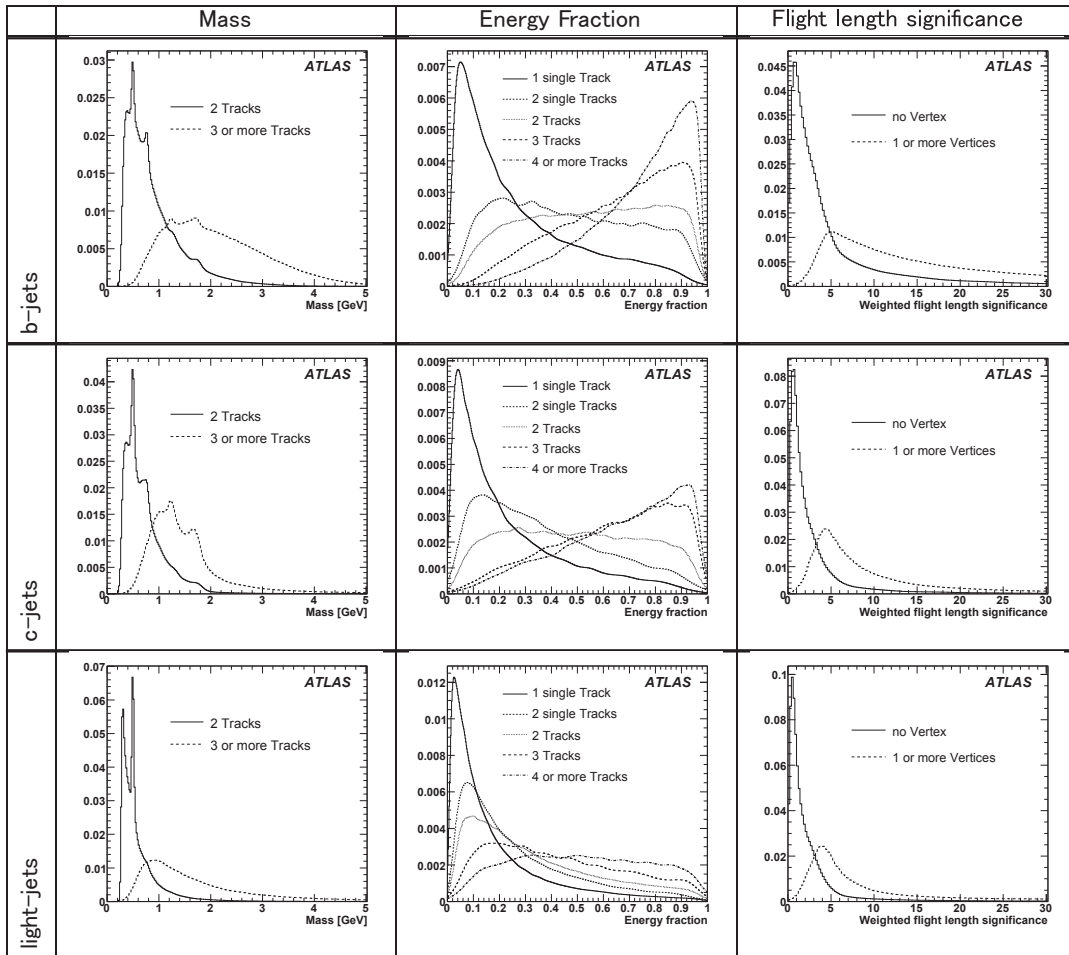


Figure B.13: Probability density function (PDF) of the parameters to identify the b -jet, c -jet and light flavor jet.

derived from the muon with the jet cluster, therefore the muon momentum is calculated as after energy loss and $E_x^{\text{calo},\mu}$ term is add to the E_T^{miss} . If there are significant difference between the only muon spectrometer measurement and the combined measurement with inner detector and muon spectrometer, the muon energy loss in calorimeters is parameterized and subtracted from $E_x^{\text{calo},\mu}$.

Figure B.16 shows the E_T^{miss} distributions in the $W \rightarrow e\nu$ events (left) and $W \rightarrow \mu\nu$ events (right). The MC predictions are in good agreement with data in these plots. Figure B.17 (left) shows the expected E_T^{miss} linearity of the $W \rightarrow e\nu$ and $W \rightarrow \mu\nu$ events on MC. The linearity is defined as the mean value of the ratio $(E_T^{\text{miss}} - E_T^{\text{miss, True}}) / E_T^{\text{miss, True}}$. The mean value is expected to be zero, but the bias in low E_T^{miss} is estimated about 5% and the finite resolution of the E_T^{miss} measurement deviate the reconstructed E_T^{miss} from zero.

The E_T^{miss} resolution is estimated by using the minimum bias and $Z \rightarrow \ell\ell$ events since these dijets and dileptons events are expected for the E_T^{miss} to be zero. In this estimation, the distributions of E_x^{miss} and E_y^{miss} are fitted by the Gaussian function in each the summation of energy deposit of each calorimeter cell $\sum E_T$ bin and the standard deviations of Gaussian function is examined $\sigma = k \cdot \sqrt{\sum E_T}$ since the resolution is approximated stochastic as a function of $\sum E_T$. The $\sum E_T$ is calculated as follows

$$\sum E_T = \sum_{i=1}^{N_{\text{cell}}} E_i \sin \theta_i, \quad (\text{B.4.4})$$

where the E_i and θ_i are the energy deposit and polar angle for each calorimeter cell, respectively. Figure B.18 (right) shows the fitted results of the resolution in each $\sum E_T$ bin for each sample. The MC predictions are reasonably agreement with data.

B.4.1 Systematic Uncertainties

The E_T^{miss} is contributed from the systematic uncertainties derived from any objects. The contributions from the energy scale uncertainty or the energy resolution uncertainty of objects propagate to the components of E_T^{miss} .

The major sources of own E_T^{miss} uncertainties are the cell out term and the pile-up (soft jet) term. These sources originate from the inaccuracies in the description of the detector material, the choice of shower model and the model for the underlying event in the simulation.

Cell Out Term

The energy scale uncertainty of the E_T^{miss} cell out term is estimated by using two methods; (1) based on MC simulation and; (2) the track momentum measurement instead of topocluster energy measurement.

In the uncertainty measurement based on simulation, some alternative MC samples which are changed to the description with dead material, the choice of shower model and the model of underlying events. The systematic

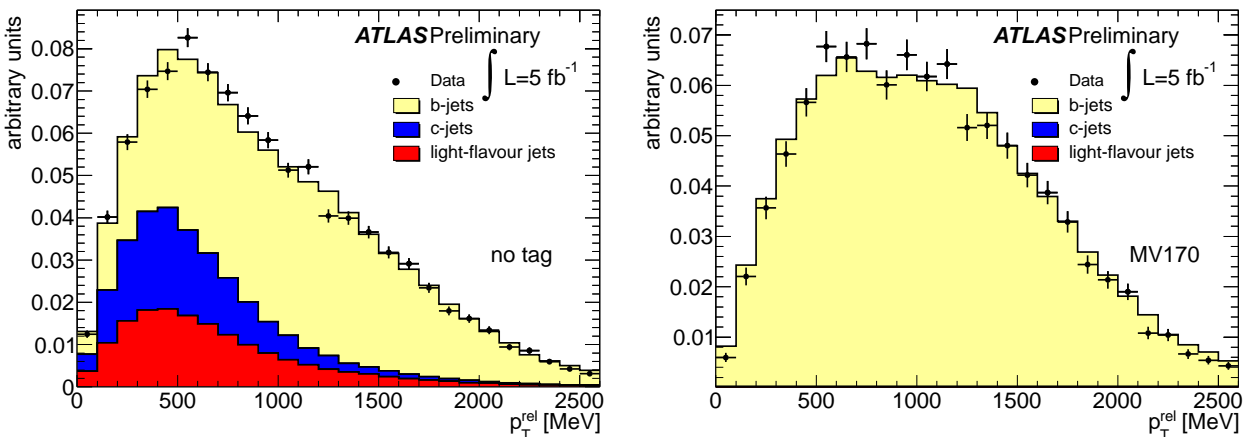


Figure B.14: Examples of template fit to the p_T^{rel} distributions in data before (left) and after (right) b -tagging by applying the multivariate method at 70% efficiency.

uncertainty of modeling in simulation comes from the quadrature of the deviations with distribution between the alternative samples and nominal sample. This method leads the 2.6% uncertainty for the E_T^{miss} cell out term.

In the track momentum measurement, the all selected tracks satisfy the track qualities and are extrapolated to the second layer of the electromagnetic calorimeter to match the topocluster. The track momentum sum is compared with the matching topocluster energy and a shift of the energy scale is fitted to a function depending with the momentum. The function is described as following

$$1 \pm a \times \left(1 + \frac{b}{p_T}\right) \quad (\text{B.4.5})$$

The a is obtained by comparing the ratio of topocluster energy to track momentum E/p in observed data and MC simulation. The value in the forward region, where tracks can not be used to validate the energy scale, is estimated from the transverse momentum balance between the one jet in the central region and one jet in forward region. The coefficient b addresses the possible change in the clustering efficiency and scale in a non-isolated environment. The results are obtained as $a = 3(10)\%$ for $|\eta| < (>) 3.2$ and $b = 1.2$ GeV in data and MC simulation.

The $E_T^{\text{miss,CellOut}}$ uncertainty is evaluated to shift the topocluster energies up and down by using the Equation B.4.5. The fraction of $E_T^{\text{miss,CellOut}}$ uncertainty is evaluated from:

$$\frac{\Delta^{\text{CellOut}+} + \Delta^{\text{CellOut}-}}{2 \cdot E_T^{\text{miss,CellOut}}}, \quad (\text{B.4.6})$$

where

$$\Delta^{\text{CellOut}+} = \left| E_T^{\text{miss,CellOut}+} - E_T^{\text{miss,CellOut}} \right|, \quad (\text{B.4.7})$$

$$\Delta^{\text{CellOut}-} = \left| E_T^{\text{miss,CellOut}-} - E_T^{\text{miss,CellOut}} \right|. \quad (\text{B.4.8})$$

The $E_T^{\text{miss,CellOut}+}$ and $E_T^{\text{miss,CellOut}-}$ correspond to Equation B.4.5. The value of fractional $E_T^{\text{miss,CellOut}}$ uncertainty is approximately 13%.

Pile-up Calibration

The E_T^{miss} resolution in the presence of pile-up is degraded by three main effects.

- Because of the higher activity in the detector, the energy deposit in the calorimeters increases. This causes the sampling term to grow accordingly.

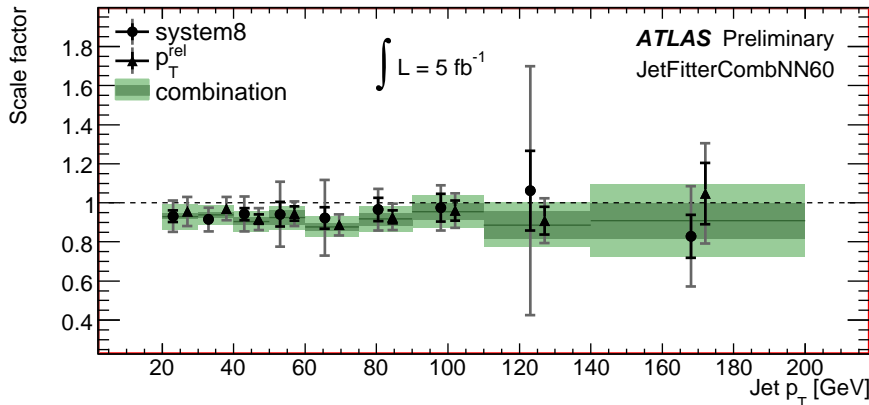


Figure B.15: Examples of template fit for the p_T^{rel} distributions before (left) and after (right) b -tagging by applying the multivariate method at 70% efficiency.

- The noise level in the calorimeter cells increases.
- More energy is lost because the calorimeters can not start to take data at appropriate timing.

To reduce this pile-up effects, the off-set subtraction is applied to the topocluster. The off-set value is estimated by using the depth of the topocluster and the vertex multiplicity as function of the pseudo-rapidity in the minimum bias events, and the E_T^{miss} is recomputed from off-set subtracted topoclusters. The shift of energy scale is regarded as systematic uncertainty and the value is estimated about 3%. The systematic uncertainties of each component with E_T^{miss} are shown in Figure B.19 in $W \rightarrow e\nu$ and $W \rightarrow \mu\nu$ channel. The total uncertainty with E_T^{miss} is estimated 1%-7% for both $W \rightarrow e\nu$ and $W \rightarrow \mu\nu$ events.

B.5 Luminosity Measurements

The luminosity as functions of time and μ which is an average number of inelastic interactions per bunch crossing are obtained by several detectors and multiple algorithm independently [48]. The luminosity L is described by using the inelastic cross section σ_{inel} and the rate of inelastic collisions R_{inel} as following,

$$L = \frac{R_{\text{inel}}}{\sigma_{\text{inel}}}. \quad (\text{B.5.1})$$

For a storage ring, operating at a revolution frequency f_r and bunch pairs colliding per revolution n_b , this expression can be rewritten by using the average number of inelastic interactions per bunch crossing μ as

$$L = \frac{\mu n_b f_r}{\sigma_{\text{inel}}}. \quad (\text{B.5.2})$$

The total inelastic cross section σ_{vis} and the observed interaction rate per crossing μ_{vis} can be expressing by using efficiency ϵ of a particular detector and algorithms as $\sigma_{\text{vis}} = \epsilon\sigma_{\text{inel}}$ and $\mu_{\text{vis}} = \epsilon\mu_{\text{inel}}$, then the luminosity can be expressed as

$$L = \frac{\mu_{\text{vis}} n_b f_r}{\sigma_{\text{vis}}}. \quad (\text{B.5.3})$$

Here the luminosity in arbitrary unit $R_x(\delta)$ is introduced. The value is measured during a horizontal scan at the time the two beams are separated by the distance δ and $\delta = 0$ represents the case of zero beam separation. Defining the parameter Σ_x as

$$\Sigma_x = \frac{1}{\sqrt{2\pi}} \frac{\int R_x(\delta) d\delta}{R_x(0)} \quad (\text{B.5.4})$$

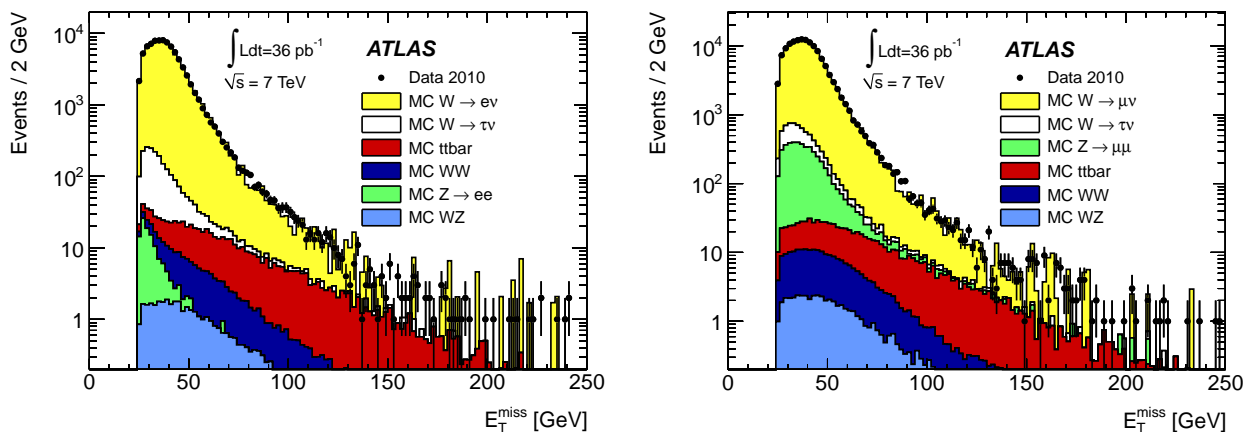


Figure B.16: E_T^{miss} distributions both data and MC predications with the $W \rightarrow e\nu$ events (left) and $W \rightarrow \mu\nu$ events (right). The MC samples are normalized by entries of data and the theoretical cross section. [70]

and similarly for Σ_y . The luminosity can be rewritten as

$$L = \frac{n_b f_r n_1 n_2}{2\pi \Sigma_x \Sigma_y} \quad (\text{B.5.5})$$

where n_1 and n_2 are the bunch populations (number of protons per bunch) in beam 1 and beam 2. The Σ_x and Σ_y are measured by using *van der Merr (vdM)* scan. This method scans to cross the two beams along the x and y directions and estimates the beam width from the number of interaction events. In order to calibrate the luminosity measurement, the visible interaction rate per bunch crossing $\mu_{\text{vis}}^{\text{MAX}}$ which is observed at the peak of the scan curve as applied by a particular algorithm

$$\sigma_{\text{vis}} = \mu_{\text{vis}}^{\text{MAX}} \frac{2\pi \Sigma_x \Sigma_y}{n_1 n_2} \quad (\text{B.5.6})$$

is used.

For the μ_{vis} measurement four event count algorithms are performed as “EventOR”, “EventAND”, “EventA” and “EventC”. The LUCID and BCM detectors are placed in the forward (labeled “A”) and backward (labeled “C”) direction from the interaction point as symmetry. For event counting algorithms, a threshold is applied to the analogue signal output from each readout channel, and every channel with a response above this threshold is counted as containing “hit”. The EventOR algorithm reports the mean number of hits per bunch crossing detected by at least one hit in either A side or C side. Assuming that the number of interactions in a bunch crossing can be detected by a Poisson distribution, the probability of observing an OR event can be computed as

$$P_{\text{EventOR}}(\mu_{\text{vis}}^{\text{OR}}) = \frac{N_{\text{OR}}}{N_{\text{BC}}} \quad (\text{B.5.7})$$

$$= 1 - e^{-\mu_{\text{vis}}^{\text{OR}}} \quad (\text{B.5.8})$$

where N_{OR} is the number of events satisfying the event-selection criteria of the OR algorithm and N_{BC} is the total number of bunch crossing in a given time interval. The $\mu_{\text{vis}}^{\text{OR}}$ is calculated by using the number N_{OR} and total number of bunch crossing N_{BC} ,

$$\mu_{\text{vis}}^{\text{OR}} = -\ln\left(1 - \frac{N_{\text{OR}}}{N_{\text{BC}}}\right) \quad \text{when } \mu_{\text{vis}} \ll 1. \quad (\text{B.5.9})$$

In the case of an EventAND algorithm the probability of observing at least one hit on both side of the detectors is expressed as

$$P_{\text{EventAND}}(\mu_{\text{vis}}^{\text{AND}}) = \frac{N_{\text{AND}}}{N_{\text{BC}}} \quad (\text{B.5.10})$$

$$= 1 - 2e^{-1 + (\sigma_{\text{vis}}^{\text{OR}} / \sigma_{\text{vis}}^{\text{AND}}) \mu_{\text{vis}}^{\text{AND}} / 2} + e^{-(\sigma_{\text{vis}}^{\text{OR}} / \sigma_{\text{vis}}^{\text{AND}}) \mu_{\text{vis}}^{\text{AND}}} \quad (\text{B.5.11})$$

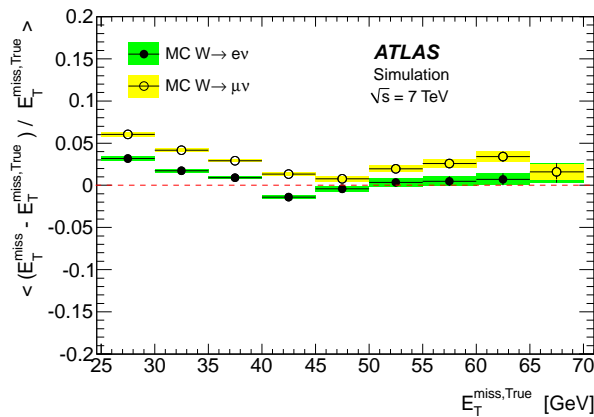


Figure B.17: E_T^{miss} linearity in $W \rightarrow e\nu$ and $W \rightarrow \mu\nu$ MC events as a function of $E_T^{\text{miss, True}}$. [70]

This relationship can not be inverted analytically to determine $\mu_{\text{vis}}^{\text{AND}}$ as a function of $N_{\text{AND}}/N_{\text{BC}}$ thus a numerical inversion is performed instead.

In the luminosity measurement the largest source of systematic uncertainty is the bunch population. Each beam is also monitored by two DC current transformers (DCCT) which are high accuracy devices but not have any ability to separate individual bunch populations. The uncertainty derived from this device is measured as 3.0%. In addition the uncertainty coming from calibration to σ_{vis} are considered and the value is measured as 1.6%. The total uncertainty of the luminosity of 3.7% is assigned for this analysis.

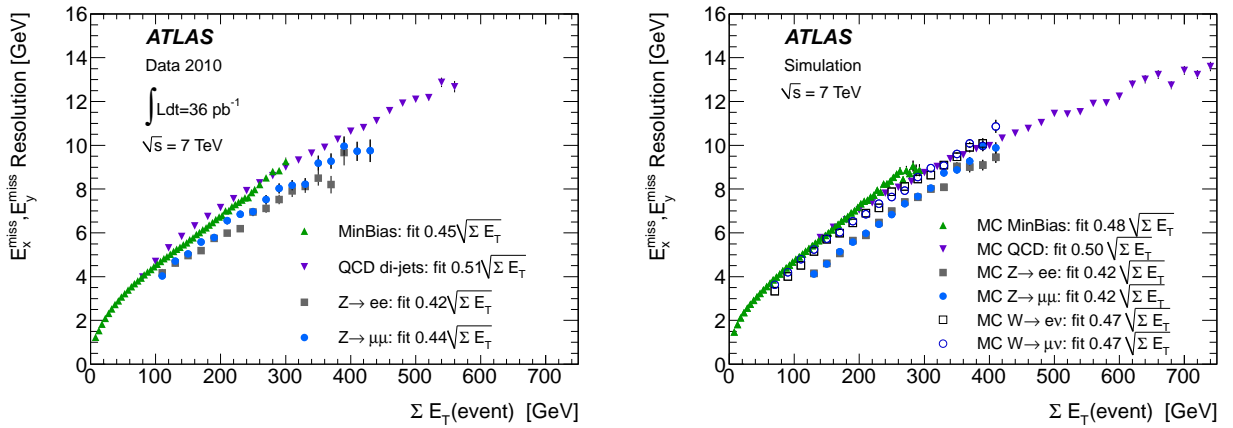


Figure B.18: E_T^{miss} resolution of both observed data (left) and MC simulation (right) as a function of the total transverse energy in the event calculated by summing the p_T of muons and the total transverse energy in the calorimeter. The resolution of the two E_T^{miss} components is fitted with a function of $\sigma = k\sqrt{\Sigma E_T}$ and the fitted values of the parameter k , expressed in $\text{GeV}^{1/2}$. [70]

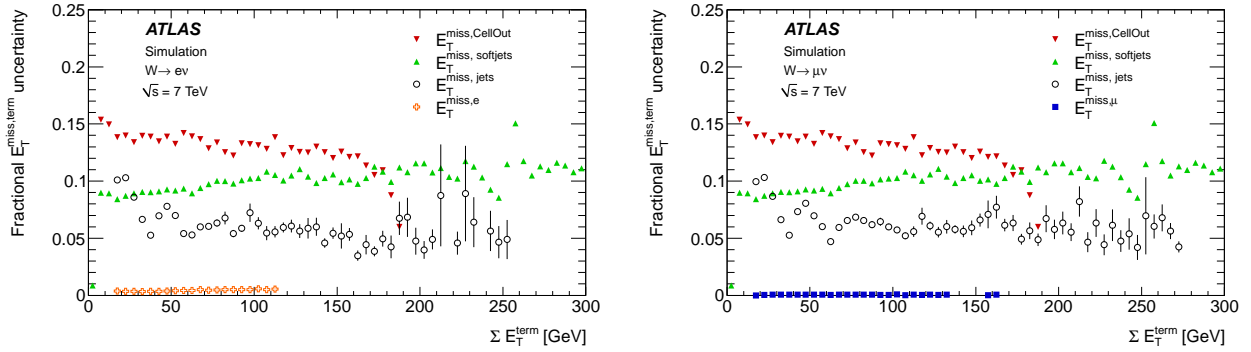


Figure B.19: Fractional systematic uncertainty on different E_T^{miss} terms as a function of respective ΣE_T^{term} in $W \rightarrow e\nu$ events (left) and $W \rightarrow \mu\nu$ events (right).

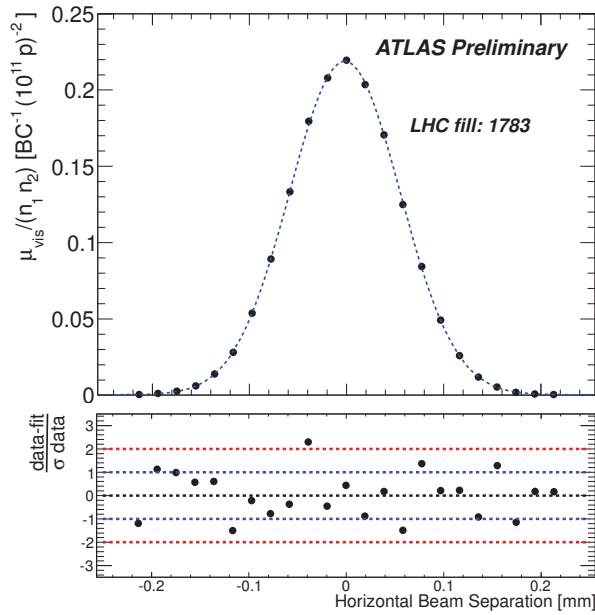


Figure B.20: Specific interaction rate versus nominal beam separation for the EventOR algorithm of BCM (horizon) in the x plain at May 15th 2011. The residual deviation of the data from the Gaussian plus constant term fit, assuming statistical error only, is shown in the bottom panel.

Appendix C

Simultaneous Fit

C.1 Profiling Likelihood Method

The distributions of background and signal include the uncertainties, thus these distributions can not be determined uniformly. This analysis estimates the most probable distributions by using a likelihood method [71]. The likelihood function L consists of two parameters, signal strength μ and nuisance parameter θ . If each bin of a histogram is distributed by Poisson probability, the likelihood function is composed of the product of the Poisson probability between all bins as following

$$L(\mu, \theta) = \prod_{i=1}^N \frac{(\mu s_i + b_i)^{n_i}}{n_i!} e^{-(\mu s_i + b_i)} \quad (\text{C.1.1})$$

where s_i , b_i and n_i are entries of predicted signal, background and observed data in i -th bin, respectively. Then the expectation value of the sum of the signal and background n_i is

$$E[n_i] = \mu s_i + b_i \quad (\text{C.1.2})$$

in the histogram $n = (n_1, n_2, \dots, n_N)$.

To test a hypothesized value of μ and θ , the profile likelihood ratio described below is considered

$$\lambda(\mu) = \frac{L(\mu, \hat{\theta})}{L(\hat{\mu}, \hat{\theta})} \quad (\text{C.1.3})$$

where the $\hat{\mu}$ and $\hat{\theta}$ in the denominator are values maximizing L so-called ‘‘maximum-likelihood (ML) estimator’’. In the numerator the $\hat{\theta}$ is a value maximizing the L at an arbitrary μ thus the $\hat{\theta}$ is depending on μ . It is convenient to introduce the t_μ so-called ‘‘test statistics’’ as following

$$t_\mu = -2 \ln \lambda(\mu) \quad (\text{C.1.4})$$

and the probability density function is calculated by this t_μ .

For the method, it is possible that the signal strength $\hat{\mu}$ is obtained as negative value, however the signal process should contribute as the positive. Therefore this likelihood function is switched by the $\hat{\mu}$ and alternative test statistics \tilde{q}_μ are provided as following

$$\tilde{q}_\mu = \begin{cases} -2 \ln \tilde{\lambda}(\mu) & (\hat{\mu} \leq \mu) \\ 0 & (\hat{\mu} > \mu) \end{cases} = \begin{cases} -2 \ln \frac{L(\mu, \hat{\theta}(\mu))}{L(0, \hat{\theta}(0))} & (\hat{\mu} < 0), \\ -2 \ln \frac{L(\mu, \hat{\theta}(\mu))}{L(\hat{\mu}, \hat{\theta}(\hat{\mu}))} & (0 \leq \hat{\mu} \leq \mu), \\ 0 & (\hat{\mu} > \mu). \end{cases} \quad (\text{C.1.5})$$

The probability density function (pdf) of \tilde{q}_μ is described as $f(\tilde{q}_\mu | \mu')$ at signal strength μ' . When we discuss whether discovery or exclusion for the searching model, we can conclude to compare the observed data with the a hypothesis including signal events (signal-plus-background hypothesis) H_1 or null hypothesis (background-only hypothesis) H_0 by using the pdf as $f(\tilde{q}_\mu | \mu)$. If the test statistics of the observed data $\tilde{q}_{\mu, \text{obs}}$ is farther

from the $f(\tilde{q}_\mu|0)$ distribution of H_0 , the background-only hypothesis H_0 can be excluded, in other word we can conclude to discover a new particle. On the other hand, for the exclusion with a signal model we compare the observed data with the signal-plus-background hypothesis H_1 . If there are discrepancy between observed data and signal-plus-background hypothesis, we can conclude that the signal model can be excluded.

In order to estimate the discrepancy, the p -value is introduced as

$$p_\mu = \int_{\tilde{q}_{\mu,\text{obs}}}^{\infty} f(\tilde{q}_\mu|\mu) d\tilde{q}_\mu. \quad (\text{C.1.6})$$

In practice, the p -value of 0.05 (corresponding to 95% CL (confidence level) or 1.64σ) for the exclusion threshold is often used meanwhile for the discovery p_0 is 2.87×10^{-7} (corresponding to 99.99998% CL or 5σ).

C.2 Asymptotic approach

The profile likelihood method takes long times to search the ML estimators $\hat{\mu}$ and $\hat{\theta}$ or 95% CL signal strength $\mu_{95\%CL}$ by scanning μ and $\hat{\theta}$, thus the asymptotic formula is applied [72]. The distribution of profile likelihood ratio are approximated by the χ^2 distribution as following

$$-2 \ln \lambda(\mu) = \frac{(\mu - \hat{\mu})^2}{\sigma^2} + \mathcal{O}(1/\sqrt{N}). \quad (\text{C.2.1})$$

The large number of sample entries can neglect the $\mathcal{O}(1/\sqrt{N})$ term. The standard deviation σ of $\hat{\mu}$ is obtained from the covariance matrix of the estimator $V_{ij} = \text{cov}[\hat{\theta}_i, \hat{\theta}_j]$ composed of signal strength and all nuisance parameters. In the large sample limit, the bias of ML estimators $\mathcal{O}(1/\sqrt{N})$ are negligible therefore the inverse of the covariance matrix can be described as

$$V_{ij}^{-1} = -E \left[\frac{\partial^2 \ln L}{\partial \theta_i \partial \theta_j} \right]. \quad (\text{C.2.2})$$

The θ_i represent both μ and all nuisance parameters θ ($\theta_0 = \mu$ and $\sigma^2 = V_{00}$). In the case, the pdf of test statistic $q_\mu = -2 \ln \lambda(\mu)$ is approximated to be a non-central chi-square distribution for one degree of freedom,

$$f(q_\mu; \Lambda) = \frac{1}{2\sqrt{q_\mu}} \frac{1}{\sqrt{2\pi}} \left\{ \exp \left[-\frac{1}{2} \left(\sqrt{q_\mu} + \sqrt{\Lambda} \right)^2 \right] + \exp \left[-\frac{1}{2} \left(\sqrt{q_\mu} - \sqrt{\Lambda} \right)^2 \right] \right\}, \quad (\text{C.2.3})$$

where the non-centrality parameter Λ is

$$\Lambda = \frac{(\mu - \hat{\mu})^2}{\sigma^2}. \quad (\text{C.2.4})$$

The uncertainties of each parameter can be calculated by the covariance matrix. The formula is described as

$$\Delta \theta_i = \sum_{j,k} F^T(\theta_i, \theta_j) \tilde{V}_{jk}^{-1} F(\theta_i, \theta_k) \quad (\text{C.2.5})$$

$$= \sum_{j,k}^i \Delta \theta_j V_{jk}^{-1} \Delta \theta_k \quad (\text{C.2.6})$$

where \tilde{V}_{jk}^{-1} is the inverse of the submatrix obtained from restricting the full covariance matrix to the parameters of interest.

In order to estimate the σ , Asimov data set which evaluates the estimators for all parameters is introduced. To simplify the notation is defined as following

$$\nu_i = \mu' s_i + b_i. \quad (\text{C.2.7})$$

The $\ln L$ becomes zero at ML estimators $\hat{\theta}_j$, then the derivatives of $\ln L$ satisfies

$$\frac{\partial \ln L}{\partial \theta_j} = \sum_{i=1}^N \left(\frac{n_i}{\nu_i} - 1 \right) \frac{\partial \nu_i}{\partial \theta_j} = 0 \quad (\text{C.2.8})$$

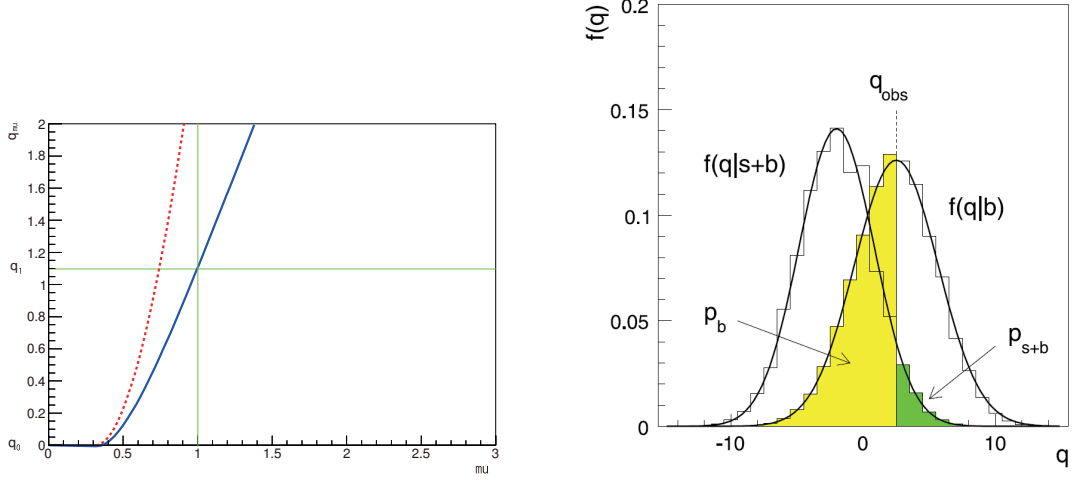


Figure C.1: Example of q_μ (left) and the distributions both $f(\tilde{q}_\mu|\mu = 0)$ and $f(\tilde{q}_\mu|\mu = 1)$ (right) [71].

In the Asimov data set $n_{i,A}$ are equal to the expectation value

$$n_{i,A} = E[n_i] \nu_i = \mu' s_i(\theta) + b_i(\theta), \quad (\text{C.2.9})$$

and the ‘‘Asimov likelihood’’ L_A and corresponding profile likelihood ratio λ_A are given

$$\lambda_A(\mu) = \frac{L_A(\mu, \hat{\theta})}{L_A(\hat{\mu}, \hat{\theta})} = \frac{L_A(\mu, \hat{\theta})}{L_A(\mu', \hat{\theta})}. \quad (\text{C.2.10})$$

Because the Asimov data set corresponding to a signal strength μ' gives $\mu' = \hat{\mu}$, then

$$-2 \ln \lambda_A(\mu) \approx \frac{(\mu - \mu')^2}{\sigma^2} = \Lambda \quad (\text{C.2.11})$$

is obtained from Equation C.2.1. By using the equation, the variance σ^2 is obtained as following

$$\sigma_A^2 = \frac{(\mu - \mu')^2}{q_{\mu,A}} \quad (\text{C.2.12})$$

where $q_{\mu,A} = -2 \ln \lambda_A(\mu)$.

For finding the median exclusion, significance for the hypothesis μ assuming that there is no signal, $\mu' = 0$ is substituted into Equation C.2.12

$$\sigma_A^2 = \frac{\mu^2}{q_{\mu,A}}, \quad (\text{C.2.13})$$

and discovery case $\mu = 0$ is tested

$$\sigma_A^2 = \frac{\mu'^2}{q_{0,A}}. \quad (\text{C.2.14})$$

C.3 Experimental Sensitivity

The experimental sensitivity is estimated from the discrepancy of pdf $f(\tilde{q}_\mu|\mu)$ between the background-only hypothesis and the signal-plus-background hypothesis. Figure C.1 (left) shows an example of the distributions of \tilde{q}_μ . The values of \tilde{q}_0 and \tilde{q}_1 are obtained from the profile likelihood function scanned with the signal strength μ . The toy pseudo-experiment or asymptotic method give the pdf of the $f(\tilde{q}_\mu|0)$ and $f(\tilde{q}_\mu|1)$. Figure C.1 (right) shows a example of the pdf $f(\tilde{q}_\mu|0)$ and $f(\tilde{q}_\mu|1)$. The observed confidence level of the signal-plus-background

hypothesis CL_{s+b} and the background-only hypothesis CL_b are given as

$$CL_{s+b} = 1 - p_\mu = 1 - \int_{\tilde{q}_{\mu, \text{obs}}}^{\infty} f(\tilde{q}_\mu | \mu = 1) d\tilde{q}_\mu, \quad (\text{C.3.1})$$

$$CL_b = 1 - p_b = \int_{\tilde{q}_{\mu, \text{obs}}}^{\infty} f(\tilde{q}_\mu | \mu = 0) d\tilde{q}_\mu. \quad (\text{C.3.2})$$

On the other hand, the expected confidence level are given to replace the $\tilde{q}_{\mu, \text{obs}}$ to the $\text{median}[q_\mu | \mu=1]$ and $\text{median}[q_\mu | \mu=0]$ for the exclusion and discovery, respectively. In this analysis the CL_s is introduced to suppress the statistical fluctuation

$$CL_s = \frac{CL_{s+b}}{1 - CL_b}. \quad (\text{C.3.3})$$

If $CL_s > 0.95$, the signal point is regarded as exclusion. On the other hand, if $CL_b > 1 - 2.87 \times 10^{-7}$, then the signal point is regarded as discovery.

The error band of $\pm N\sigma$ for the expected limit of signal strength are estimated as follow

$$\text{band}_{N\sigma} = \mu' + \sigma [\Phi^{-1}(1 - \alpha) \pm N] \quad (\text{C.3.4})$$

where Φ is the cumulative distribution of the standard Gaussian, $(1 - \alpha)$ is a confidence level, respectively. The standard deviation σ is given by the Asimov data set.

C.4 Fit Configuration

C.4.1 Fit Parameters

The main background normalizations and the signal yields are estimated by applying the simultaneous fit that means the same profiling value for each parameter is implemented in the all control regions and signal regions. The two type of fit parameters are provided as following. The profiling likelihood method are applied to the both parameters and these are calculated by using the pdf.

- Free parameters
The normalization of signal component and main backgrounds are fitted by using free scales without any constrains.
- Nuisance parameter
All systematic and statistic uncertainties are inputted as the nuisance parameters. Each nuisance parameter is performed to the distribution or weight by applying the $\pm 1\sigma$ uncertainty. The likelihood function profiles the most probable value of each free parameter within the $\pm 1\sigma$ bandwidth of nuisance parameters. The nuisance parameters are constrained by using the covariance matrix in Equation C.2.6.

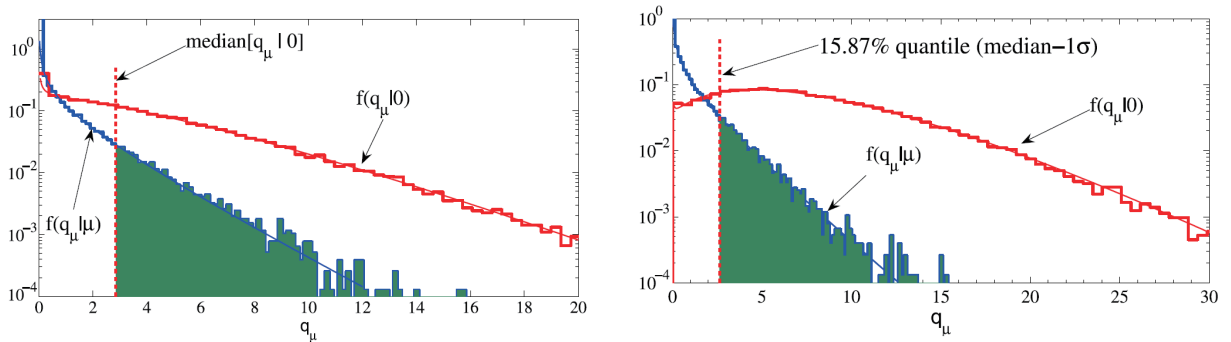


Figure C.2: Distributions both $f(\tilde{q}_\mu | \mu = 0)$ and $f(\tilde{q}_\mu | \mu = 1)$ and relation to the $\text{median}[q_\mu | \mu = 0]$ (left) and $\text{median}[q_\mu | \mu = 0] - 1\sigma$ (right) [71]. The $\pm 1, \pm 2\sigma$ band of the expected limit estimated these distributions.

- Probability Density Function (pdf)

Both free and nuisance parameters are estimated the probability density function (pdf) of the profile likelihood ratio \tilde{q}_μ in each bin of all histograms of the control regions and signal regions, respectively.

The optimal values and errors of both the free parameters and nuisance parameters are determined simultaneously by calculating the likelihood function to fit to data in both the control regions and signal regions and the covariance matrix.

C.4.2 Fit Configurations

To conclude whether the searching model exists or not, the background-only model and the signal-plus-background model are compared with the observed data. The three type configurations are prepared to discuss such issues as below

- Background-only fit
This configuration assumes that the distributions in both the control regions and signal regions consist of background-only components. Then the normalizations of only background are fitted simultaneously to data in the regions on the condition that the any signal contributions do not exist everywhere.
- Discovery fit
The discovery fit is applied to the background-only hypothesis and the observed data, and estimate the discrepancy between the hypothesis and data as the confidence level of background-only hypothesis CL_b . This configuration inputs a dummy signal event into the signal regions and fit it to data, although the background-only hypothesis is fitted to data in the control regions and the normalizations of backgrounds are determined in the control regions. In this case, the dummy signal events in signal regions are independently scaled by compensating the discrepancy between data and background-only hypothesis, then the normalization of dummy signal is equivalent with the signal cross section.
- Exclusion fit
In case that the estimation of the discrepancy between the signal-plus-background hypothesis and the observed data is significant, we can conclude the signal model is excluded. This configuration compares the signal-plus-background hypothesis with observed data. The confidence level of the hypothesis CL_s are estimated by scanning the signal strength μ in 20 steps between $\pm 4\sigma$ from the most probable value of $\hat{\mu}$. The upper limit for signal strength μ' is determined as the p -value fall below 5%.

C.4.3 Fit Options

The background distribution is determined by calculating the most probable value within the nuisance parameters. There are some kind of the fit method which determine the width of nuisance parameter. In this analysis, the width of nuisance parameters are determined by taking the difference of distributions where $\pm 1\sigma$ uncertainties are applied. The width is inputted into the fit as a probable density function and the fit is executed within the width. These fitting options are described below

- overallSys
The overallSys inputs the nuisance parameters into the distribution uniformly. The option scales the background distribution by using α to be fitted to data within the width which is determined by nuisance parameters. The α is the global scale factor in units of the width. Therefore this option vary the normalization of distribution but the shape of distribution does not change. The nuisance parameter is constrained by the covariance matrix as $\gamma \cdot \sigma$ where γ is coefficient of nuisance parameter and σ is the input nuisance parameter. Figure C.3 shows the histograms before and after fitting.
- HistoSys
The HistoSys inputs the nuisance parameter into each bin in distribution. Therefore the widths of nuisance parameters are different bin by bin. The background distribution is fitted within the widths to minimize the likelihood function as well as overallSys. The HistoSys calculate the α as scale factor in units of the width. The distribution after fit is varying because of difference of widths. The nuisance parameters are constrained as $\gamma \cdot \sigma$ by taking the covariance matrix as well as overallSys. Figure C.3 also shows the histograms before and after fitting.

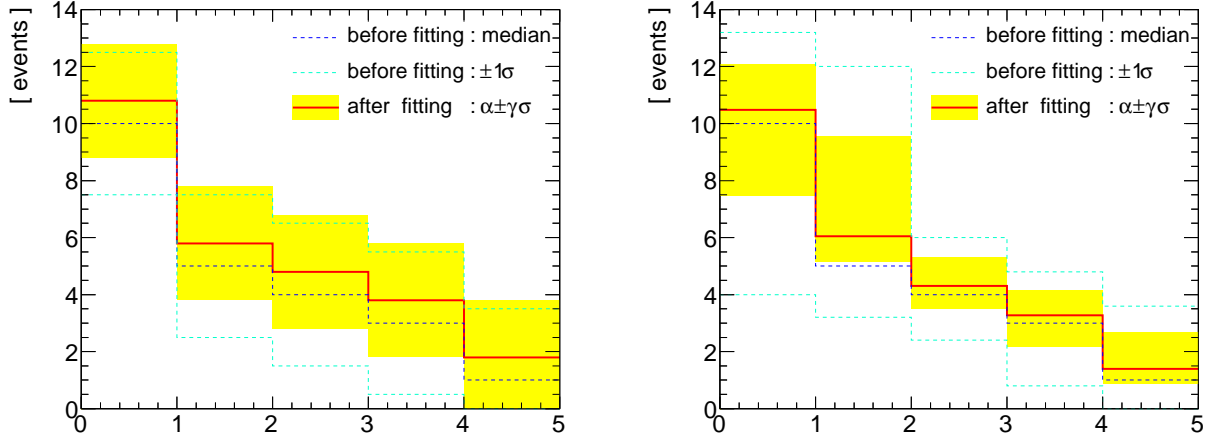


Figure C.3: Example of the overallSys (left) and HistoSys (right) options. The dashed lines show the distribution and uncertainty. The overallSys gives all histogram bins the same space to fit uniformly while the HistoSys gives each histogram bin the corresponding space to fit.

- normHistoSys
The normHistoSys option is the same operation as the HistoSys except the normalization. This option keeps the normalization but changes the shape.
- MCStatError
This option calculates a Poisson statistical uncertainty derived from the MC statistic. This uncertainty is applied independently to the each bin and does not effect to shift the content of histogram but multiply to the uncertainty of each bin as $(\alpha \pm \gamma) \cdot \sigma$.

C.5 Closure Test

The analysis employs HistFitter tool provided from ATLAS SUSY one lepton analysis group. This tool calculates the likelihood function and the covariance matrix by inputting the systematic uncertainties and the interesting parameters. In this section, this tool would be confirmed whether the fitting results are correct or not by using pseudo-data. The pseudo-data are generated to the same as the background MC samples including W +jets, Z +jets, $t\bar{t}$, single-top and dibosons MC samples. In addition the pseudo-data samples are added the signal samples where numbers of the events are multiplied by $\times 0.1$, $\times 0.2$, $\times 0.5$, $\times 0$, $\times 1$, $\times 2$, $\times 5$ and $\times 10$, respectively. The signal-plus-background distribution are fitted to that of pseudo-data and confirmed that the fitting results show the signal strengths as 0.1, 0.2, 0.5, 0, 1, 2, 5 and 10, respectively. In order to make the simple condition, only statistical uncertainty is applied to each bin. The fitting results are shown in Figure C.5 and Table C.2. These results show the sample corresponding with each signal strength is fitted by its signal strength. Therefore fitting results obtained from this tool are valid.

It is afraid that the signal strength is constrained by fitting in the control regions. Therefore the signal yield is confirmed in low statistic region for the signal model. The fit result at $m_{\tilde{g}} = 665$ GeV and $m_{LSP} = 585$ GeV for the simplified SUSY $\tilde{g}\text{-}\tilde{g}$ pair production in both W +jets and $t\bar{t}$ control regions and signal region is shown in Figure C.6. The background events are constrained strictly due to large statistic in the control regions while the statistical uncertainty becomes large for signal events. Therefore the signal strength is determined to compensate for the discrepancy between observed data and background estimation in the signal regions. In the signal point the signal yield is small, thus the figures show the signal contribution is visible though the uncertainty is large. According to the results, the signal strength can be fitted properly by HistFitter tool.

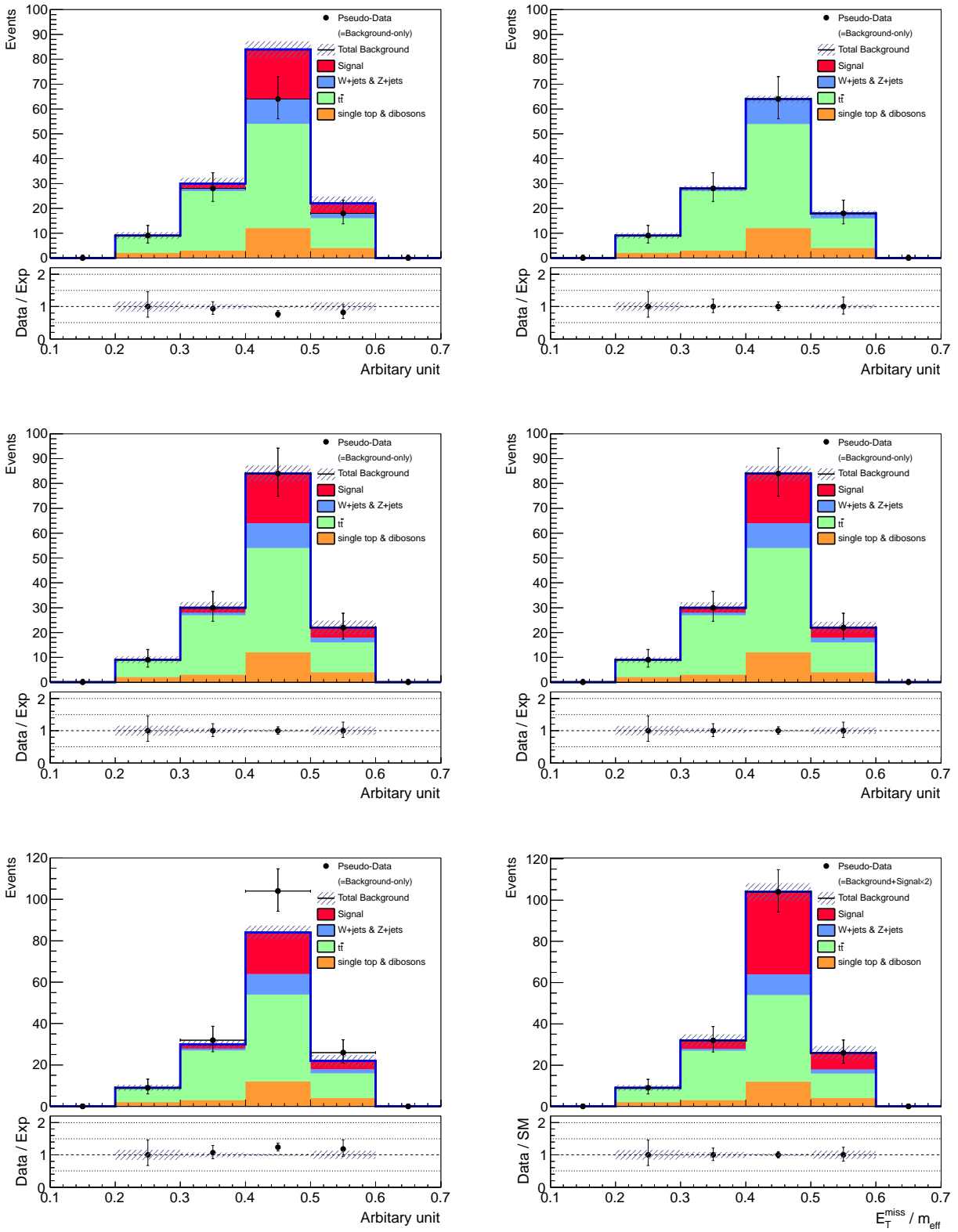


Figure C.4: Results of closure test with the HistFitter before fitting (left) and after fitting (right). The pseudo-data including $\times 0$ (top), $\times 1$ (middle) and $\times 2$ (bottom) of signal events are fitted by the background samples and signal samples.

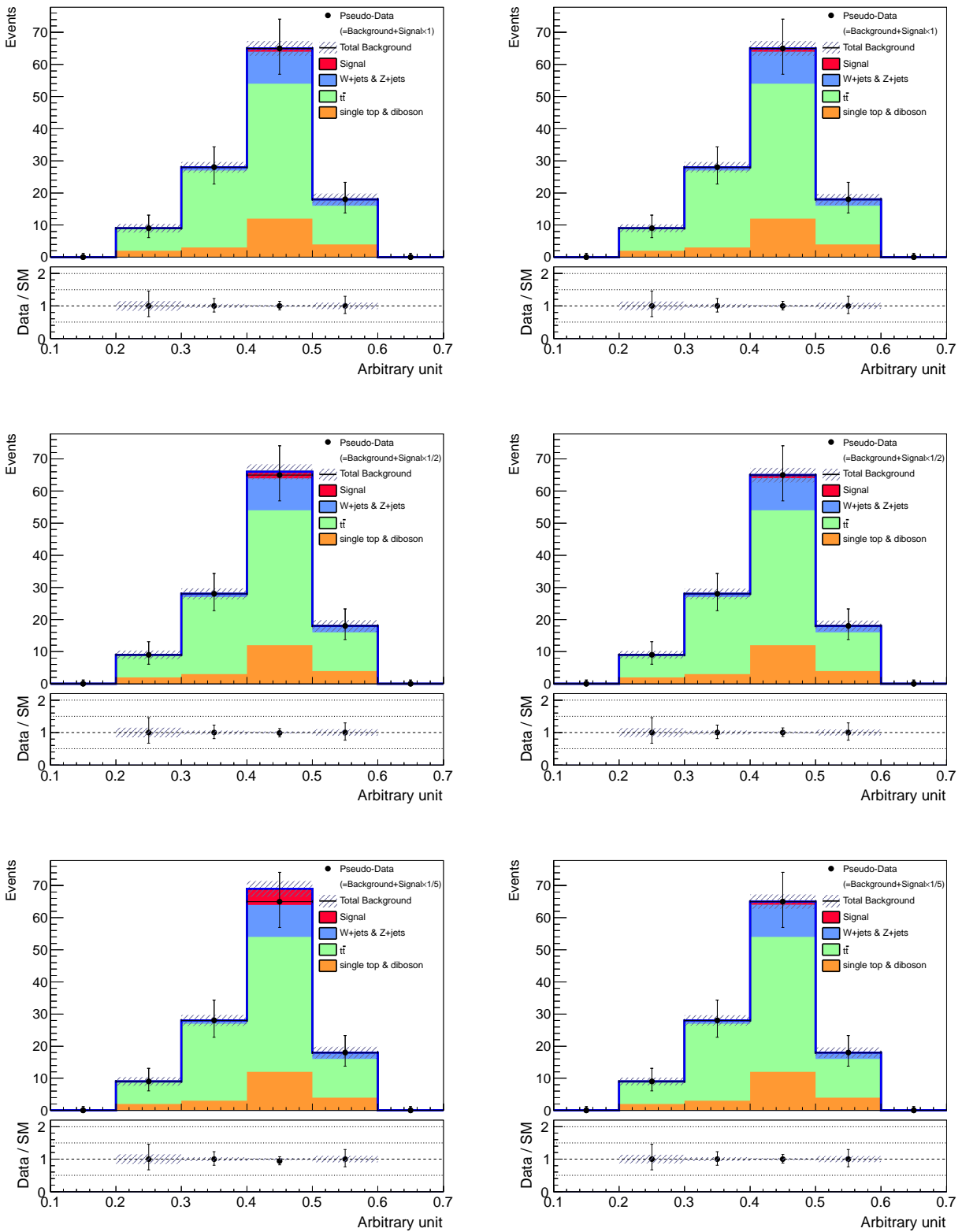


Figure C.5: Results of closure test with the HistFitter before fitting (left) and after fitting (right). The pseudo-data including signal events are fitted by the background samples plus $\times 1$ (top), $\times 5$ (middle) and $\times 10$ (bottom) signal events.

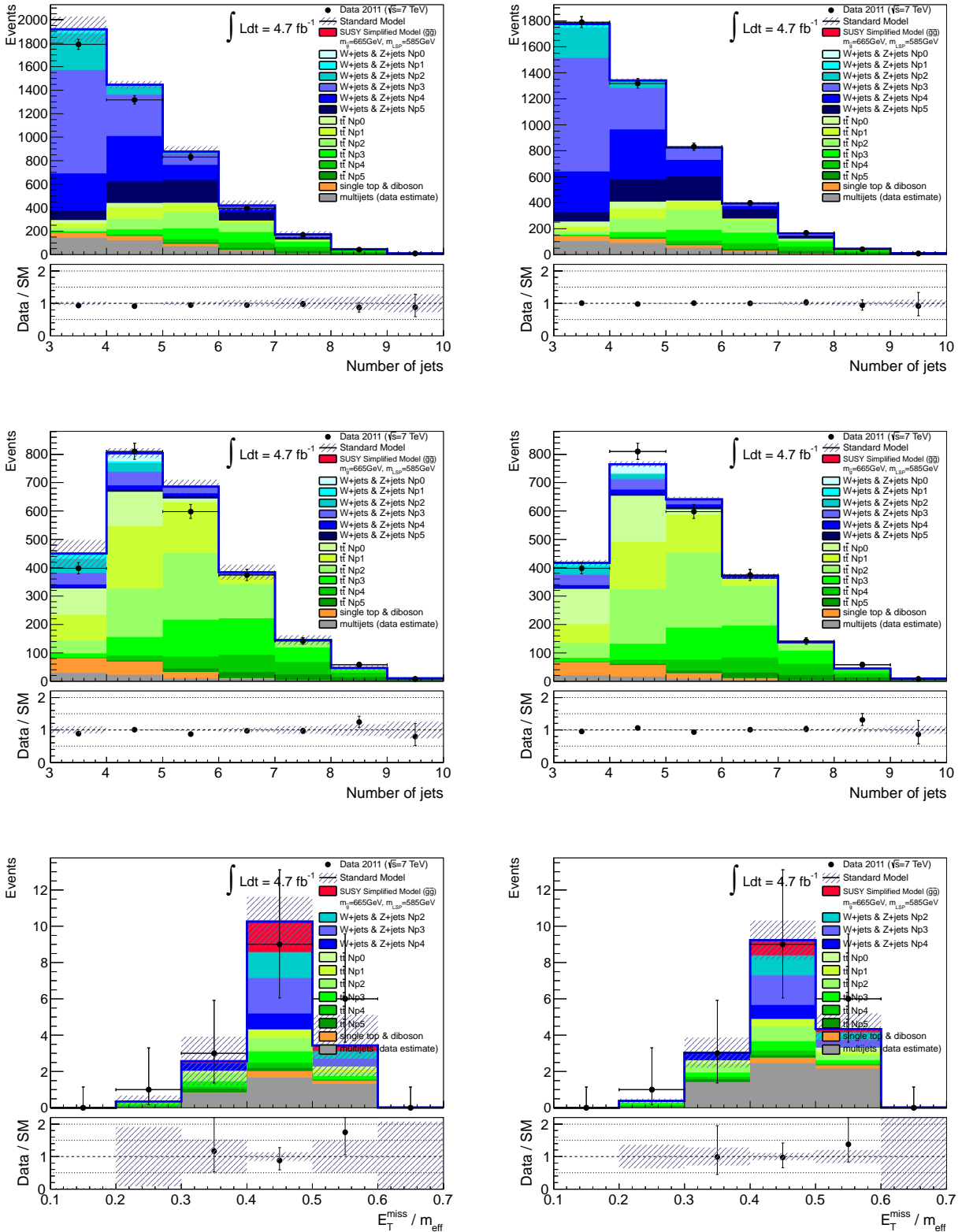


Figure C.6: Simultaneous fit results in HistFitter before fitting (left) and after fitting (right). Used signal model is simplified SUSY model at $m_{\tilde{g}} = 665$ GeV, $m_{\tilde{LSP}} = 585$ GeV.

signal strength	$\times 0$	$\times 1$	$\times 2$	$\times 5$	$\times 10$
signal	$(0.03 \pm 897) \times 10^{-3}$	1.00 ± 0.33	2.00 ± 0.43	5.01 ± 0.69	10.00 ± 1.03
W+jets & Z+jets	1.00 ± 0.02	1.00 ± 0.03	1.00 ± 0.03	1.00 ± 0.03	1.00 ± 0.03
$t\bar{t}$	1.00 ± 0.02	1.00 ± 0.02	1.00 ± 0.02	1.00 ± 0.02	1.00 ± 0.02
single top & dibosons	1.00 ± 0.06	1.00 ± 0.09	1.00 ± 0.06	1.00 ± 0.09	1.00 ± 0.09

signal strength	$\times 0.1$	$\times 0.2$	$\times 0.5$	$\times 1.0$
signal	0.09 ± 0.42	0.20 ± 1.22	0.48 ± 3.03	1.00 ± 10.1
W+jets & Z+jets	1.00 ± 0.02	1.00 ± 0.03	1.00 ± 0.03	1.00 ± 0.03
$t\bar{t}$	1.00 ± 0.02	1.00 ± 0.02	1.00 ± 0.02	1.00 ± 0.02
single top & dibosons	1.00 ± 0.06	1.00 ± 0.09	1.00 ± 0.09	1.00 ± 0.09

Table C.1: Results of the closure test in HistFitter tool.

normalizations			
signal ($m_{\tilde{g}} = 665$ GeV, $m_{\text{LSP}} = 585$ GeV)	0.61 ± 1.03		
W+jets & Z+jets Np0	1.0	$t\bar{t}$ Np0	0.69 ± 0.24
W+jets & Z+jets Np1	1.0	$t\bar{t}$ Np1	1.11 ± 0.07
W+jets & Z+jets Np2	1.21 ± 0.13	$t\bar{t}$ Np2	1.00 ± 0.09
W+jets & Z+jets Np3	0.80 ± 0.11	$t\bar{t}$ Np3	0.94 ± 0.06
W+jets & Z+jets Np4	0.98 ± 0.07	$t\bar{t}$ Np4	0.94 ± 0.06
W+jets & Z+jets Np5	0.76 ± 0.22	$t\bar{t}$ Np5	0.94 ± 0.06
single top & dibosons	1.00 ± 0.06		

Table C.2: Fit results of HistFitter tool by using simplified SUSY model at $m_{\tilde{g}} = 665$ GeV, $m_{\text{LSP}} = 585$ GeV.

C.6 Signal-Strength-Only Fit Results

Until 2011 summer results, the background events are normalized in only the control regions, not simultaneous fit in both control regions and signal regions. In the old method, background are corrected by the normalizations in Table 7.3, but shape corrections and signal contributions to the control regions and signal regions are neglected.

The exclusion regions for simplified SUSY model and UED model after applying the old method are shown in Figure C.7.

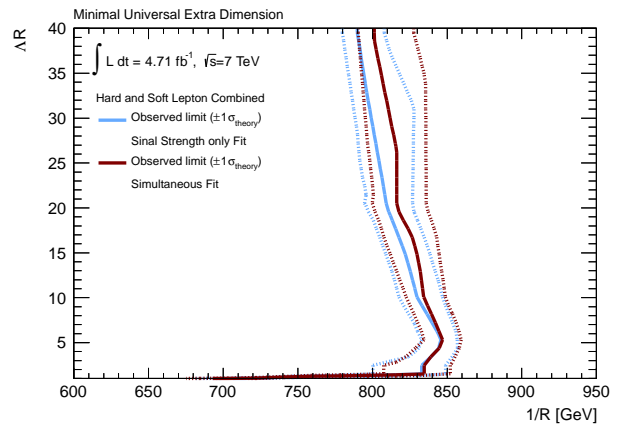
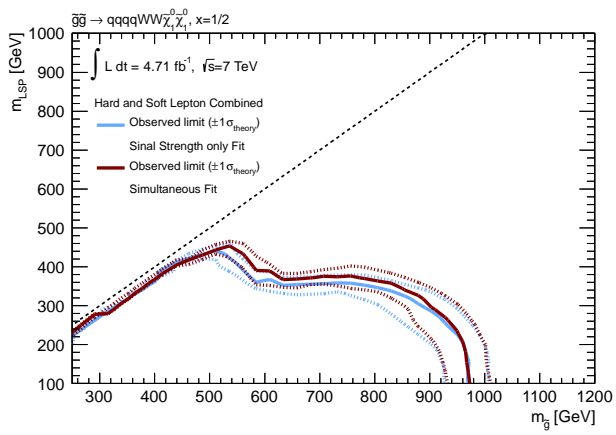


Figure C.7: 95% CL_s exclusion limits for simplified SUSY model (left) and UED model (right) by using signal strength only fit.

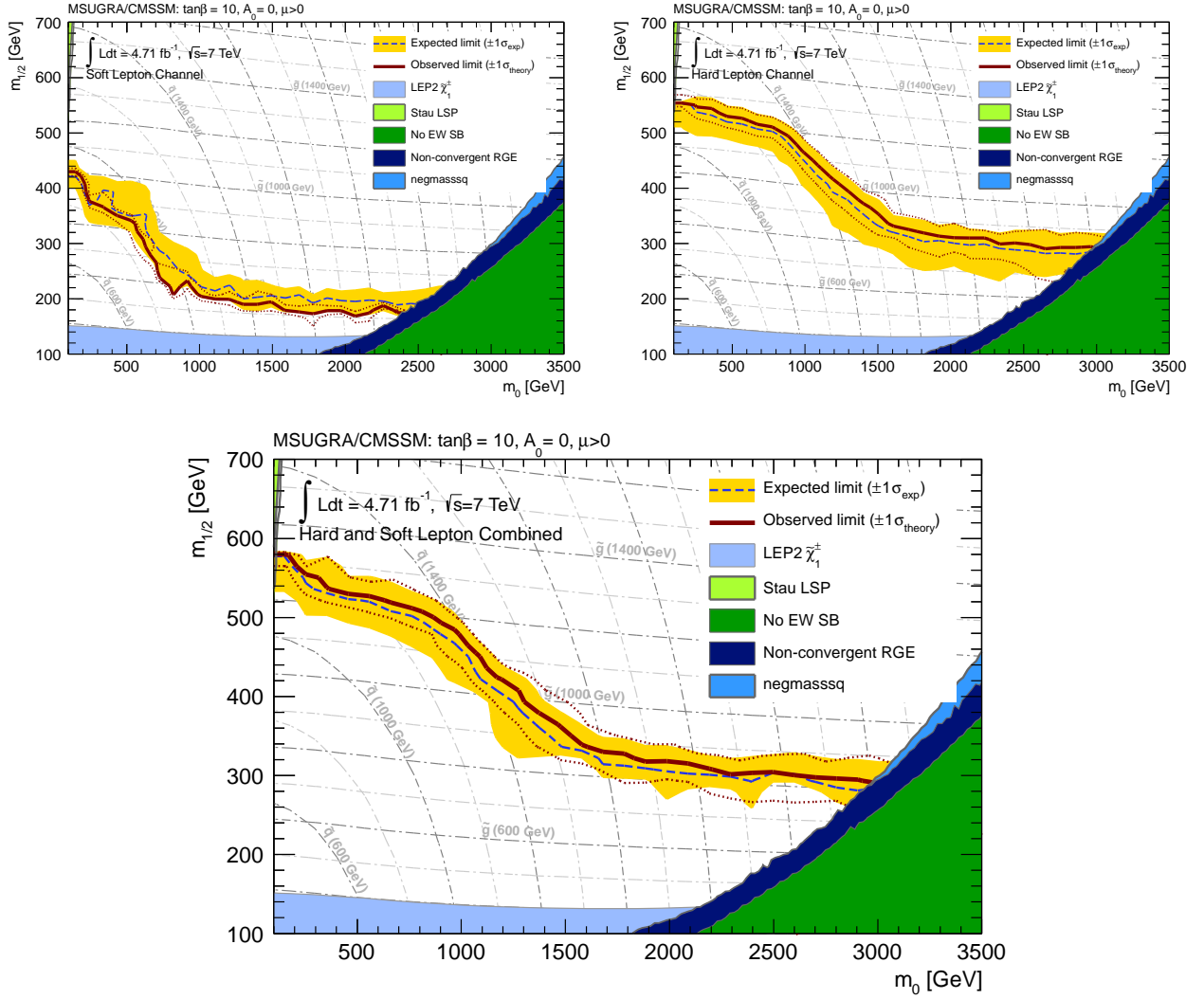


Figure C.8: Exclusion limits at 95% CL with the MSUGRA in the soft lepton channel (top-left), hard lepton channel (top-right) and combined result (bottom), respectively.

C.7 Exclusion Region for SUSY models

In following sections, the exclusion region at 95% CL_s upper limit for MSUGRA, simplified SUSY models containing squark pair productions and gluino pair production with fixing m_{LSP} at 60 GeV are shown.

MSUGRA exclusion region

The excluded regions for the MSUGRA are shown in Figure C.8. The red solid line and dashed line show the observed exclusion limit with the nominal and the $\pm 1\sigma$ theoretical cross section, respectively. The blue dashed line and yellow band show the nominal and $\pm 1\sigma$ exclusion limit, respectively. The exclusion region of the hard and soft lepton channel combined reaches the $m_0 \sim 3000$ GeV and $m_{1/2} \sim 580$ GeV. These results correspond with $m_{\tilde{g}} \sim 800$ GeV and $m_{\tilde{q}} \sim 1200$ GeV.

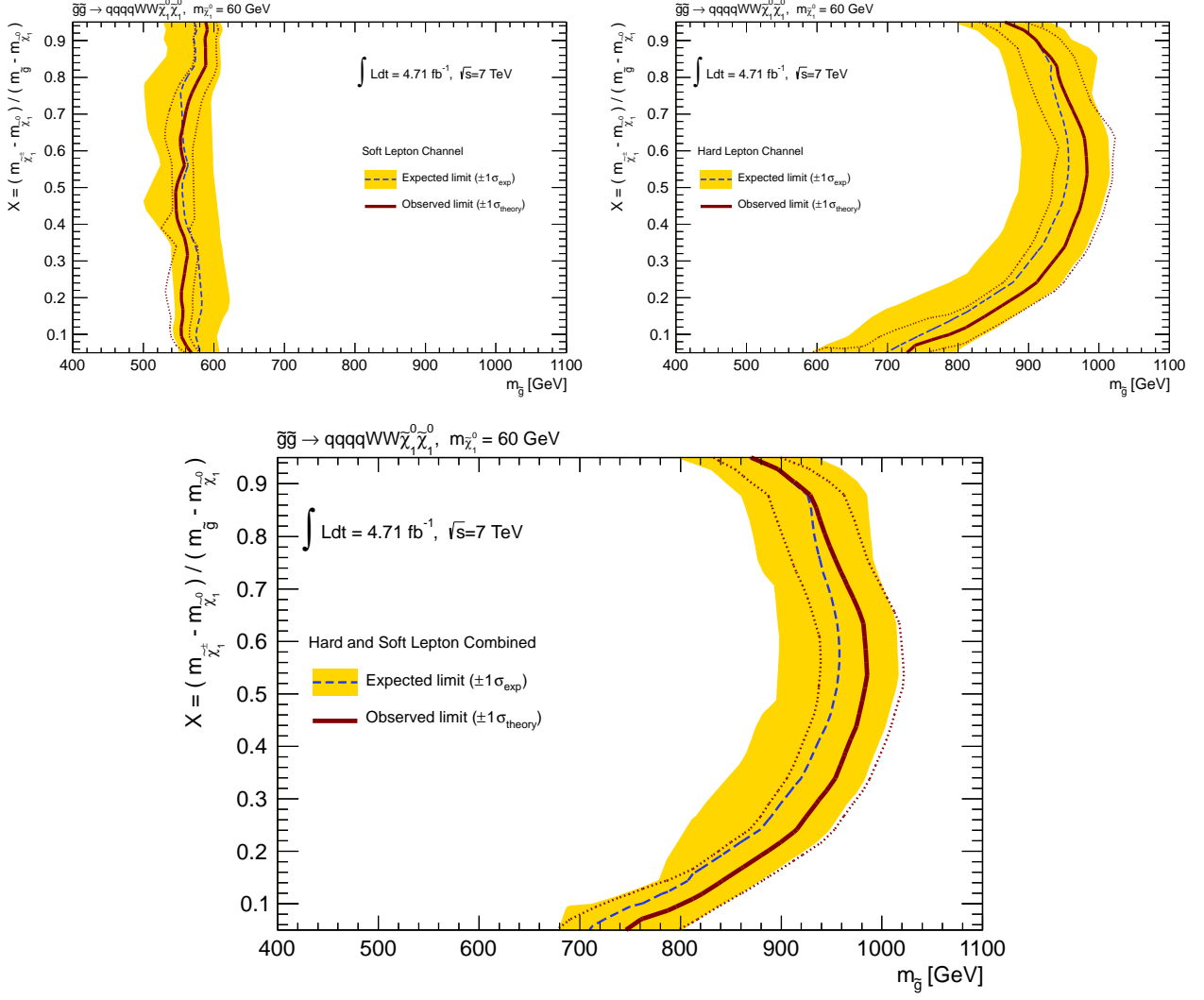


Figure C.9: Exclusion limits at 95% CL with the simplified model gluino pair production with $X = (m_{\tilde{g}} - m_{\tilde{\chi}_1^\pm})/(m_{\tilde{g}} - m_{\tilde{\chi}_1^0})$ samples fixing the LSP mass at 60 GeV for the soft lepton channel (top-left), hard lepton channel (top-right) and combined results (bottom), respectively.

Simplified SUSY model (\tilde{g} - \tilde{g} Pair Production with fixing at $m_{\text{LSP}} = 60$ GeV)

The simplified model is considered for varying the chargino mass and the LSP mass is fixed at 60 GeV. The soft lepton channel is sensitive to the small $X (= [m_{\tilde{\chi}_1^\pm} - m_{\tilde{\chi}_1^0}]/[m_{\tilde{g}} - m_{\tilde{\chi}_1^0}])$ region since the mass difference between chargino and neutralino are small. The exclusion limit for the signal samples are shown in Figure C.9. The soft lepton channel contributes little to exclude the signals since the exclusion limit for the hard lepton channel extend to large $m_{\tilde{g}}$ region. In the combined result, the exclusion limit reaches the $m_{\tilde{g}} \sim 740$ GeV at small X region and $m_{\tilde{g}} \sim 860$ GeV at large X region.

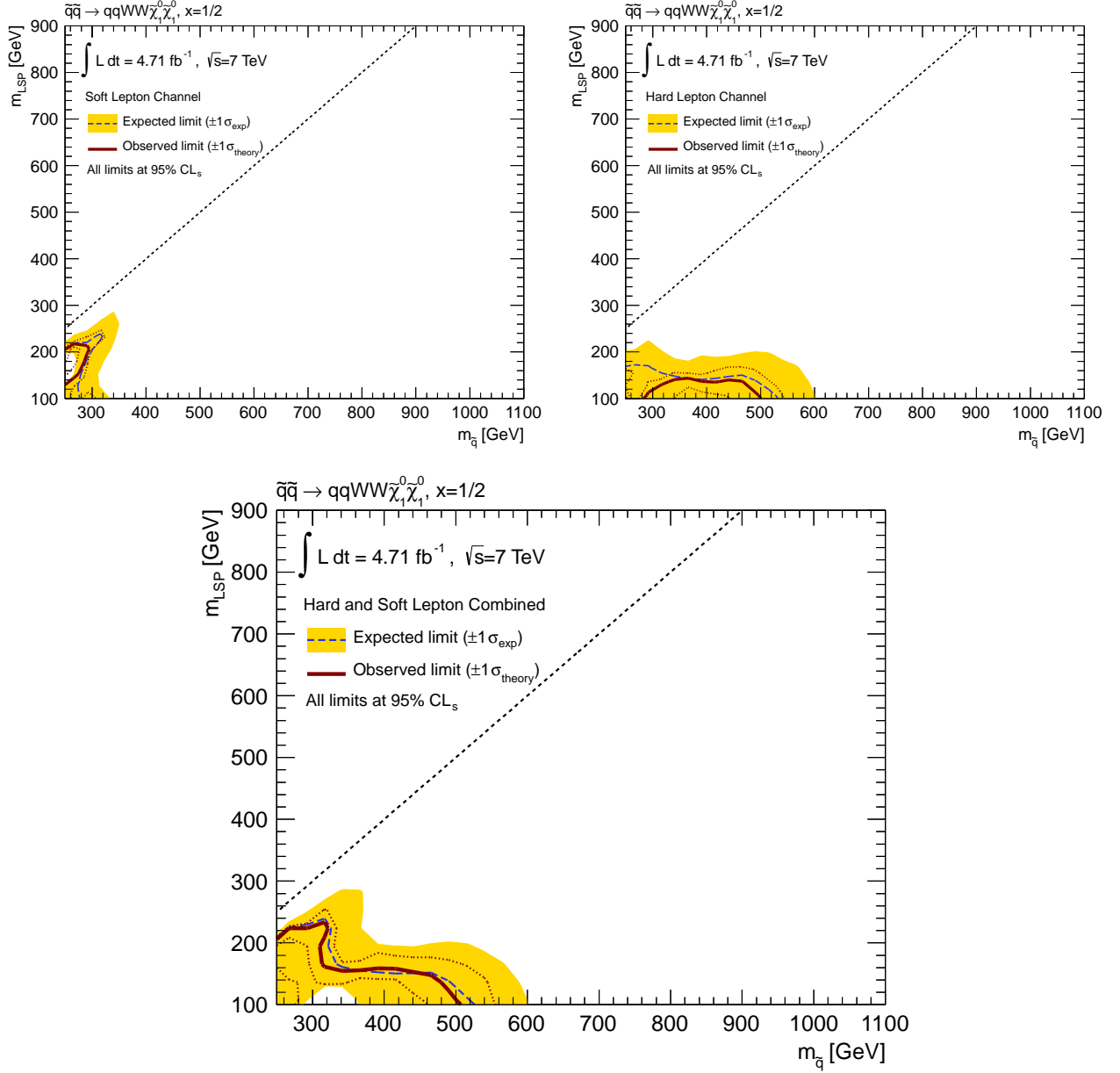


Figure C.10: Exclusion limits at 95% CL with the simplified model squark pair production with $X = (m_{\tilde{\chi}_1^\pm} - m_{\tilde{\chi}_1^0}) / (m_{\tilde{q}} - m_{\tilde{\chi}_1^0}) = 1/2$ samples for the soft lepton channel (top-left), hard lepton channel (top-right) and combined results (bottom), respectively.

Simplified SUSY model (\tilde{q} - \tilde{q} Pair Production)

The cross sections of \tilde{q} - \tilde{q} pair production are smaller than that of \tilde{g} - \tilde{g} pair production due to parton distribution function. The signal sensitivity in diagonal region for the squark production are larger than the hard lepton channel as well as gluino production. Figure C.10 shows the exclusion limit at 95% CL on the $m_{\tilde{q}}$ - m_{LSP} plane and the limit reaches to $m_{\tilde{q}} \sim 320$ GeV in such region.

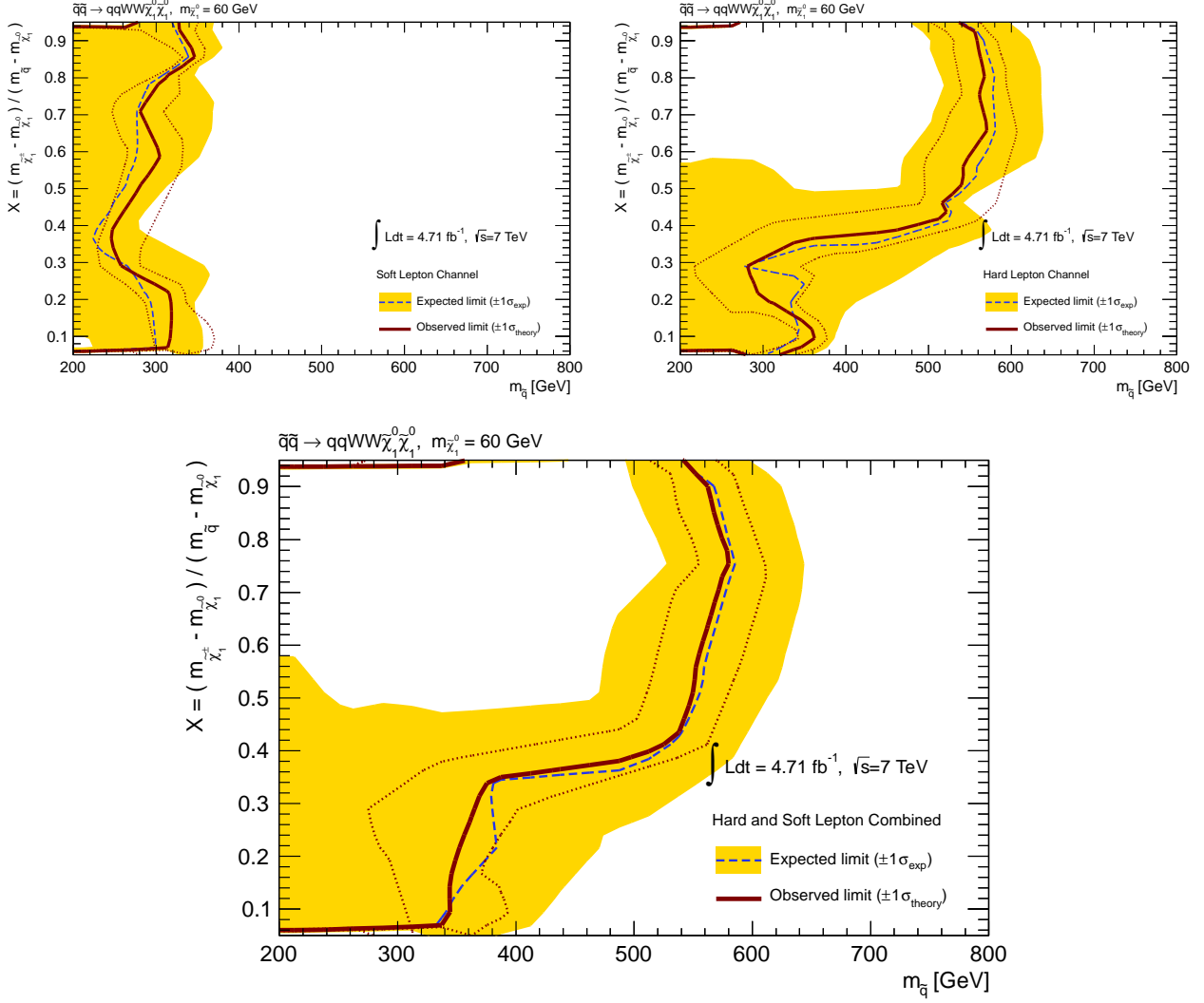


Figure C.11: Exclusion limits at 95% CL with the simplified model squark pair production with $X = (m_{\tilde{\chi}_1^\pm} - m_{\tilde{\chi}_1^0}) / (m_{\tilde{q}} - m_{\tilde{\chi}_1^0})$ samples fixing the LSP mass at 60 GeV for the soft lepton channel (top-left), hard lepton channel (top-right) and combined results (bottom), respectively.

Simplified SUSY model (\tilde{q} - \tilde{q} Pair Production with fixing at $m_{\text{LSP}} = 60$ GeV)

The exclusion limits for \tilde{q} - \tilde{q} production with fixing the LSP mass at 60 GeV are shown in Figure C.11. The contribution from the soft lepton channel is shown at small X region around $m_{\tilde{q}} \sim 350$ GeV. The exclusion limit reaches to $m_{\tilde{q}} \sim 540$ GeV in large X region and $m_{\tilde{q}} \sim 340$ GeV in small X for combined result.

Appendix D

Electromagnetic Scale Calibration in Tile Calorimeter

D.1 Introduction

In the summer and autumn of 2004, the combined ATLAS test beam (CTB) took place at CERN beam line of SPS [73]. This was the first time all the detectors in ATLAS were tested together and many of the systems were final production versions. The level-1 trigger, combining signals from the calorimeter and muon system has also been tested during the test beam.

Our purpose on this analysis is to validate the EM scale by calculating the energy depositions of single muon per unit length (i.e. $dE/d\ell$) and comparing the values to the MC predictions with the tile calorimeter. We also validate the layer inter-calibration. The EM scale validation were already performed by using the cosmic ray muons in 2008, 2009 and 2010 [74]. These results show

- upper limits on the average non uniformity of the response of the cells within a layer that was estimated to be about 2%.
- the response of the third longitudinal layer of the barrel differs from the ones of first and second barrel layer by about 4 and 3 sigma respectively.
- the differences between the energy scales of each layer obtained using muons and the value set at test beams using electrons was found to range between -3% and +1%.
- the stability of the Tile calorimeter response to cosmic rays in the years 2008, 2009 and 2010 was estimated to be at the level of 1% in the long barrel layer.

The cosmic-ray muons are not projective and a reconstruction of the path in each cell is necessary to determine $dE/d\ell$. Their momentum ranges between 10 GeV and 30 GeV. The CTB muons are projective and monochromatic. They have been used to cross-check the results obtained using cosmic-rays.

D.2 Experimental Setup

D.2.1 CTB setup

The H8 beam line provided hadrons, electrons, muons with energies from 1 up to 350 GeV for the combined ATLAS test beam. The H8 beam was created by extracting a up to 400 GeV/c proton beam from the Super Proton Synchrotron. Typical intensity of this primary beam are a few 10^{12} protons per burst. The secondary beam created from a Beryllium target and had energies from 10 to 350 GeV. A secondary filter target, 8 or 16 mm of lead or 1000mm Polyethylene, plus absorber, air or lead, can be placed in the beam to produce a tertiary beam of “pure” electrons (lead plus air) or pions (Polyethylene plus air).

In this combined ATLAS test beam, several detectors, for example the Scintillators (S1, S2, S3 in Figure D.3), the Beam Chambers (BC0, BC1, BC2 in Figure D.3), Cherenkov Counters were installed on the beam line to obtain beam information. The beam line consisted of a number of magnets, quadrapole and dipoles, for focusing and bending the particles in order to select the required momentum by controlling the magnet currents.

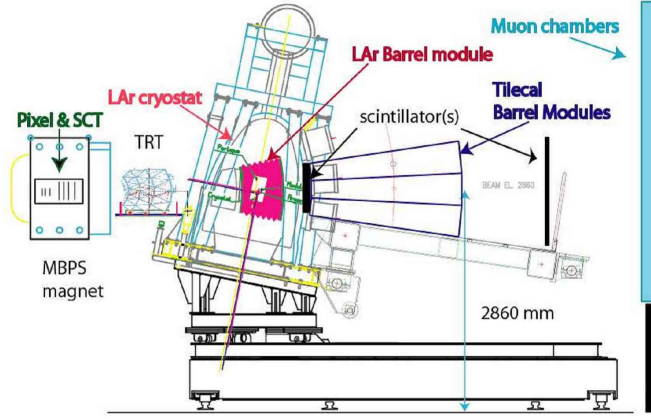


Figure D.1: Schematic view of the test beam table setup.



Figure D.2: Photo of the test beam setup.

η	η_{min}	η_{max}	ϕ_{min}	ϕ_{max}
0.25	0.10	0.41		
0.35	0.19	0.50		
0.45	0.30	0.61	0.8836	0.9818
0.55	0.39	0.70		
0.65	0.39	0.85		

Table D.1: Definition of calorimeter window

D.2.2 The Tile calorimeter

The ATLAS Tile Calorimeter (TileCal) is the central hadronic calorimeter for the ATLAS detector at the LHC [75]. Within the ATLAS detector, the tile calorimeter is located outside the liquid Argon calorimeter between the Liquid Argon electromagnetic calorimeter and the muon system. The detector is divided into three main sections, a central long barrel (LB) and two smaller extended barrels (EB) on each side. Each tile calorimeter barrel has three segmented radial sampling layers. The inner most layer is referred to as the A layer, the middle layer is the BC (or just B in the EB) and the outer most layer is the D layer. For the A and BC layers, the segmentation in $\Delta\eta$ is 0.1. The D layer is larger and each cell spans a range of $\Delta\eta = 0.2$. Each barrel consists of 64 wedges evenly spaced around. The granularity is 0.1. In this study, only a part of the LB and three wedges with the ϕ direction is used. The reach in terms of pseudo-rapidity η for the LB is from 0.0 to 1.0. Its construction consists of alternating steel and scintillator tiles orientated transversely with respect to the beam direction. A tile calorimeter cell consists of many steel absorber plates with scintillator sandwiched in between. On the two sides of each scintillating tile, wavelength shifting has been installed that shifts the ultraviolet light produced by the scintillator down to the visible light spectrum before delivering the light to a photomultiplier tube (PMT). The majority of cells are read out by two PMTs for redundancy.

D.3 Reconstruction and Event Selection

D.3.1 Reconstruction

We measure the energy depositions of muons in the tile calorimeter cells with given η and ϕ values. This window size is defined in Table D.1. The following criteria are used to reconstruct the energy depositions in the tile calorimeter.

- Select the cell in $|E| > 1\sigma_{noise}$, where E and σ_{noise} are the energy depositions in each cell and the electronic noise, respectively.
- Sum up the cell energies within a given calorimeter window in η (see the Table 1).

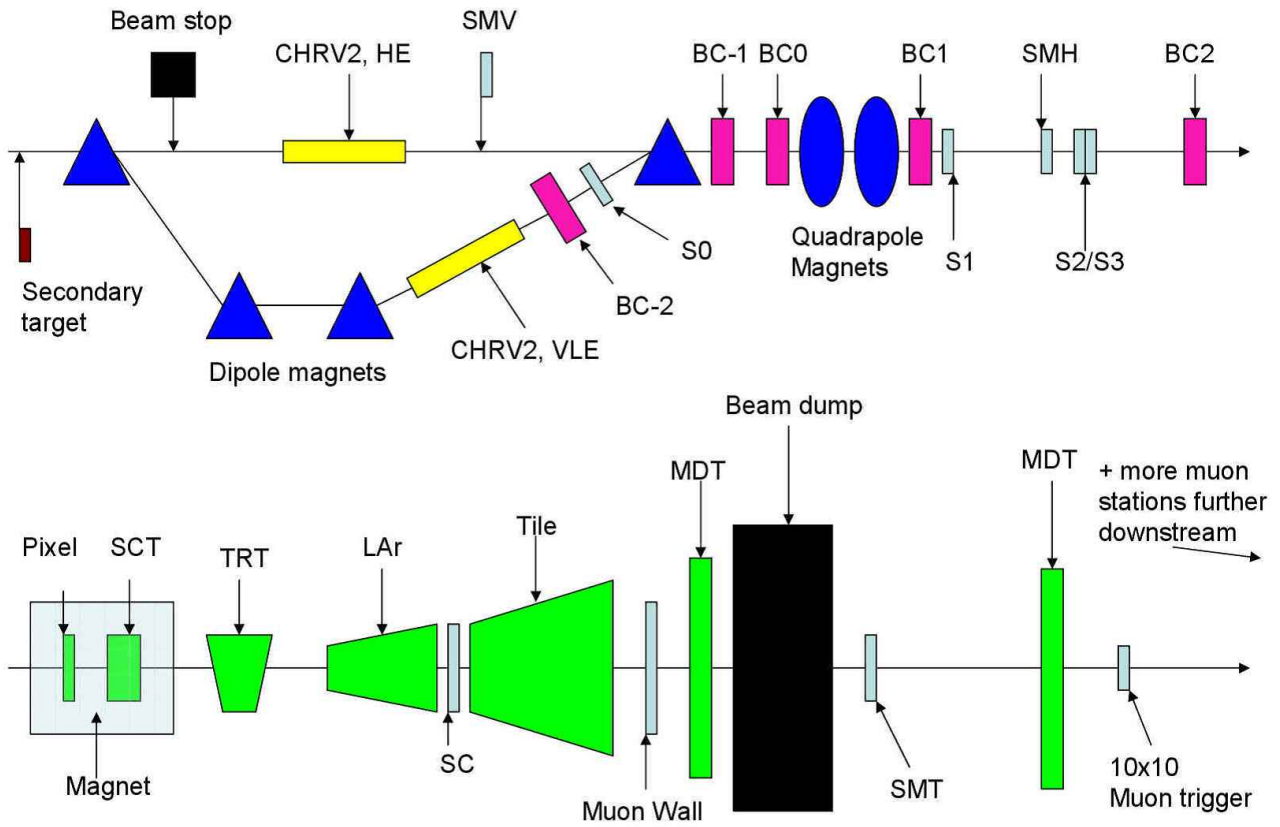


Figure D.3: Schematic outline of the beam line instrumentation, and also of the ATLAS sub-detector elements. In this test beam, the scintillators (S1, S2, S3) and beam chambers (BC0, BC1, BC2) were installed. The beam energy were determined by bending at dipole magnets. The muons fired the muon trigger.

D.3.2 Event Selection

For calculating $dE/d\ell$ of minimum ionizing muons, we apply the following selection criteria to the CTB data.

1. Require physics trigger.
2. Require signal from the muon tag scintillator (SMT). The SMT was placed downstream after the first beam dump and its dimensions is $40 \times 40 \times 2.0$ cm³ (see Figure D.3).
3. Remove the pile up events.

We remove the events in which the scintillator show high activities, since the pile-up events cause large energy deposition in the scintillators. Figure D.4 shows the distribution of energy deposition in the S3 scintillator. We apply 5% truncation to these energy distribution in the scintillators to cut pile up events.

4. Reject events in which muons point away from the center of beam.

By using beam chamber information, we reject the events in which muons point away from the center of beam. Applying this event selection is used the most downstream beam chamber BC2 since we can consider that the position in this beam chamber is near to the hit position on the tile calorimeter surface. Figure D.5 shows the hit distribution of beam muons in the BC2. This beam profile indicates that the muon hit position were spread to positive x direction by the bending magnet. We then apply 5% truncation to the hit distribution of this beam chamber (BC2).

5. Reject events other than MIP events.

We remove the events in which the tile calorimeter show high activities, since the multi-scattering events cause large energy deposition in the tile calorimeter. We then apply 1% truncation to the energy distribution in each layer of the tile calorimeter.

D.3.3 The Monte Carlo simulation

We generate the simulation events to compare with the CTB data as follows,

- The CTB was taken place in the beam energy equal to 20GeV, 50 GeV and 100 GeV, η equal to 0.25, 0.35, 0.45, 0.55 and 0.65. Then, in simulation, 10,000 single muon events are generated for each η and beam energies.
- We assume that the effects from the inner detector is negligible, muons are generated on the inner-surface of the Liquid Argon calorimeter (radius = 1400 mm) and injected into the center of a cell reproducing the experimental situation.
- The beam profile is emulated by smearing along η -direction uniformly between -25 mm and 25 mm from beam center (see Figure 5).

We consider that the detector geometry has been not changed but the reconstruction algorithm has been changed from the CTB setup. Then, the MC samples are generated using;

- Athena software release version 16.2.1.5
- ATLAS geometry version ATLAS-GEO-16-00-00
- signal reconstruction used the digitization algorithm which was used in the then CTB setup at 2004

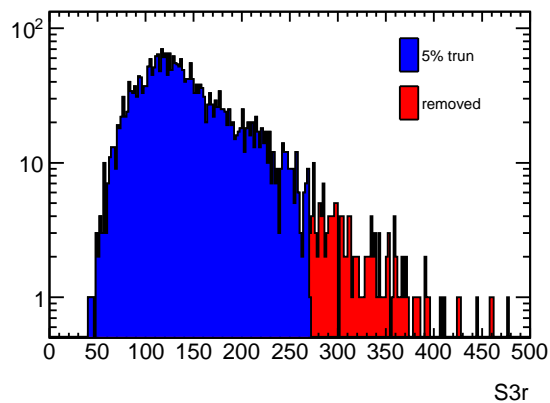


Figure D.4: Distribution of the energy deposition in the S3 in ADC channel units. The higher energy deposition events rejected by applying 5% truncation. The remaining events (MIP-like events) and the rejected ones are in blue and red, respectively.

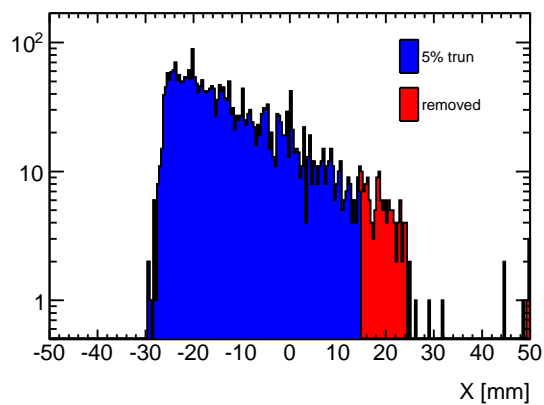


Figure D.5: Distribution of the x -coordinate of the impact point of the muon in the BC2 chamber. The events far from beam core are rejected by applying 5% truncation. The remaining events (beam core events) and rejected events are in blue and red, respectively.

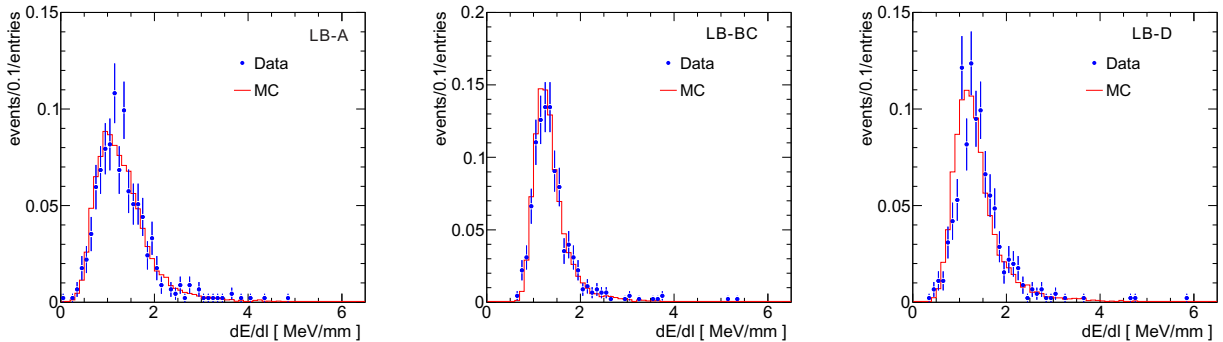


Figure D.6: The distribution of $dE/d\ell$ obtained in the LB-A, LB-BC, and LB-D layers using muons with energy equal to 20 GeV and η equal to 0.25. The data and MC events are shown by filled circles and solid lines, respectively. The distributions are normalized to one.

D.4 Results

D.4.1 $dE/d\ell$ distributions

The Figure D.6 shows the $dE/d\ell$ distributions in each layer in the case of muon beams with $\eta = 0.25$ and energy = 20 GeV. The path length ℓ is given by $\ell = r \cosh(\eta)$, where the r is the radius of each cell ($r = 300$ mm in LB-A, 840 mm in LB-BC and 380 mm in LB-D, respectively). We estimate the truncated mean $\langle dE/d\ell \rangle$ by applying the 1% truncation to these distributions. After that, we apply the constant fit to the distribution of truncated mean as a function of η .

D.4.2 Data/MC ratios

In Figure D.7, each top figure shows the $dE/d\ell$ distributions for data and MC events in each η . Each bottom figure shows the ratios of $dE/d\ell$ between data and MC events in each η . These figures are fitted by the constant parameter function since the ratios of $(dE/d\ell)^{data} / (dE/d\ell)^{MC}$ must be constant against η . However, we observe the large fluctuations in the distributions of ratios in some layers and beam energies. Table D.2 summarizes the resulting $\langle dE/d\ell \rangle$ of data and MC events, and ratios between them. The reduced χ^2 and χ^2 -probabilities are also reported. The fitting results produce bad χ^2 probabilities, especially at beam energy equal to 50 GeV and LB-D. These bad χ^2 probabilities indicate that the systematic effects of the measured points are larger than the statistical fluctuations.

First, we check whether these ratio distributions have η -dependence. We assume that the better χ^2 probability are given when we use the events in more center of beam if there is not η -dependence, since the fluctuation

Beam Energy	Layer	$dE/d\ell$ [GeV/m] Data	$dE/d\ell$ [GeV/m] MC	Ratio	χ^2 / NDF	Probability
20 GeV	LB-A	1.288 ± 0.009	1.333 ± 0.002	0.966 ± 0.007	5.18 / 4	26.9%
	LB-BC	1.327 ± 0.006	1.375 ± 0.002	0.966 ± 0.005	11.49 / 4	2.2%
	LB-D	1.381 ± 0.008	1.362 ± 0.002	1.014 ± 0.006	5.36 / 4	25.2%
50 GeV	LB-A	1.357 ± 0.010	1.414 ± 0.003	0.958 ± 0.007	11.56 / 4	2.1%
	LB-BC	1.416 ± 0.008	1.473 ± 0.003	0.962 ± 0.006	15.42 / 4	0.4%
	LB-D	1.463 ± 0.009	1.463 ± 0.003	1.001 ± 0.006	22.84 / 4	0.01%
100 GeV	LB-A	1.496 ± 0.009	1.520 ± 0.004	0.983 ± 0.006	9.78 / 4	4.4%
	LB-BC	1.557 ± 0.007	1.598 ± 0.004	0.970 ± 0.005	2.19 / 4	70.1%
	LB-D	1.591 ± 0.008	1.566 ± 0.004	1.017 ± 0.006	9.81 / 4	4.3%

Table D.2: Results obtained applying a constant fit to the experimental and simulated $\langle dE/d\ell \rangle$ distribution as a function of η . The results of the ratios are also reported. The last column shows the χ^2 probability of these last fits. Only statistical uncertainties are shown in this table.

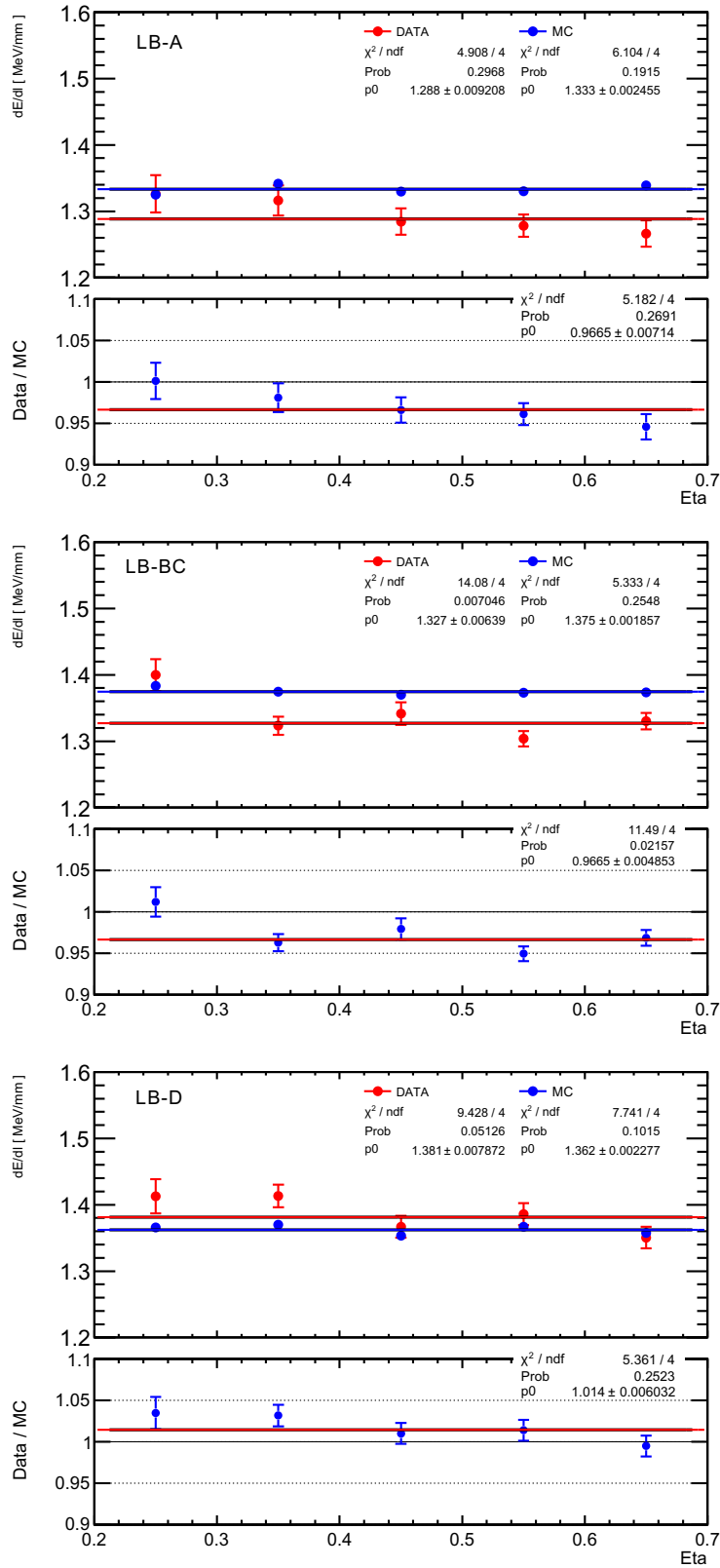


Figure D.7: Each top distribution shows the mean of dE/dl distribution in each η obtained using the CTB data (red points) and the MC samples (blue points) in LB-A, LB-BC, and LB-D, respectively. Each bottom distribution shows ratios between the mean of dE/dl distribution in the data and the mean of dE/dl distribution in the MC samples in the LB-A, LB-BC, and LB-D, respectively.

	Ratio	χ^2/NDF	Probability
not applied IP	1.001±0.006	22.84 /4	0.01%
IP < 2 σ	1.013±0.007	17.82 /4	0.13%
IP < 1 σ	1.009±0.010	12.98 /4	1.1%

Table D.3: Fitting results of the ratios of the $dE/d\ell$ between the data and the MC samples in each η point with the energy equal to 50 GeV and the LB-D layer.

with the path length become small. Then, for selecting the events in center of beam, we categorize the events based on the impact point on the tile calorimeter which are calculated to extrapolate track by using the beam chamber information. We check whether the fitting results make improve when we select events more center of beam. Table D.3 shows these results. In this table, the “not apply IP” means these values are estimated by using the distributions of ratios applied only the selection criteria. The “IP < 2 σ ” and the “IP < 1 σ ” mean these values are obtained by using the distributions of ratios in the events applied the selection criteria and within 2 σ and 1 σ of the impact point distributions, respectively. Figure D.8 shows the distributions of the ratios of $dE/d\ell$ between the data and the MC samples by using the beam core events. These results show that the η -dependence does not have a significant effect on the $dE/d\ell$ measurement and the χ^2 probabilities gives a bad value even if we select the more beam core events. Therefore, we conclude that the ratio distributions have larger fluctuations than the η -dependence in this region.

D.4.3 Non uniformity of cell responses

Since the fitting results show the bad fitting probabilities, we introduce the “non-uniformity” term which accounts for the difference of cell responses, for example optical contact between the scintillators in the calorimeter and the PMTs. We assume that this difference causes the large fluctuations of $dE/d\ell$ in data since the cell response is uniform in the MC samples. We measure the ratios between the data and the MC samples by applying maximum likelihood method with the parameters of non-uniformity s^ℓ and the mean of ratio distribution μ^ℓ .

We assume that the data/MC ratios follow Gaussian distributions with respect to the mean of the ratio, the maximum likelihood function is given as:

$$L = \prod_{c=1}^5 \frac{1}{\sqrt{(\sigma_c^{\ell 2} + s^{\ell 2}) 2\pi}} \exp \left[-\frac{1}{2} \left(\frac{R_c^\ell - \mu^\ell}{\sqrt{\sigma_c^{\ell 2} + s^{\ell 2}}} \right)^2 \right] \quad (\text{D.4.1})$$

where R_c^ℓ and σ_c^ℓ are the mean and the statistical errors of data/MC ratios, respectively. We use R_c^ℓ and σ_c^ℓ , and find values producing a maximum of L . These results are summarized in Table D.4 and Figure D.9. In LB-BC and E=20GeV, LB-BC and E=100GeV, the \hat{s}^ℓ are not able to be derived since the fitting can not converge due to statistical fluctuations.

Beam Energy	Layer	CTB		Cosmic	
		$\hat{\mu}^\ell$	\hat{s}^ℓ	$\hat{\mu}^\ell$	\hat{s}^ℓ
20 GeV	LB-A	0.966±0.007	0.012±0.007	0.968±0.003	0.028±0.003
	LB-BC	0.970±0.008	- (*)	0.974±0.002	0.020±0.002
	LB-D	1.014±0.006	0.003±0.018	1.005±0.003	0.024±0.003
50 GeV	LB-A	0.962±0.012	0.019±0.010		
	LB-BC	0.965±0.011	0.020±0.010		
	LB-D	1.001±0.013	0.026±0.011		
100 GeV	LB-A	0.983±0.005	0.014±0.009		
	LB-BC	0.970±0.005	- (*)		
	LB-D	1.015±0.009	0.014±0.008		

Table D.4: Fitting results of mean of $dE/d\ell$ ($\hat{\mu}^\ell$) and the fluctuation derived from the non uniformities in cell (\hat{s}^ℓ), respectively. The cosmic results are also shown. These results are obtained by using the maximum likelihood function. The (*) means that the minimum value of L can not be calculated since the fit does not converge due to statistical fluctuations.

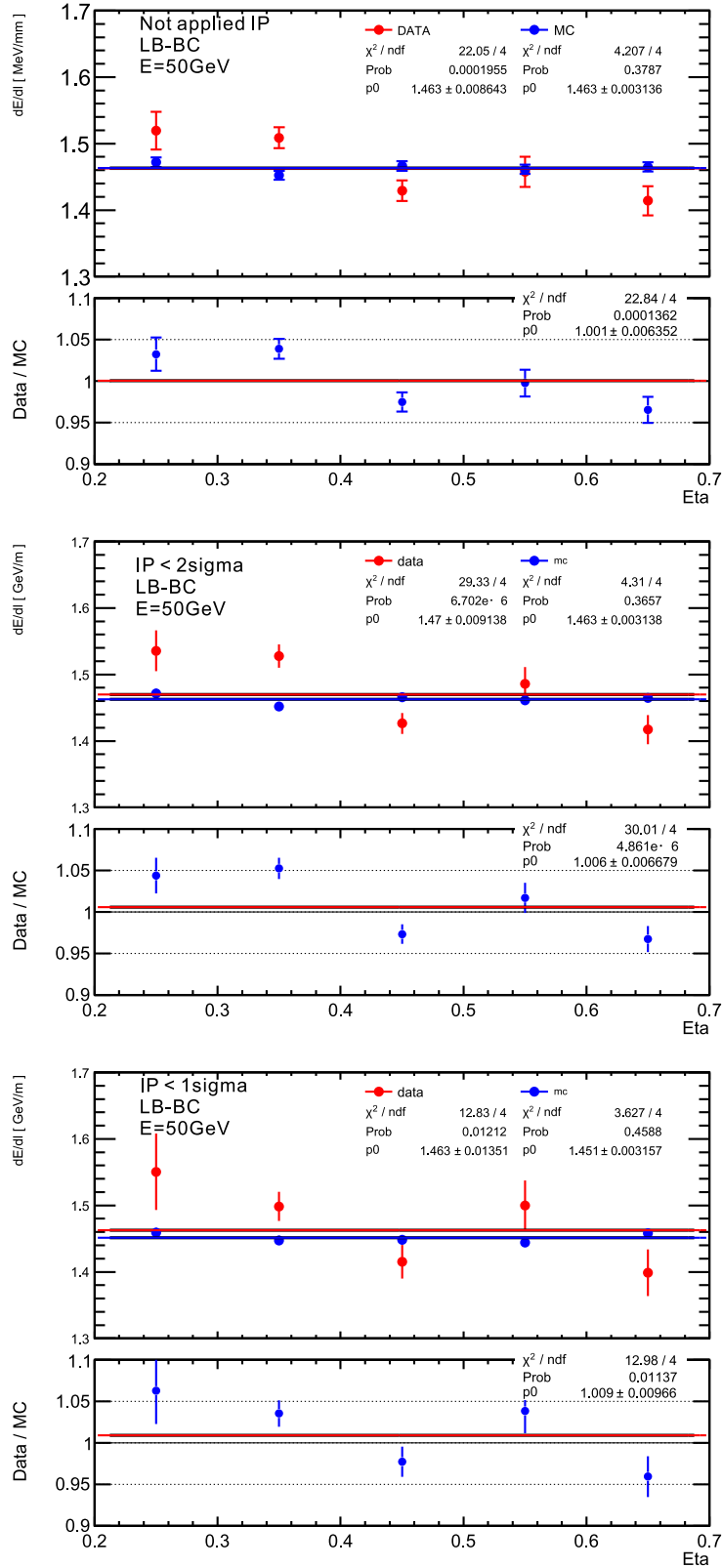


Figure D.8: Each top plot is the distribution of $dE/d\ell$ as a function of η obtained using the CTB data (red points) and the MC samples (blue points). Each bottom plot is the distribution of ratios of $dE/d\ell$ between the data and the MC samples. All figures are in LB-BC and $E = 50$ GeV. The upper figure shows the results applied only truncation to the hit position distribution. The center figure shows results applied truncation to the hit position and required the events within two sigma of the distribution of the impact point. The lower figure shows results applied truncation to the hit position and required the events within one sigma of the distribution of the impact point.

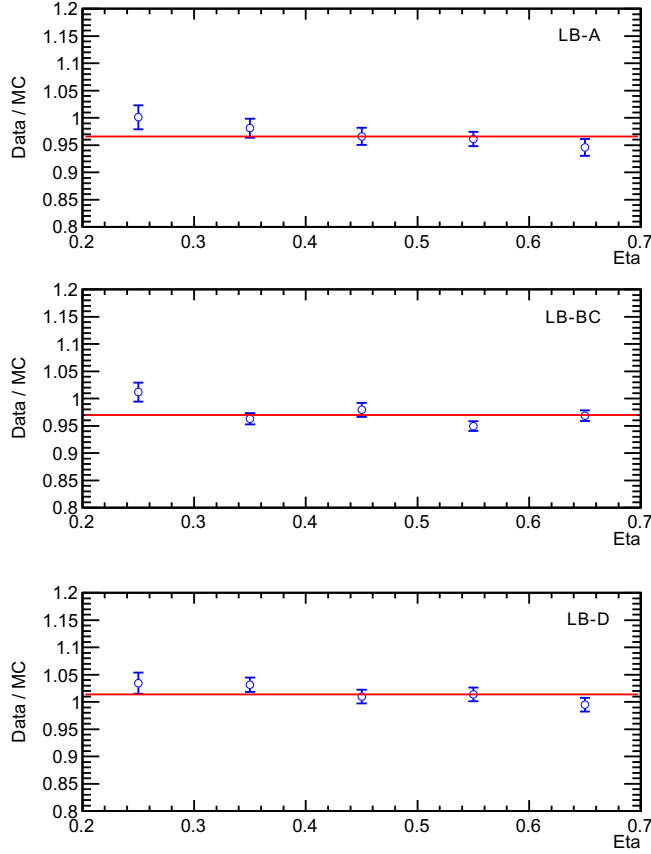


Figure D.9: The distribution of ratios between the data and the MC samples and fitting results obtained applying the Maximum Likelihood Method for the LB-A, LB=BC and LB-D layers , respectively. The beam energy is equal to 20 GeV.

D.4.4 Systematic uncertainties

We consider the followings as systematic uncertainties which affect the $dE/d\ell$ measurements.

- Pile up
- Response uniformity in cell
- Pion contamination

Pile up

When we estimate the uncertainties of the pile up, we change the cut value of truncation from 1% to 10%. Figure D.10 show the results of fitting to the ratio distributions of $dE/d\ell$ by using the maximum likelihood method in each value of truncation. In addition, the results for each layer and each truncation value in the energy equal to 20 GeV are shown in Table D.5. We quote an uncertainty by taking maximum $\hat{\mu}^\ell$ difference between truncation value. The effect of pile up is estimated to be less than 0.6%, and is smaller than the statistical fluctuations.

Response uniformity in cell

If the response differs from point by point in one cell, the difference of cell response affects the measurement of energy depositions in layer. We separated three regions in beam by using beam chamber information as Figure D.12, and estimate this uncertainty by maximum $\hat{\mu}^\ell$ difference between each beam region. This results are showed in Figure D.13. The systematic uncertainty of response uniformity a cell is estimated to be less than 1.4%, and is smaller than the statistical fluctuations.

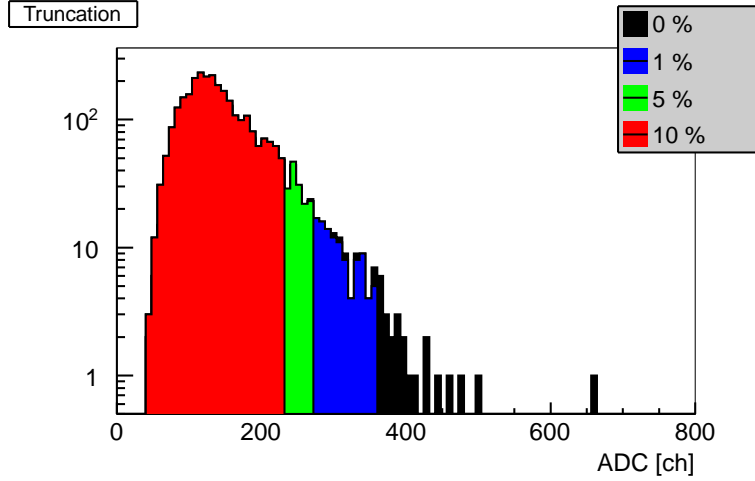


Figure D.10: Distribution of energy deposition in S3 and the region separated by the truncation at 10%, 5%, and 1%, respectively.

Pion contamination

We check effect of energy fluctuation caused by pion decay in flight by using a toy MC simulation. The fluctuation of muon energy is estimated to be less than 0.2%. This uncertainty is negligible against the statistical uncertainty in this CTB data. However we must discuss this contaminations with the beam experts because this MC condition may have some difference from the CTB condition.

Summary of systematic uncertainties

We estimate the systematic uncertainties of 1)pile up, 2)response of a cell and 3)pion contamination. As for the first two item, we do not quote any numbers because the systematic effects are not visible due to the limited statistics. Then, we are planing to estimate the systematic uncertainties by using MC samples now. In addition, we have to consider the other sources of systematic uncertainties, for example the beam momentum spread and truncation of the $dE/d\ell$.

D.5 Conclusion

We compared the CTB data with the MC events by measuring $dE/d\ell$. The results show 1)the fluctuations derived from non uniformity of the cell response are about 2%, 2)the response of the LB-D in the tile calorimeter is different from that of the LB-A and LB-BC layer by about 4%. We quote systematic uncertainties tentatively, but these are need to be revised using MC samples to compensate for statistical shortage. In addition, we have to estimate any other systematic uncertainties e.g. the beam momentum spread and the effect of truncation of $dE/d\ell$. These results are consistent with those of the cosmic-ray analysis [73].

	Data/MC 10% truncation	Data/MC 5% truncation	Data/MC 1% truncation	sys.(%)
LB-A	0.966 ± 0.006	0.966 ± 0.007	0.972 ± 0.007	0.6%
LB-BC	0.969 ± 0.007	0.966 ± 0.004	0.967 ± 0.005	0.3%
LB-D	1.013 ± 0.010	1.014 ± 0.006	1.017 ± 0.006	0.3%

Table D.5: Fitting results by using the maximum likelihood method to distributions of ratio of $dE/d\ell$ between the CTB data and the MC samples applied truncation at 10%, 5% and 1% to each distribution of scintillator. The difference of the fitting results are estimated as the effects of systematic uncertainties derived from the pile up events.

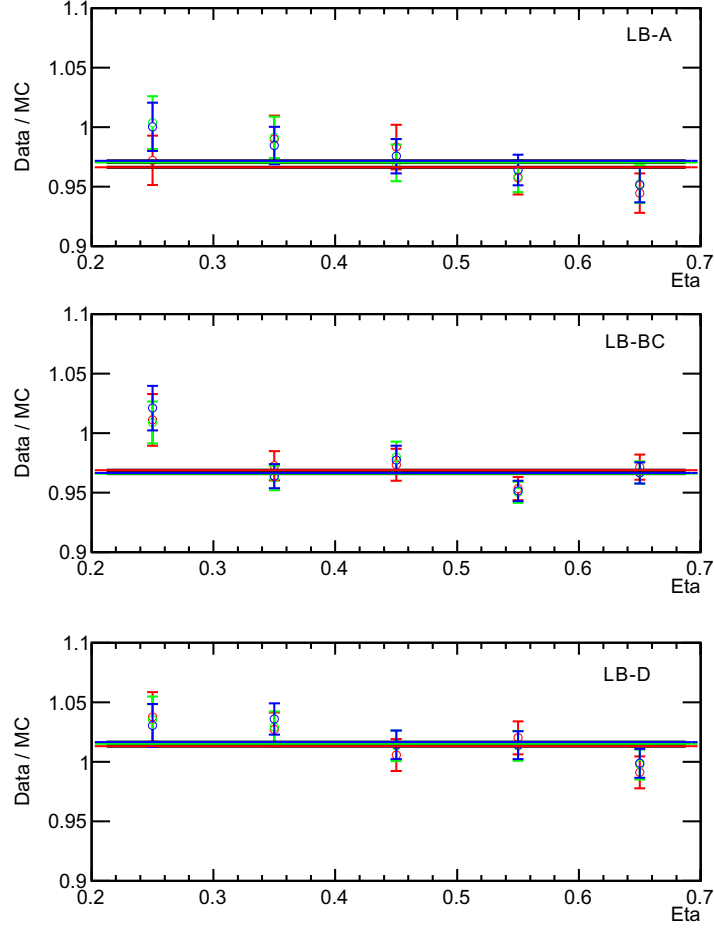


Figure D.11: Fitting results of ratio distributions by using maximum likelihood method in each truncation cut. The top figure shows the results in the LB-A, the middle figure shows in the LB-BC and the bottom figure shows in the LB-D, respectively. The red points correspond to the results in the 10% truncation, the green points correspond to the 5% truncation and the blue points correspond to the 1% truncation, respectively.

	Data/MC Left in beam	Data/MC Center in beam	Data/MC Right in beam	sys.(%)
LB-A	0.993 ± 0.019	0.956 ± 0.008	0.985 ± 0.014	1.4%
LB-BC	0.970 ± 0.018	0.972 ± 0.009	0.957 ± 0.008	1.4%
LB-D	1.010 ± 0.016	1.012 ± 0.007	1.026 ± 0.015	1%

Table D.6: Fitting results by applying the maximum likelihood method to the data/MC distribution. We separate the beam into three region to be same number of events in each region. The difference of the fitting results are estimated as the effects of systematic uncertainties derived from the difference of response in a cell.

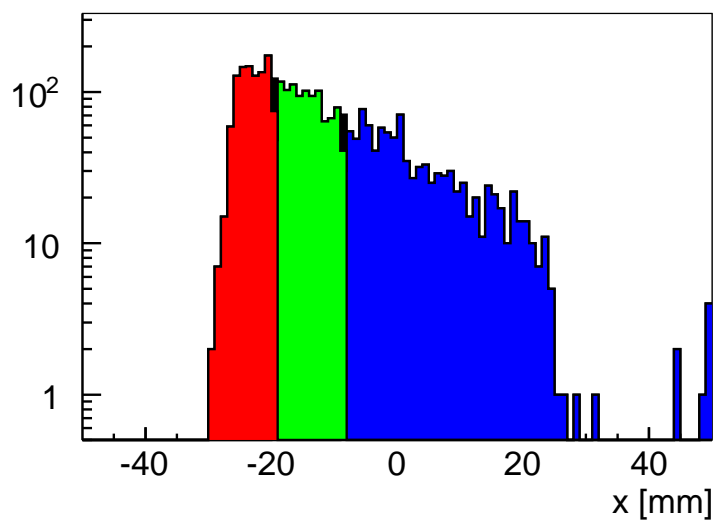


Figure D.12: Distribution of the hit position in BC2 and the region separated to be the same number of events in each region. We estimate the systematic uncertainties derived from the difference of response in a cell.

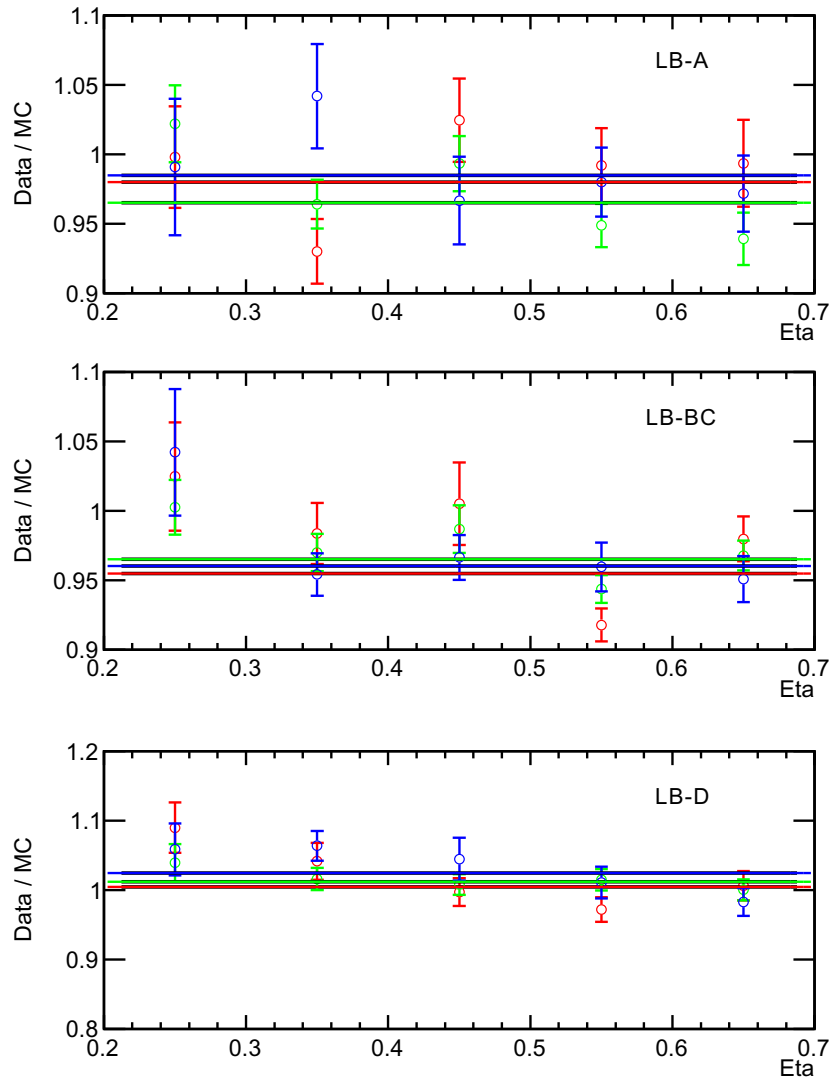


Figure D.13: Fitting results of ratio distributions by using maximum likelihood method in each region of hit position in BC2. The top figure shows the results in the LB-A, the middle figure shows in the LB-BC and the bottom figure shows in the LB-D, respectively. The red points correspond to the results in the left region in the beam position along beam line, the green points correspond to the center region, and the blue points correspond to the right region, respectively.

Bibliography

- [1] S. L.Glashow, *Partial-symmetries of weak interactions*, Nucl. Phys **22** (1961) 579.
- [2] S.Weinberg, *A Model of Leptons*, Phys. Rev. Lett. **19** (1967) 1264–1266.
- [3] H. Miyazawa, *Baryon Number Changing Currents*, Prog. Theor. Phys. **36** (6) (1966) 1266–1276.
- [4] P. Ramond, *Dual Theory for Free Fermions*, Phys. Rev. **D3** (1971) 2415–2418.
- [5] Y. A. Gol’fand and E. P. Likhtman, *Extension of the Algebra of Poincare Group Generators and Violation of p Invariance*, JETP Lett. **13** (1971) 323–326. [Pisma Zh.Eksp.Teor.Fiz.13:452-455,1971].
- [6] A. Neveu and J. H. Schwarz, *Factorizable dual model of pions*, Nucl. Phys. **B31** (1971) 86–112.
- [7] A. Neveu and J. H. Schwarz, *Quark Model of Dual Pions*, Phys. Rev. **D4** (1971) 1109–1111.
- [8] J. Gervais and B. Sakita, *Field theory interpretation of supergauges in dual models*, Nucl. Phys. **B34** (1971) 632–639.
- [9] D. V. Volkov and V. P. Akulov, *Is the Neutrino a Goldstone Particle?*, Phys. Lett. **B46** (1973) 109–110.
- [10] J. Wess and B. Zumino, *A Lagrangian Model Invariant Under Supergauge Transformations*, Phys. Lett. **B49** (1974) 52.
- [11] J. Wess and B. Zumino, *Supergauge Transformations in Four-Dimensions*, Nucl. Phys. **B70** (1974) 39–50.
- [12] T. Kaluza, *Zum Unitatsproblem in der Physik*, Math. Phys. (1921) 966–972.
- [13] O. Klein, *Quantentheorie und funfdimensionale Relativitatstheorie*, Z.Phys. (1926) 895–906.
- [14] N.Arkani-Hamed, S.Dimopoulos, and G.Dvali, *The hierarchy problem and new dimensions at a millimeter*, Phys. Lett. **B429** (1998) 263.
- [15] L.Randall and R.Sundrum, *Large Mass Hierarchy from a Small Extra Dimension*, Phys. Rev. Lett. **83** (1999) 3370.
- [16] N.Arkani-Hamed, H.C.Cheng, B.A.Dobrescu, and L.J.Hall, *Self-breaking of the standard model gauge symmetry*, Phys.Rev. **D62** (2000) 096006.
- [17] B.A.Dobrescu and E.Poppitz, *Number of Fermion Generations Derived from Anomaly Cancellation*, Phys.Rev.Lett **87** (2001) 031801.
- [18] T.Appelquist, B.A.Dobrescu, E.Ponton, and H.U.Yee, *Proton stability in six dimensions*, Phys.Rev.Lett. **87** (181802) 2001.
- [19] T.Appelquist, B.A.Dobrescu, E.Ponton, and H.U.Yee, *Neutrinos vis-a-vis the six-dimensional standard model*, Phys.Rev. **D65** (2002) 105019.
- [20] M.Baak, M.Goebel, J.Haller, A.Hoecker, D.Kennedy, K.Mönig, M.Schott, and J.Setlzer, *Updated Status of the Global Electroweak Fit and Constraints on New Physics*, arXiv:1107.0975 [hep-ph].
- [21] ALEPH, DELPHI, L3, OPAL, SLD, the LEP Electroweak Working Group and the SLD Electroweak and Heavy Flavour Groups Collaboration, *Precision Electroweak Measurements on the Z Resonance*, arXiv:0509008 [hep-ex].

- [22] P. D. Group Phys.Rev **D86** (2012) 010001.
- [23] Tevatron Electroweak Working Group and CDF and D0 Collaborations Collaboration, *Updated Combination of CDF and D0 Results for the Mass of the W Boson*, arXiv:0908.1374 [hep-ex].
- [24] The Tevatron Electroweak Working Group1 for the CDF and D0 Collaborations Collaboration, *Combination of CDF and D0 Results on the Width of the W boson*, arXiv:1003.2826 [hep-ex].
- [25] The Tevatron Electroweak Working Group for the CDF and D0 Collaborations Collaboration, *Combination of CDF and D results on the mass of the top quark using up to 5.6 fb⁻¹ of data*, arXiv:1007.3178 [hep-ex].
- [26] A.H. Chamseddine, R.L. Arnowitt and P. Nath, Phys. Rev. Lett. **49** (1982) 970; R. Barbieri, S. Ferrara and C.A. Savoy, Phys. Lett. **B119** (1982) 343; L.E. Ibanez, Phys. Lett. **B118** (1982) 73; L.J. Hall, J.D. Lykken and S. Weinberg, Phys. Rev. **D27** (1983) 2359; N. Ohta, Prog. Theor. Phys. **70** (1983) 542.
- [27] G. L. Kane, C. F. Kolda, L. Roszkowski, and J. D. Wells, *Study of constrained minimal supersymmetry*, Phys. Rev. **D49** (1994) 6173, arXiv:hep-ph/9312272 [hep-ph].
- [28] D. Alves, E. Izaguirre, and J. Wacker, *Where the Sidewalk Ends: Jets and Missing Energy Search Strategies for the 7 TeV LHC*, arXiv:1102.5338 [hep-ph].
- [29] D. S. M. Alves, E. Izaguirre, and J. Wacker, *Where the Sidewalk Ends: Jets and Missing Energy Search Strategies for the 7 TeV LHC*, arXiv:1102.5338 [hep-ph].
- [30] D.Hooper and S.Profumo, *Dark matter and collider phenomenology of universal extra dimensions*, Phys. Repo **453** (2007) 29–115.
- [31] CMS Collaboration, *Search for Supersymmetry at the LHC in Events with Jets and Missing Transverse Energy*, Phys. Rev. Lett **107** (2011) 221804.
- [32] CMS Collaboration, *Search for new physics with single-leptons at the LHC*, CMS-PAS-SUS-11-015.
- [33] ATLAS Collaboration, *Search for squarks and gluinos using final states with jets and missing transverse momentum with the ATLAS detector in proton-proton collisions*, Phys. Lett. **B710** (2012) 67.
- [34] ATLAS Collaboration, *Search for supersymmetry in final states with jets, missing transverse momentum and one isolated lepton in $\sqrt{s} = 7$ TeV pp collisions using 1 fb⁻¹ of ATLAS data*, Phys. Rev. **D85** (2012) 012006.
- [35] C. Lin, *A Search for Universal Extra Dimensions in the Multi-Lepton Channel from Proton-Antiproton Collisions at $\sqrt{s} = 1.8$ TeV*, .
- [36] CERN Collaboration, L. Evans and P. Bryant, *LHC Machine*, JINST **3** (2008) S08001.
- [37] *Calorimeter Calibration*, <http://www.physics.smu.edu/~dgoldin/LArCalo/Calibration/Calibration.html>.
- [38] ATLAS Collaboration, H. Spieler, *Electronics and data acquisition*, Nucl.Inst.Meth.A **666** (2012) 197–222.
- [39] J.M.Campbell, J.W.Huston, and W.J.Stirling, *Hard Interactions of Quarks and Gluons: a Primer for LHC Physics*, Rept.Prog.Phys. **70** (2007) 89, arXiv:0611148 [hep-ph].
- [40] M. L. Mangano, M. Moretti, F. Piccinini, R. Pittau, and A. D. Polosa, *ALPGEN, a generator for hard multiparton processes in hadronic collisions*, JHEP **0307** (2003) 001, arXiv:hep-ph/0206293 [hep-ph].
- [41] S. Frixione and B. R. Webber, *Matching NLO QCD computations and parton shower simulations*, JHEP **0206** (2002) 029, arXiv:hep-ph/0204244 [hep-ph].
- [42] G. Corcella, I. Knowles, G. Marchesini, S. Moretti, K. Odagiri, et al., *HERWIG 6: An Event generator for hadron emission reactions with interfering gluons (including supersymmetric processes)*, JHEP **0101** (2001) 010, arXiv:hep-ph/0011363 [hep-ph].
- [43] J. Alwall, M. Herquet, F. Maltoni, O. Mattelaer, and T. Stelzer, *MadGraph 5 : Going Beyond*, JHEP **1106** (2011) 128, arXiv:1106.0522 [hep-ph].

- [44] ATLAS Collaboration, *Properties of Jets and Inputs to Jet Reconstruction and Calibration with the ATLAS Detector Using Proton-Proton Collisions at $\sqrt{s} = 7$ TeV*, ATLAS-CONF-2010-053.
- [45] M. Cacciari, G. P. Salam, and G. Soyez, *The anti- k_T jet clustering algorithm*, JHEP **04** (2008) 063, [arXiv:0802.1189](https://arxiv.org/abs/0802.1189) [hep-ph].
- [46] M. Cacciari and G. P. Salam, *Dispelling the N^3 myth for the k_T jet-finder*, Phys. Lett. **B641** (2006) 57–61, [arXiv:hep-ph/0512210](https://arxiv.org/abs/hep-ph/0512210).
- [47] ATLAS Collaboration, G. Aad et al., *Luminosity Determination in pp Collisions at $\sqrt{s} = 7$ TeV Using the ATLAS Detector at the LHC*, Eur.Phys.J. **C71** (2011) 1630, [arXiv:1101.2185](https://arxiv.org/abs/1101.2185) [hep-ex].
- [48] ATLAS Collaboration, G. Aad et al., *Improved Luminosity Determination in pp Collisions at $\sqrt{s} = 7$ TeV using the ATLAS Detector at the LHC*, ATL-CONF-2012-080.
- [49] ATLAS Collaboration, *Measurement of the charge asymmetry in top quark pair production in pp collisions at $\sqrt{s} = 7$ TeV using the ATLAS detector*, Euro.Phys.Jour.C **72** (2012) 2039.
- [50] P. M. Nadolsky and et. al, *Implications of CTEQ global analysis for collider observable*, Phys.Rev.D **78** (2008) 013004.
- [51] A. D. Martin, W. J. Stirling, R. S. Thorne, and G. Watt, *Parton distributions for the LHC*, Euro.Phys.Jour.C **63** (2009) 189.
- [52] ATLAS Collaboration, *Search for Supersymmetry with jets and missing transverse momentum and one lepton at $\sqrt{s} = 7$ TeV*, ATLAS-CONF-2011-090 (2011) .
- [53] M. Kramer, A. Kulesza, R. van der Leeuw, M. Mangano, S. Padhi, T. Plehn, and X. Portell, *Supersymmetry production cross sections in pp collisions at $\sqrt{s} = 7$ TeV*, [arXiv:1206.2892](https://arxiv.org/abs/1206.2892) [hep-ph].
- [54] H.-C. Cheng, K. T. Matchev, and M. Schmaltz, *Bosonic supersymmetry? Getting fooled at the CERN LHC*, Phys.Rev.D **66** (2002) 056006.
- [55] W. Lampl, S. Laplace, D. Lelas, P. Loch, H. Ma, S. Menke, S. Rajagopalan, D. Rousseau, S. Snyder, and G. Unal, *Calorimeter Clustering Algorithms: Description and Performance*, ATL-LARG-PUB-2008-002. ATL-COM-LARG-2008-003.
- [56] ATLAS Collaboration, G. Aad et al., *Expected electron performance in the ATLAS experiment*, Cern-phys-pub-2011-006, 2011.
- [57] ATLAS Collaboration, G. Aad et al., *Electron performance measurements with the ATLAS detector using the 2010 LHC proton-proton collision data*, [arXiv:1110.3174](https://arxiv.org/abs/1110.3174) [hep-ex].
- [58] CDF Collaboration, *First measurement of inclusive W and Z cross section from Run II of the Fermilab Tevatron Collider*, Phys. Rev. Lett. **94** (2005) 091803, [arXiv:0406078](https://arxiv.org/abs/0406078) [hep-ex].
- [59] D0 Collaboration, *Measurement of the shape of the boson rapidity distribution for $p\bar{p} \rightarrow Z/\gamma^* \rightarrow e^+e^- + X$ events produced at \sqrt{s} of 1.96 TeV*, Phys. Rev. **D76** (2007) 012003, [arXiv:0702025](https://arxiv.org/abs/0702025) [hep-ex].
- [60] ATLAS Collaboration, T. Cornelissen, M. Elsing, I. Gavrilenko, W. Liebig, E. Moyse, and A. Salzburger, *The new ATLAS Track Reconstruction (NEWT)*, Jour.Phys.CONf **119** (2008) 032014.
- [61] S. Hassani, L. Chevalier, E. Lancon, J. F. Laporte, R. Nicolaidou, and A. Ouraou, *A muon identification and combined reconstruction procedure for the ATLAS detector at the LHC using the (MUONBOY, STACO, MuTag) reconstruction packages*, Nucl.Inst.Meth. **A572** (2007) 77–79.
- [62] ATLAS Collaboration, *Muon reconstruction efficiency in reprocessed 2010 LHC proton-proton collision data recorded with the ATLAS detector*, ATLAS-CONF-2011-063. <https://cdsweb.cern.ch/record/1345743>.
- [63] ATLAS Collaboration, *A measurement of the ATLAS muon reconstruction and trigger efficiency using J/ψ decays*, ATLAS-CONF-2011-021. <https://cdsweb.cern.ch/record/1336750>.
- [64] ATLAS Collaboration, *Performance of the ATLAS muon trigger in 2011*, ATLAS-CONF-2011-099. <http://cds.cern.ch/record/1462601>.

- [65] ATLAS Collaboration, *Jet energy scale and its systematic uncertainty in proton-proton collisions at $\sqrt{s} = 7$ TeV with ATLAS 2010 data*, ATL-CONF-2011-032.
- [66] ATLAS Collaboration, *Determination of the jet energy measurement uncertainty using photon-jet events in proton proton collisions at $\sqrt{s} = 7$ TeV*, ATLAS-CONF-2011-031.
- [67] ATLAS Collaboration, *Measurements of multijet production cross sections in proton-proton collisions at 7 TeV center-of-mass energy with the ATLAS Detector*, ATLAS-CONF-2011-031.
- [68] ATLAS Collaboration, *Validation of the ATLAS jet energy scale uncertainties using tracks in proton-proton collisions at $\sqrt{s} = 7$ TeV*, ATLAS-CONF-2011-067.
- [69] G.Piacquadio and C.Weiser, *A new inclusive secondary vertex algorithm for b-jet tagging in ATLAS*, Jour.Phys.Conf **119** (2008) 032032.
- [70] ATLAS Collaboration, *Performance of Missing Transverse Momentum Reconstruction in Proton-Proton Collisions at $\sqrt{s} = 7$ TeV with ATLAS*, Eur.Phys.Jour.C **72** (2012) 1844.
- [71] G. Cowan, K. Crammer, E. Gross, and O. Vitells, *Asymptotic formulae for likelihood-based tests of new physics*, Euro.Phys.Jour.C **71** (2011) 1554.
- [72] A.Wald, *Tests of a Statistical Hypotheses Concerning Several Parameters When the Number of Observations is Large*, Trans.Ame.Meth.Soci **54** (1943) 426-482.
- [73] ATLAS Collaboration, *Beamline instrumentation in the 2004 combined ATLAS testbeam*, ATL-TECH-PUB-2005-001 (2005) .
- [74] ATLAS Collaboration, *Calibration of the ATLAS hadronic barrel calorimeter TileCal using 2008, 2009 and 2010 cosmic rays data*, ATL-TECH-PUB-2005-001 (2005) .
- [75] ATLAS Collaboration, *The ATLAS Tile Calorimeter performance at the LHC*, ATL-TILECAL-PROC-2011-004 (2011) .